Physics of Sound Wave Radiation from Vibrating Surfaces

John Coffey, Cheshire, UK.

March 2015, minor revision June 2015

Key words: acoustics, vibration, sound wave, Helmholtz's equation, radiation, far-field, near-field, spherical wave, monopole, dipole, Green's theorem, Kirchhoff & Rayleigh-Sommerfeld theory, computer model, prolate & oblate spheroid, spheroidal wave functions, ellipsoid, integral equation

1 Introduction

This article is the eighth in a series describing my personal investigations into acoustics. Unlike other articles on *www.mathstudio.co.uk* it is not specifically related to violins and violas. It deals with the properties of sound around a vibrating object and methods for calculating the wave field radiated outwards to a listener. It is not an original research or review article, but rather an account of my own studies, reading, practical and numerical experiments and computer programming. The subject has been studied extensively for well over 100 years and there is a vast literature and comprehensive textbooks such as by Morse and Ingard and by Allan Pierce. It turns out that there are many subtleties in developing a scheme for calculating the sound field from a general object. My investigations probably retrace well trodden paths which have led to the boundary element method (BEM) which is the leading method today. In June 2015 I revised §2 and 3 to change some notation and enlarge on a few points.

When we hear a voice, a musical instrument or the radio, the sound reaching our ears is coloured by reflections and absorption within the room. This article, however, deals only with the radiation of sound from the source direct to the listener, without any reflection or absorption. The approach is through the physics and mathematics of acoustics, particularly the wave equation. It is usual to relate the wavelength of sound to the physical size of the object. 'Low frequency' therefore means that the object is small compared with the wavelength, and 'high' that the wavelength is small compared with both the object and its major features. Similarly 'near' and 'far' refer to distance from the object measured in wavelengths. Sound's behaviour at these two limits of size-to-wavelength ratio is quite different. At low frequencies, if the object vibrates so that all parts of its surface move radially in and out in phase, sound is radiated weakly into all directions, irrespective of the detailed structure of the object. If half the object moves out while the other half moves inward, it acts as a dipole and radiates forwards and backwards along the axis of motion, but little to the sides. At high frequencies, in contrast, the shape of the object and its vibrational mode can have a strong influence on the sound field, causing it to vary markedly with direction. Large objects also radiate more energy, so the signal received at a distance is stronger.

By way of an index, here is a note on the eleven sections in the body of the article. §12 is a summary of the salient points covered, and as such it complements the outline here. In addition are 7 Appendices, in §13 to 19, which contain much of the mathematical background and detail.

- Section §2 describes the basic properties of plane and spherical waves and their representation by mathematics. There is a short derivation of the wave equation for plane waves and a point source, and a statement of Helmholtz's equation for continuous sinusoidal waves. It introduces the displacement potential ϕ which is proportional to acoustic pressure, and the particle displacement ξ which is proportional to particle velocity. These quantities features throughout the article.

- §3 applies the wave equation in the low frequency limit and in the near field of a small source. Outwards travelling waves have the pressure and particle displacement in phase with each other. However there is also an out-of-phase reactive component which locks up energy immediately next to the object. This is the reason why small objects cannot produce a loud sound at low frequencies. It has implications for the design of musical instruments.

- §4 deals with two and three simultaneous sources of sound to illustrate the phenomenon of constructive and destructive interference between wave trains. Interference is demonstrated by a simple home experiment with loudspeakers and a microphone.

- §5 comments on exact solutions of the wave equation which are valid for all wavelengths. Regrettably, exact solutions are known only for the most simply shaped objects. Such solutions are found by separation of the variables in an appropriate co-ordinate system corresponding to an object of simple geometry. I describe the case of spherical waves in spherical co-ordinates, while Appendix 4, §16, outlines the corresponding theory for prolate (elongated) and oblate (squashed) spheroids. Appendix 7, §19, introduces the yet more general ellipsoids. A separate document on *www.mathstudio.co.uk* gives the exact solution for the companion situation of small, point-like source vibrating in the surface of an otherwise rigid sphere (added July 2015).

- §6 opens by stating Green's vector theorem which is the basis of two classic formulations for modelling sound radiation, namely the Kirchhoff and Rayleigh-Sommerfeld formulations. These links the field $\phi(Q)$ at any listening point Q to the distribution of potential ϕ_0 and/or its normal derivative over the surface of the vibrating object. They were originally devised to explain light diffraction at a small hole in an illuminated screen. Kirchhoff theory is not inherently restricted to planar surfaces, but the Rayleigh-Sommerfeld theory is. I have written a computer program to implement both the Kirchhoff and Rayleigh-Sommerfeld formulae for a convex object of fairly arbitrary shape. It models the object's surface by a mesh of triangular elements. Details of supporting calculations are given in Appendix 1, §13. All variants of the Kirchhoff and Rayleigh-Sommerfeld theories have significant limitations which are explained in §6 and elsewhere throughout the article.

- §7 describes validation of the Rayleigh-Sommerfeld computer program by comparison with cases of a planar radiating surface which can be evaluated analytically. Several numerical examples show that it produces results very close to the well known analytical results for a vibrating circular piston – a classic piece of physics.

- §8 uses the Rayleigh-Sommerfeld program to try to account for features seen in the two- and three-source experiments of §4.

- The remainder of the article is concerned with finite convex bodies. To keep things fairly simple, from here to the end of the article I concentrate on the 'breathing mode' in which all parts of the object move in and out in phase. §9 returns to Kirchhoff's formulation of Green's theorem to show in some detail how it applies to radiation from a symmetrically pulsating sphere, and a spherical sector surrounded by a baffle plate. There is supporting discussion of the integrals in Appendices 2 and 3, §14 and 15.

- §10 gives examples of applying the computer program in the Kirchhoff formulation to radiation from spheres then to prolate and oblate spheroids in cases where the exact pressure and displacement over the surface are both given. The program should in principle reproduce the exact field, and I have found that this is closely to be true in all cases examined except one. Working with Helmholtz'equation in spheroidal co-ordinates is not easy; the background is provided in Appendix 4, §16. I also give examples of a version of the Rayleigh-Sommerfeld formulation in which the surface integral is restricted to only those triangular mesh elements which can be seen by the listener at Q – that is, they are within the geometric cone of rays subtended at Q. Though this simplified model has little theoretical justification, it appears to work fairly well and may be a useful approximation.

- In the final substantive section, §11, I first report some finite element modelling of hollow elastic spheroids to demonstrate that the breathing mode can actually occur, and to see how the displacement varies over the surface. I then comment briefly on other approaches to solving the wave equation and boundary conditions. Much research has gone into the boundary integral equation approaches. Appendix 6 in §18 gives some introductory background through example of a one-dimensional integral equation. The remainder of §11 discusses some personal ideas for relating the surface pressure to the surface normal displacement, which is crucial to extending Kirchhoff theory to arbitrary convex bodies without baffles. One idea relates surface pressure and displacement to the size and aspect ratio of the object. This calls upon ellipsoidal co-ordinates, which are introduced in Appendix 7, §19. A second idea has been to look for a relation linked through the local curvature of the wavefronts. Calculations to explore – and eventually reject – this conjecture given in Appendix 5, §17. The conjecture, though almost certainly false, is nevertheless interesting in its own right.

Figures are numbered consecutively through the whole article. Equations are numbered consecutively through the main body, but in the appendices the numbering starts afresh with each appendix. Thus Eq A5.3 in the third numbered equation in Appendix 5. About 40% of the article is in these appendices, which start on page 91.

In June 2015 I changed some of the explanation in §2 and 3, adding more detail on the background physics of plane and spherical waves.

2 Basic physics of sound waves

2.1 Plane waves

Before studying the wave equation for a small spherically symmetric source, let us first derive the acoustic wave equation for the simpler case of a plane wave, and use it to see the relation between particle displacement, particle velocity and acoustic (excess) pressure.

Suppose we have a wide space of still air – it could be air in a straight pipe – in which sound travels only along the x direction, and consider an element of air between positions x and $x + \delta x$ (Figure 1, top panel). If the air were still the static pressure would be p_0, but the air is in motion so the pressure is a function of time and position. The excess pressure $p(t) - p_0$ is called the acoustic pressure. The top panel in Figure 1 shows the instantaneous situation when the pressures on each side of the air element are the same. A moment later the pressure has increased to the left, so that an unbalanced force $A\delta p$ is applied to the left face, A being the sectional area. This net force causes two changes to the air element:

1. it accelerates the element to the right.
2. it compresses the element.

The displacement $\xi(t)$ varies with x. The acceleration increases the kinetic energy of the element, and the compression against elastic restoring forces increases its potential energy. Each of these effects contributes a mathematical relation which, when combined, produce the wave equation. All oscillating systems involve the interplay of so-called inertial (mass-related) and elastic forces.

Take the acceleration first. The mass of the element is $\rho A\,\delta x$ where ρ is the density at pressure p. By Newton's Second Law its centre of mass is given acceleration:

$$A\,\delta p \;=\; -\rho A\,\delta x\,\frac{\partial^2 \xi}{\partial t^2} \qquad \text{so} \quad -\frac{\delta p}{\delta x} \;\to\; -\frac{\partial p}{\partial x} \;=\; \rho\,\frac{\partial^2 \xi}{\partial t^2}\,. \tag{1}$$

The negative sign is introduced because the pressure gradient is negative when the acceleration is to the right.

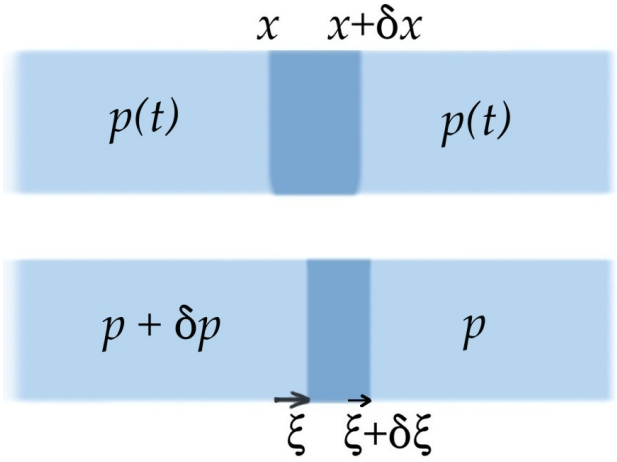

Figure 1: An element of air between x and $x + \delta x$ before and after the pressure is increased by δp.

The second equation involves the elasticity of the fluid. For a gas we use the state law for a perfect gas under adiabatic conditions, that for a fixed mass occupying volume V, pV^γ is constant. γ is the ratio of the specific heats c_p/c_v. Differentiating,

$$\frac{\delta p}{p} \;=\; -\gamma\,\frac{\delta V}{V}\,.$$

The volume strain $\delta V/V$ (the fractional change in volume) is called the 'dilatation', Δ. The elastic constant is the bulk modulus, K, defined as the pressure change needed to produce unit volume strain:

$$K \;\equiv\; \left|\frac{\delta p}{\delta V/V}\right| \;\equiv\; \frac{\delta p}{\Delta} \qquad \text{so} \quad K = \gamma p\,.$$

To put some numbers on this, the atmospheric pressure P is 1 bar $= 10^5$ Pa and c_p/c_v is 7/5 for the diatomic molecules N_2 and O_2 which make up most of air. K is therefore about $1\cdot 4\times 10^5$ Pa.

The initial volume of the element is $V = A\,\delta x$. It contains mass $m = \rho A\,\delta x$ which remains constant under compression. Since the element's length after the pressure increase is $\delta x\left(1+\frac{\partial\xi}{\partial x}\right)$, the volume change $\delta V = A\,(\partial\xi/\partial x)\,\delta x$ and the fractional change is

$$\Delta \;=\; \frac{\partial \xi}{\partial x}\,.$$

Note that when δp is positive, as in Figure 1, both δV and $\partial\xi/\partial x$ are negative. We therefore have the second required equation

$$\delta p \;=\; -K\,\frac{\partial \xi}{\partial x} \qquad \text{so} \qquad \frac{\partial}{\partial x}\delta p \;=\frac{\partial p}{\partial x} \;=\; -K\frac{\partial^2 \xi}{\partial x^2}\,. \tag{2}$$

Combining Eqs 1 and 2 through the two expressions for the pressure gradient

$$K\,\frac{\partial^2 \xi}{\partial x^2} \;=\; \rho\,\frac{\partial^2 \xi}{\partial t^2}, \qquad \text{or} \qquad \frac{\partial^2 \xi}{\partial x^2} \;=\; \frac{1}{c^2}\,\frac{\partial^2 \xi}{\partial t^2}. \tag{3}$$

This describes a plane wave of displacement travelling along the x axis with velocity $c = \sqrt{K/\rho}$.

Related to dilatation is the 'condensation', s, which is the fractional change in density, $\delta\rho/\rho$. It is straightforward to show that $s = -\Delta$. Consider the derivative $\partial p/\partial\rho$. From the gas law

$$\frac{\delta p}{p} \;=\; +\gamma\,\frac{\delta \rho}{\rho} \qquad \text{so} \qquad \frac{\delta p}{\delta \rho} \;\to\; \frac{\partial p}{\partial \rho} \;=\; \frac{\gamma p}{\rho} \;=\; \frac{K}{\rho} \;=\; c^2\,.$$

This gives some further insight into the velocity of sound – it is a measure of the pressure increase needed to produce a small change in gas density. Clearly the more it resists compression, the higher the velocity of sound.

Before looking at the general solution of Eq 3, it is important to calculate the kinetic and potential energies, and from them calculate the wave equation by another route. The kinetic energy, $\mathcal{T}$, of the air element in Figure 1 is

$$\tfrac{1}{2}mv^2 \;=\tfrac{1}{2}A\,\rho\,\delta x\,\dot{\xi}^2 \qquad \text{or} \quad \tfrac{1}{2}\rho\,\dot{\xi}^2 \text{ per unit volume}\,.$$

Here the dot denotes the time derivative. Behind this familiar formula are the definitions of kinetic energy as work done in setting a mass in motion, and of power W as the rate of working. Consider

therefore that the excess force $A\,\delta p$ on the face of the element moves its centre of mass a distance $\dot\xi\,\delta t$ in time δt. The rate at which work is done is $A\,\delta p\,\dot\xi$. From Newton's Second Law, Eq 1, the force is $-m\ddot\xi$ so the rate of working W is $|-m\ddot\xi\,\dot\xi|$. Observe that

$$\frac{\partial}{\partial t}(\dot\xi^{\,2}) \;=\; 2\dot\xi\,\ddot\xi \qquad \text{so that} \qquad W \;=\; \frac{\partial}{\partial t}\left(\frac{m}{2}\,\dot\xi^{\,2}\right),$$

establishing the all too familiar formula.

The potential energy, $\mathcal{V}$, is the work done by the force in compressing the element of gas. The pressure difference is initially 0 and it increases to δp so over the time interval the mean excess pressure is $\delta p/2$. The associated force $A\,\delta p/2$ moves a distance $\delta\xi = (\partial\xi/\partial x)\,\delta x$ so the work done is $\frac{1}{2}A\,\delta p\,(\partial\xi/\partial x)\,\delta x$. Using the relation for δp in Eq 2, the elastic energy change is $\frac{1}{2}A\,K\,(\partial\xi/\partial x)^2\,\delta x$, or

$$\tfrac{1}{2}K\left(\frac{\partial\xi}{\partial x}\right)^2 \qquad \text{per unit volume.}$$

This can be written alternatively as $\frac{1}{2}K\Delta^2$ or $\frac{1}{2}Ks^2$ or $\frac{1}{2K}p^2$.

The principle of conservation of energy states that the sum of kinetic and potential energy over the whole of this lossless system is constant, independent of time. However we cannot simply add the kinetic and potential energies for a particular volume and claim that $\partial(\mathcal{T}+\mathcal{V})/\partial t$ there is zero because the energy there will change with time as it propagates along the x axis. However we know that $\mathcal{T}$ and $\mathcal{V}$ are distributed somewhere along the x direction so

$$\frac{\partial}{\partial t}\int_{x=-\infty}^{\infty}\left[\tfrac{1}{2}\rho\,\dot\xi^2 \;+\; \tfrac{1}{2}K\left(\tfrac{\partial\xi}{\partial x}\right)^2\right]dx \;=\; 0\,.$$

$$\frac{\partial}{\partial t}\int_{x=-\infty}^{\infty}\left[\rho\,\dot\xi\,\ddot\xi \;+\; K\,\frac{\partial\xi}{\partial x}\,\frac{\partial^2\xi}{\partial t\,\partial x}\right]dx \;=\; 0\,.$$

Now integrate the potential energy term by parts:

$$\int_{-\infty}^{\infty}\frac{\partial\xi}{\partial x}\,\frac{\partial^2\xi}{\partial t\partial x}\,dx \;=\; \frac{\partial\xi}{\partial x}\,\frac{\partial\xi}{\partial t}\bigg|_{-\infty}^{\infty} \;-\; \frac{\partial\xi}{\partial t}\,\frac{\partial^2\xi}{\partial x^2}\,dx\,.$$

The first term on the right must be zero since there is no disturbance at the remote ends of the space. Consequently

$$\frac{\partial}{\partial t}\int_{-\infty}^{\infty}\frac{\partial\xi}{\partial t}\left[\rho\,\frac{\partial^2\xi}{\partial t^2} \;-\; K\,\frac{\partial^2\xi}{\partial x^2}\right]dx \;=\; 0$$

and this is satisfied when the bracket is zero: that is, when the wave equation Eq 3 holds.

It is well known that the most general solution of Eq 3 is

$$\xi(x,t) \;=\; f(x-ct)+g(x+ct) \tag{4}$$

where f and g are arbitrary continuous functions. f represents a plane wave travelling to the right and g to the left. Clearly time and space derivative of f and g are simply multiples of each other:

$$\frac{\partial f}{\partial t} \;=\; -c\,\frac{\partial f}{\partial x}\,, \qquad \frac{\partial g}{\partial t} \;=\; +c\,\frac{\partial g}{\partial x}\,.$$

An immediate consequence of this is that

$$\mathcal{T} = \tfrac{1}{2}\,\rho\left(\frac{\partial\xi}{\partial t}\right)^2 \;=\; \tfrac{1}{2}\,\rho\,c^2\left(\frac{\partial\xi}{\partial x}\right)^2 \;=\; \tfrac{1}{2}\,K\left(\frac{\partial\xi}{\partial x}\right)^2 \;=\; \mathcal{V}\,,$$

that is, in a one-dimensional travelling wave the kinetic and potential energies are equal at every point.

Now imagine a flat piston far to the left on the $-x$ axis moving abruptly to the right and initiating a pulse of displacement which travels without distortion in the $+x$ direction at velocity c, reaching the origin O at time $t = 0$. Figure 2 is a snap-shot at $t = 0$ of the displacement, pressure, velocity and acceleration of this right-travelling pulse. I have taken $\xi = \pi/2 - \arctan(x - ct)$ so at $t = 0$ $\dot{\xi} = c/(x^2 + 1)$ and $\ddot{\xi} = 2c^2x/(x^2 + 1)^2$. The excess pressure is found either from Eq 1 or Eq 2 as

$$\delta p \;=\; -\rho \int \ddot{\xi}\, dx \;=\; \frac{c^2\rho}{(x - ct)^2 + 1} \qquad \text{or} \qquad -K\frac{\partial \xi}{\partial x} \;=\; \frac{K}{(x - ct)^2 + 1}\,.$$

These are equal since $c^2 = K/\rho$. In Figure 2 I have taken $K = 1$, $\rho = 1$ so $c = 1$ also. The material to the left of the origin has already been displaced; that to the right is still at zero displacement. All the strain and hence the elastic strain energy is concentrated at the wavefront. So is the velocity and hence kinetic energy. An instant later and the wavefront will have shifted to the right, leaving the material at the origin permanently displaced. The travelling pulse therefore transfers energy, concentrated at its wavefront.

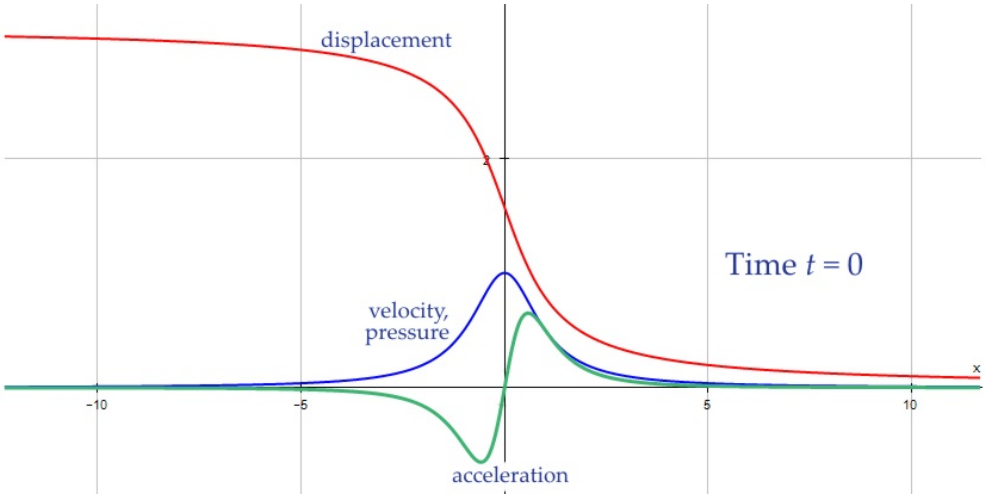

Figure 2: Snap-shot at $t = 0$ of a sound pulse travelling from left to right.

Take another simple case of a uniform plane sinusoidal wave progressing to the right, so g is zero. Take $\xi = \cos(x - ct)$ and fix observation at $x = x_0$. The particle velocity $v = \dot{\xi}$ there is $\partial\xi/\partial t = c\sin(x_0 - ct)$ which leads ξ in phase by 90°. The acceleration is $-c^2\cos(x_0 - ct)$, 180° out of phase with displacement. Similarly, the strain $\partial\xi/\partial x = -\sin(x_0 - ct)$ and so, from Eq 1, the excess pressure is $\delta p = K\sin(x_0 - ct)$, in phase with the particle velocity. The phase relations between these quantities can be illustrated in a wheel diagram, Figure 3. Picture the wheel turning anticlockwise. When any quantity reaches the highest (or lowest) point, that quantity is a positive (or negative) maximum and those in quadrature are instantaneously zero. It is a characteristic of unattenuated plane waves that pressure p and particle velocity are in phase. This is consistent with the kinetic and potential energies being equal. Consider, for instance, that at any instant t the kinetic energy per unit volume, $\frac{1}{2}\rho v^2$, is a maximum when v at its maximum, and also the elastic energy, $\frac{1}{2K}p^2$, is at its maximum when p is maximum.

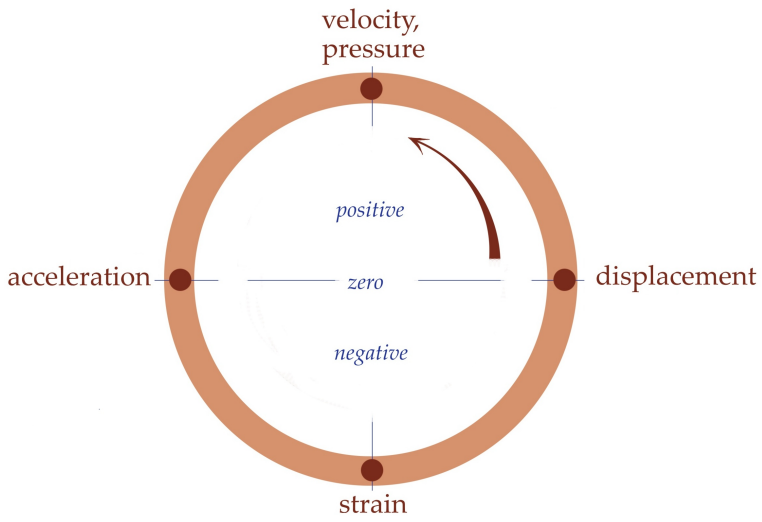

Figure 3: Rotating wheel diagram of phase relations in a right-travelling plane acoustic wave.

The excess pressure needed to cause unit particle velocity is called the 'acoustic impedance,' Z and evaluates to $Z = K/c = \rho c$. There is a direct analogy with electric circuits in which pressure matches voltage (e.m.f), particle velocity matches current. Ohm's law $V = iR$ then implies that acoustic impedance matches electrical resistance or, should out-of-phase components be present, with resistance plus reactance. In the electrical analogy power is voltage × current. Similarly the 'sound intensity' is the product pv. It measures the rate of sound energy flowing across unit area at the given position. The power radiated from a violin playing *forte* is only about 20 or 30 microwatts.

If the left-moving disturbance $g(x+ct)$ is also a harmonic wave with the same amplitude as $f(x-ct)$, a standing wave is produced:

$$\xi \;=\; \cos(x-ct) + \cos(x+ct) \;=\; 2\cos x\,\cos ct\,.$$

The particle velocity is then $-2c\cos x\,\sin ct$ whilst the pressure is $2K\sin x\cos ct$. The phase relations are therefore quite different from those of a travelling wave since at any fixed position $x = x_0$ velocity and pressure are in quadrature. Similarly, at any instant of time $t = t_0$, wherever the velocity is maximum, the pressure is zero and *vice versa*. Therefore in a standing wave the energy in any element remains constant, but cyclically transfers between kinetic and potential. In a travelling wave both kinetic and potential energy are at their maximum at the same place and same time, with that energy being passed from one element to the next at velocity c.

2.2 Spherical waves

We now look at the equivalent analysis when the waves come from a small source in the three dimensions of a large air-filled space. Thwe sound field can vary in direction, but to keep things simple we assume no directional variation – the sound is spherically symmetrical and varies only wuith range r. Figure 4 shows a element on air shaped like the frustum of a cone whose apex is at the source, at distance r from the source, and contained in solid angle Ω. Its near and far surfaces are at right angles to the local outwards unit vector $\mathbf{e_r}$, and separated by a small distance δr. The area of the inner surface is proportional to r^2; call this αr^2 where α is a constant depending on Ω. The area of the outer face is therefore $\alpha(r+\delta r)^2$. The element has volume $\alpha r^2\,\delta r$ and encloses a mass of air $\rho\alpha r^2\,\delta r$.

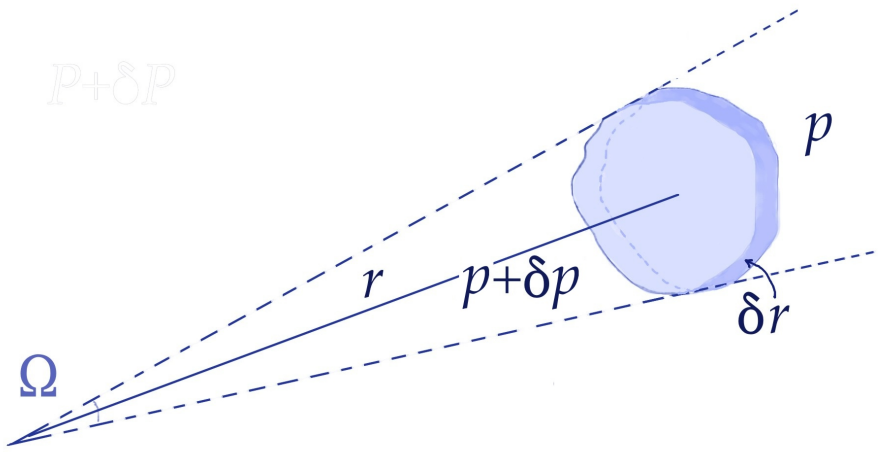

Figure 4: An element of air disturbed by a wave from a point source.

When the pressure throughout the space is p, our element is in equilibrium under the forces on its front and back faces and on the rim. The rim force has a component in the outwards direction to counterbalance the larger area and hence larger inwards force on the outer face. If the internal pressure suddenly increases from p to $p + \delta p$, this element will i) accelerate outwards, ii) become compressed along r and iii) expand sideways to remain continuous with the adjacent air. The volume of the shell increases from $\frac{\alpha}{3}([r + \delta r]^3 - r^3)$ to $\frac{\alpha}{3}([r + \delta r + \xi + \delta\xi]^3 - [r + \xi]^3)$ where $\xi(r, t)$ is the outwards displacement. Regard ξ as small compared with δr and neglect all products of small quantities. It is then straightforward to show that the change in volume is

$$\delta V \;=\; \alpha(r^2\,\delta\xi + 2r\xi\,\delta r)\,.$$

Both sides of this expression are negative if δp is positive. The extra term compared with the plane wave case arises from the lateral enlargement with r. The volume strain Δ is

$$\Delta \;\equiv\; \frac{\delta V}{V} \;=\; \left[\frac{r^2\,\delta\xi}{r^2\,\delta r} + \frac{2r\xi\,\delta r}{r^2\,\delta r}\right] \;=\; \frac{\partial\xi}{\partial r} + \frac{2\xi}{r}\;. \qquad (5a)$$

Again this is negative because the element is compressed; the volume shrinks and the displacement decreases with r. The system is spherically symmetrical so this is also the strain in every volume element at radius r. By the same argument as before, at Eq 1, this is $-\delta p/K$.

When we come to apply Newton's second law, we encounter the difficulty that acceleration and force are vectors and point into all radial directions. To deal with this complication the standard derivation of the spherical wave equation is almost invariably expressed in terms of either a velocity or a displacement scalar potential ϕ, the negative gradient ($-grad\,\phi$ or $-\nabla\phi$) of which defines the velocity vector or, respectively, the displacement vector. This device allows vector differential equations to be re-expressed as scalar ones. Throughout this article I use ϕ to be **displacement** potential.

If the motion is purely radial, the gradient operator gives the displacement to be $\boldsymbol{\xi} = -\partial\phi/\partial r\,\mathbf{e_r}$ where the bold face denotes a vector and $\mathbf{e_r}$ is a unit vector in the local r direction. The volume strain of Eq 5a then becomes

$$\frac{\delta V}{V} \;=\; \frac{-\delta\rho}{\rho} \;=\; -\frac{\partial^2\phi}{\partial r^2} - \frac{2}{r}\frac{\partial\phi}{\partial r}\;. \qquad (5b)$$

Here is a sketch of how Newton's second law applies. For the air element in Figure 4 δp causes an out-of-balance force $\alpha r^2\,\delta p = -\alpha r^2\,\partial p/\partial x\,\delta x$ which accelerates its centre of mass outwards:

$$\rho\,\alpha r^2\,\delta r\,\frac{\partial^2\xi}{\partial t^2} \;=\; \alpha r^2\,\delta p \qquad \text{so} \qquad \rho\,\frac{\partial^2\xi}{\partial t^2}\,\delta r \;=\; -\frac{\partial P}{\partial r}\,\delta r\,.$$

$$\rho\,\frac{\partial^2\xi}{\partial t^2} \;=\; K\frac{\partial}{\partial r}\left(\frac{\partial\xi}{\partial r}+\frac{2\xi}{r}\right).$$

Write this is terms of the displacement potential ϕ:

$$\frac{\rho}{K}\,\frac{\partial^2\phi}{\partial t^2} \;=\; \frac{\partial^2\phi}{\partial r^2}+\frac{2}{r}\frac{\partial\phi}{\partial r} \;=\; \nabla^2\phi\,, \tag{6a}$$

the Laplacian operator in spherical co-ordinates. This is the well known wave equation for spherically symmetrical waves (no variation with direction). As with plane waves they have velocity c given by $c^2 = K/\rho$. The equation can be expressed compactly as

$$\frac{\rho}{K}\,\frac{\partial^2(r\phi)}{\partial t^2} \;=\; \frac{\partial^2(r\phi)}{\partial r^2} \tag{6b}$$

and we see immediately from Eqs 3 and 4 for the plane wave case that the general solution is

$$\phi \;=\; \frac{1}{r}\,f(r-ct)+\frac{1}{r}\,g(r+ct). \tag{7}$$

f represents an outwards travelling wave and g an inwards one. f and g themselves are arbitrary.

§3 looks at the simple point source in more detail.

2.3 Summary of wave physics relations

It will be useful for later reference to pull together the main relationships between the quantities which apply in any co-ordinate system. If X is *any* scalar quantity associated with the wave motion, it satisfies the 3D wave equation

$$\nabla^2 X \;=\; \frac{1}{c^2}\frac{\partial^2 X}{\partial t^2}, \qquad c^2 = \frac{K}{\rho}. \tag{8a}$$

Thus X could be the displacement potential, or the velocity potential, or pressure, or density or the local temperature. Throughout this article the scalar used is ϕ, the displacement potential. Its dimensions are Length^2, or area. The displacement is $\boldsymbol{\xi} \;=\; -\nabla\phi$ and the particle velocity $\mathbf{v}$ is the time derivative of this. Both are vector quantities. ϕ has amplitude and phase so can be represented either as a sum of sine and cosine terms or as a complex function of position and time. Eq 8a can be derived by more rigorous arguments and applies to general oscillatory motion of the air, not just that in the radial direction, as in my derivation. The equation can be solved exactly for several other special cases, usually by using the method of separation of variables. I give an example of this technique for spherical waves in §5.2 and another for spheroidal waves in Appendix 4.

This is a suitable point to introduce Helmholtz's equation, which is the form taken by the wave equation for a continuous sinusoidal wave. If the time variation is as $\sin\omega t$, the double time derivative converts $\partial\phi^2/\partial dt^2$ to $-\omega^2\sin\omega t$. The time-dependent wave equation is therefore replaced,

$$\nabla^2\phi \;=\; \frac{1}{c^2}\,\frac{\partial^2\phi}{\partial t^2} \qquad \text{becoming} \qquad \nabla^2\phi \;= -\kappa^2\phi. \tag{8b}$$

This is Helmholtz's equation. Its solution for plane waves is $\phi = A\cos(\kappa x - \omega t)$ or $Ae^{i(\kappa x - \omega t)}$ where $\kappa = 2\pi/\lambda$ is the wave number, λ the wavelength, f the frequency in Hz and ω the frequency in radians per second. $c = \lambda f = \omega/\kappa$. The amplitude A has the dimension of area. The standard solution for a point source is $\phi = Ae^{i(\kappa r - \omega t)}/r$ where A now has the dimension of volume.

A note is in order about the interpretation of complex quantities in wave calculations. The physical wave and quantities such pressure, displacement and particle velocity are all real, so they must be represented by either the real or imaginary part (without the i) of the complex number, or by its magnitude and phase. Suppose the displacement in x, y, z co-ordinates is $\boldsymbol{\xi} = (\xi_x \mathbf{e_x} + \xi_y \mathbf{e_y} + \xi_z\ \mathbf{e_z})\, e^{-i\omega t}$ where the $\mathbf{e}$ are unit vectors along the axes. In general the components ξ_x *etc.,* will be complex quantities, so write $\xi_x = u_x + iv_x$, $\xi_y = u_y + iv_y$, $\xi_z = u_z + iv_z$. The real and imaginary parts of $\boldsymbol{\xi}$ are then

$$\text{Real :} \qquad (cu_x + sv_x)\mathbf{e_x} + (cu_y + sv_y)\mathbf{e_y} + (cu_z + sv_z)\mathbf{e_z}\,,$$

$$\text{Imag :} \qquad (cv_x - su_x)\mathbf{e_x} + (cy_y - su_y)\mathbf{e_y} + (cv_z - su_z)\mathbf{e_z}\,,$$

where $c = \cos\omega t$, $s = \sin\omega t$. Now these two parts are essentially the same, differing only in phase by $\pi/2$. In particular if $t = 0$, we have

$$\boldsymbol{\xi} \ = = (u_x\mathbf{e_x} + u_y\mathbf{e_y} + u_z\mathbf{e_z}) \ + i\,(v_x\mathbf{e_x} + v_y\mathbf{e_y} + v_z\mathbf{e_z})\,,$$

and if $t = \pi/(2\omega)$, $\boldsymbol{\xi}$ is the complex conjugate of this. Therefore either the real or imaginary part can represent physical quantities.

Total gas pressure = steady atmospheric pressure + oscillating acoustic pressure . From now on I will write δp simply as p to denote the acoustic pressure. The acoustic pressure causing varying displacement is a 3D generalisation of Eq 1:

$$p \ = \ -K\nabla\cdot\boldsymbol{\xi} \ = \ K\nabla^2\phi\,. \tag{9a}$$

This looks like the left side of Eq 8. Therefore we have another relation between acoustic pressure and ϕ, namely

$$p \ = \ \rho\,\frac{\partial^2\phi}{\partial t^2} \ \rightarrow \ -\omega^2\rho\,\phi \tag{9b}$$

when ϕ varies in time as $e^{-i\omega t}$. Hence for a sinusoidal wave, ϕ is proportional to p but with opposite phase. Also note that impedance $Z = -i\,\omega\,\rho\,\phi/\xi$.

3 Single sound sources at low frequency

We now apply the above wave equation to an object which behaves as a spherically symmetrical simple 'monopole' source pulsating radially. We are interested in outgoing waves only so in Eq 7 set $g = 0$ making $\phi = f(r - ct)/r$. The displacement of this general disturbance in direction $\mathbf{e_r}$ is

$$\boldsymbol{\xi} \;=\; -\nabla\phi \;=\; \left(-\frac{1}{r}f'(r-ct) + \frac{1}{r^2}f(r-ct)\right)\mathbf{e_r},$$

and the particle velocity is

$$\mathbf{v} \;=\; \frac{\partial\boldsymbol{\xi}}{\partial t} \;=\; c\left(\frac{1}{r}f''(r-ct) - \frac{1}{r^2}f'(r-ct)\right)\mathbf{e_r}\,.$$

Differentiation is with respect to the argument. Eqs 3 and 9a give the acoustic pressure as $K\nabla^2\phi = \rho\ddot{\phi}$. In spherical co-ordinates with variation only in r

$$\nabla^2\phi = \frac{1}{r^2}\frac{\partial}{\partial r}\left(r^2\frac{\partial\phi}{\partial r}\right) \quad \text{so} \quad p \;=\; \frac{K}{r}f''(r-ct) \;=\; \rho\ddot{\phi}\,.$$

Observe that the velocity, like the displacement, has two terms, the first of which has the same form as the pressure. The power dissipated by radiation is proportional to the product of these two quantities which are in phase with each other. The second term in the velocity is out of phase with the pressure so represents energy bound into a standing, non-radiating oscillatory motion. The amplitude of the energy-propagating wave falls at $1/r$, whilst the out-of-phase component falls as $1/r^2$, meaning that non-radiated energy is trapped close to the source. The work done by the vibrating source goes partly into a radiated (resistive, dissipative) component and partly into the bound (reactive, storage) component. The impedance of the wavefield is therefore complex. One cannot generate the useful, sound-carrying part without also sustaining the non-travelling, oscillating mass of air close to the source.

The 'strength' of a point source can be defined as the total mass of air which crosses an enclosing spherical surface in unit time, and this will in general vary over time. If the radius of this virtual sphere is a, its area is $4\pi a^2$. The particle velocity $v(r,t)$ is purely radial so the strength, $Q(t)$, is $4\pi a^2\rho\, v(a,t)$. With $\phi = f(r-ct)/r$,

$$Q(t) \;=\; 4\pi\rho\, c\left[a\, f''(a-ct) - f'(a-ct)\right].$$

If λ is a wavelength representative of f, and if $a \ll \lambda$, the first term is insignificant so

$$Q(t) \;\rightarrow\; -4\pi\rho\, c\, f'(a-ct) \;=\; 4\pi\rho\, a\frac{\partial\phi(a)}{\partial t}\,.$$

Differentiating again,

$$\dot{Q} \;=\; 4\pi\rho a\ddot{\phi} \quad \text{so} \quad p(a) \;=\; \frac{\dot{Q}}{4\pi a}\,.$$

In 3D the source strength is proportional to the rate of change of potential, and the pressure to the rate of change of source strength. This contrasts markedly with a 1-D wave (plane wave) for which p is proportional to Q, not to its time derivative. To see this, watch how the corresponding argument would go for a plane wave. If $\phi = f(r-ct)$, then $\xi = -f'$ and $v = cf''$. If the plane wave has sectional area A (say by being in a long parallel-side pipe), the source strength would be $Q(t) = A\rho v(t) = A\rho c f''$. From Eq 9b the pressure in 1-D is $\rho\ddot{\phi} = \rho c^2 f''$, so Q is proportional to p.

From now on let us confine ourselves to sound sources emitting a single frequency f Hz. Suppose we have a musical source pulsating about mean radius r_0 and producing peak excess pressure p_0 in the air at its surface. The instantaneous pressure will fall with r as[1]

$$p \;=\; p_0 \,\frac{r_0}{r}\,\sin\left(\kappa r - \omega t\right)\,.$$

At a general range r and time t the displacement potential will be

$$\phi \;=\; -\,\frac{A(\omega)}{r}\,\sin\left(\kappa r - \omega t\right)\,.$$

The amplitude coefficient is found by matching at the source's surface:

$$A(\omega) \;=\; \frac{p_0\, r_0}{K\kappa^2} \;=\; \frac{p_0\, r_0}{\rho\,\omega^2}\,.$$

The quantity $Q = 4\pi r_0^2\, p_0$ is the aggregate acoustic force exerted radially by the source, so is a measure of its strength.

The displacement and particle velocity defined by ϕ are

$$\boldsymbol{\xi} \;=\; \frac{A\,\kappa}{r}\cos\left(\kappa r - \omega t\right) \;-\; \frac{A}{r^2}\sin\left(\kappa r - \omega t\right)\,.$$

$$\mathbf{v} \;=\; \frac{A\,\kappa\omega}{r}\sin\left(\kappa r - \omega t\right) \;+\; \frac{A\omega}{r^2}\cos\left(\kappa r - \omega t\right)\,,$$

where the local unit vector $\mathbf{e}_r$ is understood. The ratio of reactive displacement (or velocity) to dissipative is λ/r, so the reactive component lies mostly within about one wavelength of the centre of radiation. If the source itself actually has a radius larger than λ, almost all the sound field will be radiative. On the contrary, if the source is physically much smaller than λ, it will be surrounded by a ball of air which just moves backwards and forwards with the source. The phase angle between the pressure and the displacement (or velocity) is $\tan^{-1}(1/(\kappa r))$, tending to zero as $r \to \infty$ as the wave fronts become almost planar. The moduli of $\boldsymbol{\xi}$ and $\mathbf{v}$ can be expressed variously using the relations $c = \lambda\omega$ and $c^2\rho = K$, and characteristic acoustic impedance $Z_0 = \rho c$:

$$|\xi| \;=\; \frac{A(\omega)}{r}\sqrt{\kappa^2 + \frac{1}{r^2}} \;=\; \frac{p_0}{Z_0\omega}\,\frac{r_0}{r}\,\sqrt{1 + \frac{1}{(\kappa r)^2}}\,, \tag{10a}$$

$$|v| \;=\; \frac{p_0}{Z_0}\,\frac{r_0}{r}\,\sqrt{1 + \frac{1}{\kappa^2 r^2}}\,, \qquad Z_{sphere} \;=\; Z_0\,\frac{\kappa^2 r^2}{1 + \kappa^2 r^2} \;<\; Z_0\,. \tag{10b}$$

The total radiated (dissipated) power per unit area at radius r is given by the product of local pressure and in-phase velocity, also called the sound intensity. Averaged over one cycle this is

$$\text{Rate of radiation of energy per unit area} \;=\; \left(\frac{p_0\, r_0}{r}\right)^2 \frac{c}{2K} \;=\; \frac{1}{2Z_0}\left(\frac{p_0\, r_0}{r}\right)^2\,.$$

This is the useful part of the work done by the vibrating musical instrument in projecting audible notes to a distant listener. The instantaneous reactive power is given by the product of pressure and out-of-phase velocity:

$$\text{Reactive power per unit area} \;=\; \left(\frac{p_0\, r_0}{r}\right)^2 \frac{1}{2\rho\,\omega\, r}\sin 2\left(\kappa r - \omega t\right)\,.$$

[1] Recall that $\kappa = 2\pi/\lambda$ is the wave number and $\omega = 2\pi f$ is the radian frequency. The factor 2π ensures that when r advances by one wavelength, or when t advances by one period, the sine function advances by one cycle, since $\sin(x + 2\pi) = \sin x$. In terms of the complex exponential, $e^{2\pi i} = 1$.

This averages to zero over every cycle because energy is alternately taken from the source and returned to it. Put bluntly, much of the air very close to the source just wafts about, out of phase with the pulsating object, and does nothing for a distant listener.

3.1 Small musical instruments

Bowing a violin causes the belly to vibrate, and its lowest mode is a 'breathing' one in which the top and bottom plates deflect into dish shapes in opposite senses. It is probably the surface displacement which is controlled by the player rather than the adjacent air pressure. From Eq 10a the normal displacement at the surface of the source necessary to obtain air pressure p_0 is

$$|\xi|_{r_0} \;=\; \frac{p_0}{Z_0\omega}\sqrt{1+\frac{c^2}{\omega^2 {r_0}^2}}\,. \tag{11}$$

Put in some numbers to see the implications of this. Suppose you are listening to a long *forte* note from a violin being played 10 m away, and suppose the loudness to you is 60 decibels. Then the rms pressure at your ear[2] is about $0\cdot02$ Pa. Pressure falls as $1/r$ from p_0 at the violin's surface. If we take r_0 to be $0\cdot2$ m as representative of the size of a violin, the distance ratio is 50, implying a 34 dB attenuation, so the loudness to the player is 94 dB and p_0 is $1\cdot0$ Pa. The table below gives peak displacements in microns (1/1000 mm) at four frequencies based on Eq 11. (Rms values have been multiplied by $1\cdot414$ to obtain peak values.) Notice the almost three-fold increase needed in displacement in dropping one octave.

Note	f	ξ microns
A on E string	880	$\pm0\cdot6$
Open concert A	440	$\pm1\cdot4$
A on G string	220	$\pm3\cdot9$
Open G	196	$\pm4\cdot7$

The viola is even more challenged. Take $0\cdot25$ m to be a representative dimension, and add the extra 14 dB needed to compensate for the poorer sensitivity of our ears to sound at 131 Hz, the frequency of the open C string. The required peak displacement for 60 dB 10 m away would be 40 μm. Relatively larger displacements of a viola's top plate are in fact possible at low frequencies because the low frequency resonant modes have few nodal lines, whereas the higher resonances divide the vibrating plate into several small regions. Clearly, the more the plate is so divided, the smaller the displacement of any patch. Moreover, adjacent regions, separated by the nodal lines which appear in Chladni figures, vibrate in opposite senses so the sound from them interferes destructively, cancelling the sound intensity. Hence in practice much larger displacements than those in the table above would be needed to attain 60dB. Such large displacements probably cannot be achieved, which may account in part for the poor response of some violas on the C string. We might suspect that thick, stiff plates which are solidly glued around their edges will not undergo large displacements. This largely explains why the fundamental tone from a viola's C string is almost inaudible. Instead, the low pitch is perceived by our brains from the superimposed frequencies of the harmonics at 2, 3, 4, *etc.* times the fundamental, as explained in a companion article on this web site[3].

The above is true of all small vibrating objects. They are intrinsically poor at radiating sound. A small drum, a small trumpet, a small viola, a small loudspeaker cannot produce low pitched sounds with any appreciable amplitude. For similar reasons an object cannot appreciably scatter a wave whose wavelength is much larger than the object. Long waves ignore small objects.

[2] See 'How we hear the sound of the violin and viola' on this web site, *www.mathstudio.co.uk*

[3] 'How we hear the sound of the violin and viola'on *www.mathstudio.co.uk*

3.2 Does the instrument sound different close to?

The audience may be 10 metres away, but the violinist is in the close near field of the instrument. Do they hear high and low frequencies differently? In practice what the listener hears will depend on the acoustics of the room – its reverberations and frequency-dependent absorption. Even in an open space the answer must depend on what exactly the ear responds to – pressure, displacement, air velocity, power? If pressure is the determinant, in the open air all frequencies will attenuate as $1/r$ and there will be no distortion of the sound. If on the other hand the ear responds to air displacement or velocity, there will be a slight distortion. To estimate how much take $r_0 = 0 \cdot 2$ m for a violin, $r = 0 \cdot 3$ m close to and 10 m far off, and compare amplitudes at 880 and 220 Hz. The amplitude ratio of the two notes changes by about 2 dB with distance, with the low pitched note attenuating relative to the high pitched as distance increases. In other words, the bass does sound relatively a little stronger close to, though this would be only just noticeable.

To investigate this in practice I have carried out a simple listening test with a 100 mm diameter loudspeaker unit, not mounted in a baffle. While moving towards and away from this, I listened to a variety of high and low frequency pure sine tones (generated by computer using GoldWave software) played either separately or together. Though the loudness fell as I moved away, I could not discern any difference in behaviour between notes at 2000 Hz and those at 200 Hz, except perhaps when my ear was up close to the speaker. Very close (a few centimetres), the bass notes did sound more distinct. However this may have been that my head was disturbing the radiation by introducing standing waves by reflection from my head.

Myself and a volunteer repeated the test with a pair of earphones and obtained a much more dramatic change with distance and frequency. We started with the earphones in the usual listening position covering both ears, and then lifted them off and moved them slowly a distance away until the notes could no longer be heard. Both high and low frequency tones were set to nominally the same loudness with the earphones worn normally. The high pitched ones persisted to a distance of 30 cm to 50 cm, but the low pitched (< 200 Hz) became almost inaudible when less than 5 cm from the ears. Standing waves within each ear muff seem likely to be important here; perhaps we were effectively listening to the earphones' clever design. Taken together with the tests on a single loudspeaker, these observations are inconclusive.

The literature on the internet about what makes a good violin states the importance of sound volume and hence carrying power and projection of tone. There is a range of opinion on whether violins sound differently to the player and the audience. Here are some quotes found on the internet at *www.violinist.com*.

- "The worst judge of how a violin sounds is the person who plays it."
- "With experience one is able to judge a violin that will sound good to an audience. Similarly one is also able to project in a manner which is rich, full, and powerful on stage, but up close may sound rough and edgy."
- "I had to play in a concert organised by my teacher, showcasing a few of his pupils. One student let me try his violin, bought recently for lots of money from a leading London dealer. I think it was a Bergonzi. Compared with my cheap half-size it seemed harsh and edgy. But when I listened at the back of the hall, I thought it sounded beautiful. By comparison, and at the same distance, my teacher's Alfred Vincent seemed 'bottled up' - it didn't carry as well."

- "Not all performance is in a concert hall. If you happen to do any work in a recording studio, you will find that the violin that sounds bright and scratchy close up will record that way."
- "Is it possible to find an instrument that sounds good under ear and also projects to the back of the hall, or are the two qualities mutually exclusive?"
- "You hear people (often dealers) say that a violin may sound ugly up close, but don't worry, it will sound beautiful at a distance .... not so. A violin should sound wonderful under your ear! If it sounds loud, like a loud necktie, you don't want it. This is not a powerful violin, it is a screaming ugly violin!!! What makes a violin carry is the same thing that makes Pavarotti's voice carry: richness of overtones".
- "Older violins are often praised for how far their sound can travel – the projection." (from The Telegraph, 8th April 2014.)

Notice that in these comments it is the high frequency 'scratchy' notes which are thought to attenuate with distance rather than the bass, and indeed they do. I have heard some musicians claim that top quality classic violins have more 'carrying power' than cheap ones – that a poor violin can sound loud close to yet the sound does not carry to the back of the hall. Others speak of their instrument having 'focus' rather than loudness. Much of this may be subjective impressions, perhaps relating to how the instruments are being played rather than to the physics of sound waves. Clearly, though, the near-to-far differences in sound are a topic of concern to anyone choosing a violin.

4 Dipoles and multiple sources

This section is mainly about interference between waves from separate point-like sources. Suppose there is a planar array of two or more small sources fairly close together. They may all vibrate exactly in phase, or adjacent ones exactly 180° out of phase, or some other set of phase differences. If the array is tilted with respect to the listener, there will be additional phase differences due to the altered path differences. Elementary physics tells us that the waves will interfere and affect the amplitude and hence loudness as the phase difference varies with source spacing, distance, direction and frequency. In this analysis I regard the sources as independent – no interaction between them.

4.1 Basic theory of dipoles and tripoles

The dipole consists of two closely spaced, out of phase sources as illustrated in Figure 5. Suppose point sources S_1, S_2 are d apart, each radiating a spherical wave with pressure amplitude A_1, A_2. S_2 radiates as $A_2 \exp i(\kappa r - \omega t)/r$ and S_1 similarly but α out of phase. If $r >> d$, the path difference to listening point Q, distance r away, is $d \sin\theta$. The combined pressure is

$$\frac{e^{i(\kappa r - \omega t)}}{r}\left(A_2 + A_1 e^{i(\kappa d \sin\theta + \alpha)}\right).$$

The amplitude of this is

$$\frac{1}{r}\sqrt{A_1^2 + A_2^2 + 2A_1 A_2 \cos(\kappa d \sin\theta + \alpha)}\,. \qquad (12a)$$

Figure 6 presents three cases of this equation, amplitude versus angle θ. All have $d = 0 \cdot 12$ m, $r = 2$ m, $c = 342$ m/sec and $f = 1368$ Hz, at which $\lambda = 1/4$ m:

- red curve: in phase, $A_1 = A_2 = 1$ (equal source strengths). Observe constructive interference at $\theta = 0$ which doubles the amplitude to 2.
- blue curve: 180° out of phase, $A_1 = A_2 = 1$. Destructive interference at $\theta = 0$, but constructive at angles above $\theta = 45°$.
- green curve: A_1 increased to $1 \cdot 5$ and oscillating at $\alpha = 45°$.

The model can only be valid for $-\pi/2 < \theta < \pi/2$ radians, but I have retained the curves beyond this region (shaded blue) to emphasise the symmetries.

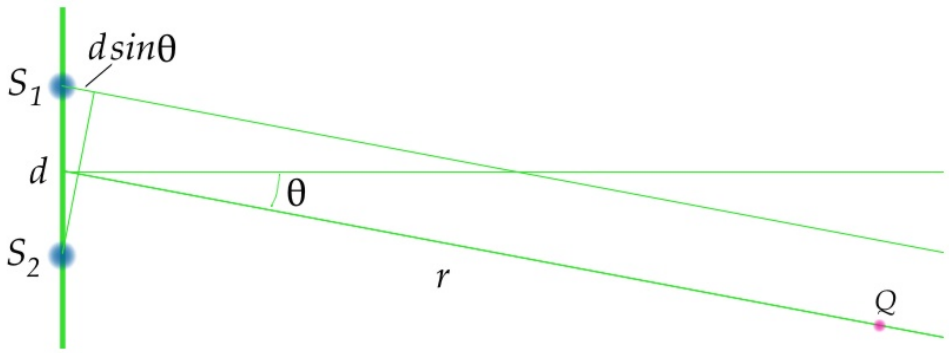

Figure 5: Simple model of a dipole with point sources S_1 and S_2.

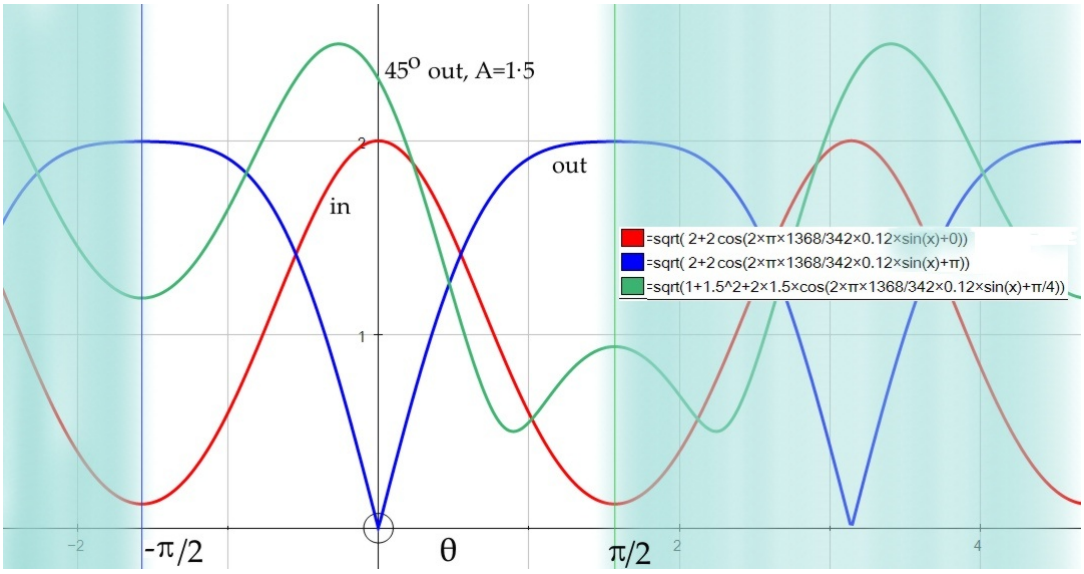

Figure 6: Amplitude in the far field of a dipole for three conditions of phase and source strength.

Eq 12a can be refined to acknowledge that an extended flat source such as a loudspeaker will radiate mainly in its forwards (normal) direction and hardly at all obliquely to the side. So introduce a directional factor $\mathcal{D}(\theta)$, the functional form of which will depend on the extended source:

$$\frac{\mathcal{D}(\theta)}{r}\sqrt{A_1^2 + A_2^2 + 2A_1A_2\cos(\kappa d\sin\theta + \alpha)}\,. \qquad (12b)$$

A college experiment to measure radiation directivity patterns from monopoles, dipoles and quadrupoles has been described by Daniel Russell and colleagues[4]. I have also carried out my own home-made experiment, described in §5.2 below.

A situation of greater interest to myself is the radiation from a vibrating plate, such as the top plate of a violin. Such a plate has many normal modes of oscillation in each of which the surface divides into cells, with adjacent cells moving in opposite transverse directions. These modal patterns can be modelled with finite element analysis and observed experimentally as Chladni figures, as described in an earlier article on *www.mathstudio.co.uk* [5]. Examples of three modes of a box are shown in Figure 7 as calculated by the LISA 8 FEA program. The details are not important, but for the record the box is 30 cm by 15 cm and 4 cm high, made of a material with Young's modulus 1×10^{10} SI units. The top is 2·5 mm thick, the sides 1 mm and the base is rigid. The point to observe is that the surface cells are much smaller than the wavelength of the sound that they radiate, so they behave essentially as independent point sources. The modes shown at the top and bottom of Figure 7 are both dipoles, oscillating at 423 Hz and 875 Hz respectively. The wavelength in air at 423 Hz is 79 cm compared with a distance between the cell centres of only 15 cm. At 668 Hz λ = 51 cm, again about 5 times the cell spacing. Wave interference from these sources must affect the loudness heard by a distant listener and so is relevant to our understanding of violin-family instruments. The question is 'how large is this effect'.

The central mode in Figure 7 is what we my call a 'tripole', consisting as it does of three equal sources in a line, the outer two being in phase with each other but 180° out from the middle

[4]Russell, Titlow and Bemmen, Amer. J. Phys, Vol 67, No 8, 1999, p660-664.

[5] 'The vibration of plywood plates by experiment and finite element analysis: edge constraints and box structures'.

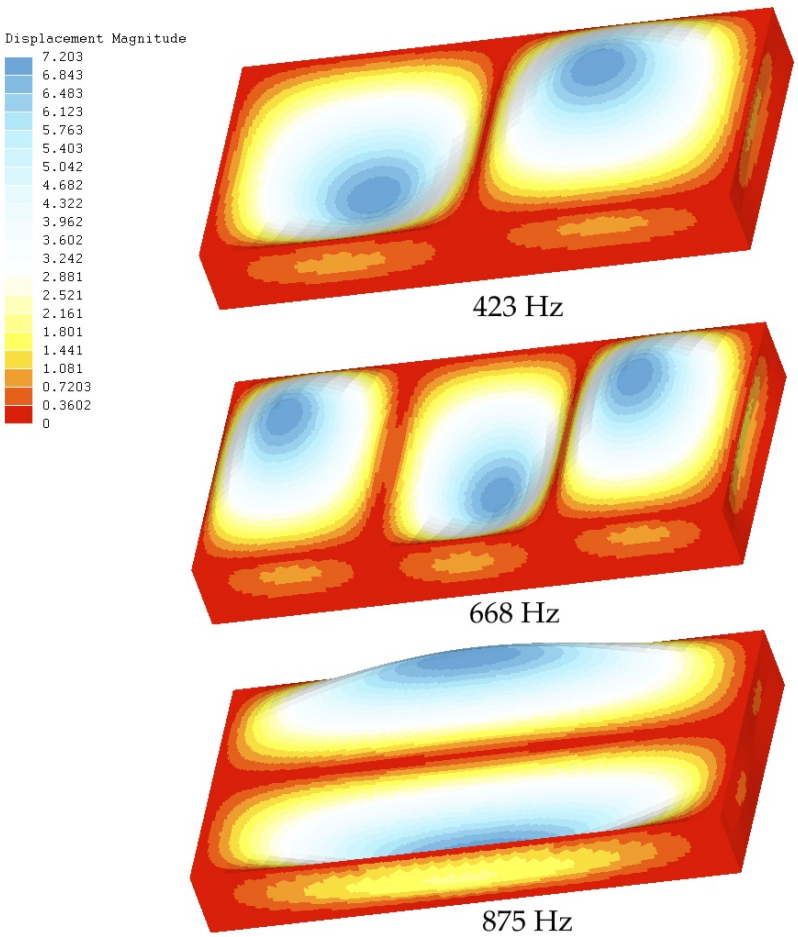

Figure 7: FEA calculation of displacement in three normal modes of vibration of a hypothetical box.

one. If all three were in phase, the signal would be

$$\frac{e^{i\kappa r}}{r}\left(1+e^{i\kappa d\sin\theta}+e^{-i\kappa d\sin\theta}\right) \;=\; \frac{e^{i\kappa r}}{r}\left(1+2\cos(\kappa d\sin\theta)\right)\,, \tag{13a}$$

whilst with the outer two out-of-phase,

$$\frac{e^{i\kappa r}}{r}\left(1-e^{i\kappa d\sin\theta}-e^{-i\kappa d\sin\theta}\right) \;=\; \frac{e^{i\kappa r}}{r}\left(1-2\cos(\kappa d\sin\theta)\right)\,. \tag{13b}$$

These two functions are plotted in Figure 8 for a case similar to Figure 6, namely $d = 12$ cm, 1368 Hz, $r = 200$ cm. Normal to the array (red curve at $\theta = 0$) two out-of-phase sources cancel each other so the signal received is due only to the third, amplitude 1. There is a phase inversion as θ moves from one lobe to another, as happens at about $0\cdot35$ radians = 20° in the out-of-phase graph. The condition is $\sin\theta = \lambda/(6d)$.

4.2 Illustration by experiment

I have been keen not to let theory run too far ahead of experiment, so have carried out my own measurements on sound fields from 2 and 3 adjacent sources. The arrangement is shown in Figure 9. Three nominally identical 8 ohm loudspeakers were mounted on a wooden board with holes cut so that the full $8\cdot5$ cm diameter of each speaker cone was exposed and free to radiate. The speakers

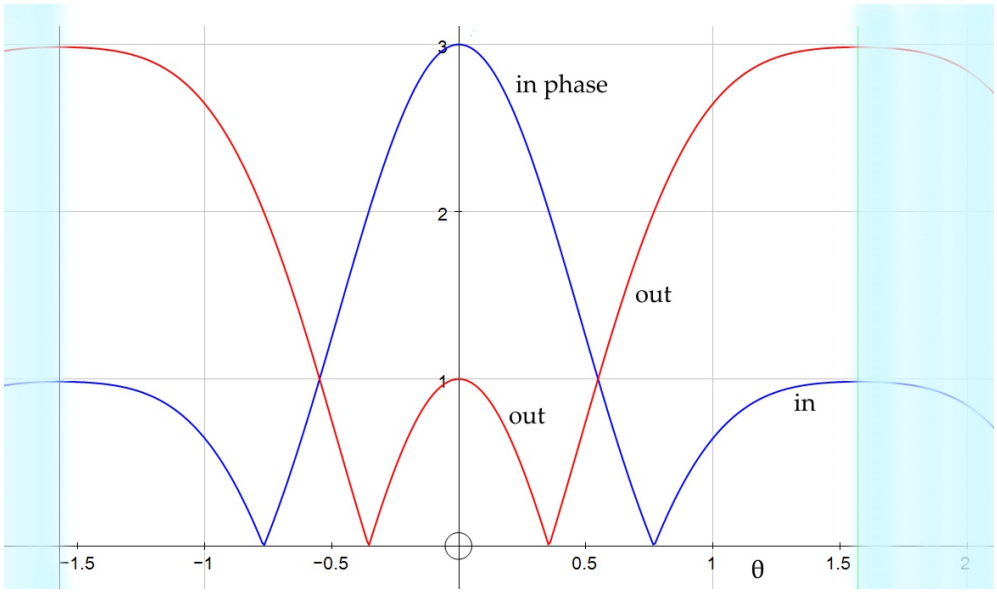

Figure 8: Amplitude from tripole array of three point sources, 12 cm apart, at 1368 Hz. Blue: all in phase. Red: central source out of phase with outer two. θ is radians.

were 12 cm apart between centres and driven in parallel from the one power amplifier. The input to the amplifier was a digitally generated continuous sine wave at selected frequency. A microphone was positioned 2 m away in the plane of the speakers, and the received signal recorded digitally at CD quality as the angle θ of the wooden board was changed. This was effected by having the board fixed to the upper end of a vertical pole, the lower end of which fitted into a fixed socket in the ground about which the pole could turn. The wiring of the three speakers included switches so that three combinations could be driven:

1. the central speaker alone, rotating about a vertical axis A through its centre.

2. two adjacent speakers either in phase or 180° out of phase, rotating about a vertical axis B through the midpoint of their centres. In addition the right hand speaker only could be switched off in this configuration.

3. all three speakers in operation, with the two outer always in phase with each other but in or out of phase with the central speaker, and rotating about central axis A.

The second two configurations mimic the upper and middle vibrational modes in Figure 7. Speakers not in use were covered by wooden caps to preserve a uniform planar baffle, and cushions were attached behind the speakers to limit sound leakage. The experiment was set up out of doors away from reflecting surfaces, so suffered somewhat from environmental noise.

The aim of the experiments was to demonstrate constructive and destructuve interference between the component sources. A natural starting point is to determine the radiation directivity of a single source. From the recorded digitised waveform I selected very short samples at angular positions 5° or 10° apart, typically turning the array on its pivot from 0° to 60° or even 90° then turning in reverse back to −5°. Figure 10 plots these amplitudes for 228, 684, 1368 and 1710 Hz. The joining lines indicate the sequence of points. The wavelengths are respectively 150, 50, 25 and 20 cm.

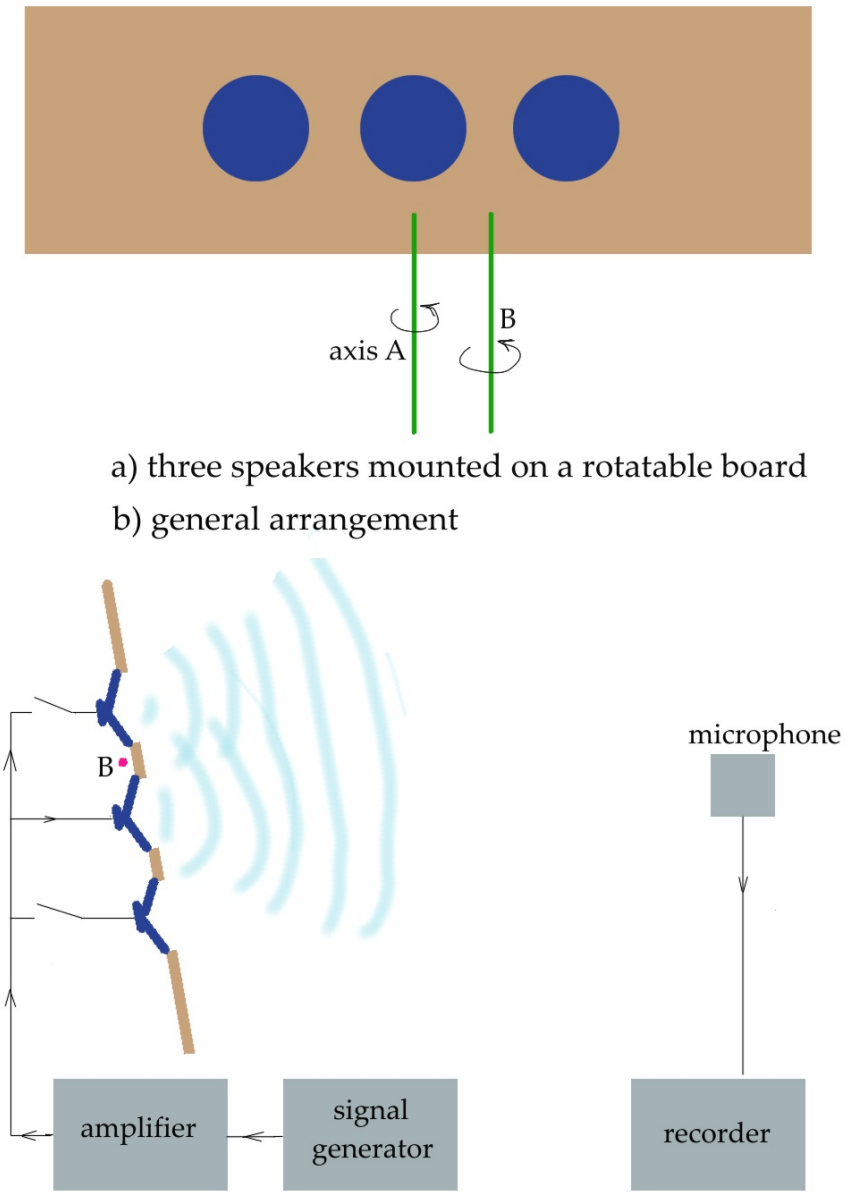

Figure 9: Experimental arrangement for recording sound amplitudes from 1, 2 or 3 loudspeakers driven with a continuous sine tone. b) shows the set up when $\theta = 10°$. B marks the rotation axis.

I have to admit that these plots are not as I would expect. Assuming that the speaker cone behaves as a piston, I had expected a steady fall in signal to value close to zero amplitude at all frequencies, with the high frequencies decreasing more steeply with angle. Instead

- all graphs show a significant signal level at 90° (grazing), and
- the two higher frequency plots have a large kink.

Sound at grazing angle may be due to sound leaking from behind the speaker, escaping past or through the cushions. The kink at high frequency might indicate that the speaker cone was not vibrating uniformly, but flexing in some higher vibrational mode. The wooden baffle was 12 mm thick, so perhaps a further effect is due to sound reflecting from the wall of the circular hole cut

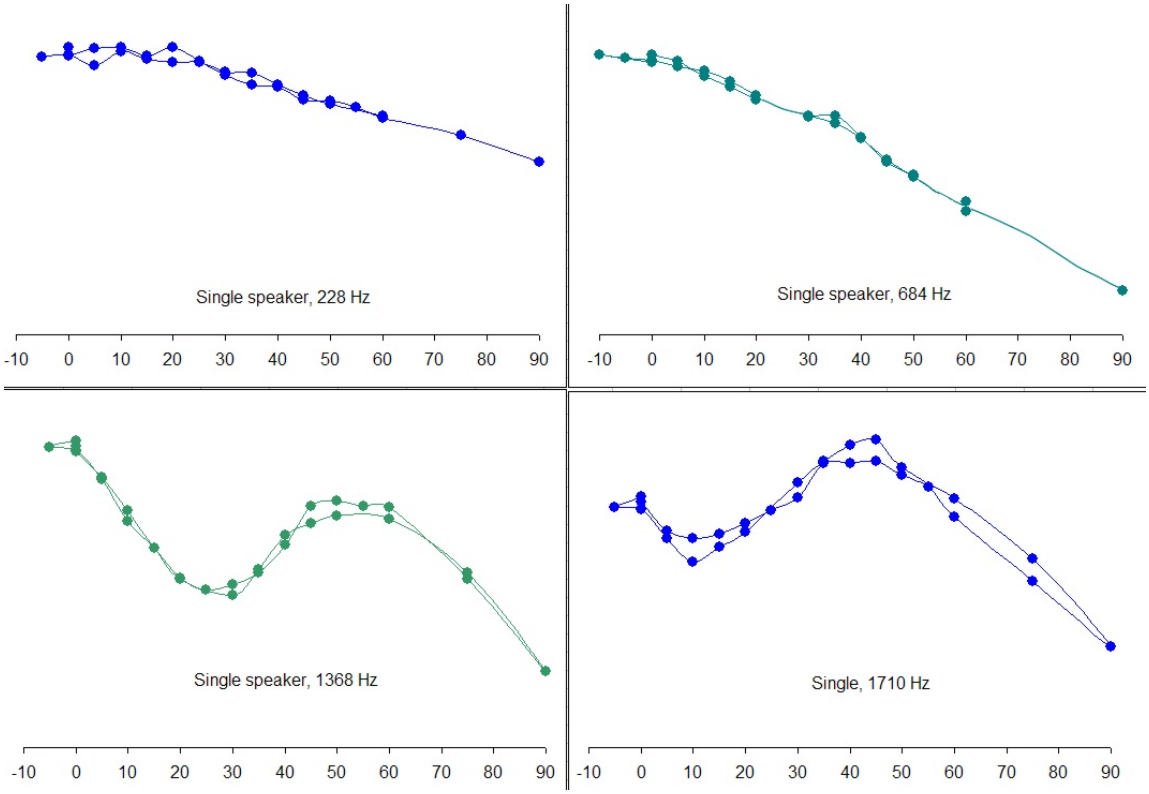

Figure 10: Single source. Amplitude received (arbitrary linear scale) at 2 m range from a single 8 cm diamater loudspeaker as it rotates through −5° to 90°, at 4 frequencies.

through the wood. In §8.2 I consider the possibility of non-piston-like vibration of the speaker cone. For the time being we will just have to note these angular variations and make some qualitative allowance when looking at similar directivity plots for arrays of two or three speakers.

A selection of such dipole and tripole results are presented in Figures 11 to 14. Though the quality of data could be improved by experimental refinements, the overall picture is clear. Figure 11 shows the effect of switching two speakers from in- to out-of-phase at 855 Hz (third speaker disconnected). The central green points are for a single speaker, for comparison. The blue curve shows a roughly doubling in amplitude as both speakers are switched in phase. The red and purple curves, from two separate experimental runs, show the destructive interference normal to the plane of the baffle, in this case at about $\theta = -5°$. (This offset from 0 is not significant.) The red out-of-phase series shows a decline at $\theta > 45°$, represented by the $\mathcal{D}(\theta)$ factor in Eq 12b.

Figure 12 shows the effect of doubling the frequency to 1710 Hz. The 'wedge' cut by destructive interference into the amplitude curve has narrowed. There is clear evidence of the signal falling away for $|\theta| > 40°$. The rather confused collection of data points near $\theta = 0$ is caused by experimental variations, mainly due to backlash in the rather Heath-Robinson equipment used.

Figure 13 is for the same dipole at Figures 11 and 12 but at 1368 Hz. The conditions are those used to plot Figure 6. The graph looks busy because there are in- and out-of-phase data points for two experimental runs. Between these the equipment was dismantled and set up again a few days later. The amplitudes for the two runs have been scaled to give a fair match, but within each run the in- and out- data points have not been scaled relative to each other. There is sharp destructive

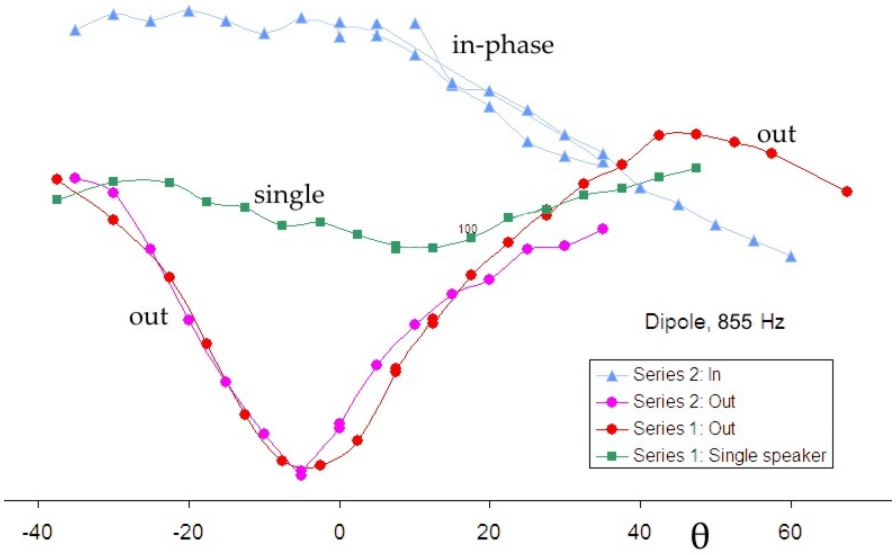

Figure 11: Dipole at λ = 40 cm. Amplitude at a microphone 2 m from two loudspeakers, 12 cm apart, at 855 Hz.

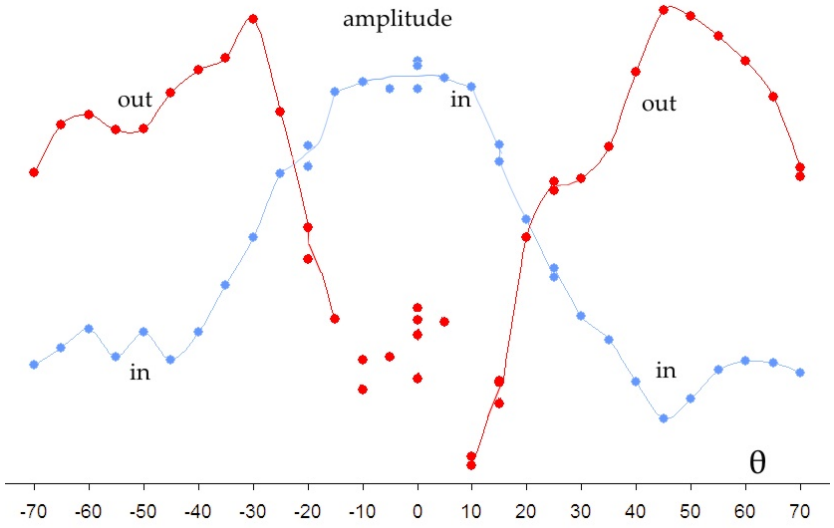

Figure 12: Dipole at λ = 20 cm. Two-speakers at 1710 Hz. Blue: in-phase. Red: out-of-phase.

interference near normal, and again there is evidence of the out-of-phase signal (purple and red) falling off for $\theta > 45°$. The theoretical curve (dark red) used is Eq 12a, equivalent to $\mathcal{D}(\theta) = 1$ in Eq 12b. The blue-grey line is the corresponding in-phase theoretical curve and is in fair agreement with the green and blue data series. Of course, a loud speaker in a baffle is not a point source, so close agreement with the theoretical curves should not be presumed.

Moving to the tripole arrangement, the left and right panels in Figure 14 show the effect of switching the phase of the middle loud speaker at 684 Hz (λ = 50 cm) and 1710 Hz (λ = 20 cm). The continuous curves in the right panel are the theoretical predictions of Eq 13a, b for three point sources. The role of interference is again clear, and the falling off in signal about $|\theta| > 45°$ is again evidence of a directionality related to the extended area of the radiating surface.

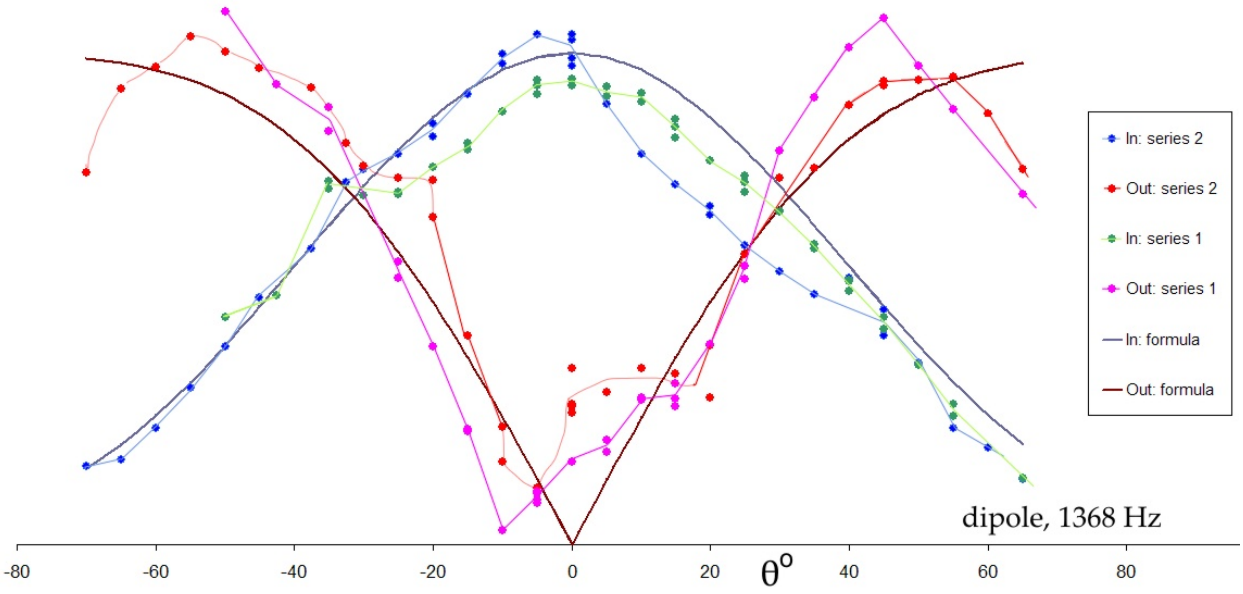

Figure 13: Dipole at λ = 25 cm. In- and out-of-phase amplitudes radiated from two adjacent speakers at 1368 Hz (λ = 25 cm). Two experimental runs compared with Eq 12a. Run 1: green (in) and purple (out). Run 2: blue (in) and red (out).

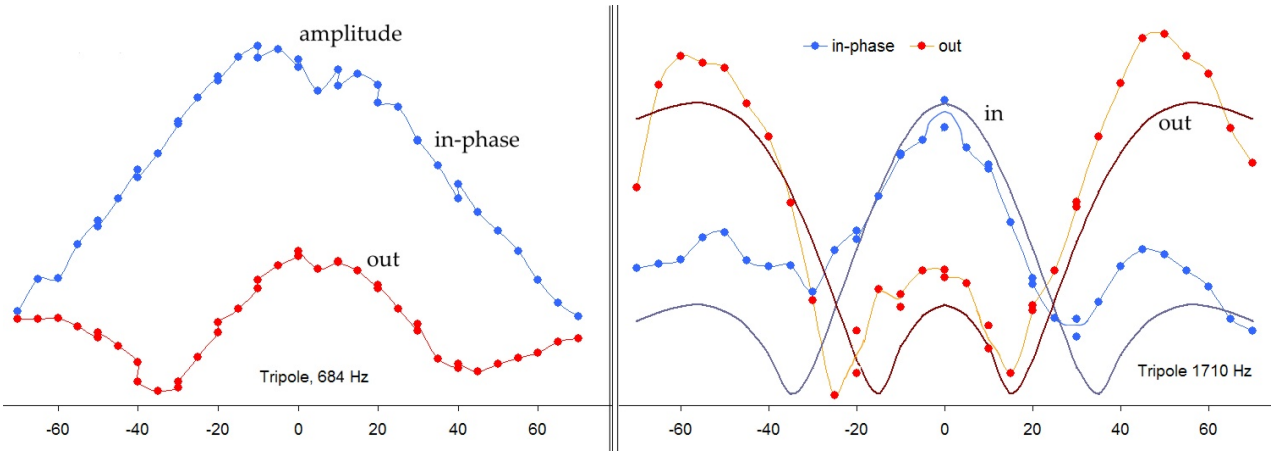

Figure 14: Tripole. Amplitude at 2 m range from three speakers in a line, with all in-phase (blue) or central one out of phase (red). Left panel: 684 Hz, Right, 1710 Hz.

The results of this home-made experiment are largely as expected. The most striking phenomenon is the almost complete cancellation of the sound from the dipole in a direction at right angles to the line joining the two sources. The only surprises have been the strange directivity of a single speaker around about 1 kHz, and the presence of an appreciable sound level in the plane of the dipole or tripole array. Most of the remainder of this article deals with the directionality of radiated sound, represented mathematically by the path differences between the various oscillating components in the source, and the directionality factor $\mathcal{D}(\theta)$ of Eq 12b. I do offer some comparison between theory for planar radiators and experiment in §8, and proffer a plausible explanation for the kink in the directivity shown in the high frequency panels of Figure 10.

5 Exact solutions of the acoustic wave equation

5.1 General features

The violin family of instruments playing in their mid registers are examples of objects which radiate sound at wavelengths comparable with the box dimensions. We know in general that the sound will have only modest variation with direction and that the lower frequencies will suffer from energy locked in a reactive component of motion in the near-field. Without specific model simulation little more can be said. There has been intense research into finding reliable, versatile numerical methods for solving the wave equation for any frequency subject to the given boundary conditions, with the boundary integral and boundary element methods now being most widely used. I say a little about these in §11.2.

Exact analytic solutions of the wave equation are valid for any wavelength, but these exist only for the most simple shapes – the plane, cylinder, sphere and prolate (stretched, cigar-shaped) and oblate (squashed, discus-shaped) spheroids, and the general ellipsoid. For each of these the wave equation can be solved by separation of variables in a co-ordinate system matching the object's geometry. Solutions take the form of sums of special functions, each of which in turn is defined by an infinite series or equivalent integral and may require sophisticated numerical techniques for evaluation. Because of this any difference in practice between an analytic solution with numerical evaluation of special functions and a wholly numerical method lies mainly in proving the stability, convergence and accuracy of the numerical scheme. The literature on exact solutions has been well reviewed in a compendium compiled by Bowman, Senior and Uslenghi entitled 'Electromagnetic and acoustic scattering by simple shapes' (North-Holland John Wiley, 1969). Such solutions in principle allow the radiated wave field to be calculated for a general variation of vibration amplitude over the object's surface. Therefore they are applicable to all modes of vibration of the object, not just the lowest breathing mode. The main value of exact solutions is in the validation of more flexible approximate and asymptotic methods. In the next subsection I give an account of the solution in spherical co-ordinates.

Appendix 4, §16, gives an account of the equivalent solutions in prolate and oblate spheroidal co-ordinates. I have confined this to an appendix because it is technically messy even though it follows the same path of derivation as in spherical co-ordinates. Solutions in spheroidal co-ordinates are valuable because of the greater generality of these shapes, but unfortunately the analytic solutions are complicated. The oblate spheroidal harmonic functions were examined in depth as early as 1922 by J.W.Nicholson (Phil Trans Roy Soc London A vol 224, 1924. p48-93). The classic monograph on spheroidal wave functions is by Carson Flammer, now in Dover publications (2005 reprinting of a 1957 report). Three researchers who spent much time calculating spheroidal wave functions were B.J.King, R.V.Bajer and A.L.van Buren of the US Naval Research Laboratory, presumably because of its relevance to submarine design and detection. A fairly recent summary of wave function computation is by the Australian team of Falloon, Abbot and Wang (J.Phys A: Math. Gen. Vol 36, p5477, 2003), and they are now available in computational software such as Mathematica[6].

Regarding the application of solutions for spheroids, George Chertock was one of the US Navy's sonar scientists and he published a full solution of sound radiation from a prolate spheroid in 1961 (J. Acoustic Soc. Amer, vol 33, p871-876). He separated the wave equation in prolate spheroidal

[6]I have found several cases in which the value of a spheroidal wave function given by Mathematica 10 is clearly incorrect, being either spuriously zero or diverging to infinity. From correspondence with Wolfram I understand that these failures are due to rounding errors causing incorrect cancelling of many large alternating terms in series expansions. The 'work-around' is to increase the working precision to over 50.

co-ordinates and calculated the sound field in two special cases: i) a rigid spheroid oscillating along its axis, and ii) opposite ends of the spheroid oscillating in opposite directions in what he colourfully calls the 'accordian mode'. More recently Boisvert and Van Buren calculated the exact acoustic directivity of a rectangular piston in the side of a rigid prolate spheroid (J.A.S.A, vol 116, 2004, p1932-1937). They illustrate their paper with several polar plots of sound amplitude. Their results were intended for submarines, but also describe a rectangular loud speaker in a rugby-ball-shaped enclosure. This work is an extension of the case, described in Morse and Ingard's classic book, of a circular piston-like area vibrating on a rigid sphere.

In §10 I use the results in Appendix 4 to compare the predictions of a computer program I have written with the exact solutions for radiation of sound from spheroids.

5.2 Helmholtz's equation in spherical co-ordinates

Helmholtz's equation is the acoustic wave equation when the time variation of the field at every point is $e^{-i\omega t}$:

$$\nabla^2\phi \;=\; -\kappa^2\phi \qquad\qquad Copy\ of\ Eq(8b)$$

where ϕ is the displacement potential (or alternatively the velocity potential). Spherical co-ordinates (r,θ,ψ) are respectively r: the radial distance from the centre of the sphere, O, θ: the polar or latitude angle away from a reference polar direction (usually the Cartesian z axis), and ψ: the azimuthal or longitudinal angle round from a second reference direction (usually the x axis). The Laplacian in spherical co-ordinates looks very complicated and Helmholtz's equation is

$$\frac{1}{r^2}\frac{\partial}{\partial r}\left(r^2\frac{\partial\phi}{\partial r}\right) \;+\; \frac{1}{r^2\sin\theta}\frac{\partial}{\partial\theta}\left(\sin\theta\frac{\partial\phi}{\partial\theta}\right) \;+\; \frac{1}{r^2\sin^2\theta}\frac{\partial^2\phi}{\partial\psi^2} \;+\; \kappa^2\phi \;=\; 0\,. \qquad (14)$$

The classic 'separation of variables' method assumes a solution of the form $\phi = \mathcal{R}(r).\Theta(\theta).\Psi(\psi)$. This is substituted and the result multiplied by $(r\sin\theta)^2/\phi$, at which point Helmholtz's equation starts to separate into the sum of terms respectively only in r, θ and ψ:

$$\frac{\sin^2\theta}{\mathcal{R}}\frac{d}{dr}\left(r^2\frac{d\mathcal{R}}{dr}\right) \;+\; \frac{\sin\theta}{\Theta}\frac{d}{d\theta}\left(\sin\theta\frac{d\Theta}{d\theta}\right) \;+\; \frac{1}{\Psi}\frac{d^2\Psi}{d\psi^2} \;+\; (\kappa r\sin\theta)^2 \;=\; 0\,.$$

The term in Ψ,ψ, being independent of all other terms, must equal a constant. Call it $-m^2$ for reasons which will become clear. The solution of

$$\frac{d^2\Psi}{d\psi^2} + m^2\Psi = 0 \quad \text{is} \quad \Psi = e^{im\psi}\,. \qquad (15)$$

This equation is in fact the equation of simple harmonic motion and the m are eigenvalues. Since $e^{im\psi}$ must equal $e^{im(\psi+2\pi)}$, both appertaining at the same azimuth ψ, m must be an integer. So all solutions of Helmholtz's equations must have azimuthal variation corresponding to the eigenvector $e^{im\psi}$ which effectively wraps a sine wave neatly around the sphere.

To separate the $\mathcal{R}$ and Θ terms, replace $\frac{1}{\Psi}\frac{d^2\Psi}{d\psi^2}$ by $-m^2$ and divide the above by $\sin^2\theta$:

$$\frac{1}{\mathcal{R}}\frac{d}{dr}\left(r^2\frac{d\mathcal{R}}{dr}\right) \;+\; \frac{1}{\sin\theta\;\Theta}\frac{d}{d\theta}\left(\sin\theta\frac{d\Theta}{d\theta}\right) \;-\; \frac{m^2}{\sin^2\theta} + \;(\kappa r)^2 \;=\; 0\,.$$

Again we can pick out terms only in one variable, and terms only in R or Θ must equal the same constant

$$\frac{1}{\mathcal{R}}\frac{d}{dr}\left(r^2\frac{d\mathcal{R}}{dr}\right) \;+\; (\kappa r)^2 \;=\; -\;\frac{1}{\sin\theta\;\Theta}\frac{d}{d\theta}\left(\sin\theta\frac{d\Theta}{d\theta}\right) \;+\frac{m^2}{\sin^2\theta} \;=\; constant\,.$$

The constant is usually written $l(l+1)$ where l is an integer. The equation in θ is a version of the Associated Legendre equation and that in r is a form of Bessel's equation, both of which are well documented in the literature. They are usually massaged from the above in standard forms as follows:

Polar angle equation. Change the variable from θ to $x = \cos\theta$ and note that for any function F of θ

$$\frac{dF}{d\theta} = \frac{dF}{dx}\frac{dx}{d\theta} = -\sin\theta\frac{dF}{dx} \qquad \text{and} \quad \sin\theta\frac{dF}{d\theta} = -(1-x^2)\frac{dF}{dx}\,.$$

$$\text{Hence} \qquad \frac{1}{\sin\theta}\frac{d}{d\theta}\left(-(1-x^2)\frac{d\Theta}{dx}\right) + \left(l(l+1) - \frac{m^2}{1+x^2}\right)\Theta = 0\,,$$

$$\frac{d}{dx}\left((1-x^2)\frac{d\Theta}{dx}\right) + \left(l(l+1) - \frac{m^2}{1+x^2}\right)\Theta = 0\,,$$

$$(1-x^2)\frac{d^2\Theta}{dx^2} - 2x\frac{d\Theta}{dx} + \left(l(l+1) - \frac{m^2}{1+x^2}\right)\Theta = 0\,. \tag{16}$$

These last two express the Associated Legendre equation in its usual forms. $m = 0$ reduces it to Legendre's equation. Its form is an eigenvalue equation: Operator on Θ = constant $\times\Theta$. Its solutions are found using a trial polynomial series; they are the the Legendre polynomials. The polynomial series 'of the first kind', $P_l(x)$, begins

$$P_0(x) = 1, \quad P_1(x) = x, \quad P_2(x) = \tfrac{1}{2}(3x^2-1), \quad P_3(x) = \tfrac{1}{2}(5x^3-3x), \ \ldots$$

The Associated equation can be obtained from the plain Legendre equation by differentiating it m times with respect to x, as described in the textbooks. Its solutions are $P_l^m(x)$. The $m = 0$ series is as above and series for $m = 1$, 2 and 3 commence with these:

$$m=1: \quad P_1^1(x) = -\sqrt{1-x^2} = -\sin\theta, \qquad P_2^1(x) = -3x\sqrt{1-x^2} = -\tfrac{3}{2}\sin 2\theta,$$
$$P_3^1(x) = -\tfrac{3}{2}(5x^2-1)\sqrt{1-x^2} = -\tfrac{3}{8}(\sin\theta + 5\sin 3\theta),$$

$$m=2: \quad P_2^2(x) = 3(1-x^2) = \tfrac{3}{2}(1-\cos 2\theta), \qquad P_3^2(x) = 15x(1-x^2) = \tfrac{15}{4}(\cos\theta - \cos 3\theta),$$

$$m=3: \quad P_3^3(x) = -15(1-x^2)^{3/2} = -\tfrac{15}{4}(3\sin\theta - \sin 3\theta), \qquad P_4^3(x) = -105x(1-x^2)^{3/2}$$

Note that $P_l^m = 0$ if $m > l$. Graphs of the first few are shown in Figure 15. Those in the left panel, for $m = 0$ apply when the geometry is a surface of revolution, giving the field rotational symmetry about the polar axis.

Radial equation. This is

$$r^2\mathcal{R}'' + 2r\mathcal{R}' + \left[\kappa^2 r^2 - l(l+1)\right]\mathcal{R} = 0\,. \tag{17}$$

It looks rather like Bessel's equation

$$r^2\frac{d^2\mathcal{Z}}{dr^2} + r\frac{d\mathcal{Z}}{dr} + (r^2 - n^2)\mathcal{Z} = 0$$

and can be transformed into this first by the substitution $\mathcal{R} = \mathcal{Z}/\sqrt{\kappa r}$ which produces

$$r^2\mathcal{Z}'' + r\mathcal{Z}' + \left[\kappa^2 r^2 - l(l+1) - \tfrac{1}{4}\right]\mathcal{Z} = 0.$$

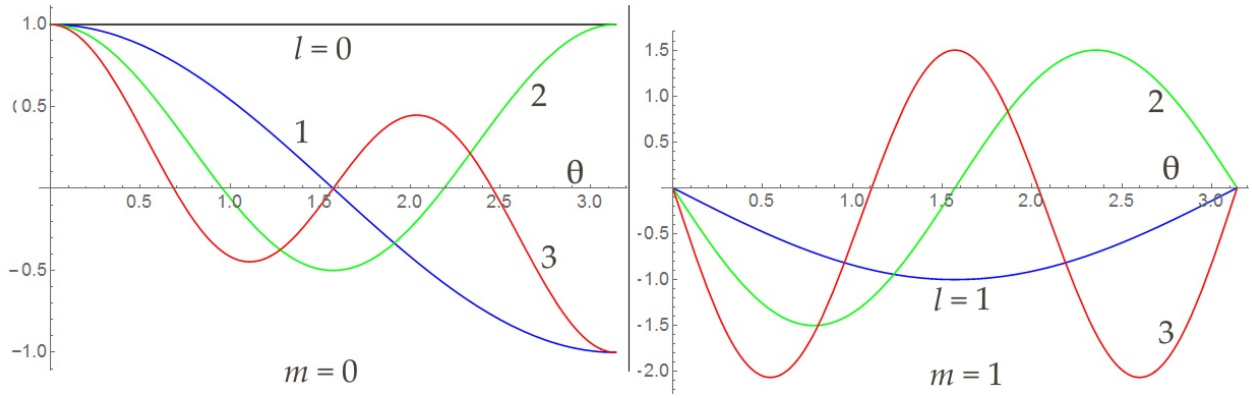

Figure 15: The first few Associated Legendre polynomials plotted as functions of θ. Left: $P_0^0(\cos\theta)$ to P_2^0. Right: P_1^1 to P_3^1. $0 \le \theta \le \pi$.

We need a further change of variable: $\kappa r \to x$, $d\mathcal{Z}/dr = \kappa\, d\mathcal{Z}/dx$. Thus

$$x^2\mathcal{Z}'' + x\mathcal{Z}' + [x^2 - (l+\tfrac{1}{2})^2]\mathcal{Z} \;=\; 0$$

is the radial equation, where the derivatives are now with respect to $x = \kappa r$. It is Bessel's equation for half-integer order and its solutions are $J_{l+1/2}(x)$ and $Y_{l+1/2}(x)$. The solutions of Eq 17 are therefore the so-called spherical Bessel functions of the first and second kind, $j_l(x)$ and $y_l(x)$, related to the ordinary Bessel functions by[7]

$$j_l(x) = J_{l+\frac{1}{2}}(x)\sqrt{\frac{\pi}{2x}}, \qquad y_l(x) = Y_{l+\frac{1}{2}}(x)\sqrt{\frac{\pi}{2x}}\,.$$

When evaluated, the $\sqrt{x}$ factors cancel to leave some quite simple polynomials multiplying $\sin x$ and $\cos x$. With $x = \kappa r$ the first few are

$$j_0(x) = \frac{\sin x}{x}, \qquad y_0(x) = -\frac{\cos x}{x}\,.$$

$$j_1(x) = \frac{\sin x}{x^2} - \frac{\cos x}{x}, \qquad y_1(x) = -\frac{\cos x}{x^2} - \frac{\sin x}{x}\,.$$

$$j_2(x) = \left(\frac{3}{x^3} - \frac{1}{x}\right)\sin x - \frac{3}{x^2}\cos x, \qquad y_2(x) = -\left(\frac{3}{x^3} - \frac{1}{x}\right)\cos x - \frac{3}{x^2}\sin x\,.$$

These are illustrated in Figure 16. Note that the y kind diverge at the origin. The general solution of the radial equation is an arbitrary linear combination of these.

Any sum of individual exact solutions of the wave equation is also a solution. A commonly employed method for solving the acoustic wave equation subject to given boundary conditions is to assume an assembly of point solution with suitable values of the eigenvalues l and m, and try to match the coefficients to the required boundary values.

5.3 Examples

I will tie all this together with three examples.

Case 1: Spherically symmetric source. First take both $m = 0$ and $l = 0$, imposing no variation with direction so tere is spherical symmetry. Notice that neither m nor l actually features

[7] The $\pi/2$ is a conventional normalisation factor of no structural significance.

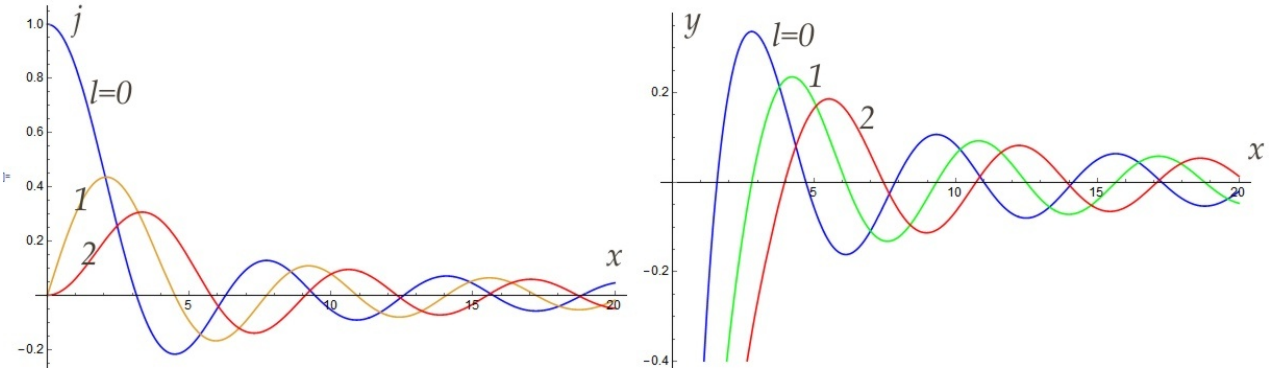

Figure 16: Spherical Bessel functions of the first kind (left panel) and second kind (right).

in Helmholtz's equation, Eq 14. The role of l is to link the R and Θ functions into their correct pairs. The displacement potential is simply

$$\phi(r,\theta) \;=\; C_1\, j_0(\kappa r) + C_2\, y_0(\kappa r) \;=\; C_1\,\frac{\sin\kappa r}{\kappa r} - C_2\,\frac{\cos\kappa r}{\kappa r}$$

where C_1 and C_2 are arbitrary constants. Direct substitution does indeed prove that this is a solution of Eq 17 for $l = 0$. Moreover if $C_1 = i$, $C_2 = -1$, this becomes the familiar elementary complex solution $\phi(r) = e^{i\kappa r}/(\kappa r)$ of Helmholtz's equation for a point source or sink.

Case 2: $\cos\theta$ variation For the second example take $m = 0$, $l = 1$. The variation with polar angle is therefore as $\cos\theta$ and the radial variation is $C_1\, j_1(\kappa r) + C_2\, y_1(\kappa r)$:

$$\phi \;=\; \left[C_1\left(\frac{\sin\kappa r}{(\kappa r)^2} - \frac{\cos\kappa r}{\kappa r}\right) \;+\; C_2\left(\frac{\cos\kappa r}{(\kappa r)^2} + \frac{\sin\kappa r}{\kappa r}\right)\right]\cos\theta\,. \tag{18}$$

Again direct substitution proves this to be a solution. If $C_1 = -1$ and $C_2 = i$, a complex solution is

$$\phi \;=\; \frac{e^{i\kappa r}}{\kappa r}\left(1 + \frac{i}{\kappa r}\right)\cos\theta\,.$$

Its complex conjugate is also a solution. When κr is large, this describes a spherical wave modulated in angle by $\cos\theta$. It is probably clearer, however, if we stick to only real functions, so take the case $C_1 = -1$, $C_2 = 1$. The grad operator in spherical co-ordinates is

$$\nabla(\phi) \;=\; \frac{\partial\phi}{\partial r}\mathbf{e_r} + \frac{1}{r}\frac{\partial\phi}{\partial\theta}\mathbf{e}_\theta + \frac{1}{r\sin\theta}\frac{\partial\phi}{\partial\psi}\mathbf{e}_\psi\,.$$

This evaluates to a displacement of

$$\xi(r,\theta) \;=\; -\nabla(\phi) \;=\; -\frac{\cos\theta}{k^2 r^3}\left[(\kappa^2 r^2 - 2\kappa r - 2)\cos\kappa r \;-\; (\kappa^2 r^2 + 2\kappa r - 2)\sin\kappa r\right]\mathbf{e_r}$$

$$+\;\frac{\sin\theta}{k^2 r^3}\left[(\kappa r + 1)\cos\kappa r \;+\; (\kappa r - 1)\sin\kappa r\right]\mathbf{e}_\theta\,. \tag{19}$$

This displacement field is illustrated in the three contour plots of Figure 17 over $-2 \le z \le 2$, $-2 \le \rho \le 2$, $\rho^2 = x^2 + y^2$, for $\kappa = 2\pi/0{\cdot}4$. The contour scale on the radial plot has red $> 1\cdot 4$, but in the circumferential plot red is only $> 0\cdot 06$, much weaker. Clearly the motion is predominantly along the polar (z) direction, horizontal axis. The contours of potential look very similar to the left panel of Figure 17. At each position the displacement is radial, being normal to the equipotential surfaces.

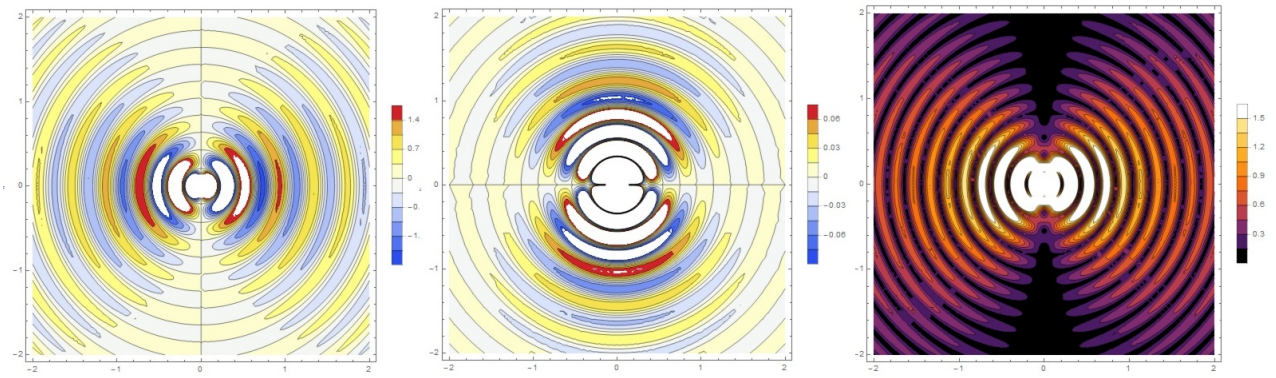

Figure 17: Contours of displacement ξ in Eq 19 for $\lambda = 0 \cdot 4$. Left: radial component ξ_{radial}. Centre: circumferential ξ_θ. Right: absolute value, $|\xi|$. White areas correspond to large off-scale values.

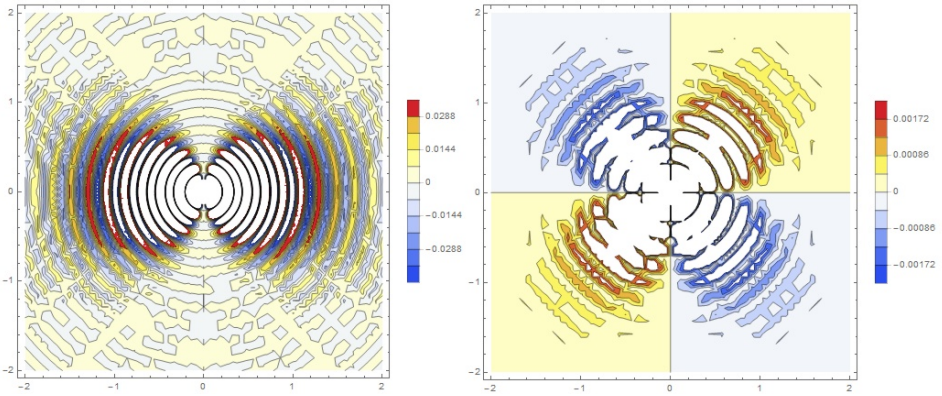

Figure 18: Power components in radial (left) and circumferential (right) directions.

The circumferential component of displacement is interesting. Since differentiation with respect to θ leaves the radial factor unchanged, the $\mathbf{e}_\theta$ displacement component is essentially the potential function rotated by 90°, as Figure 17 shows. This has consequences for the flow of energy through this field. The power is proportional to the product of potential (pressure) and displacement (and hence particle velocity). This product varies with θ as $\sin 2\theta$, the integral of which over 0 to π is zero. The two contour plots in Figure 18 show $\phi\,\xi_r$ (left) and $\phi\,\xi_\theta$ (right). The circumferential contribution is much smaller in absolute value, and is directed at 45° to the polar axis. The blue (negative) and red (positive) colours indicate that the energy in this component flows in or out respectively from the centre. This to and fro motion each cycle carries no energy away from the centre, but rather locks energy in these diagonal channels in a near-field behaviour analogous to that described in §3 for a point source of spherical waves. Put another way, the circumferential motion is entirely reactive, not radiative.

It is fair to ask 'what body in motion could produce a field as in Figures 17 and 18?'. Any motion of a sphere in a fluid must produce radial motion of the fluid. This is because only motion of the sphere normal to its local surface can produce motion in the air or liquid; since the fluid cannot support shear, motion parallel to the local tangent plane has no effect. Suppose that a rigid sphere oscillates along its polar axis, z with amplitude ξ_0. At point P at polar angle θ the component of displacement normal to the surface is $\xi_0 \cos\theta$, which is the polar dependence of radial displacement in Eq 17. So it seems to me that that an axially vibrating rigid sphere would either create precisely the field in this example, or something very like it.

Case 3: Dipole To examine this conjecture let us evaluate the field of an (out-of-phase) dipole. I will take the two point sources to be

$$\phi_1 = \frac{\sin \kappa r_1}{\kappa r_1}, \qquad \phi_2 = -\frac{\sin \kappa r_2}{\kappa r_2}, \quad r_{1,2}^2 = R^2 + d^2 \pm 2Rd\cos\theta.$$

They are a distance $2d$ apart along the polar axis, and again θ is the polar angle. R is the distance from their midpoint as origin and the + sign is associated with r_2. Clearly the two sources will cancel each other if $d = 0$, and complicated interference patterns can form if d is greater than about quarter a wavelength. I will focus on the field when d is very small. To find this expand $\phi_1 + \phi_2$ as a Maclaurin series about $d = 0$. The term linear in d is

$$\phi_{dipole} \rightarrow \ \ 2d\kappa\cos\theta\left(-\frac{\cos\kappa R}{\kappa R} + \frac{\sin\kappa R}{\kappa^2 R^2}\right)$$

and terms in d^2 are zero. This shows the simple $\cos\theta$ dependence of Eq 18 and indeed the two expressions become identical if $C_1 = 2\kappa d$ and $C_2 = 0$. Thus the eigenvalue case $l = 1,\ m = 0$ is realised by a dipole of infinitesimal spacing, and by a rigid sphere oscillating along the polar axis.

Note in passing that the case $l = 1,\ m = 1$ applies both a $\cos\theta$ and $\cos\psi$ variation and so divides the sphere into four quadrants, each moving outwards as its neighbours move inwards. This is an example of a quadrupole field.

Case 4: Point source on a rigid sphere In July 2015 I looked into this case and have described it in a separate article on *www.mathstudio.co.uk*. I conclude that, as expected, the sound appears to come from the small area on the sphere which is in motion. In the near field the air particles move in ellipses, but the non-radial component on displacement falls as $1/r^2$ while the radial component falls only as $1/r$. Therefore the ellipses collapse into straight lines with increasing range until in the distant far field all motion is radial.

6 Kirchhoff and Rayleigh-Sommerfeld theories

This section describes two closely related methods for calculating the sound pressure, displacement and velocity at a point away from a radiating object by adding the wavelets emitted from elementary sources distributed over the object's surface. They essentially implements Huygens' Principle: that a wave propagates as if elementary wavelets are emitted at every point along a wavefront (the locus of points with the same phase), and interfere constructive or destructively to form the advancing wavefront at a subsequent time and/or place. In 1818 this was used by Fresnel to explain diffraction patterns formed by light passing through narrow slits and pin holes. Later in the 19th century the theory was placed on a firmer mathematical footing by Gustav Kirchhoff, Lord Rayleigh and Arnold Sommerfeld. The approaches of these pioneers lead to formulae which are quite similar. When implemented in a computer program the methods can fit well with using finite element analysis (FEA) to predict the vibratory motion of a large object composed of a mesh of triangular.

6.1 Foundation of Kirchhoff and Rayleigh-Sommerfeld theories

Derivations of the Kirchhoff and Rayleigh-Sommerfeld radiation formulae are described in textbooks on optics, but I give an account here to explain their use and validity. The basis of both is Green's symmetrical theorem of vector calculus which relates two scalar quantities defined within a closed 3D region Ω to their values on the enclosing boundary Σ. Calling these scalars ϕ and $\mathbf{G}$,

$$\iiint_{\Omega} (\phi\,\nabla^2\mathbf{G} - \mathbf{G}\,\nabla^2\phi)\,d\Omega \;=\; \iint_{\Sigma} (\phi\,\nabla\mathbf{G}\cdot\mathbf{n} - \mathbf{G}\,\nabla\phi\cdot\mathbf{n})\,d\Sigma\,. \tag{20}$$

Since both theories originated in light diffraction by a small aperture in a flat black screen, I will develop them in the corresponding acoustic case, which is a vibrating piston surrounded in a flat baffle. We shall see shortly, however, that restriction to a plane only applies of necessity to the Rayleigh-Sommerfeld formulation. The construction relevant to Kirchhoff's theory is given in Figure 19a, and that for the Rayleigh-Sommerfeld in 19b. The surface Σ is the same in both cases and has two parts

- an outer part consisting of a vast closed hemispherical surface comprising the piston-like radiating element S, the infinite planar baffle in which is placed, plus a hemispherical cap which extends to infinity,
- an internal surface consisting of a small spherical bubble which encloses the listening point Q.

$\mathbf{n}$ is a unit vector normal to the plane of the element, pointing out of Σ: that is, outwards from the hemispherical space but towards Q on the interior surface. Take ϕ to be the displacement potential of the sound field. The other scalar $\mathbf{G}$ is a mathematical device called the Green's function, which is an elementary solution of the wave equation. The two theories differ in their choice of $\mathbf{G}$ as will be explained shortly.

For the time being forget that S represents a piston and just regard S as part of the surface Σ where the field is non-zero. Also assume only time harmonic vibration at a single frequency ω radians/sec. Therefore the relevant wave equation is Helmholtz's, Eq 8b. In principle more complex periodic motions can be modelled by Fourier superposition. Now since both ϕ and $\mathbf{G}$ are solutions of Helmholtz's equation, the difference $\phi\,\nabla^2\mathbf{G} - \mathbf{G}\,\nabla^2\phi$ in Eq 20 is zero everywhere within Σ. The left side of Eq 20 vanishes whatever the form of ϕ and $\mathbf{G}$, and we may conclude that the surface integrals over the outer and inner surfaces of Σ must be equal and opposite.

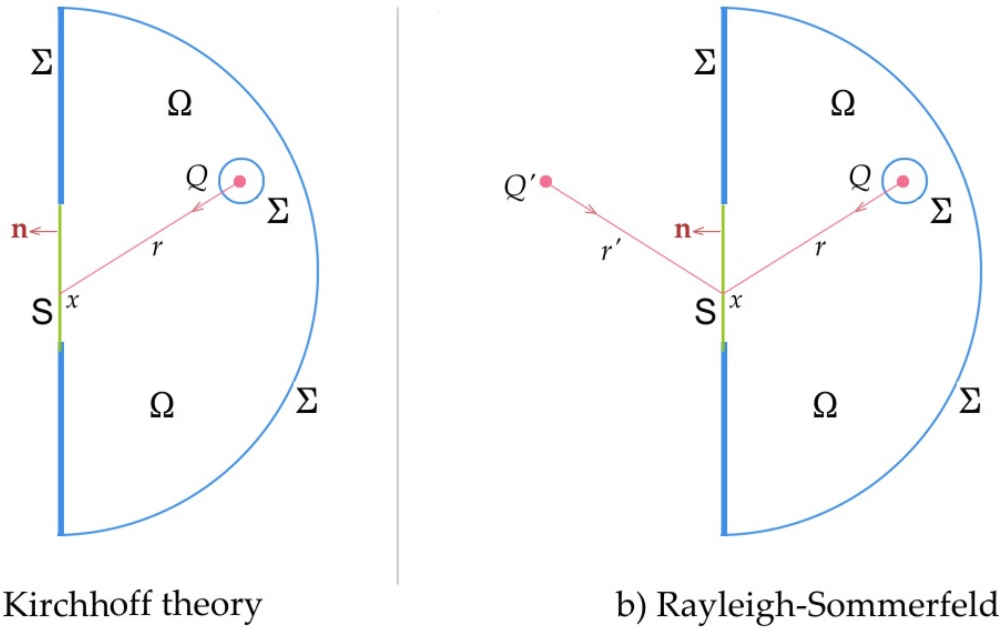

Figure 19: Construction around a radiating planar object S in the Kirchhoff and Rayleigh-Sommerfeld theories. The spherical bubble around Q means that Q is outside of Σ.

Case 1: Kirchhoff's formula : Kirchhoff took the Green's function to be a point source at Q, with spatial variation $e^{i\kappa r}/r$ where r is the radial distance from Q (Figure 19a). Evaluate this over the bubble around Q in the limit of it shrinking to zero.

$$\nabla \boldsymbol{G}\cdot\mathbf{n} \;\equiv\; \nabla\left(\frac{e^{i\kappa r}}{r}\right)\cdot\mathbf{n} \;=\; \left(i\kappa-\frac{1}{r}\right)\frac{e^{i\kappa r}}{r}\,\mathbf{e_r}\cdot\mathbf{n} \;=\; -\left(i\kappa-\frac{1}{r}\right)\frac{e^{i\kappa r}}{r}$$

where $\mathbf{e_r}$ is a unit vector pointing outwards from Q which, here, is equal and opposite to $\mathbf{n}$. The term in $\nabla\phi\cdot\mathbf{n}$ tends to zero as $r\to 0$ because $\nabla\phi$ is locally almost constant and $\mathbf{n}$ is inwards at every point on the bubble, causing contributions from opposite sides of the bubble cancel. The surface area of the bubble is $4\pi r^2$. Only terms of $\phi\,\nabla\mathbf{G}\cdot\mathbf{n}$ in $1/r^2$ do not tend to zero as $r\to 0$. Hence the bubble integral reduces to $4\pi\phi(Q)$. Kirchhoff formulation states Green's theorem as

$$\phi(Q) \;=\; \frac{-1}{4\pi}\iint_{\Sigma_{outer}}\left(\phi\,\nabla\mathbf{G}\cdot\mathbf{n}-\mathbf{G}\,\nabla\phi\cdot\mathbf{n}\right)d\Sigma\,,\qquad \mathbf{G} \;=\; \frac{e^{i\kappa r}}{r}\,. \tag{21a}$$

There is no approximation in this. In Kirchhoff's formulation the boundary $S+\Sigma$ can be any simple closed surface. As noted above, the closed half sphere of Figure 19a is traditionally used because the theory was originally developed to explain diffraction of a beam of light normally incident on a planar screen with a small hole in it. A very plausible postulate is now made to reduce the integral over the whole of Σ to an integral only over the planar part. This is the 'Sommerfeld radiation condition' which states that the field over the hemispherical dome tends to zero as the dome expands to infinity. The radiation condition eliminates the possibility of secondary sources on the dome radiating sound to the listener at Q. One argument for this is that, travelling to infinity, the outgoing wave would be so time delayed, and the re-emitted reflected wave doubly time delayed, that no sound from the hemispherical dome could interfere with the waves direct from S.

A much more dubious requirement is now imposed to reduce the area of integration further to only the vibrating surface S. This is the so-called Kirchhoff approximation to the boundary conditions

on the baffle. Kirchhoff argued that, if the motion of the vibrating area S is predominantly normal (z direction), then the field over the baffle should be small and can be taken to be zero. Indeed, he assumed that it becomes zero abruptly at the perimeter of the piston-like element S. When these arguments are believed to hold, Kirchhoff formula for the field at Q is

$$\phi(Q) \;=\; \frac{-1}{4\pi}\iint_S \left[\phi_0(S)\left(i\kappa-\frac{1}{r}\right)\mathbf{e_r}\cdot\mathbf{n}-\nabla\phi_0(S)\cdot\mathbf{n}\right]\frac{e^{i\kappa r}}{r}\,dS \qquad (21b)$$

where S is the vibrating part of the system and the subscript $_0$ emphasises that this is the value actually on the surface. Note again that Green's theorem does not require that the baffle plus piston together form a plane. When the Kirchhoff formula is applied to light diffraction, S is an aperture in a screen illuminated from behind. In §9 I show how Σ can be deformed so that the formula applies to an isolated object such as a sphere. The dot product $\mathbf{e_r}\cdot\mathbf{n}$ is the cosine of the angle β which the line from Q to S makes with the local outwards normal. $\cos\beta$ is called the 'obliquity factor'. Notice that it applies only to the term in ϕ_0. The other term $-\nabla\phi_0(S)\cdot\mathbf{n}$ is the normal displacement of the surface.

The crucial practical weakness of Kirchhoff's formulation is that it requires both ϕ and its derivative over the whole of S to be known inputs. This is not realistic because pressure (ϕ) and displacement ($-\nabla\phi$) are not independent but linked through the wave equation we are trying to solve[8]. Therefore to apply Kirchhoff's formula to a general object with prescribed ϕ you would have to guess $\nabla\phi_0\cdot\mathbf{n}$, or *vice versa*.

Case 2: Rayleigh-Sommerfeld formulae : The inconsistencies which attend Kirchhoff's approach prompted Rayleigh and later Sommerfeld to propose a different Green's function which at least leads to a self-consistent formula. This is illustrated in Figure 19b. In this case the mathematics strictly requires S to be a plane. $\mathbf{G}$ consists of two spherical waves coming from sources at Q and at Q', where Q' is the mirror image of Q reflected in the plane of the piston and baffle. There are two variations depending on whether the two sources are in phase or out of phase. In the out-of-phase case this ingenious construction ensures that $\mathbf{G}=0$ in the plane S of the piston, which in turn means that $\nabla\phi\cdot\mathbf{n}$ does not need to be known there. The alternative in-phase version makes $\partial\mathbf{G}/\partial n=0$ in the plane of S. When out-of-phase

$$\mathbf{G} \;=\; \frac{e^{i\kappa r}}{r}-\frac{e^{i\kappa r'}}{r'}$$

where r is the distance from Q to a general point x on the piston element, and r' is the corresponding distance from Q'. In taking the gradient of this we use unit vectors $\mathbf{e_r}$ and $\mathbf{e'_r}$ pointing to x from Q and Q' respectively. The contribution of $-e^{i\kappa r'}/r'$ to the bubble surface integral around Q is zero since terms in r^2/r'^2 tend to zero with r. In the plane of S the normal components of $\mathbf{e_r}$ and $\mathbf{e'_r}$ are in opposite directions so $\mathbf{e'_r}\cdot\mathbf{n}=-\mathbf{e_r}\cdot\mathbf{n}$. Also the lengths r and r' are equal. As a result

$$\left.\frac{\partial\mathbf{G}}{\partial n}\right|_x \;\equiv\; \nabla\mathbf{G}\cdot\mathbf{n} \;=\; 2\left(i\kappa-\frac{1}{r}\right)\frac{e^{i\kappa r}}{r}\,\mathbf{e_r}\cdot\mathbf{n}\,.$$

Invoking the two assumptions above, namely the Kirchhoff surface field approximation on the baffle part of Σ and Sommerfeld's radiation condition at infinity, the so-called 'dipole' version of the Rayleigh-Sommerfeld expression for the field at Q is

$$\text{Dipole}: \qquad \phi(Q) \;=\; -\frac{1}{2\pi}\iint_S \phi_0(S)\left(i\kappa-\frac{1}{r}\right)\frac{e^{i\kappa r}}{r}\,\mathbf{e_r}\cdot\mathbf{n}\,dS\,. \qquad (22a)$$

[8] Kirchhoff theory is applied to scattering problems. One term can be omitted by taking the object as either soft (air pressure at surface $\phi_S=0$) or hard (displacement at surface, $\partial\phi/\partial n=0$). The Kirchhoff approximation in scattering is that the field of S (or respectively its normal derivative) is exactly what it would be if the scatterer were an infinite planar surface tangent to the actual object.

If the alternative Green's function with a + sign had been taken, we would have obtained

$$\text{Monopole :} \qquad \phi(Q) \;=\; +\frac{1}{2\pi}\iint_S \nabla\phi(S)\cdot\mathbf{n}\Big|_0 \frac{e^{i\kappa r}}{r}\,dS\,. \tag{22b}$$

This is called the 'monopole' version and has no obliquity factor. Clearly if the surface is vibrating in a mode in which all motion is normal to the surface, the normal displacement is also the total displacement ξ_0.

The Kirchhoff formula is the mean of the two Rayleigh-Sommerfeld versions, as can be seen by adding two point sources at Q and subtracting two at Q' in Figure 19. All three formulations are built from the quantities $\phi_0\,\nabla G\cdot\mathbf{n}$ and $\boldsymbol{G}\,\nabla\phi_0\cdot\mathbf{n}$. Several writers interpret these respectively as a dipole layer and a monopole layer, which is where the above names come from. The layer of dipoles has surface density equal to ϕ_0, and the monopole layer has density equal to the normal component of displacement. The dipole concept accounts for the $\cos\beta$ obliquity factor in this term alone. It seems paradoxical that the equation can be interpreted as sheets of monopoles $e^{i\kappa r}/r$ and dipoles lying in the vibrating surface when the $e^{i\kappa r}/r$ arises from the Green's function centred on Q, the distant listening point.

6.2 The computer program

We now have three formulae expressing the radiated field $\phi(Q)$, derived under different conditions. Accordingly I have written three versions of the same basic computer program:

1. one to implement the Kirchhoff formulation Eq 21 with potential ϕ_0 and normal displacement both defined on the object,

2. one to implement the Rayleigh-Sommerfeld formulation Eq 22a with surface potential ϕ_0 as input.

3. one to implement the Rayleigh-Sommerfeld formulation Eq 22b with normal displacement $\boldsymbol{\xi_0}\cdot\mathbf{n}$ defined on the object,

The program developed in stages. The earliest version used the dipole Rayleigh-Sommerfeld formula Eq 22a, since this is the one most commonly stated in textbooks. This version is required to compare with exact solutions of Helmholtz's equation, which are always in terms of ϕ. The approach is not original, and I first used it myself in 1986 to calculate the scattering of ultrasound from the jagged faces of hypothetical, postulated cracks in steel pressure components. That model still has a role in the validation of ultrasonic non-destructive inspection procedures for safety-critical components. The model is constructed in two stages:

1. select a point Q for the listener and calculate by analytic integration (Appendix 1) the approximate scalar field radiated by a single triangular surface element, assuming that it behaves as a uniform piston independently of its surrounding elements; that is, there is no spilling of waves from adjacent elements over the surface of the given element,

2. using complex arithmetic numerically add up the field contributions at Q from all elements on the surface of the object, taking account of the obliquity factor. In doing so, weight the contribution from each element with the known amplitude of potential as obtained by FEA.

For any single element, whose width is small compared with the distance to Q, the exact distance from S to Q can be written as $r + \varepsilon(s)$ where r is the distance to the centroid. Moreover call $\mathbf{e_r} \cdot \mathbf{n} = \cos\beta$, an obliquity factor for the element as a whole. Finally let ϕ have the same value ϕ_0 over the whole element. The contribution from one element to $\phi(Q)$ is then

$$-\frac{\phi_0}{2\pi}\left(i\kappa - \frac{1}{r}\right)\cos\beta\,\frac{e^{i\kappa r}}{r}\iint_{element} e^{i\kappa\,\varepsilon(s)}\,ds\,.$$

The integral is a standard case and can be done analytically as described in Appendix 1, §13. I will point out, however, that in almost all cases the wavelength will much exceed the width of any finite element, in which case the integral reduces to the element's area S. The $\cos\beta$ obliquity factor turns this into the projected area of the element as seen from Q. The total model in the version of Eq 22a is summarised by the formula

$$\phi(Q) \;=\; \sum_{elements}\frac{\phi_0}{2\pi}\left(\frac{1}{r} - i\kappa\right)\cos\beta\,\frac{e^{i\kappa r}}{r}\iint_{each\ element} e^{i\kappa\,\varepsilon(s)}\,ds\,. \qquad (23a)$$

Initially I did not use the above formula with ϕ_0 as input, preferring to input an assumed normal displacement. Displacement is physically more tangible than potential and in any case the displacement vector for each mesh element are the data provided by finite element calculations of a vibrating object. Since I was initially working only with Eq 22a, I conjectured that the surface potential could be estimated from the normal displacement as follows. Because the vibrating surface in the Rayleigh scheme is flat and surrounded by a planar baffle, the motion immediately next to it is essentially that of a plane wave in the z direction, the direction $-\mathbf{n}$: therefore $\phi \approx e^{i(\kappa z - \omega t)}$. The corresponding displacement is $\boldsymbol{\xi} \equiv -\nabla\phi = -i\kappa\phi\,\mathbf{e_z}$, and $\phi = i\xi/\kappa$. Therefore I replaced ϕ_0 in Eq 23a with $i\xi_0/\kappa$ where ξ_0 is the prescribed magnitude of the normal component of surface displacement. $i\xi_0/\kappa$ is here a proxy for ϕ_0. A displacement version derived from Eq 22a has the formula

$$\phi(Q) \;=\; \sum_{elements}\frac{\xi_0}{2\pi}\left(1 + \frac{i}{\kappa r}\right)\cos\beta\,\frac{e^{i\kappa r}}{r}\iint_{each\ element} e^{i\kappa\,\varepsilon(s)}\,ds\,. \qquad (23b)$$

How does this compare with Eq 22b obtained using the + case Green's function? They are clearly not the same since Eq 22b has no obliquity factor. They would be the same (apart from a − sign) if ϕ had the form of a point source, $\xi_0 e^{i\kappa r}/r$. This is paradoxical since Eq 23b was obtained on the assumption of a plane wave at the plane surface. The only explanation I can offer is that Eq 23b still describes the secondary wave sources as dipoles, whereas Eq 22b describes them as monopoles and so the two formulae are essentially different despite both requiring the normal displacement to be input. Nevertheless, they each must give the same answer if applied *exactly* to a vibrating piston in a flat plane. I say 'exactly' advisedly because this comparison cannot be made without first having the exact solution to the wave equation and boundary conditions over the piston and entire baffle. This is because the field around the edge of the piston is not that of a plane wave, and we cannot guess either the exact distribution of ϕ or its normal derivative over the whole boundary. We can only proceed on the assumption that the transition around the edge of the piston is narrow compared with the area of the piston. In other words, a high frequency approximation. Against this background I have continued to use both dipole variants, Eq 23a and b, when the vibrating surface is flat and finite.

The displacement at Q is $\boldsymbol{\xi} = -\nabla\phi\,|_Q$. In the computer program this is found numerically by evaluating ϕ at Q itself and also at twelve adjacent points, namely $(q_x \pm h, q_y, q_z)$, $(q_x \pm 2h, q_y, q_z)$, and similarly in the y and z dimensions, h being is a small distance. The first derivative in x is

$$\frac{\partial\phi}{\partial x} \;\approx\; \frac{1}{12h}(\phi_{-2} - 8\phi_{-1} + 8\phi_{+1} - \phi_{+2}) \qquad (24a)$$

and similarly for the y and z components of $\boldsymbol{\xi}(Q)$. For time variation $e^{-i\omega t}$ the particle velocity is $\partial\boldsymbol{\xi}/\partial t = -i\omega\boldsymbol{\xi}$. Following Eq 9a, the pressure is given by $p = K\nabla^2\phi$, but since ϕ satisfies Helmholtz's equation, this is $p = -K\kappa^2\phi$. The program alsos uses five-point evaluation to find the second derivatives:

$$\frac{\partial^2\phi}{\partial x^2} \approx \frac{1}{12h^2}(-\phi_{-2} + 16\phi_{-1} - 30\phi_0 + 16\phi_{+1} - \phi_{+2}) \qquad (24b)$$

from which $\nabla^2\phi$ is calculated. Comparison of this direct numerical approximation to $\nabla^2\phi$ with ϕ itself is a significant test of the program. For each of their real and imaginary parts their ratio should be $-\kappa^2$ at all points Q.

The program is written in BBC Basic for Windows (*www.rtrussell.co.uk*), a sophisticated version of Basic, and runs under Windows on a desktop or laptop. It first reads a file of nodes and triangular elements which constitute the mesh modelling the object, the file structure being compatible with the LISA 8 and MecWay FEA programs. The mesh can be scaled independently in the x, y and z directions to change, for instance, a sphere into a spheroid. Two other inputs are the potential or normal displacement at each element, and the array of fields points Q at which the radiated sound field is to be calculated. The program carries out the calculations in Appendix 1 to determine the real and imaginary parts of the contribution to $\phi(Q)$ coming from one element of the surface in turn. The contributions are multiplied by the complex factors in Eq 21, 22b, 23a or b as required and added numerically. The real and imaginary parts of the $\phi(Q)$ and its first and second derivative are finally written to an output file, with a header listing the parameters of the case.

6.3 Scope and expected limitations

Here are some general comments regarding the model behind the computer program and its likely range of validity.

In Appendix 1 ϕ for a single triangle has been calculated in the element's far-field. Therefore no triangular element in the mesh should be so large, or the range so small, that the calculation is pursued into its near-field. The terms 'near-field' and 'far-field' relate respectively to distances from the surface at which the path length from all points on the object either causes or does not cause

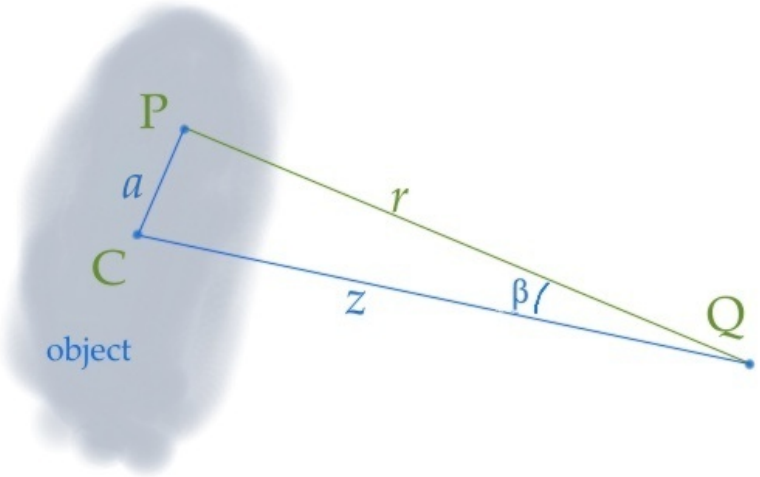

Figure 20: Illustrating the path difference $r - z$ between wavelets from C and P received at Q. $r^2 = z^2 + d^2$.

destructive interference. Figure 20 illustrates the geometry. C is the centroid of the element, P a general point on the surface a distance a from C, and Q the listener. Path differences $r - z$ less than $\lambda/8$ are almost insignificant, as is the case where the axial distance z is large. Wherever $r - z > \lambda/4$ there is a negative component and some destructive interference occurs. Hence the on-axis amplitude will have a maximum near $r - z = \lambda/4$, which roughly marks the near-field-far-field boundary. By the binomial theorem $r - z \approx a^2/(2z)$. If a_{max} is large enough compared with λ, there will be subsidiary maxima and minima in the near-field. The approximation in Appendix 1 therefore holds only so long as

$$a_{max}^2 \; < \; \frac{\lambda z}{2}, \qquad \text{or} \quad \frac{z}{\lambda} \; > \; 2\left(\frac{a_{max}}{\lambda}\right)^2 \tag{25}$$

for every triangular element, where a_{max} is roughly the average distance from the centroid to the vertices. To be clear, however, the model should be able to predict the field within the near-field of the whole object.

An obliquity factor $\cos\beta$ appears in the 'dipole term' in both the Kirchhoff formulation and in one version of the Rayleigh-Sommerfeld. Intuitively it makes sense because its effect is to weight the radiate sound into the forwards direction, perpendicular to the vibrating surface. It prevents any sound skimming along the surface of the object. The monopole sources, weighted by $\nabla\phi(S) \cdot \mathbf{n}$, do not have such restriction and so do predict radiation from the face of the piston out along the plane of the surface. So with a flat piston and baffle one version of the Rayleigh-Sommerfeld formulation disallows waves along the baffle whilst the other predicts them. Another paradox! In fact waves in the boundary are ruled out by the Kirchhoff boundary approximation (a concept distinct from Kirchhoff's derivation) which stipulates that the field on the baffle and other non-vibrating parts surface be treated as if strictly zero. This is necessary for the monopole formulation though not for the dipole. It is possible to argue that neither dipole nor monopole formulation would give the exact solution to any given case, because at the edge of the piston the discontinuity in motion must create a disturbance which propagates outwards in all directions, including along the baffle – the so-called edge waves – but we do not know their true amplitude. This is another way of the practical limitations of all these formulations; they are formally exact and all embracing, but cannot be used in practice except in approximation.

A further consideration of the obliquity factor is that for an element $\cos\beta < \frac{1}{2}$ for $\beta > 60°$. Therefore if Q is very close, only those elements whose centroids are within a 60° cone will contribute significantly to the field. Therefore the calculated field may be unduly sensitive to the structure of the mesh where $z < a_{max}/2$.

If you were to use the Rayleigh-Sommerfeld model to compute the directionality of sound radiated from a violin-family instrument, you would be applying it to an object with gently curved surfaces in free space. The main effect of deviation of the top violin plate from a plane will be to introduce path and hence phase differences between the elementary sources over the surface. The computer program deals with this by design. However, the violin is not well represented by its top plate in a rigid baffle. Perhaps the nearest approximation by an exact solution of the wave equation is for an ellipsoid, though I have been unable to find tabulated values of the associated wave functions. It is not obvious, therefore, how the Rayleigh-Sommerfeld theory should be applied if it were pushed beyond its assumptions and applied to a much more highly curved surface such as a spherical sector, or in the extreme to a whole sphere, spheroid or ellipsoid. In addition to phase differences there would then be some subtle but significant other effects:

1. In setting up the model each triangular element is flat and is treated as if it were in an infinite planar baffle, independent of all other elements. Once the object's surface is appreciably curved,

there is an inconsistency between the local planar tile elements which make up the surface and the global surface itself. The global curvature implies that Kirchhoff's formula, Eq 21, should be used, but then of course one would need to provide values – either known or guessed – for both $\partial\phi/\partial n$ and ϕ on S.

2. In the dipole Rayleigh-Sommerfeld theory the angle β cannot exceed 90° because the surface is assumed planar, but on a curved surface β certainly will exceed 90° for some elements. Indeed, some elements will be on the back side of the object.

3. If β were limited to $< 90°$, it would be equivalent to allowing only surface points within the cone of rays whose apex is at Q to contribute to the field at Q.

In §9 I address these issues by examining how Green's theorem predicts the field from a vibrating sphere under various situations. I present reasons to carry out the integration over the whole vibrating surface, and in §9, §10 and Appendix 2 give examples where the obliquity factor $\cos\beta$ is negative.

If we look to other candidate methods for tackling such problems, the Finite Element Method can indeed solve Helmholtz's equation, but only in a closed finite space. One would need to model the violin embedded in a larger space (a room, say), but then solutions will include all manner of standing waves within the room, and the directivity of the violin itself will be obscured. The Boundary Element Method with added multipoles seems to have the capability to model only outwards travelling waves in an infinite space. I have had some success using the free student version of FastBEM available from Advanced CAE Research, building on software originally from the University of Cincinnati. There is further comment on alternative approaches in §11.2

7 Verification of model for planar radiating objects

To check the computer code for errors I have carried out a series of systematic trial calculations on simple objects, looking at symmetry and internal consistency, or to compare with well documented analytical answers. Two objects have been modelled in sinusoidal motion, both with a prescribed peak surface displacement of $0 \cdot 01$ units at all nodes:

1. a right-angled triangle vibrating like a piston, normal to its surface,
2. a planar circular disc vibrating like a piston,

Each is assumed to be surrounded by a planar baffle over which the field is zero. §8 reports comparisons with some of the experimental results for two and three loudspeakers in §4.2.

7.1 Right-angled triangle

The analysis in Appendix 1 gives expressions for the far-field radiated from an arbitrary triangular piston vibrating normal to its surface. The tests in this section are simply to see whether the computed far-field from such a triangle is independent of the mesh of elements used to represent it. Figure 21 shows the six meshes tried, respectively with 1, 2, 4, 16, 16 and 64 sub-elements.

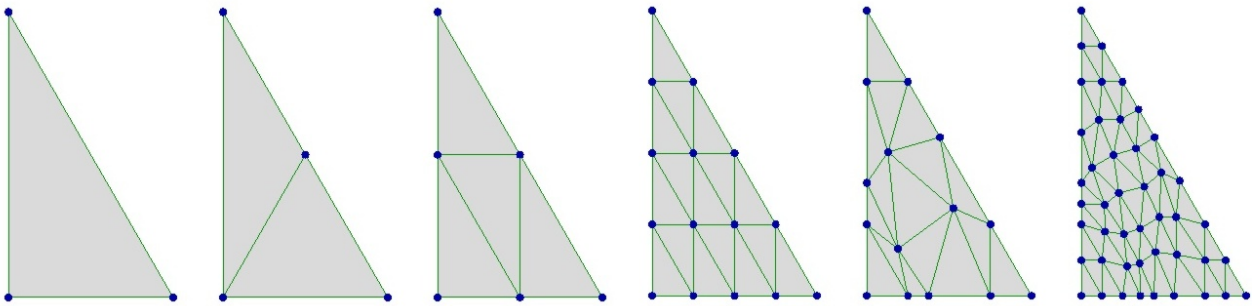

Figure 21: Six meshes representing a planar right-angled triangle, each with unit area.

The distance from centroid to the outermost vertex is $1 \cdot 3$ units, so if λ is set to $0 \cdot 3$, the near-field ends at about $r = 10$ (see Eq 25). I have calculated the field across planes parallel to the triangle at $z = 5$, 10 and 20 units for a selection of the six meshes, taking the origin at the centroid. With $\lambda = 0 \cdot 3$, values for the 4, 16 and 64 element meshes agree well at $z = 5$, but it is not until $z = 20$ that values for the 1-element and multiple-element meshes agree; *i.e.* beyond about two near-field lengths. Figure 22 compares values at $z = 5$ across the section $y = 0$, showing amplitude values calculated for 1, 2, 4 and 16 elements. The 1-element mesh over-estimates the on-axis amplitude ($x = 0$) and shows incorrect structure in the weak side lobes. Because the near-field length of a single element decreases at the square of its width, even replacing one triangle by two extends the validity of the model to positions Q much closer to the piston. Figure 22 illustrates this in that the 2-, 4- and 16-element graphs are quite close together; indeed, the 4- and 16-element ones are almost identical.

Figure 23 compares amplitude values at $z = 20$, again across the section $y = 0$. It shows good agreement for 1, 2 and 64 elements, so at this greater range even the 1-element model is reliable. Figure 24 is a contour plot of $|\phi|$ obtained from this 1-element mesh (that is, using only the formulae in Appendix 1) at $z = 20$. The outline of the triangular piston is in red. Note the symmetric ellipses even though the triangle is far from symmetric, and note the weak side lobes in both x and

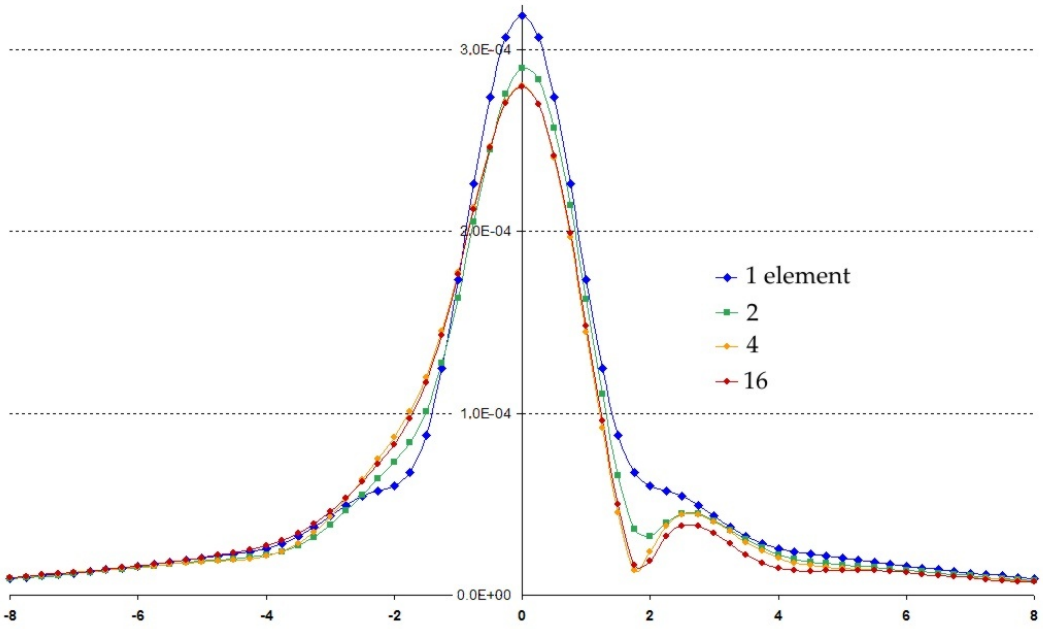

Figure 22: Field from single right-angled triangle. $|\phi|$ as x varies across the $y = 0$ section at $z = 5$ for $\lambda = 0 \cdot 3$. Comparison for meshes of 1, 2, 4 and 16 elements.

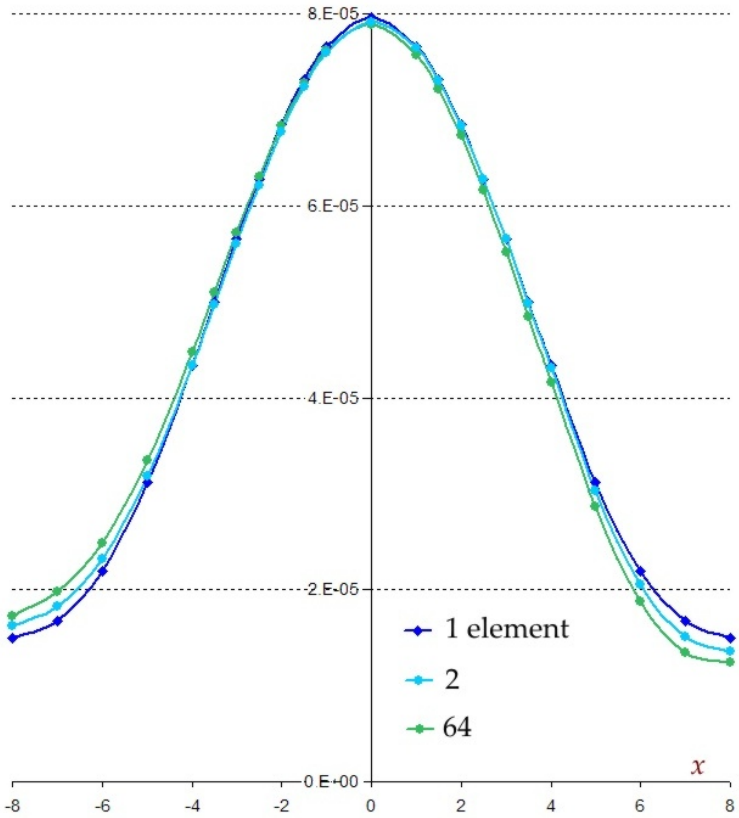

Figure 23: Far-field of single right-angled triangle. Variation in $|\phi|$ with x calculated with 1, 2 and 64 elements for $\lambda = 0 \cdot 3$ at $z = 20$, $y = 0$.

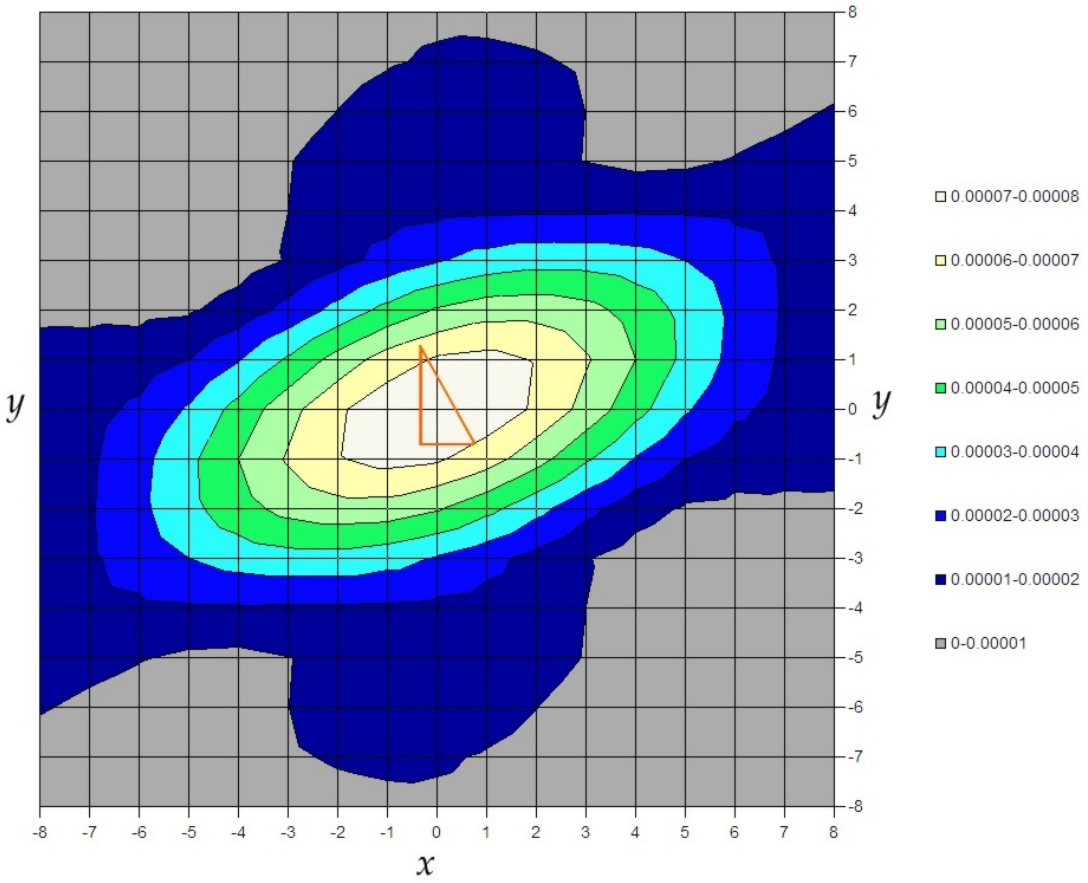

Figure 24: Contour plot of $|\phi|$ in far-field of the single triangle (in red). $z = 20$, $\lambda = 0 \cdot 3$.

y directions. As is typical of far-field diffraction patterns, the central lobe is narrower in directions perpendicular to the larger dimension of the object. This is because, for a given obliquity, destructive interference between opposite ends of the triangle is more pronounced in these directions. Text books on optics prove that there is a Fourier transform relationship between the field over the object and its angular spectrum in the far field.

7.2 Circular piston

The circular piston has been chosen as a test of the computer program because the dipole Rayleigh-Sommerfeld integral can be evaluated analytically to various degrees of approximation.

7.2.1 On-axis field

Consider first the on-axis field of a uniform piston of radius a, centre O, vibrating harmonically normal to its surface. Thus $x = y = 0$ and z is the range.

If a' is the distance from O to an arbitrary surface point P, the un-approximated Rayleigh-Sommerfeld integral from Eq 23a is

$$\frac{\phi(Q)}{\phi_0} = -\frac{1}{2\pi}\int_{\psi=0}^{2\pi}\int_{a'=0}^{a}\left(i\kappa - \frac{1}{r}\right)\frac{e^{i\kappa r}}{r}\,\frac{z}{r}\,a'\,da'.d\psi\,, \qquad r^2 = z^2 + a'^2 \tag{26a}$$

$$= \int_0^a \left(\kappa z \sin(\kappa r) + \frac{z}{r}\cos(\kappa r)\right)\frac{a'}{r^2}\,da' \;+\; i\int_0^a \left(-\kappa z\cos(\kappa r) + \frac{z}{r}\sin(\kappa r)\right)\frac{a'}{r^2}\,da'\,. \tag{26b}$$

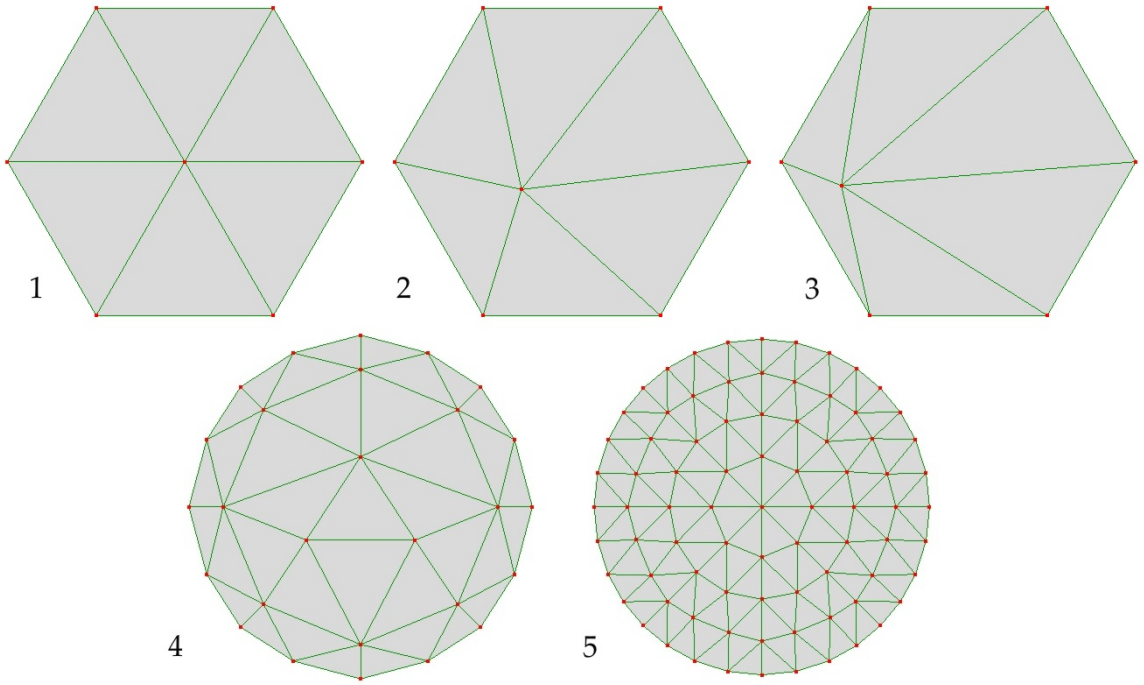

htb]

Figure 25: Five meshes with 6, 36 and 128 elements, each modelling a circular disc of unit radius.

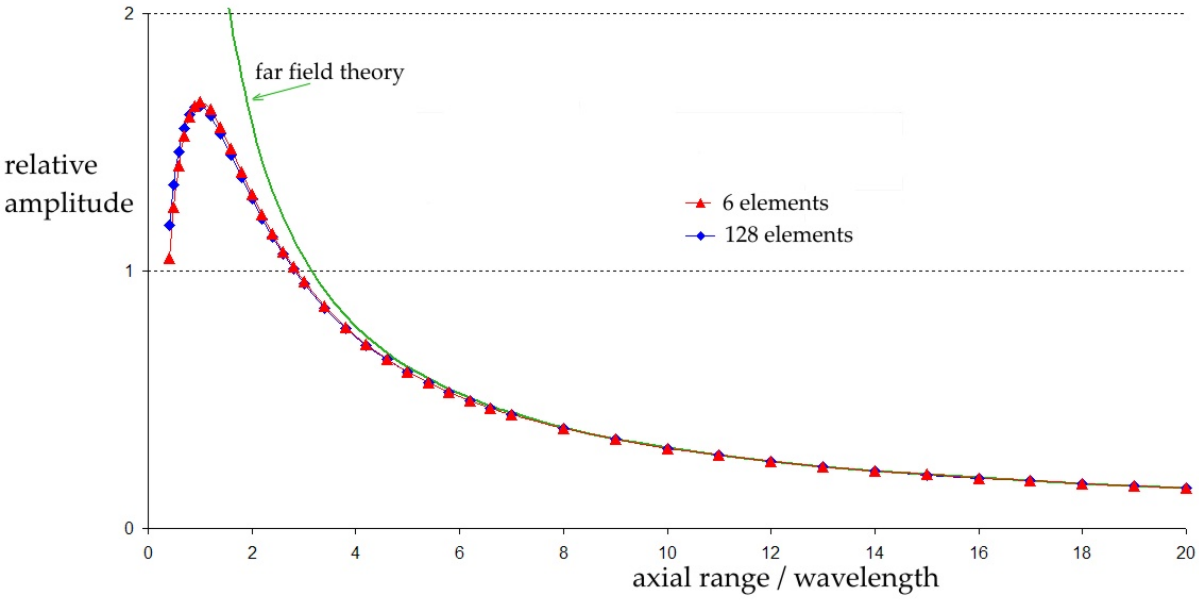

htb]

Figure 26: Calculations for mesh models 2 and 5 compared with simple far field theory for $a/\lambda = 1$.

The far-field approximation takes $r \approx z$:

$$\left.\frac{\phi(Q)}{\phi_0}\right|_{axis} \approx \left[\kappa z \sin(\kappa z) + \cos(\kappa z)\right] \frac{a^2}{2z^2} \;+\; i\left[-\kappa z \cos(\kappa z) + \sin(\kappa z)\right] \frac{a^2}{2z^2}\,. \tag{27a}$$

$$\left|\frac{\phi(Q)}{\phi_0}\right|_{axis} \approx \tfrac{1}{2}\left(\frac{a}{z}\right)^2 \sqrt{(\kappa z)^2 + 1} \;=\; \tfrac{1}{2}\left(\frac{\hat{a}}{\hat{z}}\right)^2 \sqrt{4\pi^2 \hat{z}^{\,2} + 1} \tag{27b}$$

where $\hat{a} = a/\lambda$, $\hat{z} = z/\lambda$. For z very large this tends to S/z where $S = \pi a^2$ is the piston's area.

Five polygonal meshes approximating a circular disc have been compared with this theory, all shown in Figure 25. The first three are variations on a regular hexagon of six triangles. In mesh 1 all are equilateral triangles, whilst in 2 and 3 the central point has been displaced in the plane. If results from these agree, it should add to confidence that the analysis and programming for a single triangle are correct. The other two meshes, 4 and 5, have 36 and 128 elements respectively. The area of each mesh is π units, so each models a circle with unit radius.

Consider first the 6- and 128-element meshes, numbers 2 and 5 in Figure 25, in comparison with the far field formula, Eq 27b. Figure 26 plots these three curves for $a = 1$, $\lambda = 1$, $0{\cdot}4 \le z/\lambda \le 20$. Both mesh models fit well to the far-field formula for $z/\lambda > 8$. The difference between the two meshes is tiny. Both show near-field deviation from the far-field model for $z/\lambda <\approx 2$, consistent with Eq 25.

We now look to a better analytical approximation than Eq 27b. In a paper published in 2004[9] Marathay and McCalmont show that Eq 26 can be evaluated exactly for points Q on the axis. They were concerned to show the importance of the $1/r$ term within the $(i\kappa - 1/r)$ factor in the Rayleigh-Sommerfeld formula. Building upon their integration method I have determined the real and imaginary parts of the potential $\phi(Q)$ as follows. The clever move is to integrate with respect to r rather than a'. Take the real part of Eq 26b; it is now written

$$\int_z^{\sqrt{z^2+a^2}} \left[\kappa z \frac{\sin \kappa r}{r} + z \frac{\cos \kappa r}{r^2}\right] dr. \tag{28}$$

Integrate the second term in this integrand by parts, splitting it into $u = \cos \kappa r$ and $dv = dr/r^2$. Then

$$\int \frac{z \cos \kappa r}{r^2}\, dr \;=\; -\frac{z \cos \kappa r}{r} - \int \frac{z\kappa \sin \kappa r}{r}\, dr\,.$$

The second term here exactly cancels the first term in Eq 28 and leaves the on-axis field for all z as

$$\Re \frac{\phi(Q)}{\phi_0} \;=\; \cos \kappa z - \frac{z}{\sqrt{z^2 + a^2}} \cos(\kappa \sqrt{z^2 + a^2})\,. \tag{29a}$$

Likewise

$$\Im \frac{\phi(Q)}{\phi_0} \;=\; \sin \kappa z - \frac{z}{\sqrt{z^2 + a^2}} \sin(\kappa \sqrt{z^2 + a^2})\,, \tag{29b}$$

$$\left|\frac{\phi}{\phi_0}\right|^2 \;=\; 1 \;+\; \frac{z^2}{z^2 + a^2} \;-\; \frac{2\,z}{\sqrt{z^2 + a^2}} \cos\left(k\sqrt{z^2 + a^2} - k\,z\right). \tag{29c}$$

The real part of this field is shown in Figure 27 for the same case as Figure 26, namely $a = 1$, $\lambda = 1$, for the three hexagonal meshes, 1, 2 and 3. Clearly distorting the constituent triangles within the hexagon makes little difference here. All three sets of computed values fit fairly well to the theoretical

[9] "On the usual approximation used in the Rayleigh-Sommerfeld diffraction theory", J. Optical Soc. Amer A/Vol 21 No 4. April 2004

curve (green) for z as small as about $0 \cdot 5$. Some of the difference may genuinely be due to the mesh being a hexagon while the theory is for a circle. Closer to the surface, the theoretical curve must tend to 1 by definition, and the model curves must go to 0 because the obliquity angle β is there 90° for all six triangles. All this behaviour of the computed field is consistent with the general limitations in §6.2.

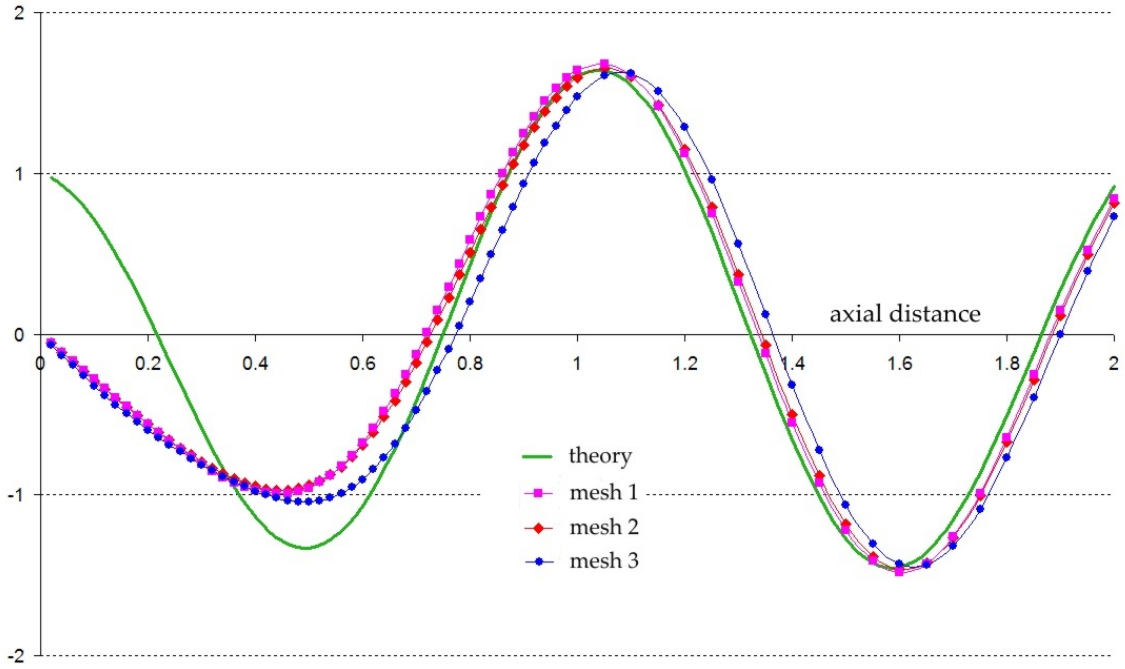

Figure 27: Real part of $\phi(z)$ along the axis in the near-field of a hexagonal piston radiator, $a = 1$, $\lambda = 1$. Results for the three hexagon meshes in Figure 25 are compared with Eq 29a.

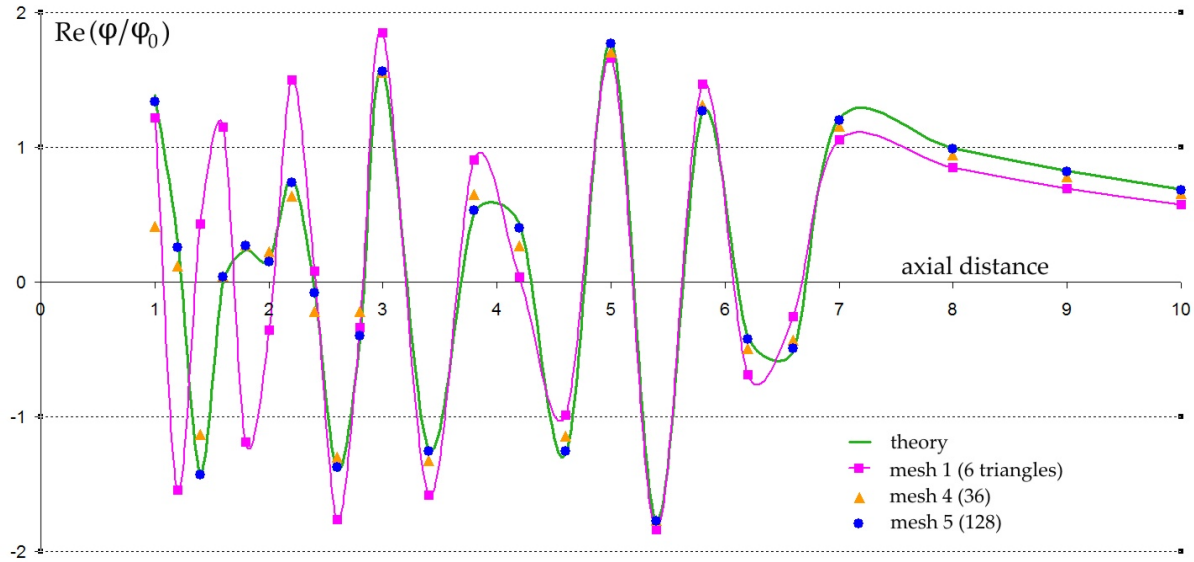

Figure 28: Real part of near-field on-axis amplitude for polygons Nos 1 (6 elements), 4 (36 elements), 5 (128 elements). $a = 1$, $\lambda = \frac{1}{4}$.

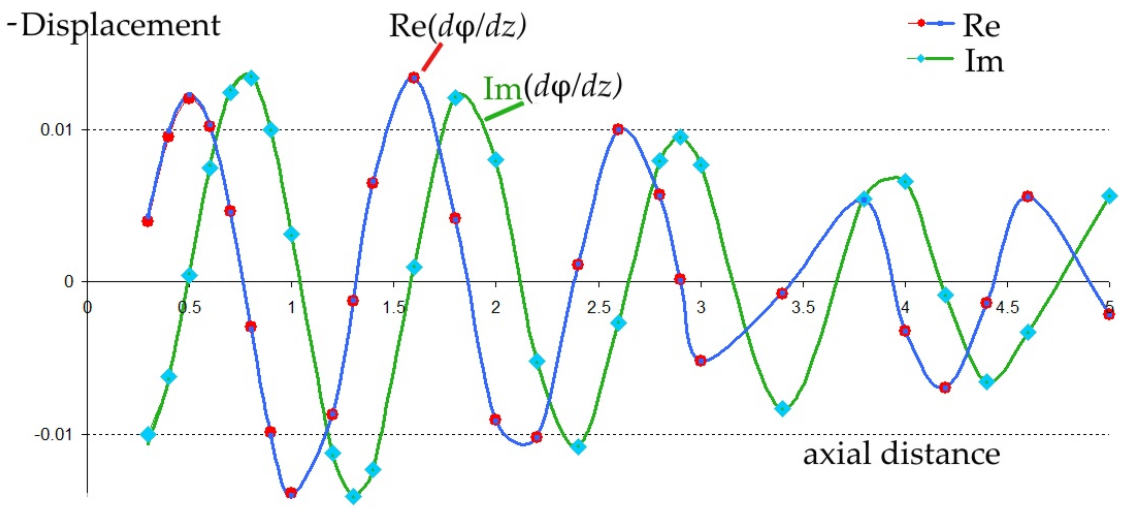

Figure 29: Real and imaginary parts of $\partial\phi/\partial z$ along the axis of a circular disc, radius $a = 1$ for $\lambda = 1$ and surface displacement amplitude $0 \cdot 01$ units. Continuous curve: Eq 30a, b. Points: model computed values.

More demanding challenges are placed upon the theory for the near-field as the ratio a/λ increases. Figure 28 compares the on-axis analytical expression for the real part of the relative amplitude with those calculated using mesh models 1, 4 and 5. The near-field length $2a^2/\lambda$ is 8 units. The values for mesh 5, with 128 elements, are almost indistinguishable from the theory for z as small 1, and those for the 36 element mesh are practically as good. Even the 6 element mesh, No 1, gives quite good agreement down to $z = 2 \cdot 5$ despite the hexagon being a poor fit to a circle. As expected, all on-axis calculations tend to the theoretical in the far field.

The program uses 5-point numerical differentiation, Eq 24a, to calculate the derivative and hence the particle displacement ξ and velocity. These values can also be compared with a formula for on-axis displacement, by differentiating Eq 29. As expected from symmetry, all on-axis displacement is in the axial (z) direction. Its real and imaginary parts are

$$\Re \frac{\boldsymbol{\xi}(Q)}{\boldsymbol{\xi}_0} = \frac{z^2 \cos\left(\kappa\sqrt{z^2+a^2}\right)}{z^2+a^2} + \frac{\sin\left(\kappa\sqrt{z^2+a^2}\right)}{\kappa\sqrt{z^2+a^2}} - \frac{z^2 \sin\left(\kappa\sqrt{z^2+a^2}\right)}{\kappa\left(z^2+a^2\right)^{\frac{3}{2}}} - \cos\left(\kappa z\right), \qquad (30a)$$

$$\Im \frac{\boldsymbol{\xi}(Q)}{\boldsymbol{\xi}_0} = \frac{z^2 \sin\left(\kappa\sqrt{z^2+a^2}\right)}{z^2+a^2} - \frac{\cos\left(\kappa\sqrt{z^2+a^2}\right)}{\kappa\sqrt{z^2+a^2}} + \frac{z^2 \cos\left(\kappa\sqrt{z^2+a^2}\right)}{\kappa\left(z^2+a^2\right)^{\frac{3}{2}}} - \sin\left(k z\right). \qquad (30b)$$

Figure 29 plots the real and imaginary parts of $\nabla\phi$ along the z axis for $a = 1$, $\lambda = 1$. The continuous curves are plots of Eq 30a, b scaled by $i\,\xi_0/\kappa$ to convert from displacement to potential. The discrete points are from the program using the 128-element model with a uniform surface displacement amplitude $\boldsymbol{\xi}_0$ of 1/100 unit. The fit to the theory is nigh perfect.

7.2.2 Off-axis field

We now check some off-axis points against theory. It is well known that the far-field radiation or diffraction pattern for a circular disc has angular variation $2J_1(X)/X$ where J_1 is the first order

Bessel function and $X = \kappa a \sin\beta$, β being the polar angle from the axis of the disc. This is another example of a Fourier transform pair. It is not too difficult to derive this angular distribution from the dipole Rayleigh-Sommerfeld formula, Eq 26a. Ignore the $1/r$ compared with $i\kappa$. Suppose, without loss of generality, that the listening point Q lies in the $x-z$ plane, displaced to the $+x$ side through angle β. Let ψ be the azimuthal angle in the $x-y$ plane of the disc, with $\psi = 0$ along the x axis. An element of area of the disc at radius a' is $a'\,da'\,d\theta$. The extra wave path length from a point P at (a', ψ) on the disc, compared with the distance OQ, is $-a' \sin\beta \cos\psi$. The Rayleigh-Sommerfeld integral become

$$\frac{\phi(Q)}{\phi_0} \;=\; -\frac{i\kappa}{2\pi}\,\cos\beta\,\frac{e^{i\kappa r}}{r}\int_0^{2\pi}\int_0^{a} e^{-i\kappa a'\sin\beta\cos\psi}\,a'\,da'\,d\psi\,, \qquad r = |OQ| \tag{31}$$

We now need two standard integrals involving Bessel functions:

$$\int_0^{2\pi}\cos(z\sin\psi)\,d\psi \;=\; \int_0^{2\pi}\cos(z\cos\psi)\,d\psi \;=\; 2\pi J_0(z),$$

$$\int_0^{2\pi}\sin(z\sin\psi)\,d\psi \;=\; \int_0^{2\pi}\sin(z\cos\psi)\,d\psi \;=\; 0\,.$$

The second line disposes of the imaginary part of the exponential in Eq 26 and the first gives

$$\frac{\phi(Q)}{\phi_0} \;=\; -i\kappa\,\cos\beta\,\frac{e^{i\kappa r}}{r}\int_0^{a} J_0(\kappa a'\sin\beta)\,a'\,da'\,. \tag{32}$$

A third standard integral[10] is

$$\int t\,J_0(t)\,dt \;=\; J_1(t)\,, \qquad \int t\,J_0(Ct)\,dt \;=\; \frac{t}{C}J_1(Ct)\,,$$

C here being $\kappa\sin\beta$. We therefore arrive at the far field formula

$$\frac{\phi(Q)}{\phi_0} \;=\; -\frac{i}{\lambda}\,\pi a^2\,\cos\beta\,\frac{e^{i\kappa r}}{r}\,\frac{2J_1(\kappa a\sin\beta)}{\kappa a\sin\beta}\,. \tag{33}$$

We recognise the cosine obliquity factor, the area of the disc, a spherical wave apparently radiating from the centre O, and a beam shape factor with strong central (forwards) lobe and weaker side lobes. This, then, is the theoretical result against which to judge the computer program.

A comparison is shown in Figure 30 for the 6-element mesh No 1 with $a/\lambda = 1$, $r/\lambda = 20$. I have taken the complex amplitude of displacement potential at various angles β from the forwards direction and divided them (as complex numbers) by the value at $\beta = 0$. Theory predicts that the real part should vary as $2J_1(X)/X$ (green curve) and the imaginary part be zero. Even for this hexagonal approximation to a circle, the agreement for the real part is remarkable and the imaginary part is indeed sensibly zero. For meshes with more elements the agreement is even better.

7.2.3 $\nabla\phi$ and $\nabla^2\phi$

One further simple check is to see whether the impedance tends to the characteristic value for air, 413 SI units, at least in the far-field. The program outputs the first partial derivatives of ϕ with respect to x, y and z, giving the components of vector displacement, and the particle velocity $\mathbf{v}$

[10] Eq 11.3.20, page 484 of Abramowitz and Stegun's Handbook of Mathematical Functions.

follows immediately by differentiating with respect to time, meaning multiply by $-i\omega$. If $\phi = \phi_r + i\phi_i$, then

$$\mathbf{v} \;=\; -\omega\left[\frac{\partial\phi_i}{\partial x}\mathbf{e_x} + \frac{\partial\phi_i}{\partial y}\mathbf{e_y} + \frac{\partial\phi_i}{\partial z}\mathbf{e_z}\right] + i\omega\left[\frac{\partial\phi_r}{\partial x}\mathbf{e_x} + \frac{\partial\phi_r}{\partial y}\mathbf{e_y} + \frac{\partial\phi_r}{\partial z}\mathbf{e_z}\right]. \qquad (34a)$$

The magnitude of the real part is

$$v_r \;=\; \omega\sqrt{\left(\frac{\partial\phi_i}{\partial x}\right)^2 + \left(\frac{\partial\phi_i}{\partial y}\right)^2 + \left(\frac{\partial\phi_i}{\partial z}\right)^2} \qquad (34b)$$

and similarly for the imaginary part. The pressure is $-K\nabla^2\phi$ and, if Helmholtz's equation is truly satisfied, this will equal $K\kappa^2\phi$ so the complex impedance will be

$$Z \;=\; \frac{K\kappa^2(\phi_r + i\phi_i)}{v_r + iv_i}. \qquad (35)$$

Accepting that Helmholtz's equation does hold, I have calculated Z using computed values and Eq 35 for several cases. Figure 31 shows two, namely Z at on-axis points from discs represented by meshes 1 and 5. The values settle down correctly once Q is beyond the near-field. I do not attach physical significance to the rather wild variations in the near-field.

The program also calculates the second derivatives with respect of position (Eq 24b), so evaluating $\nabla^2\phi$. This allows a further check on the programming since ideally Helmholtz's equation

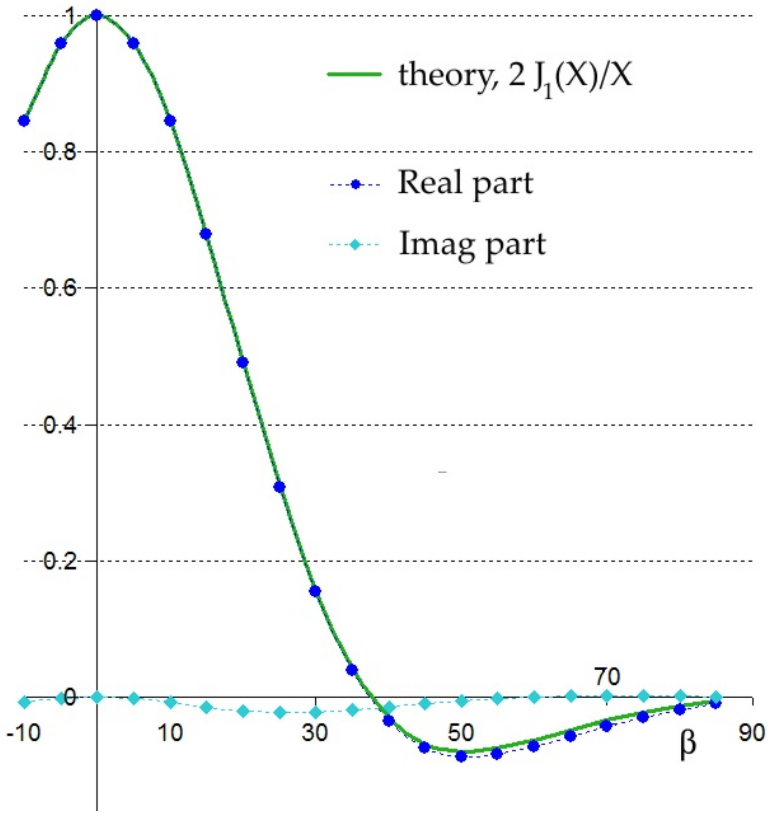

Figure 30: Real and imaginary parts of displacement potential as function of polar angle β, relative to value on axis. Regular hexagon (mesh 1) representing a circular disc, $a = 1$, $\lambda = 1$. Far-field $r = \sqrt{x^2 + z^2} = 20$, $y = 0$.

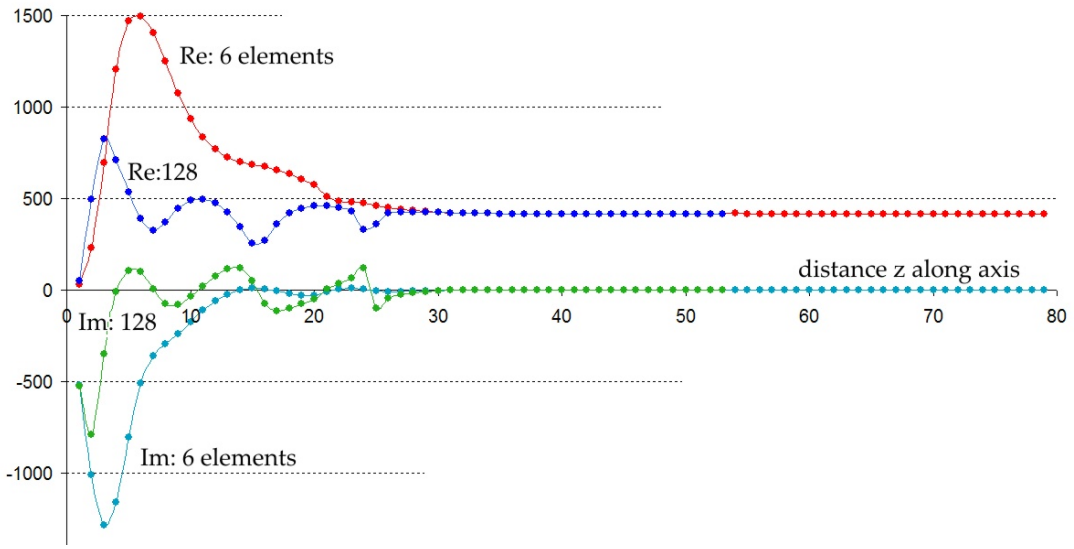

Figure 31: Real and imaginary parts of complex impedance Z as function of distance z along axis from hexagon (6-element) and circular (128-element) pistons with $a = 1$, $\lambda = 1/4$.

should hold at every point Q, with $\nabla^2\phi = -\kappa^2\phi$. The deviation of $\nabla^2\phi/\phi$ from κ^2 is a measure of the consistency of the whole model. This can be calculated in two ways:

1. separate Helmholtz's equation into real and imaginary parts, in which case $\Re[\nabla^2\phi]/\Re[\phi]$ and $\Im[\nabla^2\phi]/\Im[\phi]$ are each equal to $-\kappa^2$,

2. divide $\nabla^2\phi$ by ϕ as two complex numbers, in which case $\Re(\nabla^2\phi/\Re\phi) = -\kappa^2$ and $\Im(\nabla^2\phi/\Re\phi) = 0$.

Here is an example of the first test applied at on-axis points Q in the case $a = 1$, $\lambda = 1$. The target value is $-\kappa^2 = 4\pi^2 = -39 \cdot 478$:

$$\begin{aligned} \text{6 elements (mesh 2)} \;&: 0 \cdot 5 \le z \le 20 \;: \text{Real part} \quad -39 \cdot 75 \pm 1 \cdot 06 \\ &\quad\;\; : \text{Imag part} \quad -38 \cdot 63 \pm 5 \cdot 14 \\ \text{128 elements (mesh 5)} \;&: 0 \cdot 3 \le z \le 20 \;: \text{Real part} \quad -39 \cdot 45 \pm 0 \cdot 27 \\ &\quad\;\; : \text{Imag part} \quad -39 \cdot 46 \pm 0 \cdot 21\,. \end{aligned}$$

Even the values for 6 elements are satisfactory. As an example of the second way of taking the ratio, I have calculated it for points around an arc at $r = 10$ units, for $a = 1$, $\lambda = 1$ using mesh 5. For this the real part was $-39 \cdot 478$, almost exactly κ^2, and the imaginary part $< 3 \times 10^{-12}$ – essentially zero.

An extended version of this test is illustrated in the log-log plot of Figure 32. It plots on-axis values of the ratio $\nabla^2\phi/\phi$ for $a = 1$, $\lambda = \frac{1}{4}$. The real part approaches $\log_{10}(64\pi^2) = 2 \cdot 8005$ for almost all $z > 1$, and the imaginary part is small for $z >\approx 3$ and thereafter falls roughly as $1/z^{8/3}$. Considering that the near-field length $2a^2/\lambda \approx 8$, these results show that the model approximates solutions of Helmholtz's equation well into the near-field.

This section has shown that the circular piston provides a thorough set of tests of the model and the program coding. No unexpected deficiencies have come to light.

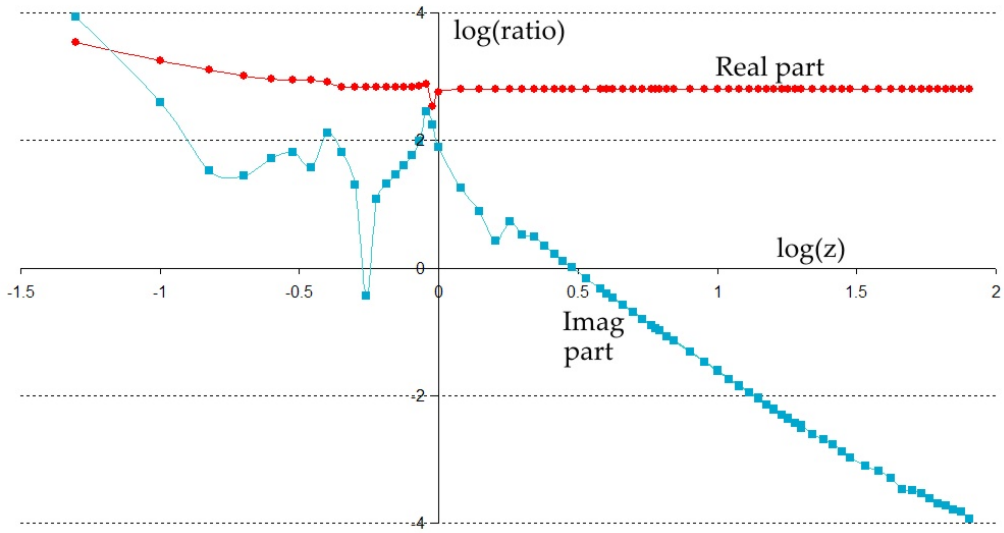

Figure 32: Log-log plot of real and imaginary parts of the ratio $\nabla^2\phi/\phi$ for points along the axis of a disc radius 1, wavelength $0 \cdot 25$ calculated with mesh 4 (36 elements).

8 Modelling the 2 and 3 sources experiment

The section extends the tests of the dipole Rayleigh-Sommerfeld computer program by comparing its output with the experimental results on dipole and tripoles presented in Figures 10 to 14 in §4.2. The first problem to address is to find a plausible semi-quantitative explanation for the kink in the directivity plots of a single speaker, so obvious in Figure 10 at 1368 Hz and 1710 Hz. This feature carries over into the corresponding graphs for the two-speaker dipoles in Figures 11, 12 and 13. If a fair match can be made to Figure 10, we can progress to multiple loudspeakers.

8.1 Normal modes of a speaker cone

In this subsection I am looking for some explanation for the kink in the directivity of a single loudspeaker, and suspect that the conical membrane is not acting as a simple rigid piston at higher frequencies. A search of the literature turns up several technical papers which document various natural modes of a speaker cone in addition to the piston-like movement which occurs at the lowest frequencies. For example, the degree dissertation of Joachim Schlechter, University of Dresden, 2006 is entitled 'Visualisation of vibrations of loudspeaker membranes', available on the Internet. He made laser measurements of movement across the surface of the membrane and developed graphical displays which reveal several modes of oscillation. Independent work by Ryan Miller, reported in a thesis to the Rensselaer Polytechnic Institute, Hartford, Connecticut, 2010, produced finite element predictions of modal patterns for various shapes of speaker membrane.

Spurred on by these studies, I have constructed a simple model of a vibrating cone using the LISA 8 FEA software. I did not try to model closely the loudspeakers actually used, but instead devised a simple hypothetical cone pictured in Figure 33. The cone diameter is 8 cm, as are the actual speakers, but I just invented plausible values of membrane thickness (1/2 mm) and Young's modulus ($0 \cdot 1$ GPa). The small inner rim of the model cone is fixed and the rest of it free to move. Of the many calculated modes I have selected the lowest frequency non-piston mode which has rotational symmetry. The normal displacement predicted by LISA 8 is plotted in the right hand panel. The membrane nearest the outer edge vibrates out of phase with that nearer the centre. If the cone moved as a piston, the corresponding graph would be a horizontal straight line.

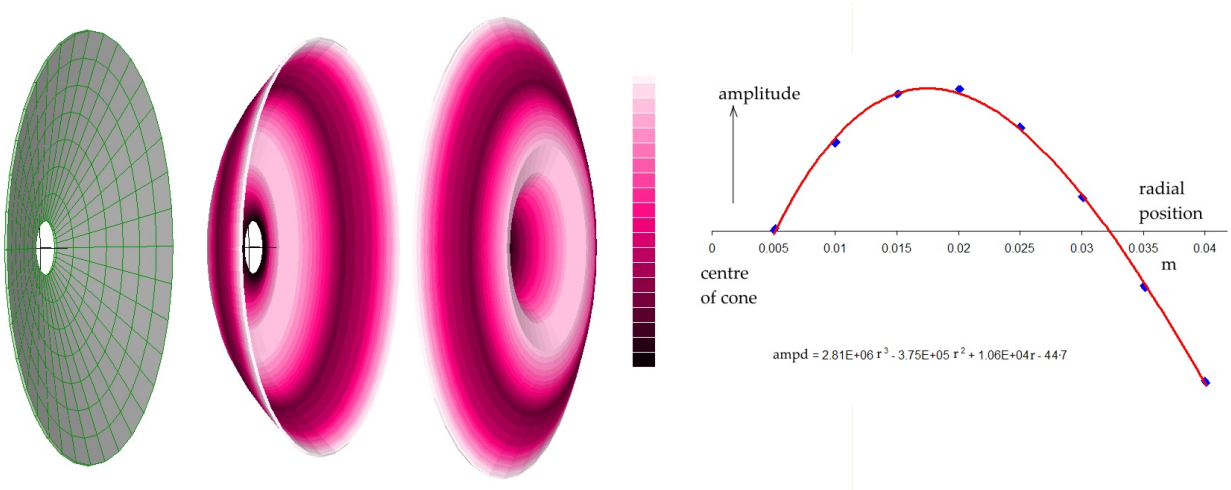

Figure 33: Hypothetical loudspeaker cone (left) vibrating in a symmetric mode, shown at two instants (black = zero displacement, pale pink = maximum). Right panel plots displacement (arbitrary scale) against radial position in metres.

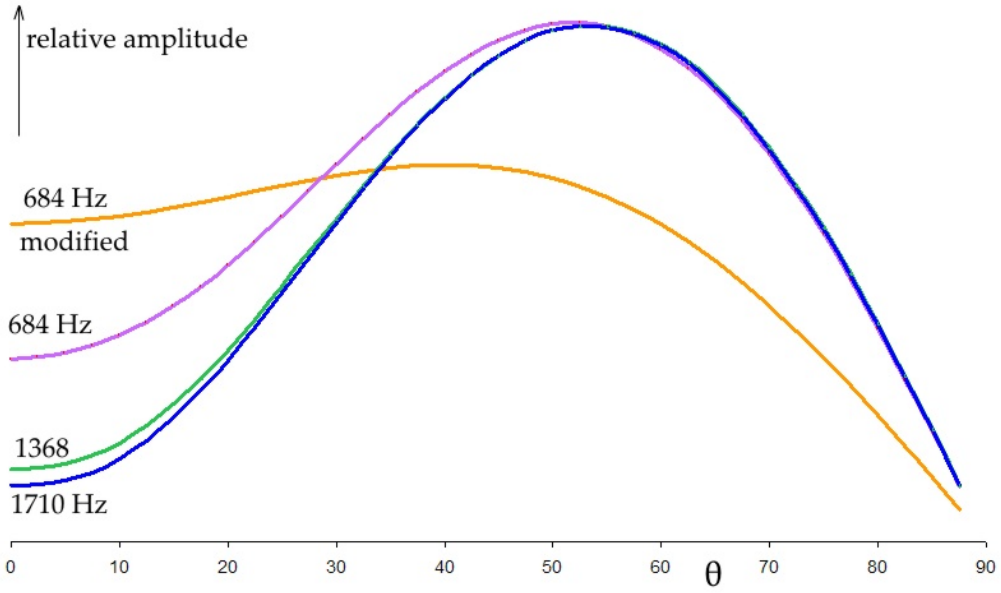

Figure 34: Far field directivity. Relative amplitude as a function of direction at 2 m range, calculated for loudspeaker 8 cm diameter oscillating in mode of Figure 29. The '684 Hz modified' curve has $0 \cdot 5\%$ of piston mode added.

I have taken the functional form of radial displacement (the cubic noted in Figure 33) into the Rayleigh-Sommerfeld computer program, assigning displacement to each mesh node according to its radial location. The surface displacement ξ_0 used for each mesh element was the mean of values at its three vertices. Calculated amplitudes are only relative to that at $\theta = 0$ so I am free to scale directivity plots for different frequencies relative to one another. Figure 34 shows the directivity in this mode at three frequencies, scaled to make clear that they all have the same form for $\theta >\approx 50°$. The kink is pronounced – indeed too pronounced.

The contribution of this mode relative to the piston-like mode will itself depend on frequency. To simulate this at 684 Hz I have added $0{\cdot}5\%$ of the piston mode, by adding a small positive constant (equal to 1/200 of maximum of the graph of Figure 33) to all displacement values. The result is plotted in the orange curve labelled '648 Hz modified'. The effect of such a small change in phase distribution over the cone is remarkable, almost completely removing the kink in directivity. The orange curve, at least for $\theta < 45°$, is quite similar to the plot in Figure 11 for a single speaker at 855 Hz (green points). Without knowing exactly how the actual speakers vibrate at different frequencies, I cannot take this further. However, I am fairly persuaded that this change in modal displacement pattern probably does account for the kink in the directivity plots in Figures 10 to 14. This has also been an interesting demonstration of the program's ability to model radiation from an object with non-uniform surface displacement.

Encouraged by the above, I find that adding a constant value equal to $2{\cdot}5\%$ of the maximum displacement in Figure 33 produces at 1710 Hz a fair match to the single speaker directivity plotted in Figure 10, bottom right panel. The green curve in Figure 35 is the theoretical directivity for this model surface vibrational amplitude. Also plotted are the experimental values at 1710 Hz, previously shown in Figure 10.

8.2 Modelling 2 and 3 simultaneous loudspeakers

I have used the results shown in Figure 35 for 1710 Hz to model the dipole, applying the same surface amplitude variation to each of the two 8 cm speakers 12 cm apart between centres, at 2 metres range. The results are plotted in Figure 36 against the experimental measurements at 1710 Hz (λ = 20 cm) previously shown in Figure 12. Agreement is encouraging.

The 'tripole' array had three 8 cm diameter speakers in line, 12 cm between centres. At 684 Hz the agreement with the experimental results of Figure 14 is quite good provided the three speakers are are given uniform surface displacement in the program. Figure 37 compares theory and experiment for both in and out of phase operation. Taking the displacement at each mesh node to be the same (essentially = 1) models the piston-like motion expected a low frequency. Note again that the experimental amplitude near grazing $\theta \to 90°$ is higher than the theory predicts.

At 1710 Hz, however, agreement for the tripole is poor. At 1710 Hz I should be able to use the higher mode illustrated in Figure 33 – the one used to give a plausible explanation for the kink in the directivity curve – for the dipole in Figure 36. Regrettably, using this the agreement for three speakers is poor; there is little predicted difference whether the central speaker is in or out of phase with the outer two. Perhaps this is because if the area of the speaker cone moving outwards at any moment is about equal to that moving inwards (see Figure 33), switching the phase will have negligible effect at long range. These inconsistent results between dipole and tripole at 1710 Hz must dent confidence in the explanations offered so far, but I cannot explore the matter further, lacking the means to measure the actual displacement of the speaker cone as a function of position and frequency.

The whole topic is worth visiting again with a more controlled experimental arrangement and the facility to measure the cone's vibrational displacement.

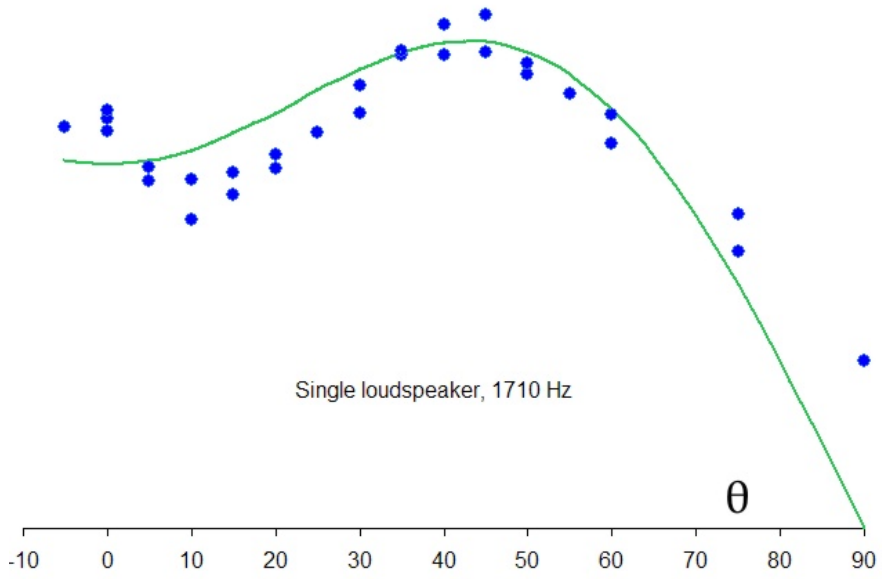

Figure 35: Theoretical directivity of a single loudspeaker at 1710 Hz, obtained by assuming it oscillates in the mode of Figure 33 with a 2·5% constant added to the surface amplitude to represent a small component of piston-like motion. Experimental points are those of Figure 10.

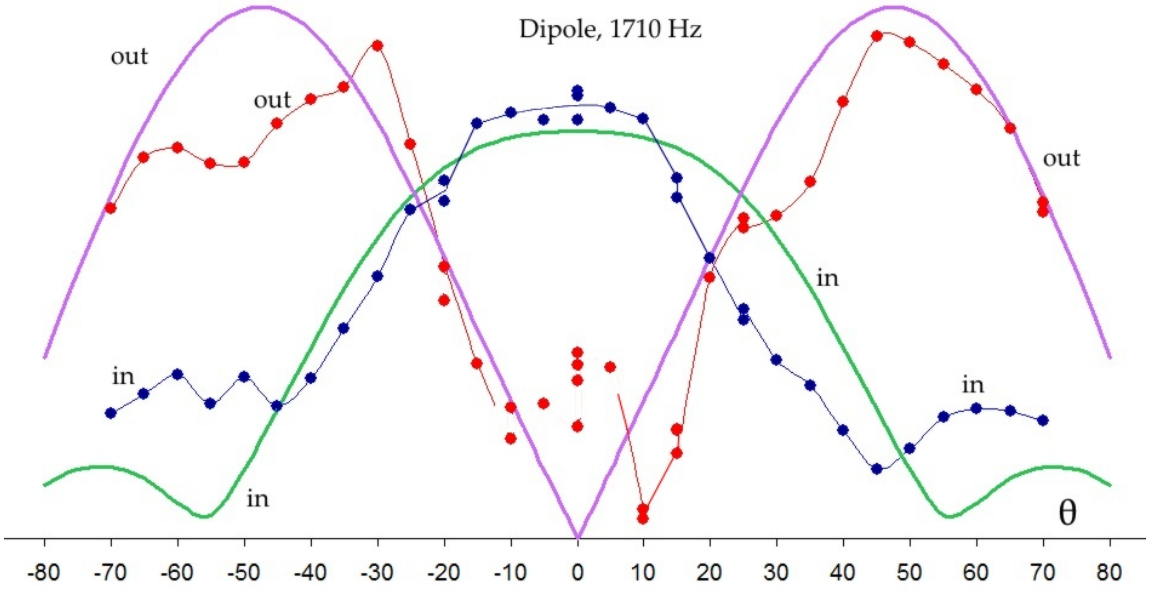

Figure 36: Comparison of computed directivity of a two-speaker dipole with experimental measurements. Graphs show amplitude both when in and out of phase.

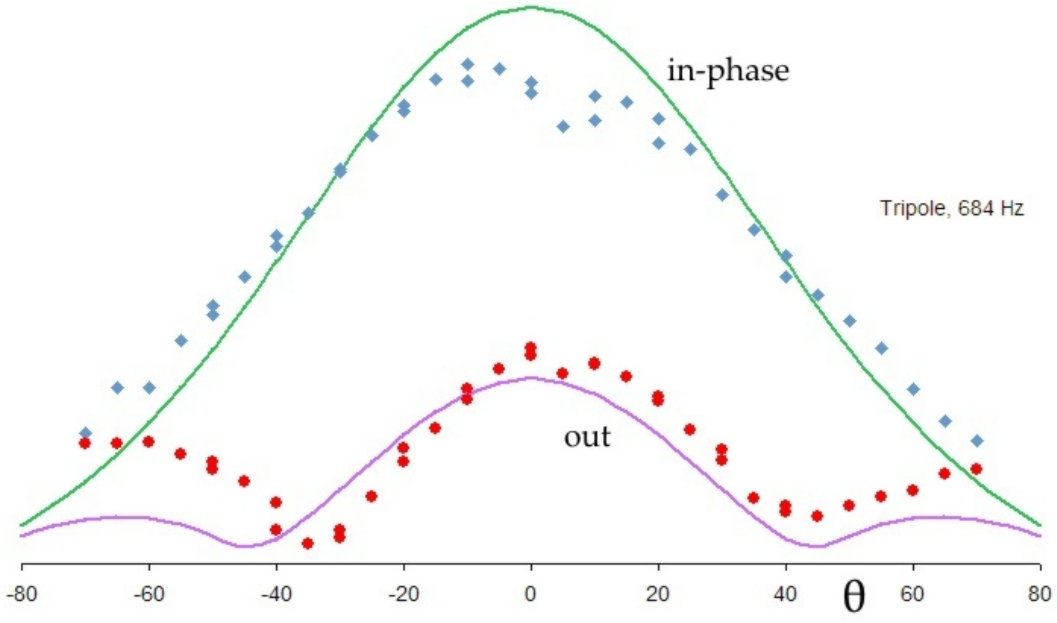

Figure 37: Comparison of theory and experiment for linear array of three speakers at 684 Hz ($\lambda = 50$ cm.). Theory assumes uniform surface displacement. Experimental points are those of Figure 14, last panel.

9 Kirchhoff formulation for radially vibrating sphere

This section leaves planar surfaces and opens up thoughts on how radiation from generally curved objects in free space might be modelled. The dipole Rayleigh-Sommerfeld formulation, shown in §7 to be successful for a flat radiator in a coplanar baffle, has no theoretical justification on curved surfaces. Only the Kirchhoff formulation of Green's theorem, Eq 21a, with integration over the whole surface Σ (but excluding the infinite hemisphere) remains rigorously correct. Accordingly I have gone back to this formulation and worked through a number of cases involving a perfect sphere in the breathing mode of oscillation – that is, pulsating uniformly and radially. I have looked into the structure of the integrand and the contribution of various parts of the sphere, and baffle if present, to the integral which describes the field. My aim has been to understand at close hand how Green's theorem functions, and to see where approximations might be made. One example is worked through in this section, and another in Appendix 2, which is essentially a continuation of this section. Appendix 3 explains a method for evaluating semi-infinite integrals of highly oscillatory functions.

9.1 Complete sphere in breathing mode

This first case is really just a numerical demonstration of the correctness of Kirchhoff's formulation on a sphere without a baffle. The arrangement is illustrated in Figure 38. A unit sphere, vibrating in breathing mode, is enclosed in a concentric sphere of nominally infinite radius. The space between the inner and outer spheres is penetrated by an infinitesimally narrow tube running along the negative z axis to join the two spheres. This tube, the two spheres and the bubble around Q form the boundary of a space Ω within which Helmholtz's equation holds. We want to find the displacement potential $\phi(Q)$ at the point Q on the $+z$ axis a distance R from the centre, O.

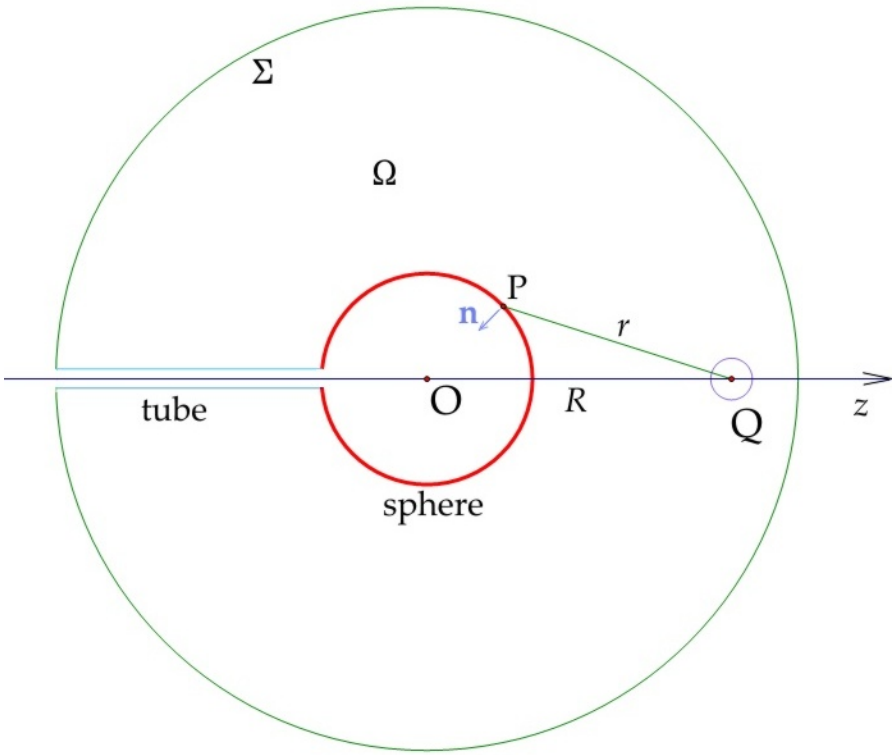

Figure 38: Cross-section through space Ω bounded by unit sphere (red) and infinite outer sphere.

The outwards normal $\mathbf{n}$ from Ω points radially towards the centre O of the inner sphere, radius 1. On the tube it points radially towards the negative z axis. The diagram also shows the bubble around Q which contributes $4\pi\phi(Q)$ to the surface integral. Following from Eq 21a the potential at Q is

$$\phi(Q) \;=\frac{-1}{4\pi}\iint_{\Sigma}\left[\phi(x)\left(i\kappa-\frac{1}{r}\right)\mathbf{e_r}\cdot\mathbf{n}-\nabla\phi(x)\cdot\mathbf{n}\right]\frac{e^{i\kappa r}}{r}\,dS\,. \qquad \textit{Copy of (21)}$$

In this case we do know both the potential and its derivative on the component surfaces of Σ. Bear in mind that the vector displacement $\boldsymbol{\xi}$ is related to its potential by $-\nabla\phi=\boldsymbol{\xi}$, equivalent in amplitude terms to $-\partial\phi/\partial R=\xi$ where R is the radial distance.

- Over the outer sphere the Sommerfeld radiation condition, imposing strictly outgoing waves, rules out any re-radiation back to Q. The integral over this surface is zero.
- On the infinitesimally narrow tube the displacement is along z, perpendicular to the local $\mathbf{n}$, so here $-\nabla\phi(x)\cdot\mathbf{n}=0$. ϕ in the tube falls as $1/R$ but the surface is shrunk to zero so the integral can be taken as zero.
- On the unit sphere $\boldsymbol{\xi}$ is in the exact opposite direction to $\mathbf{n}$ so $-\nabla\phi(x)\cdot\mathbf{n}=\boldsymbol{\xi}\cdot\mathbf{n}=-\xi_0$, where ξ_0 is the amplitude of surface displacement, which we can take to be 1.

To obtain ϕ_0 itself over the inner sphere, use the exact result for a sphere that $\phi=Ae^{i\kappa R}/R$. Then

$$-\frac{\partial\phi(R)}{\partial R} \;=\; -\frac{Ae^{i\kappa R}}{R}\left[i\kappa-\frac{1}{R}\right] \;=\; -\left[i\kappa-\frac{1}{R}\right]\phi(R) \;=\; \xi(R)\,.$$

At the surface of the sphere $R=a$, the radius, so

$$\phi_0 \;=\; \frac{-\xi_0}{i\kappa-\frac{1}{a}}\,. \qquad (36)$$

Kirchhoff's formula becomes

$$\phi(Q) \;=\frac{+1}{4\pi}\iint_{sphere}\xi_0\left[\frac{\left(i\kappa-\frac{1}{r}\right)}{\left(i\kappa-\frac{1}{a}\right)}\mathbf{e_r}\cdot\mathbf{n}\;+\;1\right]\frac{e^{i\kappa r}}{r}\,dS \qquad (37)$$

where r is measured from P on the surface of the sphere, and the integral is over the whole surface of the sphere.

To evaluate this an element of area around point P is selected and the path length r to Q determined. P is parameterised by polar angle θ from the z axis and by azimuthal angle ψ around the z axis. The element of area is $a^2\sin\theta\,d\theta\,d\psi$. By symmetry the integral over ψ is simply 2π. We also need the obliquity factor, $\cos\beta$. This can be found using vector geometry since $\mathbf{n}=-\mathbf{p}$ and $\mathbf{e_r}=\mathbf{p}-\mathbf{q}$ where $\mathbf{p}$ and $\mathbf{q}$ are the position vectors of P and Q. Alternatively use the school geometry in Figure 39. Either way

$$\cos\beta \;=\frac{R\cos\theta-a}{r} \quad\text{and}\quad r^2 \;=\; R^2+a^2-2aR\cos\theta$$

whether $\theta<\pi/2$ or $\theta>\pi/2$. Pulling this together, for ξ_0 constant over the sphere,

$$\phi(Q) \;=\; \frac{\xi_0\,a^2}{2}\int_0^{\pi}\left[\frac{\left(i\kappa-\frac{1}{r}\right)}{\left(i\kappa-\frac{1}{a}\right)}\cos\beta\;+\;1\right]\frac{e^{i\kappa r}}{r}\,\sin\theta\,d\theta\,. \qquad (38)$$

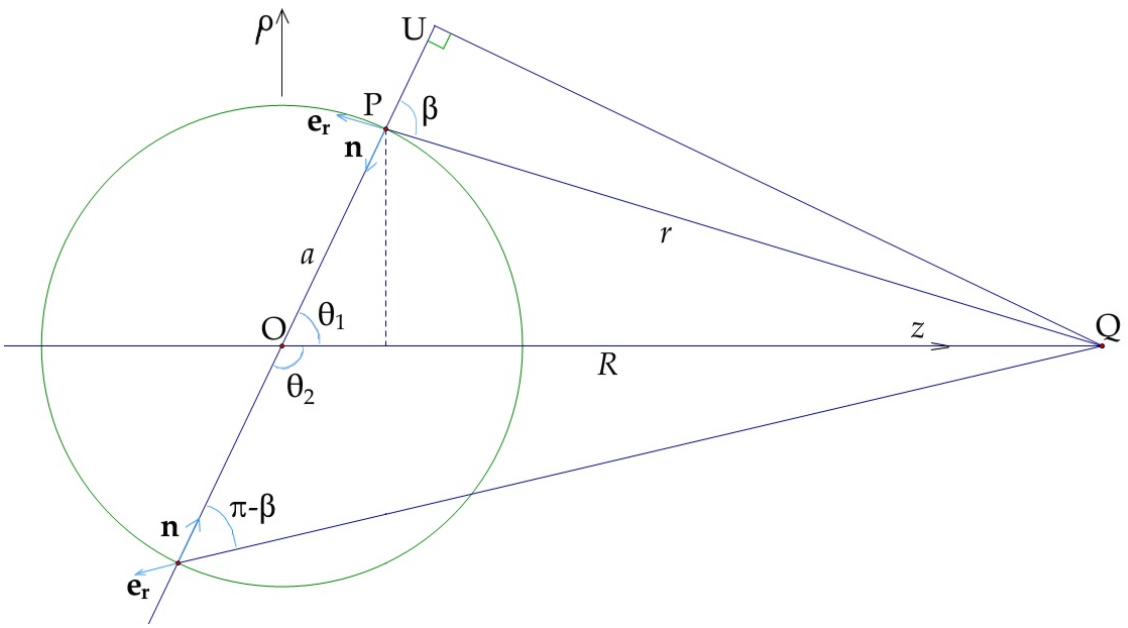

Figure 39: Construction on cross-section of sphere, radius a, for evaluating r and $\cos\beta$. Length PU is $R\cos\theta_1 - a$ for $\theta_1 < \pi/2$.

To compute the integral we need the real and imaginary parts of the integrand. Note that

$$\frac{i\kappa - \frac{1}{r}}{i\kappa - \frac{1}{a}} \;=\; \frac{M_r}{rN} - i\frac{M_i}{rN}$$

where

$$M_r \;=\; a(\kappa^2 ar + 1)\,, \qquad M_i \;=\; \kappa a(r-a)\,, \qquad N \;=\; \kappa^2 a^2 + 1\,.$$

Let $\mathfrak{c} = \cos\kappa r$ and $\mathfrak{s} = \sin\kappa r$. Then

$$\Re\left[\frac{\left(i\kappa - \frac{1}{r}\right)}{\left(i\kappa - \frac{1}{a}\right)}\cos\beta \;+\; 1\right]\frac{e^{i\kappa r}}{r} \;=\; \frac{1}{r^2 N}\left[\mathfrak{c}\,(M_r\cos\beta + rN) + M_i\mathfrak{s}\cos\beta\right], \tag{39a}$$

$$\Im\left[\frac{\left(i\kappa - \frac{1}{r}\right)}{\left(i\kappa - \frac{1}{a}\right)}\cos\beta \;+\; 1\right]\frac{e^{i\kappa r}}{r} \;=\; \frac{1}{r^2 N}\left[\mathfrak{s}(M_r\cos\beta + rN) \;-\; M_i\mathfrak{c}\cos\beta\right]. \tag{39b}$$

The real and imaginary parts of the integrand (equal to $\frac{1}{2}a^2\sin\theta \times$ Eq 39a, b) are oscillatory as Figure 40 illustrates for the case $a = 1$, $\lambda = 1/4 \equiv \kappa = 8\pi$, $R = 1\cdot 3$. The smaller κ, the more oscillatory the functions, and this is a challenge to numerical integration because of the cancellation of adjacent half cycles. The amplitude is largest on the side of the sphere nearest Q ($\theta < 90°$), but there is no sharp cut off in the geometrical shadow. Using the integrand in Eq 39a, b I have evaluated the real and imaginary parts of the integral numerically for many distances R for several values of a and κ, taking $\xi_0 = 1$. A selection is listed in the three right-most columns of Table 1.

Now compare the results of quadrature with the exact values, found as follows. The source potential is $\phi = Ae^{i\kappa R}/R$ and

$$-A\,\frac{e^{i\kappa a}}{a}\left(i\kappa - \frac{1}{a}\right) \;=\; \xi(a) \equiv \xi_0 \quad \text{so} \quad A \;=\; \xi_0\, a^2\, e^{-i\kappa a}\,\frac{(i\kappa a + 1)}{k^2 a^2 + 1}\,. \tag{40a}$$

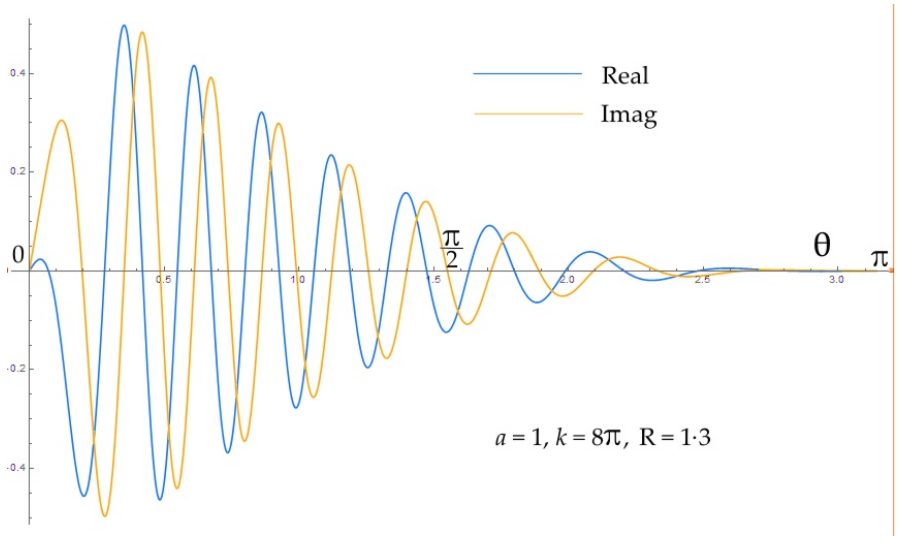

Figure 40: Real (blue) and imaginary (orange) parts of the integrand of Eq 39 over $0 \le \theta \le \pi$ for $a = 1$. $\kappa = 8\pi$, $R = 1 \cdot 3$.

$$\Re\,\phi(R) \;=\; \frac{\xi_0\, a^2}{RN}\left[\cos\kappa(R-a) - \kappa a\,\sin\kappa(R-a)\right], \tag{40b}$$

$$\Im\,\phi(R) \;=\; \frac{\xi_0\, a^2}{RN}\left[\sin\kappa(R-a) + \kappa a\,\cos\kappa(R-a)\right]. \tag{40c}$$

It is most gratifying to find that over a wide range of parameters the numerical integration agrees to over 6 significant figures with the exact values, including agreeing in sign. Table 1 gives a sample for $a = 1$, $\lambda = 1/4$. This also attests to the quality of the integration software, though for some values of a the algorithm did not converge. This notwithstanding, I have tested the quadrature against the exact expressions of Eq 40 for sufficiently many random values of a, λ and R to be satisfied of their agreement.

The calculations illustrate the correctness of Kirchoff formulation of Huygen's principle, which of course was not in doubt. It shows that summing the elementary monopole and dipole sources over the entire surface of the actual sphere reproduces the field which would be produced by a single point source at O. I worked through some other examples of sound radiation from a point source, not published here. They demonstrate how the boundary Σ of the space Ω in which Helmholtz's

		Exact, Eq 40			By integration	
R	Real	Imag	Abs	Real	Imag	Abs
1.03	-0.025283470	0.029165939	0.038599299	-0.025283455	0.029165621	0.038599048
1.4	0.015765357	-0.023619972	0.028398055	0.015765357	-0.023619972	0.028398055
2	0.000790321	0.019862922	0.019878639	0.000790321	0.019862925	0.019878642
4	0.000395160	0.009931461	0.009939319	0.000395160	0.009931466	0.009939324
15	0.000105376	0.002648390	0.002650485	0.000105376	0.002648390	0.002650485
40	0.000039516	0.000993146	0.000993932	0.000039516	0.000993145	0.000993931
100	0.000015806	0.000397258	0.000397573	0.000015806	0.000397258	0.000397573

Table 1: Comparison of exact values of $\phi(R)$ with those from numerical quadrature of Kirchhoff's formula over a sphere, $a = 1$, $\lambda = 1/4$, various ranges.

equation holds can be changed in size and shape and the field at Q still remain the same provided that the values which ϕ and its derivative would have on the morphed Σ are those which would be there if only the point source was present. This is the power of Green's theorem – the boundary can be pulled about and the field inside stay the same provided the values over all the boundary remain consistent with the same fixed source or sources. Integration must be over the whole relevant area and not just that Q-facing sector of the sphere which is in direct line of sight from Q, for which $\cos\beta > 0$. This may be counter-intuitive for those of us so used to ray theory. The point is made emphatic for small spheres for which the opposite hemispheres which face towards and away from Q make equal contributions to $\phi(Q)$, as proved in Appendix 2.

9.2 Spherical sectors with baffle

Appendix 2, §14, works through the case of a breathing mode unit hemisphere surrounded by a concentric planar baffle. Numerical results show that the field at Q, anywhere in front of the hemisphere or baffle, depends only on the range R. Moreover, it is equal to the field that would be produced at Q by a complete sphere in the absence of the baffle. A physical baffle is ideally a rigid hard barrier, in some situations vanishingly thin. No displacement normal to the baffle is possible. Take the special case of a planar baffle. If a point source is placed near it, the condition $-\nabla\phi \cdot \mathbf{n} = 0$ at the barrier gives the same pressure and displacements as would be produced by an image of the source in the barrier, without the barrier being present. We have already met this in Figure 19b, §6.1 where is is used to derive the Rayleigh-Sommerfeld Green's function. The rigid planar baffle acts as an acoustic mirror. If our point of listening, Q, and the source are both to the right of the barrier, the energy that would otherwise travel off to the left is reflected by the barrier towards Q, interfering with the direct sound from the source. If the point source moves right up to the baffle, the source and its image will be essentially at the same place (though still notionally on opposite sides), and hence in phase. Therefore, if the source has amplitude $\mathcal{A}$, the combined source + image acts as a modified point source of amplitude $2\mathcal{A}$. The baffle doubles the acoustic pressure at Q due to a point source on its surface.

Apply this observation to Figure 74b in Appendix 2 where we have a radially vibrating hemisphere surrounded by a planar baffle. The local displacement on the hemisphere equals that on the whole sphere of Figure 38, which is equivalent to a point source of amplitude A in the absence of the baffle, or one of amplitude $A/2$ when the baffle is in place. The field external to the hemisphere varies only in the radial direction, so it does not matter where Q is relative to the baffle; the sound detected at Q depends only on its distance from the apparent source at the centre of the hemisphere. The numerical results in Appendix 2, Table 5, support this physical interpretation.

What can be deduced about the field from a radially vibrating spherical sector which is either more than or less than a hemisphere? Provided any physical baffle does not which disturb the radial field, the field from the sector + baffle must be equivalent to that of a point source at O. Clearly such a baffle cannot be a plane intersecting the rim of the sector and off-set from O; such a baffle would experience a circumferential force. Rather, only a conical baffle with apex at O will not perturb the field. We can conclude that a radially vibrating spherical sector in such a conical baffle will radiate as a point source at O. The conical wall will constrain the sound energy to lie within the hollow of the cone. Regarding its equivalent source amplitude, I surmise that it will be reduced from A by the ratio of sector area to 4π. Multiple reflections, equivalent perhaps to multiple distorted image sources, will enhance the sound amplitude to be equivalent to a monopole of amplitude A at O. However, apart from the planar baffle, the 'method of images' as used in electrostatics to solve Laplace's equation does not have an equivalent in acoustics.

10 Computed fields of vibrating sphere and spheroids

The first subsection here, §10.1, describes the application of my computer program to uniform spheres, implementing both the Kirchhoff and the dipole Rayleigh-Sommerfeld formulations. The second subsection extends this to prolate and oblate spheroids. To make comparison with the exact solutions of the wave equation, the expressions here take the surface potential ϕ_0 to be specified rather than the normal displacement.

10.1 Kirchhoff and Rayleigh formulae for spheres

A unit radius sphere is modelled by a convex polygon. Figure 41 shows three meshes used in these calculations to represent such a sphere. They were created using the flexible mesh generator in the LISA 8 finite element program. The first has 256 triangular elements, the second 512, the third 1024, and all have a surface area of precisely 4π. The origin O is at the body centre, from which distances are reckoned. Adjacent 45° segments about the z axis are mirror images of each other so z is a 4-fold rotation axis, whilst x and y are both 2-fold axes. In any one sphere each mesh node has been assigned the same potential, so modelling the breathing mode of uniform radial expansion and contraction. I have also set up field meshes in two planes: $x-z$ through 180° and $x-y$ through 90°. These field meshes are illustrated in Figure 42. Preliminary runs of the code with the 256-element quasi-sphere showed that the field had the symmetry of the polygon, which adds confidence in correctness of the coding. The 512-element mesh gives a good balance between modelling a sphere and computing time so the calculations below were done with this.

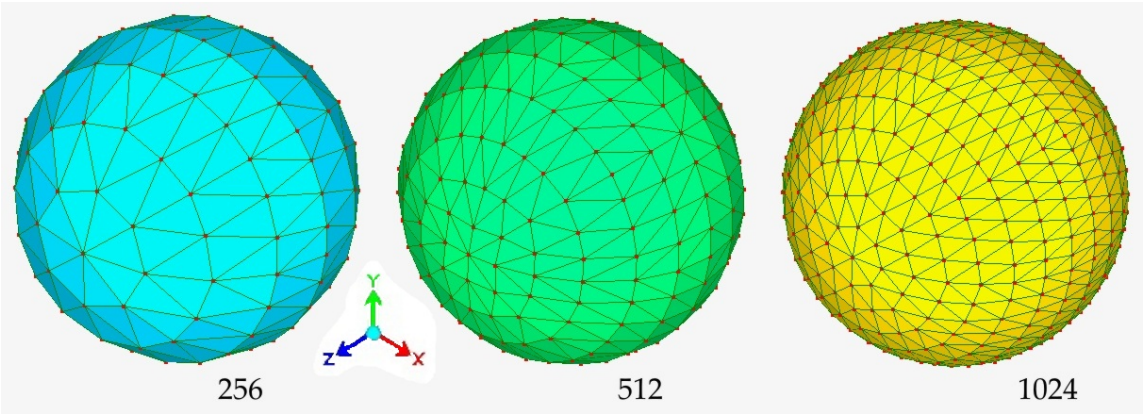

Figure 41: 256, 512 and 1024 sided polygonal meshes representing a sphere with unit radius.

10.1.1 Kirchhoff formula applied to a sphere

It has been made clear that the Rayleigh-Sommerfeld formulation applies strictly only to flat objects, whereas the Kirchhoff formulation is more versatile but requires not just the surface potential to be known but an intelligent guess made at the normal displacement as well. One case in which both potential and displacement are both correctly known ha already been studied in §9, namely the uniform sphere. Therefore it seems sensible to start by seeing whether the computer program can obtain the same results as the analysis of §9. In §9 and its companion Appendix 2 it was the surface displacement ξ_0 that was specified. The expression for $\phi(Q)$ appearing in Eq 37 can be cast in terms ϕ_0:

$$\phi(Q) \;=\; +\frac{1}{4\pi}\sum_{elements}\phi_0\left[\left(\frac{\cos\beta}{r}+\frac{1}{a}\right)-i\kappa(\cos\beta+1)\right]\frac{e^{i\kappa r}}{r}\iint_{triangle}e^{i\kappa\varepsilon}\,dS\,. \qquad (41)$$

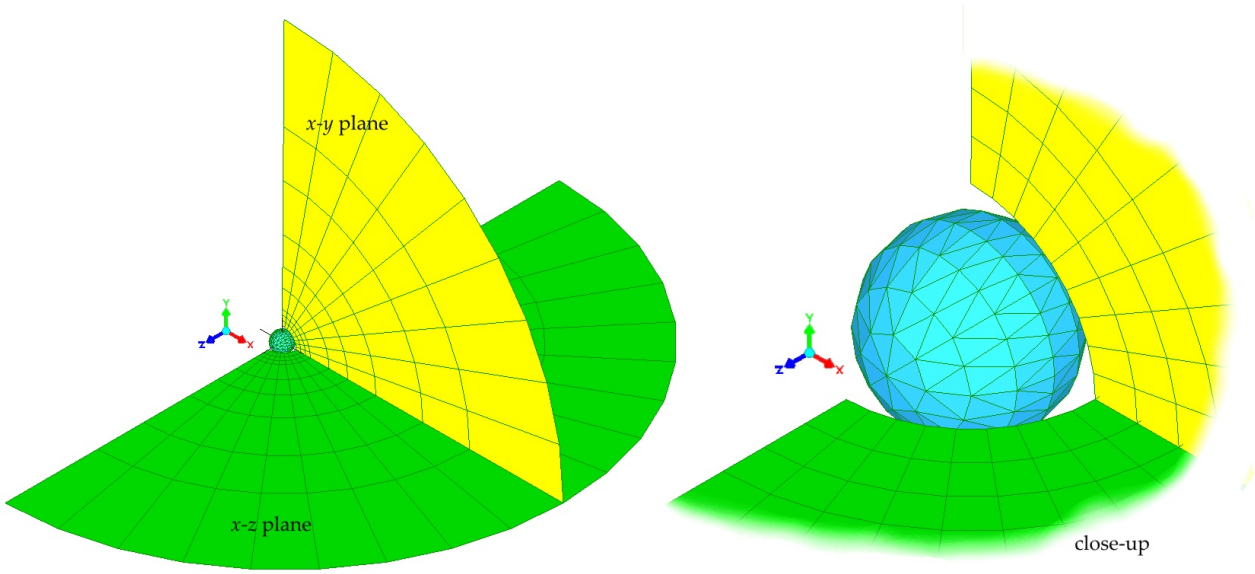

Figure 42: Fans of field points Q in the $x-y$ and $x-z$ planes centred on the unit sphere. Distant and close-up views from the same direction of the 256-element mesh.

Here a is the radius of the sphere and r the distance to Q from the centroid of the triangular mesh element. Table 2 below summarises five computer runs, the first four of which are plotted in the log-log graphs (natural logarithms) in Figure 43. In all cases $a = 1$ and 190 points are plotted, mostly on top of each other. It is gratifying to see that in all five wavelengths the gradient is almost exactly -1 and the value of ϕ_0 extrapolated from the graphs is very close to the value input.

plot colour	λ	input ϕ_0	calculated ϕ at $r = 1$
blue	1·40	2	1·971
green	0·364	1	1·00
red	3·02	$0 \cdot 5$	0·4997
orange	1·00	$0 \cdot 25$	0·2447
-	0·1	1	0·994

Table 2: Parameters of five calculations of $|\phi(r)|$ for unit sphere using Kirchhoff formulation.

I chose some wavelengths in Table 2 to correspond with internal resonances of the sphere, wary that they might distort the calculations. This is mentioned in §11.2 as a known problem for integral equation methods. As you can see, there is no evidence of this. However, I will show in §10.1.2 below that if the dipole Rayleigh-Sommerfeld formulation is applied to the sphere, such resonances have a very disturbing effect.

The calculation at $\lambda = 0 \cdot 1$ can be expected to be more affected by the jewelled surface of the polygon, even with 1024 elements. This is apparent in Figure 44 which plots the calculated magnitudes of ϕ around the $x-z$ plane, compared with the theoretical values (horizontal solid lines) at 15, 20 and 30 radii range. The graphs have the symmetry of the polygonal quasi-sphere, which in itself is evidence of correct computer coding.

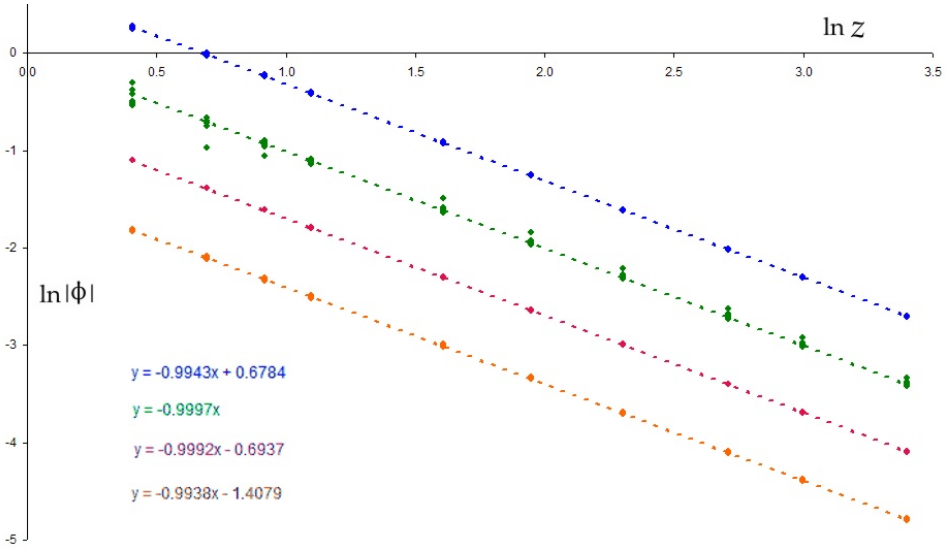

Figure 43: Log-log plots of $|\phi(z)|$ against range z for unit sphere at four different wavelengths, with surface potentials 2, 1, $0\cdot5$ and $0\cdot25$. z measured from sphere's centre.

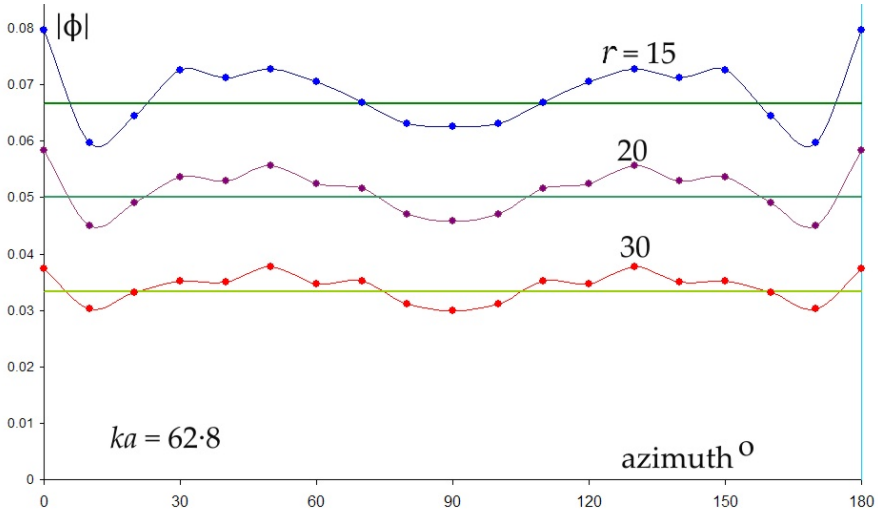

Figure 44: Computed variation in $|\phi|$ with azimuth around $x-z$ plane at three ranges at $\lambda = a/10$.

The theoretical displacement field of a sphere is

$$\xi(z) \;=\; -\phi_0 \frac{a}{z} e^{i\kappa(z-a)} \left(i\kappa - \frac{1}{z}\right) \;=\; \phi_0 \frac{a}{z} \left[\mathcal{C}_R - i\,\mathcal{C}_I\right]$$

$$\text{where}\quad \mathcal{C}_R = \kappa \sin\kappa(z-a) + \frac{\cos\kappa(z-a)}{z}\,, \qquad \mathcal{C}_I = \kappa\cos\kappa(z-a) - \frac{\sin\kappa(z-a)}{z}\,.$$

The program calculates the displacement numerically using Eq 24a. The calculated real and imaginary parts agree well with theory, and the error in magnitude is encouragingly small, as shown in Figure 45. This plots the fractional error $|\xi_{calc}/\xi_{exact}|-1$ when the program is run for the 512-element quasi-sphere (blue) and its 1024-element refinement (red) using $\kappa a = 17\cdot22$. In each case 190 points are plotted, though many of the blue have been masked by the red. We can say that roughly with 512 elements the error is typically 3 or 4%, reducing to less than 1% with 1024 elements. There are

a few outliers which are for positions Q lying precisely on the z axis. These may be a result of the mesh producing a polygon rather than a smoothly rounded sphere.

A further test of the program is to check that Helmholtz's equation holds. The program calculates the real and imaginary parts of the second derivatives of ϕ, and the ratio $\nabla^2\phi/\phi$ should equal κ^2. I have tested this on the data at $\kappa = 17 \cdot 22$ from the unit quasi-sphere with 1024 elements and find that it holds closely. $\kappa^2 = 296{\cdot}49$, and over 190 field positions the program gives all quotients $|\nabla^2\phi/\phi|$ in the range $296 \cdot 49$ to $298 \cdot 51$. Overall, the program appears to implement the Kirchhoff integral for a sphere satisfactorily. This version of the program can therefore be taken forwards with some confidence and tested against the exact theory for vibrating spheroids.

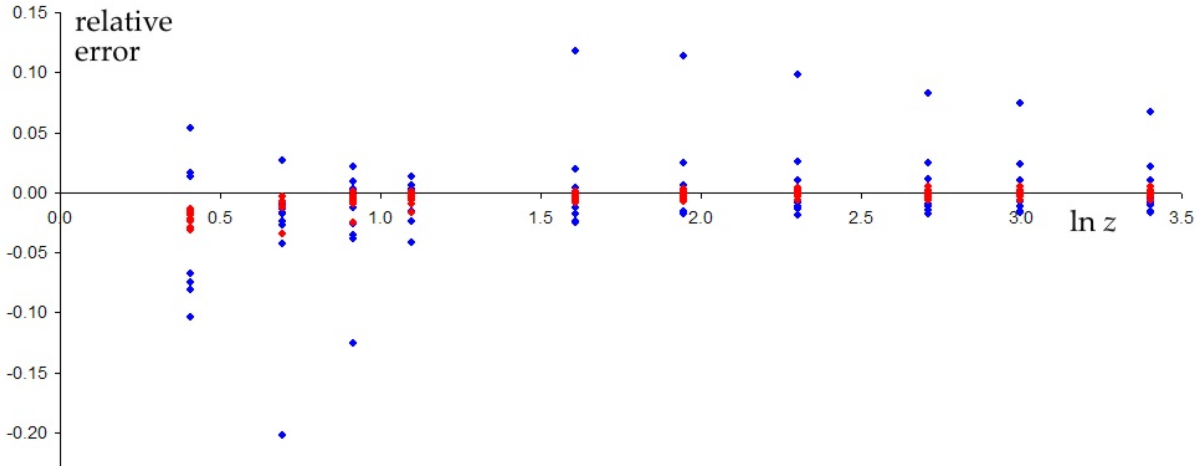

Figure 45: Fractional error in displacement magnitude for two quasi-spheres with 512 (blue) and 1024 (red) elements, plotted against log range.

10.1.2 Rayleigh-Sommerfeld applied to sphere

The Rayleigh-Sommerfeld formulations, as I keep reminding myself and readers, is strictly applicable only to flat surfaces. Therefore attempts to apply them to a curved surface can only be approximations. The formulations exist in two forms – monopole and dipole, given by Eq 22a and b. Each of these is just half of Kirchhoff's formulation of Green's theorem, so we can hardly expect one by itself to give the correct result. Numerical examples show this to be the case. This subsection looks briefly at the manner in which they fail individually, and the errors incurred.

Look first at the dipole version, in the variant of Eq 23a which requires ϕ_0 to be specified. I have input $\phi_0 = 1$ for all elements and been pleased to see that the range dependence is as $1/z$, just as in the Kirchhoff formulation above. However when the curves were extrapolated back to $z = a$ at the surface of the sphere, the values of ϕ_0 obtained are not 1 as in all cases they should have been. Instead it showed the erratic, oscillatory fluctuation in Figure 46. Its shape suggests an interference effect, with two sources alternately adding and subtracting.

To understand what is probably happening, observe that the dipole Rayleigh-Sommerfeld formula, Eq 23a, b, involves $\cos\beta$ multiplying the whole integrand, in contrast to the Kirchhoff formula which has $\cos\beta + 1$. β will be small apart from at those parts of the surface which either face towards or away from Q. The mathematics does not know that the sphere is not transparent, so the back surface, 180° round from Q, contributes at about the same strength as the front part of

the sphere. These two areas act like a dipole. In Figure 46 I have marked the κa positions of internal resonances of the sphere by green diamonds. One set is placed at $2 \cdot 5$ vertically and the other more sparse set at $0{\cdot}5$. Destructive interference occurs at this second set of resonances. The first set do not seem to affect the otherwise constructive interference. I obtained some of these resonance frequencies myself using finite element analysis, but then found a very helpful paper by Daniel Russell which lists them all (Am. J. Phys. Vol 78 No 6, 2010). The ones which cause destructive interference are spherically-symmetric, breathing-like modes where $m = l = 0$. Their motion is described by the spherical Bessel function $j_0(\kappa z) = \sin \kappa r/(\kappa r)$. Its derivative at the inner surface of the sphere, being the displacement, can be taken as zero. Differentiating the Bessel function, this boundary condition gives resonances when $\tan \kappa a = \kappa a$, with roots at $\kappa a = 4 \cdot 49$, $7 \cdot 73$, $10 \cdot 90$, $14 \cdot 07$, $17 \cdot 22$, $20 \cdot 37$, 23.52, etc. These are the values marked by the green diamonds along the line at $0 \cdot 5$ in Figure 46.

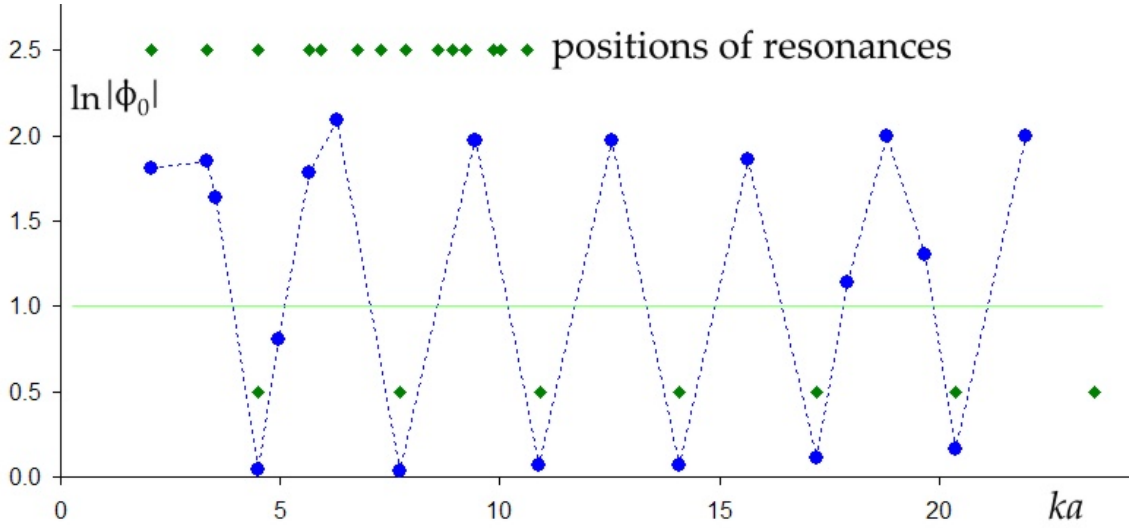

Figure 46: Surface potential predicted by Raleigh-Sommerfeld formula applied inappropriately to a sphere with $\phi_0 = 1$. Green diamonds mark resonant frequencies of inner spherical cavity.

The assumptions under which the Rayleigh-Sommerfeld formulation is derived require the radiating surface to be plane, so this dramatic failure to apply to a sphere should not be unexpected. It seems perverse to press the formulation any further, but I have evidence that the Rayleigh-Sommerfeld formulation can give useful results if the obliquity factor $\cos \beta$ is not allowed to become negative. This means that the only area of the sphere which can contribute lies within the cone subtended by Q and hence geometrically observable from Q. Of course this seems completely at odds with the analysis of §9 where it was shown that Green's theorem demands that the integration be over the entire sphere, not just the area within the ray-cone with apex Q. I can offer only a loose argument as to why the restricted integration might work. Clearly it will eliminate contributions to the field from the back region of the sphere and so will prevent the spurious interference seen above. Also it respects the assumption in the Rayleigh-Sommerfeld formulation that the surface is at least flat locally and so β cannot exceed 90°. It would be valuable to be able to use this method for objects which, whilst not flat, do not have a contributing back surface. These include loud speakers and acoustic mirrors which are essentially spherical sectors. In optics such cases are quite usual.

Accordingly I have examined a significant number of examples of the dipole Rayleigh-Sommerfeld formulation with $\cos \beta > 0$ applied to a sphere. With a fixed at 1 I varied the wavelength from 6 down to $0 \cdot 1$. As expected, there is none of the violent interference which occurs if the

integration is over the whole sphere. To that extent the results are not greatly different from using the Kirchhoff formulation. However I did notice that from small κa, less than about 10, the range dependence from the centre of the sphere is not $1/z$. Instead, it seems as if the radiated sound is centred on a point which does not coincide with the geometric centre O of the circle at $z = 0$. A typical case, $\lambda = 2$, is shown in the left panel of Figure 47. You can see in this log-log plot that at short ranges the points seem to be at too short a range and need moving to larger z in order to fall on a straight line. There is no single 'correct' way to deal with this data. The approach I have chosen is to change the independent variable to be $z + \delta$ where δ is chosen to make the gradient of the log-log graph equal to -1. Thus the right panel in Figure 47 has the same values of $|\phi|$ but now plotted against $z + 0 \cdot 6$. If $\delta > 0$, the centre of sound appears to be closer to the back (concave) surface of the sphere than the geometric centre. I find it surprising that δ is positive because in the Rayleigh formulation the individual radiating elements are concentrated on the *front* face of the sphere nearest Q, not the rear. In Figure 48 the blue curve labelled δ plots the δ values for 13 values of κ. There is clearly some wave interference effect taking place for $\ln \kappa a < 2 \cdot 5$, but above that the sound seems to emanate from O.

We would also like reassurance that the surface potential ϕ_0 as calculated from the restricted Rayleigh-Sommerfeld method gives the input value of 1. The non-linear dependence on z creates uncertainty as how to extrapolate the curve in Figure 47 back to the surface. Is this surface at 1 radius in front of the apparent centre, at $z = 1 - \delta$, or is it at $z = 1$, its geometric place? The orange curve labelled A in Figure 48 plots the first case, where $z = -\delta$. The green curve, B, plots the second case where $z + \delta = 1 + \delta$. The values of $|\phi_0|$ in both cases are within about 30% of 1 except at long wavelengths. When $\delta \approx 0$, at $\kappa a > 10$, the correct value of ϕ_0 is obtained.

What of the monopole version, which has no obliquity factor? Here all parts of the vibrating sphere contribute equally to the field at Q, differing only in their range and hence phase. In a few numerical experiments with a unit sphere of 1024 mesh elements at various wavelengths, I find that the amplitude $|\phi|$ generally falls with range as $1/r$, but its value varies erratically from the theoretical value of $1/(r\sqrt{k^2+1})$. Being a quasi-sphere, the values of $|\phi|$ at all azimuths in the $x-z$ plane should be the same. At some wavelengths this is pretty well the case, but at others there are large and haphazard variations. Two examples are shown in the log-log plots of Figure 49. The left panel is at $\lambda = 1/10$, a rational fraction of the radius. The right panel is at $\lambda = 0 \cdot 10396$, an irrational[11]. The

[11] A useful scheme for producing numbers which are far from being low denominator fractions is to expand a continued fraction whose tail is 1, 1, 1, 1, ... Here $0 \cdot 1039604 = \{0 : 9, 1, 1, 1, ...\}$.

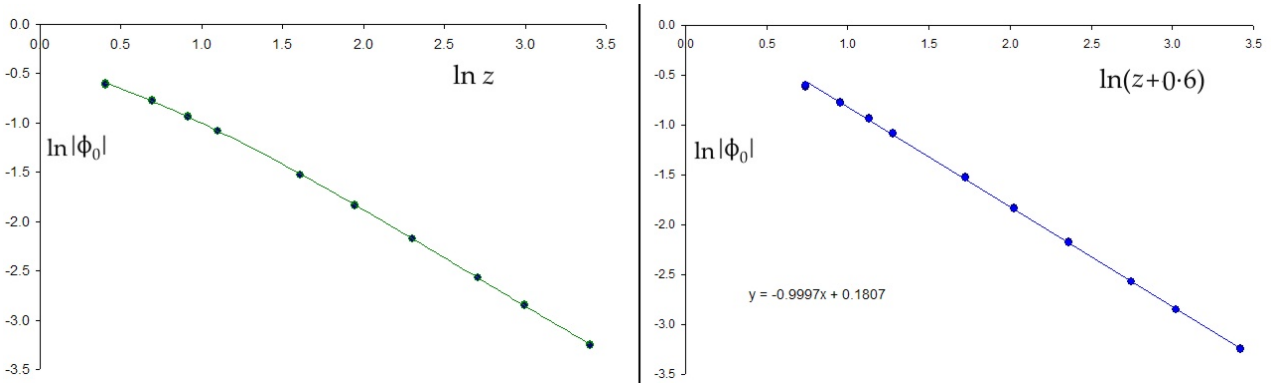

Figure 47: Log-log plots of $|\phi|$ versus range for a sphere with $\lambda = 2$ using dipole Rayleigh formula with $\cos\beta > 0$. Left: plot against z. Right: against $z + \delta$ for $\delta = 0 \cdot 6$. 190 plotted points.

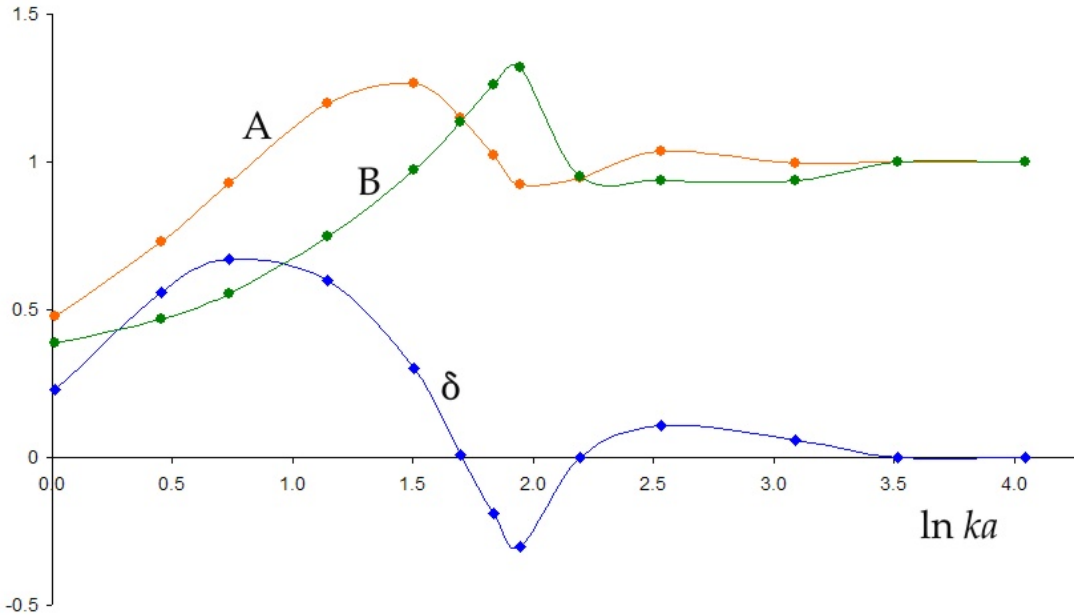

Figure 48: Summary of restricted dipole Rayleigh results as in Figure 47. Curve δ: apparent position of source with respect to geometric centre. Curve A: ϕ_0 at $z = -\delta$. Curve B: ϕ_0 at $z = 1$.

theoretical values are the green solid lines. One suspects hypersensitive interference amongst the 1024 contributions in the left panel which a 4% increase in wavelength eliminates. We can regard this behaviour as the complement of the interference seen in the dipole formulation in Figure 46.

The conclusion on this evidence is that both the dipole and monopole versions of the Rayleigh-Sommerfeld formulation, with integration over the whole convex object, fail and can be discounted from any practical use. However the dipole Rayleigh-Sommerfeld formula, when restricted to integration for $\cos\beta > 0$ and $\kappa a > 10$, seems surprising good for predicted the field from a sphere. In the next sub-section I examine how well it performs on spheroids.

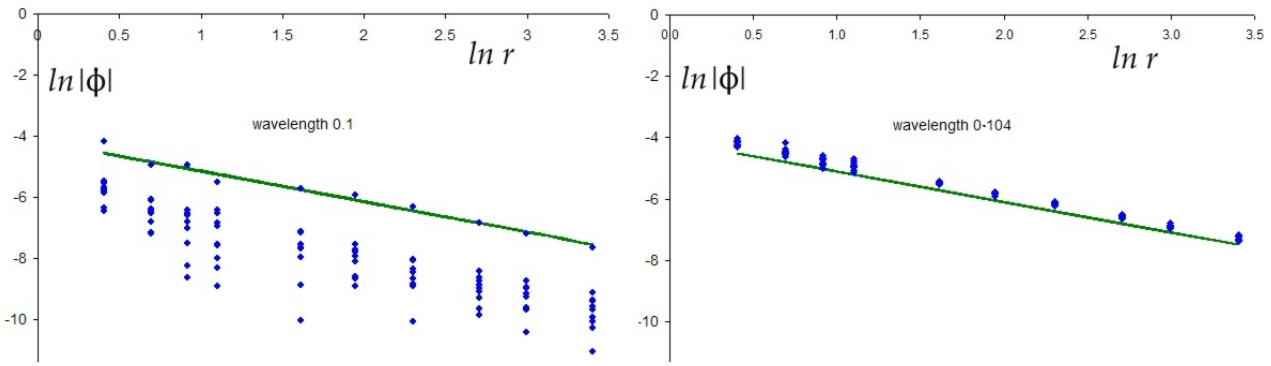

Figure 49: Log-log plots of $|\phi|$ versus range calculated at two slightly different wavelength (left $0 \cdot 1$, right $0 \cdot 10396$) using monopole Rayleigh-Sommerfeld formula on sphere, $a = 1$.

10.2 Kirchhoff theory applied to spheroids

This subsection applies the Kirchhoff version of the computer program to prolate and oblate spheroids and compares its results with the exact solutions of Helmholtz's equation, set out in Appendix 4. The Kirchhoff formula is essentially Green's theorem combined with Helmholtz's equation and requires input of both the potential and the normal displacement at the spheroid's surface. I also give some examples of the restricted dipole Rayleigh-Sommerfeld formulation in which integration is limited to the geometrically observable parts of the spheroid, that is, to $\cos\beta > 0$.

It is possible to follow the same approach with a spheroid as with the sphere in §10.1 since spheroidal wave functions, which define the potential and also its normal derivative on any given spheroid, are available through Mathematica and elsewhere. Recall that with the sphere we knew that $\phi = Ae^{i\kappa r}/r$ is an exact solution of the wave equation in spherical co-ordinates describing the radially symmetric 'breathing mode', and that the normal derivative is simply $\partial\phi/\partial r$. If $\phi_0 = 1$, $\nabla\phi_0 \cdot \mathbf{n} = 1/a + i\kappa$. The exact solution for a prolate spheroid vibrating in the breathing mode is shown in Appendix 4 to be

$$\phi(C,\zeta,\eta) \;=\; A\,R_{00}^{(3)}(C,\zeta)\,S_{00}^{(1)}(C,\eta) \;\equiv\; A\,[R_{00}^{(1)}(C,\zeta) + iR_{00}^{(2)}(C,\zeta)]\,S_{00}^{(1)}(C,\eta)\,.$$

The object is defined by $\zeta = \zeta_0$, a constant. The product ζf is the equivalent to the radius of a sphere, f being the semi-interfocal distance. R is the equivalent of a radial function with $\zeta f \to r$ at long range. S defines the variation from the central equatorial plane of the spheroid out to its pointed tips. The wavelength is present through $C = \kappa f$. The potential along the spheroid's surface is real and given by $S_{00}^{(1)}(C,\eta)$, so the amplitude factor A is $1/R_{00}^{(3)}(C,\zeta_0)$. All this is explained at length in Appendix 4.

The normal displacement[12] is given by Eq A4.9 in Appendix 4. It is

$$\nabla\phi \;\cdot \mathbf{n} \;=\; -\,\frac{1}{f}\sqrt{\frac{\zeta^2-1}{\zeta^2-\eta^2}}\;\frac{\partial\phi}{\partial\zeta}\,\mathbf{e}_\zeta\,. \tag{42}$$

The minus sign is because $\mathbf{n}$ points into the surface, as in Figure 19. This is evaluated at ζ_0 and together with ϕ_0 provides all the necessary input to the computer program. In the program the radial derivative $R_{00}^{(3)\prime}(C,\zeta)$ and the angular function $S_{00}^{(1)}(C,\eta)$ have been input as high degree polynomials fitted to sets of exact values using `SpheroidalS1Prime`$(0,0,C,\zeta_0)$, and `SpheroidalPS`$(0,0,C,\eta)$ from Mathematica.

Checks can be made on the output because the program calculates numerical values for ϕ and its derivatives with respect to Cartesian axes. The displacement at (ζ_0,η) can be found from the inverse formulae in Eq A4.4 of §16.2

$$\zeta \;=\; \frac{1}{2f}[F_+ + F_-], \qquad \eta \;=\; \frac{1}{2f}[F_+ - F_-]$$

$$\text{where} \quad F_+ \;=\; \sqrt{x^2+y^2+(z+f)^2} \quad \text{and} \quad F_- \;=\; \sqrt{x^2+y^2+(z-f)^2}\,.$$

Then

$$\frac{\partial\zeta}{\partial x} \;=\frac{x}{2f}\left[\frac{1}{F_+}+\frac{1}{F_-}\right], \qquad \frac{\partial\zeta}{\partial y} \;=\frac{y}{2f}\left[\frac{1}{F_+}+\frac{1}{F_-}\right], \qquad \frac{\partial\zeta}{\partial z} \;=\frac{1}{2f}\left[\frac{z+f}{F_+} \;+\; \frac{z-f}{F_-}\right]. \tag{43}$$

[12] The total displacement includes a term in $\frac{\partial\phi}{\partial\eta}$ which is $-\frac{1}{f}\sqrt{\frac{1-\eta^2}{\zeta^2-\eta^2}}\;\frac{\partial\phi}{\partial\eta}\,\mathbf{e}_\eta\,.$

The required ζ derivative is evaluated from the reciprocals of these as

$$\frac{\partial\phi}{\partial\zeta} = \frac{\partial\phi}{\partial x}\frac{dx}{d\zeta} + \frac{\partial\phi}{\partial y}\frac{dy}{d\zeta} + \frac{\partial\phi}{\partial z}\frac{dz}{d\zeta}.$$

Similar analysis applies to the terms in η.

Table 3 below compares equivalent terms and factors for sphere and spheroid, using the primary Kirchhoff equation Eq 21b in the form

$$\phi(Q) = \frac{-1}{4\pi}\sum_{triangles}\left[\phi_0(x)\left(i\kappa-\frac{1}{r}\right)\mathbf{e_r}\cdot\mathbf{n} - \nabla\phi(x)\cdot\mathbf{n}\Big|_0\right]\frac{e^{i\kappa r}}{r}\iint_{triangle} e^{i\kappa\epsilon}\,dS$$

where x denotes the centroid of the triangular element and ϵ is the phase difference over the one triangle as evaluated in Appendix 1. I should point out that the comparison in Table 3 is not exact because the asymptotic form of the radial function is $R_{00}^{(3)} \to -ie^{i\kappa r}/(\kappa r)$, so it differs both in the κ in the denominator and in the phase shift. I have left the spheroidal terms as they are usually written.

parameter	sphere	spheroid
normalised distance	κa	$C\zeta = \kappa f\zeta$
semi-axes	radius, a	$a = f\zeta_0,\ b = f\sqrt{\zeta_0^2-1}$
potential, ϕ	$A\frac{e^{i\kappa r}}{r}$	$A\,R_{00}^{(3)}(C,\zeta)\,S_{00}^{(1)}(C,\eta)$
on surface, ϕ_0	1	$S_{00}(C,\eta)$
amplitude coefficient, A	$ae^{-i\kappa a}$	$\frac{1}{R_{00}^{(3)}(C,\zeta_0)}$
surface displacement, $-\nabla\phi\cdot\mathbf{n}\Big\|_0$	$-\frac{1}{a}+i\kappa$	$\frac{A}{f}\sqrt{\frac{\zeta_0^2-1}{\zeta_0^2-\eta^2}}\,S_{00}^{(1)}(C,\eta)\,\frac{dR_{00}^{(3)}(C,\zeta)}{d\zeta}\Big\|_{\zeta_0}$

Table 3: Comparison of parameters in Kirchhoff formulae for sphere and prolate spheroid in breathing mode of oscillation.

The formula in the program must be evaluated with real and imaginary components. This has been done using the following subsidiary notation:

$$\phi(Q) = \sum_{triangles}\frac{-1}{4\pi r}S_{00}\left[\left(i\kappa-\frac{1}{r}\right)\cos\beta + H_R + iH_I\right](c+is)(T_R+iT_I). \qquad (44a)$$

$$H_R + iH_I = \frac{1}{fR_{00}^{(3)}(\zeta_0)}\sqrt{\frac{\zeta_0^2-1}{\zeta_0^2-\eta^2}}\left[\frac{dR_{00}^{(1)}}{d\zeta}+i\frac{dR_{00}^{(2)}}{d\zeta}\right]_{\zeta_0}, \qquad (44b)$$

$c+is = e^{i\kappa r}$, and T_R+iT_I is the result of integrating $e^{i\kappa\epsilon}$ over the triangular element. The complex products for each element multiply as follows

$$\frac{+S_{00}}{4\pi r}\left[\left(\frac{\cos\beta}{r}-H_R\right)-i(\kappa\cos\beta+H_I)\right]\left[(cT_R-sT_I)+i(cT_I+sT_R)\right]$$

Call the above

$$\frac{S_{00}}{4\pi r}\,[F_R - iF_I][G_R + iG_I]$$

by matching terms. The final formula as entered in the program is

$$\phi(Q) \;=\; \sum_{triangles} \frac{+S_{00}}{4\pi r}\,[(F_R G_R + F_I G_I) \;+\; i\,(F_R G_I - F_I G_R)]\,. \tag{44c}$$

The mesh for the spheroid's surface has been obtained simply by scaling the 512 or 1024 element quasi-sphere in Figure 41 in x, y and z. At $\lambda = 1 \cdot 4$ the near-field length of a single triangular element is about $0 \cdot 06$ units on the 512-element spheroid, and about half this on the 1024-element one. This means that field values at distances less than these from the object's surface cannot be trusted. For the calculations reported here I used the 1024 element mesh. The field of points Q had values from ζ_0 to 30 and η values at 0, $0 \cdot 1$ to $0 \cdot 8$, then $0 \cdot 88$, $0 \cdot 95$, $0 \cdot 985$ and 1. Figure 50 shows an example of a field net, with $\zeta_0 = 1 \cdot 2$ as used in Example 4. This is the inner part of a quadrant matrix which extends to $\zeta = 30$ in widening steps. The ellipse which defines the spheroid $\zeta_0 = 1 \cdot 2$ is edged in red.

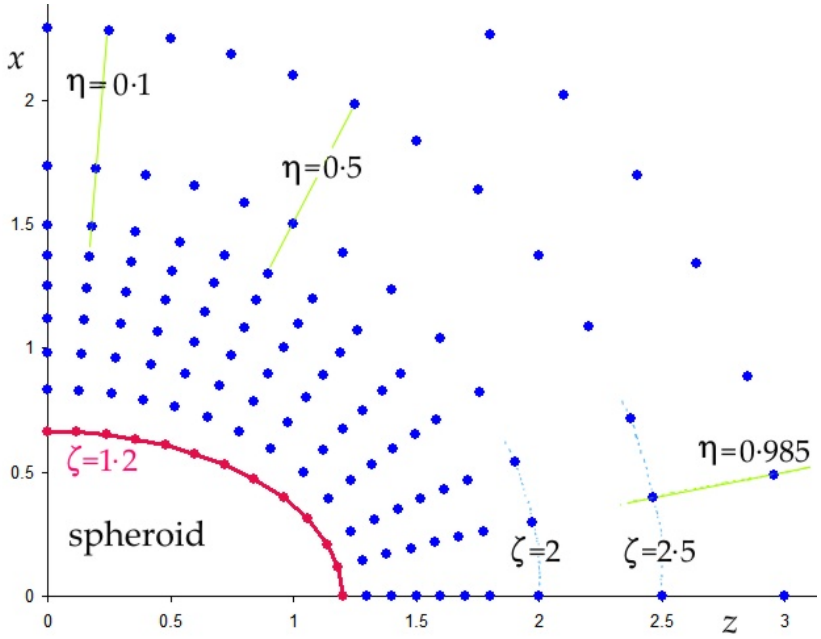

Figure 50: Inner part of array of points Q in the $x-z$ plane at which field is calculated. The surface of spheroid with $\zeta_0 = 1 \cdot 2$ is highlighted in red.

Example 1 : As a first numerical case I have taken a prolate spheroid which is only a tiny distortion of a sphere so that parallel operations with the undeformed sphere are clear. The aspect ratio is less than 1% different from unity, and the volume product ab^2 of the spheroid to be 1.

It is striking how quickly and severely the angular function $S_{00}(C, \eta)$ distorts the potential and displacement around the spheroid as frequency increases. The key parameter is $C = \kappa f$. Figure 51 plots the prolate and oblate angular functions against a measure of the distance from the rotation axis for $C = 1$ to 5. At $C = 0$ the function is a horizontal line at 1. Notice how rapidly it becomes a bell-shaped curve as C increases. Take $\zeta_0 = 8$ and $ab^2 = 1$. Then $f = \sqrt{a^2 - b^2} = 0 \cdot 12566 \approx 1/8$ and $a/b = 1 \cdot 008$, barely different from 1. If $k = 16$, $\lambda = 0 \cdot 39$ and C is only 2. Yet even at this quite long

wavelength and very slight eccentricity there is a factor of 2 in $\phi(\eta)$ from the z (rotation) axis to the equatorial plane, as $S_{00}(2,\eta)$ drops from $1\cdot18$ at the equatorial plane $z=0$ to $0\cdot63$ at the poles. The higher C curves show how motion becomes concentrated into the equatorial plane. In other words, high frequencies search out the slightest distortions from a perfect sphere. I find this quite surprising. It implies that modelling a round object as a vibrating sphere could be misleading. Furthermore, because of the way the wave equation separates in spheroidal co-ordinates, the same angular function controls the distribution of ϕ and displacement ξ at all ranges. This is quite different from the flat piston cases in §7 where there is a Fourier transform relation between surface and far field.

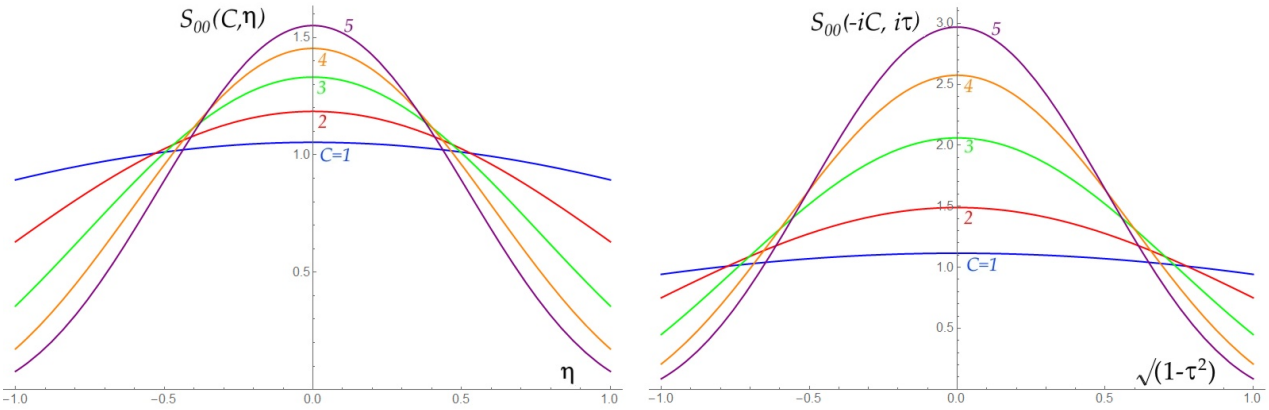

Figure 51: Angular wave functions for prolate ($S_{00}^{(1)}(C,\eta)$, left) and oblate ($S_{00}^{(1)}(-iC,i\tau)$, right) spheroids for C from 1 to 5.

The computed results for this near-sphere are satisfactory. Two examples are plotted in Figure 52. In each the exact values from Mathematica are the solid lines and the values from my program are the dots. The left panel shows the real and imaginary parts of ϕ close to the spheroid, about 1/4 unit or $0\cdot6\lambda$ above its surface. The imaginary part is slightly too small. The right panel is at $\zeta=30\equiv r\approx3\cdot77$ and plots the absolute value in green. The computed values all fall almost on the exact line. The brown line is the value for the perfect sphere. At this longer range the co-ordinate η is interpreted better as the cosine of the angle from the polar (rotation, z) axis. Accordingly, the horizontal co-ordinate in the right panel is $\cos^{-1}\eta$. You will observe that the apparent discontinuity in the gradient of $S_{00}(C,\eta)$ with η at $\eta=1$ disappears when converted to polar angle – the curve is horizontal at both 0 and π radians.

Example 2 : For this example I have increased the aspect ratio slightly so that now it is 10% different from unity, with the volume-product ab^2 still 1. The parameters are

$a/b=1\cdot1$, $a=1\cdot0656$, $b=0\cdot9687$, $f=0\cdot444$, $\zeta=2\cdot40$,
$C=\kappa f=2$, $\kappa=4\cdot5044$, $\lambda=1\cdot3949$.

It is pleasing to report that the program also works satisfactorily in this case. The graphs in Figure 53 give sample results, in each case comparing the program's values, plotted as points, with the theoretical exact solutions, the solid curves. The two panels show the real and imaginary parts of ϕ at $\zeta=2\cdot6$ and 3 respectively. At $\zeta=3$ the error in magnitude $|\phi|$ has fallen to 1%. As expected, the largest differences between theory and computation are very close to the surface where the $1/r$ factor grows large. Thus at $\zeta=2\cdot5$, just above the surface with $\zeta_0=2\cdot4$, the error is up to 20%. At $\zeta=30$, about 12 units from the object's surface, the error is less than $\frac{1}{2}$%. Perhaps no one should be surprised that the program agrees with the theory quite well since essentially it is only implementing

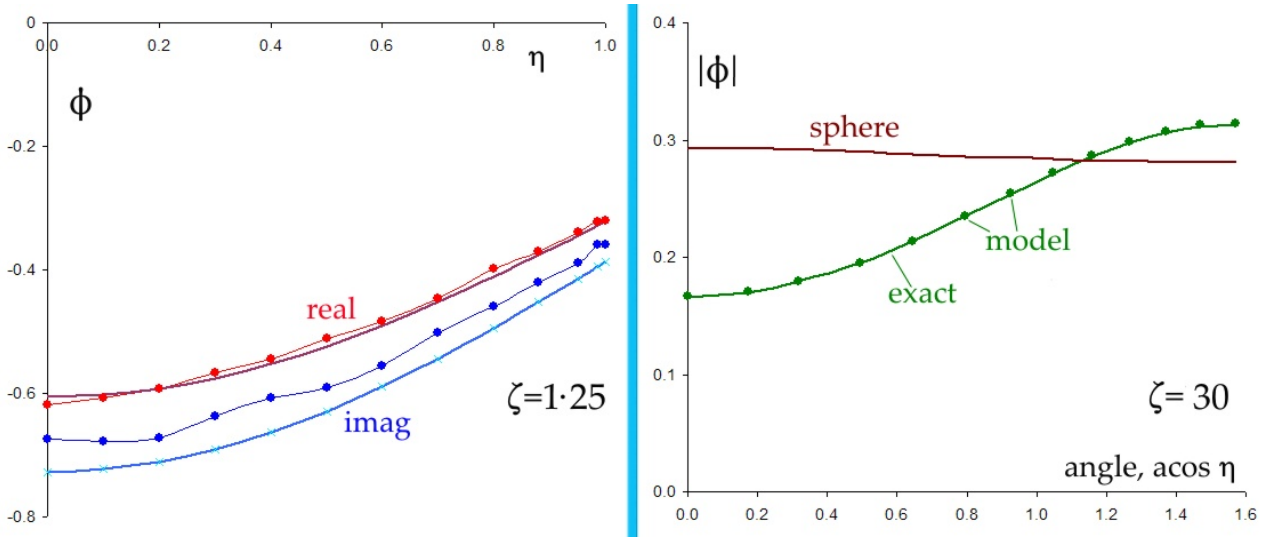

Figure 52: Example 1. Computed potential for almost spherical spheroid, $\zeta_0 = 8$. Left : real and imag parts at close range ($\zeta = 1 \cdot 25$). Right: magnitude at mid-range ($r \approx 3 \cdot 8$). $\kappa = 15 \cdot 9$.

Green's theorem using exact input. That said, the program would be of little use if it did not agree with theory under such favourable conditions.

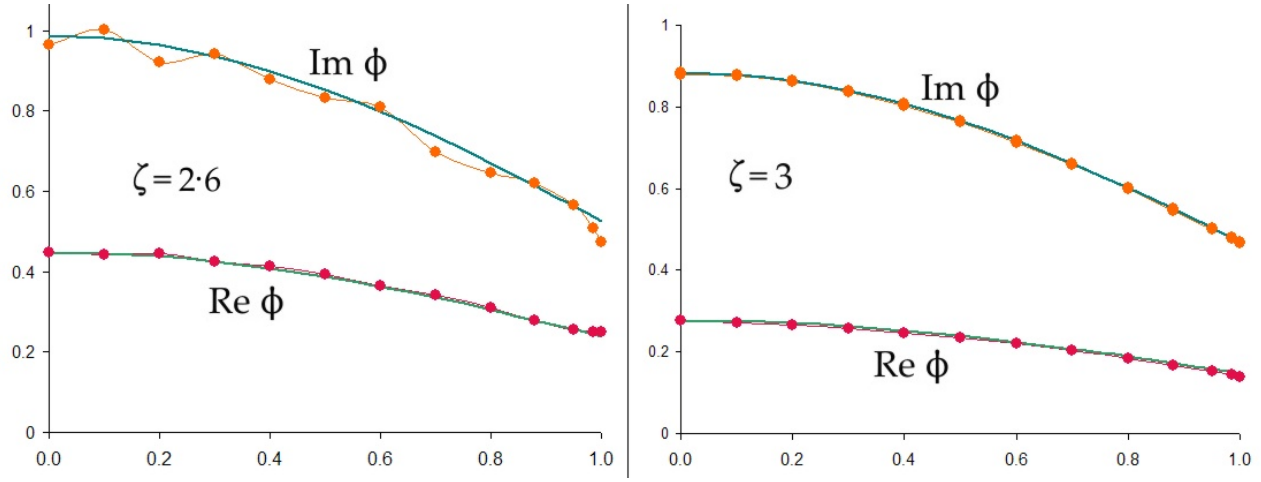

Figure 53: Example 2. Comparison of computed values with exact ones at $\zeta = 2 \cdot 6$ and 3 for $\zeta_0 = 2 \cdot 4$, $\lambda = 1 \cdot 4$.

Example 3 : This is an oblate spheroid at $C = 4$. The aspect ratio is again only 10% different from unity and has been chosen as the oblate equivalent of Example 2. Parameters are

$$b/a = 1 \cdot 1,\ a = 0 \cdot 9393,\ b = 1 \cdot 032,\ f = 0 \cdot 427,\ \sigma_0 = 2 \cdot 20,$$
$$C = \kappa f = 4,\ \kappa = 9 \cdot 37,\ \lambda = 0 \cdot 67.$$

Appendix 4, §16.3 explains the changes to the formulae necessary for oblate spheroids. Basically $R_{00}^{(3)}(C,\zeta)\, S_{00}^{(1)}(C,\eta)$ in the prolate case is replaced by $R_{00}^{(3)}(-iC, i\sigma)\, S_{00}^{(1)}(-iC,\tau)$. Once the exact potential and displacement on the surface have been calculated using these alternative spheroidal functions and input to the program, the calculation proceeds as before. Figure 54 shows sample output at two ranges: left panel at $\sigma = 2 \cdot 4$ close to the spheroid, and right panel at $\sigma = 4$, about one wavelength above the surface. The left panel shows computed real and imaginary parts at dots against the exact values as solid lines. The right panel compared magnitudes $|\phi|$. Note that the

horizontal axis is $\sqrt{1-\tau^2}$, this being the measure of distance radially out from the rotation axis. The values close to the surface are, as expected, the worst, and clearly deviate most near the centre (pole) and at the rim (equator) of the object. At a range of 12 radii the error over the central dome around the z axis, where the vibration has largest amplitude, is less than 5%. As noted above, I obtained similarly acceptable results with the prolate spheroid with $a/b = 1 \cdot 1$ at $C = 4$. Overall the results are again encouraging.

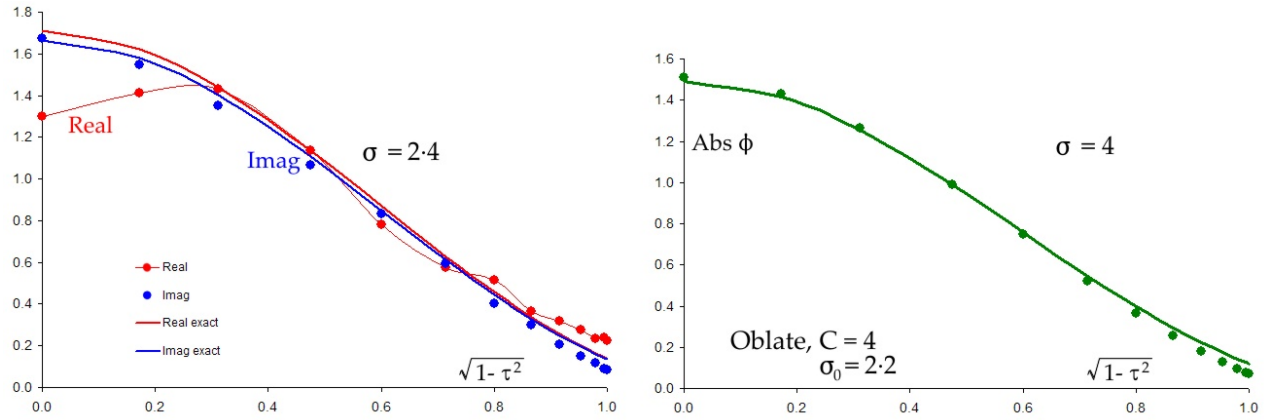

Figure 54: Example 3: Comparison of exact and computed potential for oblate spheroid $\sigma_0 = 2 \cdot 2$ at $C = 4$.

Example 4 : This is a significantly more elongated prolate spheroid than Example 2, examined at two frequencies. Parameters are[13]

$$a/b = 1 \cdot 81,\ a = 1 \cdot 2,\ b = 0 \cdot 663,\ f = 1,\ \zeta_0 = 1 \cdot 2,$$

Frequency 1 : $C = \kappa f = 8,\ \kappa = 8,\ \lambda = 0 \cdot 785.$

Frequency 2 : $C = \kappa f = 17,\ \kappa = 17,\ \lambda = 0 \cdot 37.$

This spheroid has a smaller volume than those studied above. It is pleasing to report that the program holds up well here too. As above, the poorest agreement with theory is at the closest range. Figure 55 shows $|\phi|$ versus η at three ranges, the left panel being at only $\zeta = 1 \cdot 25$ which is $0 \cdot 05$ units above the vibrating surface. This is in the nearfield of the individual triangular elements, and dominated by those few closest to Q. Despite this, the agreement is quite good, and it is better still a short distance away. At $\zeta = 30$ the error at $\eta = 0 \cdot 8$ is $0 \cdot 8\%$, and this falls to $0 \cdot 15\%$ at $\eta = 0$ on the z axis where the amplitude of vibration is largest. At the increased frequency of $\kappa = 17$ the fractional errors are larger, $|\phi|$ being $1 \cdot 7\%$ too small at $\zeta = 30$, but in acoustic terms this is not significant. The largest errors are again at short range, and Figure 56 plots the real and imaginary parts of ϕ at two close ranges. The most noticeable error is the oscillation in the real part at $\zeta = 1 \cdot 25$ (left panel), but this has disappeared by $\zeta = 1 \cdot 4$ (right).

There are two further examples of the Kirchhoff-based program in the next subsection, Examples 7 and 8, where they are compared with the restricted dipole Rayleigh-Sommerfeld program. The results with a prolate spheroid are good, but less impressive with the oblate one.

[13] I did examine $C = 21$, but found that the radial spheroidal functions given by Mathematica had a singularity and a series of zeros near $\zeta = 2$. These do not seem genuine so I have contacted Wolfram to report the possible bug.

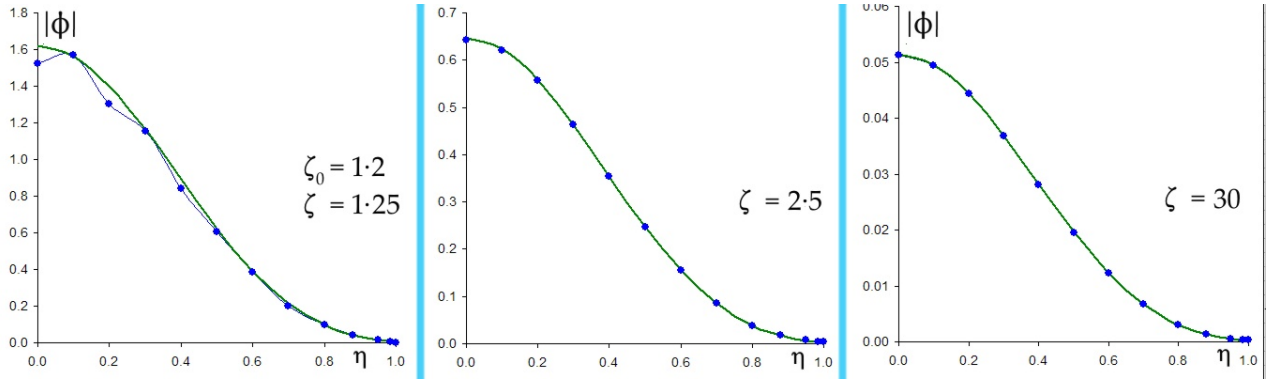

Figure 55: Example 4: $|\phi|$ versus η for prolate spheroid, $\zeta_0 = 1 \cdot 2$ at $\kappa = 8$.

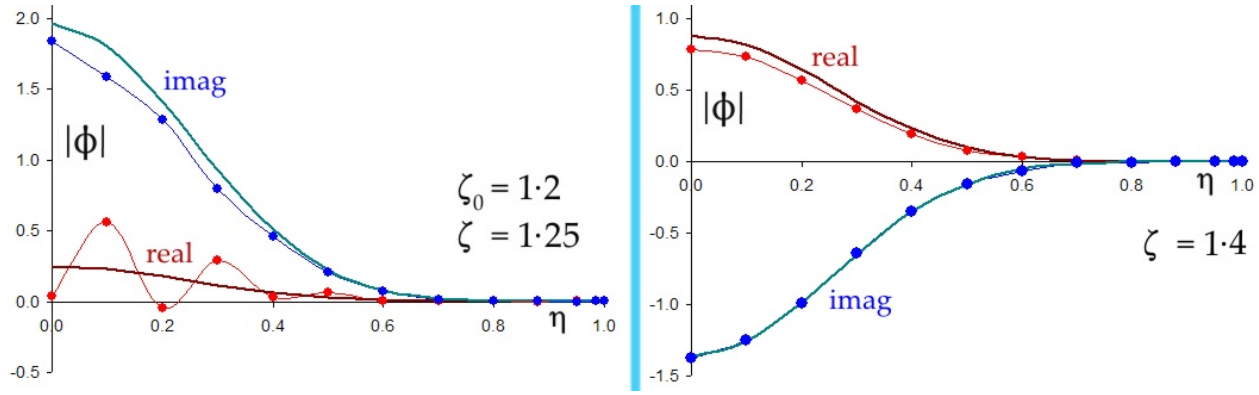

Figure 56: Example 4: Real and imaginary parts of ϕ versus η for prolate spheroid, $\zeta_0 = 1 \cdot 2$ at $\kappa = 17$.

10.3 Restricted dipole Rayleigh formulation applied to spheroids

In §10.1.2 I showed that the Rayleigh-Sommerfeld formulation, when restricted to $\cos\beta > 0$, does give quite good agreement with exact the theoretical solution of Helmholtz's equation, particularly at for $\kappa > 10$. This subsection reports a short study of this method for spheroids.

Example 5 : The parameters are
$a = 1 \cdot 131$, $b = 0 \cdot 940$, $f = 0 \cdot 628$, $\zeta_0 = 1 \cdot 8$, $C = 8$, $\lambda = 0 \cdot 493$.
The results are surprisingly good, as Figure 57 shows. This presents $|\phi|$ at three distances from the spheroid, being $\zeta = 1 \cdot 9$, $2 \cdot 4$ and 30. The green curves as again the exact values as spheroidal functions.

Example 6 : Spurred on by this good agreement, I have modelled the more prolate spheroid of Example 4 above, at the higher frequency. The parameters are

$$a/b = 1 \cdot 809,\ a = 1 \cdot 2,\ b = 0 \cdot 663,\ f = 1 \cdot 0,\ \zeta_0 = 1 \cdot 20,$$
$$C = \kappa f = 17,\ \kappa = 17,\ \lambda = 0 \cdot 37.$$

The program gives convincing results as Figure 58 shows in its six panels at increasing range.

Example 7 : This is a more highly flattened oblate spheroid than Case 3. I have run both the Kirchhoff and restricted Rayleigh versions of the program for this spheroid examined under these conditions:

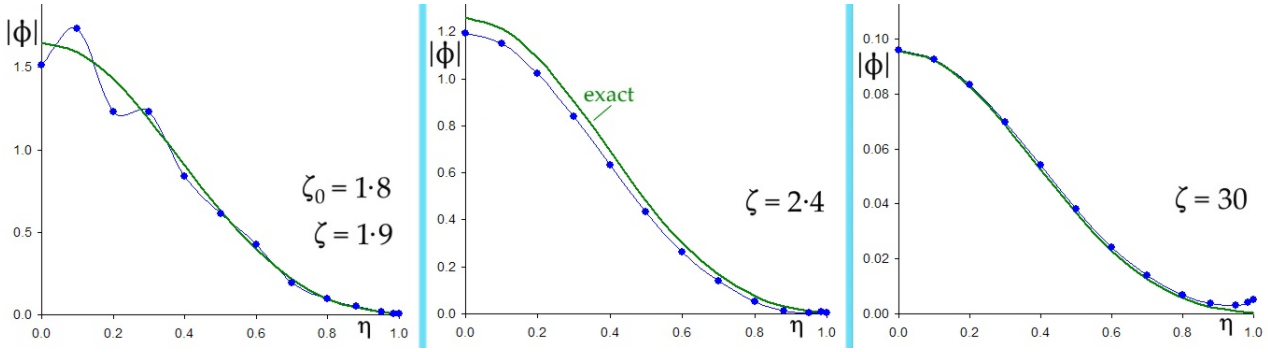

Figure 57: Example 5: Rayleigh calculation with $\cos\beta > 0$ restriction.

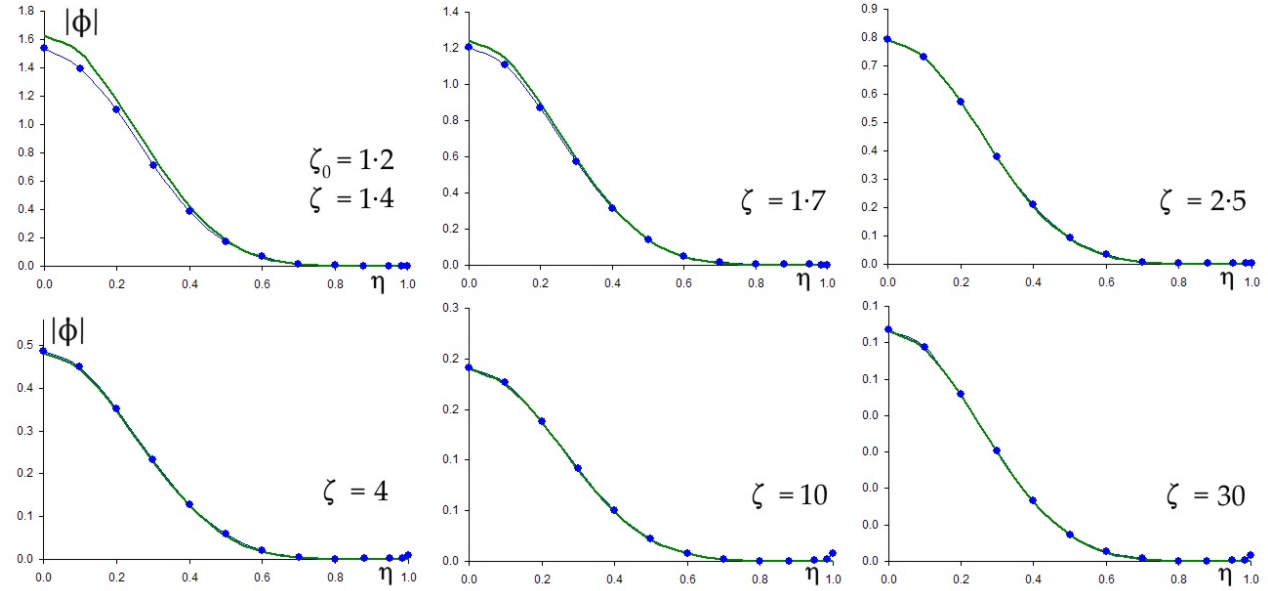

Figure 58: Example 6: Restricted Rayleigh calculation of prolate spheroid $\zeta_0 = 1 \cdot 2$. $|\phi|$ versus η at six ranges. $C = 17$. Green solid lines show exact values in spheroidal wave functions.

$b/a = 2 \cdot 69,\ a = 0 \cdot 4,\ b = 1 \cdot 077,\ f = 1 \cdot 0,\ \sigma_0 = 0 \cdot 4,$
$C = \kappa f = 10,\ \kappa = 10,\ \lambda = 0 \cdot 628.$

I would like to report complete success with this case too, but regrettably that is not so. Figure 59 shows the two model solutions for $|\phi|$ versus angular co-ordinate $\sqrt{\tau^2}$ at four ranges. At close range, $\sigma < 2$, the Kirchhoff (blue) and Rayleigh (red) points lie close to the exact solution as calculated in Mathematica using spheroidal wave functions (green). However, at longer range both the computer models give values which are too large, though they agree fairly well with each other. I checked this with an even more flattened spheroid, with $\sigma_0 = 0 \cdot 26$, $b/a \approx 4$ at $\kappa = 8$ and found the same behaviour. I have no explanation. The next example shows that good agreement is still obtained with a prolate spheroid with high eccentricity, so why not with an oblate one? It remains a mystery to me.

This case does provide a good comparison of the Kirchhoff and restricted Rayleigh in terms of how well the ratio $|\nabla^2\phi/\phi|$ equals κ^2, as required of any correct solution of Helmholtz's equation. The Kirchhoff results are by far the better. $\kappa^2 = 100$, and over the 78 data points the ratio has mean $99 \cdot 7 \pm 1 \cdot 4$, with values in the range from $93 \cdot 5$ to $107 \cdot 2$. The one point at $93 \cdot 5$ was at $\sigma = 1$. In contrast the restricted Rayleigh results do not settle down to being close to 100 until $\sigma \geq 5$, just

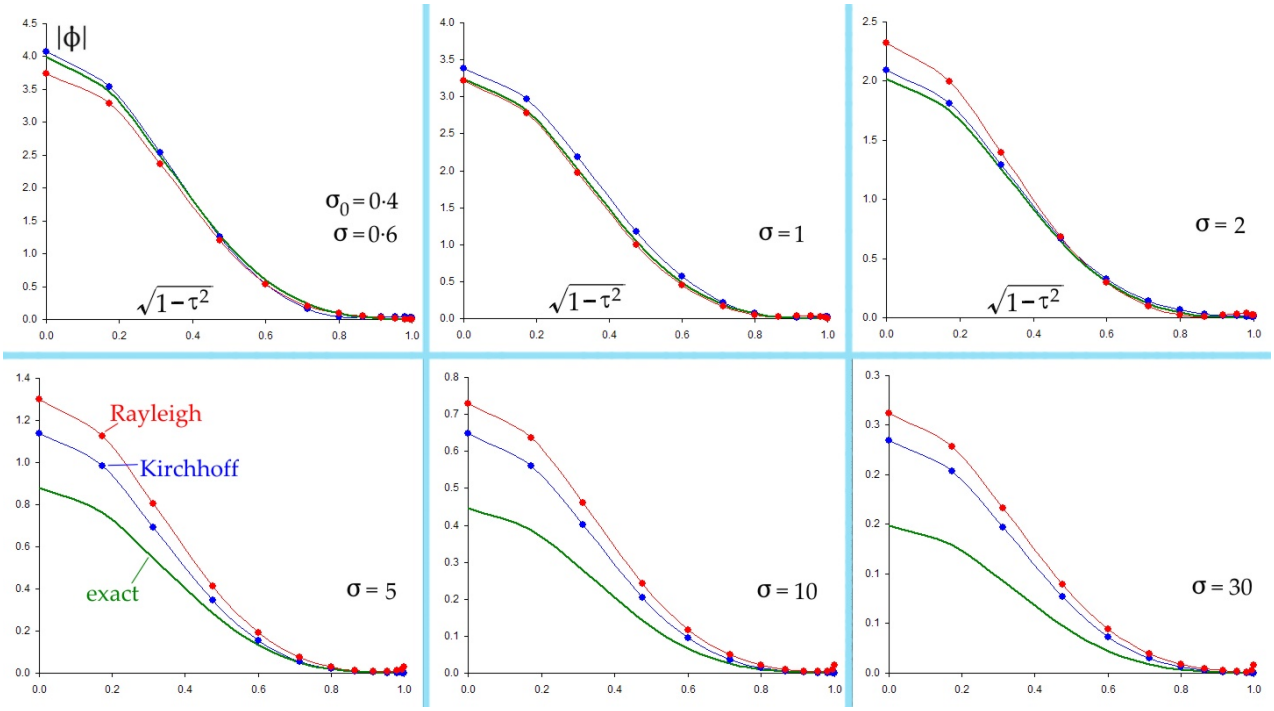

Figure 59: Example7: oblate spheroid, $\sigma_0 = 0{\cdot}4$, modelled by Kirchhoff (blue) and restricted Rayleigh-Sommerfeld (red) programs. Exact spheroidal wave functions in green.

where ϕ values deviate from the green curves in Figure 59. At shorter range the $\nabla^2\phi/\phi$ ratio varies wildly, from 38 to 2970! Thus, although the values of $|\phi|$ agree quite well with the Kirchhoff ones, they do not proclaim themselves to be true solutions of the governing acoustic equation.

Example 8 : This is a more highly elongated prolate spheroid than Example 4. Again I have run both the Kirchhoff and restricted Rayleigh versions of the program for this spheroid examined under these conditions:

$$a/b = 2 \cdot 81,\ a = 1 \cdot 07,\ b = 0 \cdot 381,\ f = 1 \cdot 0,\ \zeta_0 = 1 \cdot 07,$$
$$C = \kappa f = 10,\ \kappa = 10,\ \lambda = 0 \cdot 628.$$

Results for $|\phi|$ at three ranges are shown in Figure 60. The Kirchhoff model agrees almost exactly with Mathematica's spheroidal wave functions, and the restricted Rayleigh results are only about 10% higher, so overall both methods are satisfactory. This good agreement for a highly prolate spheroid makes the disagreement at longer range in the oblate Example 7 even more puzzling.

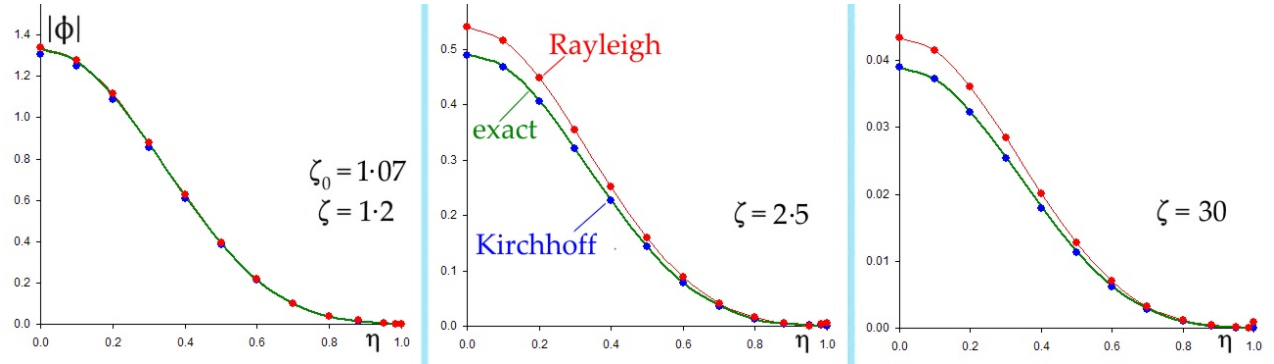

Figure 60: Example 8: $|\phi|$ for highly prolate spheroid, $\zeta_0 = 1 \cdot 07$ at three ranges.

10.4 Conclusions on the validity of the models

In summary, I have shown examples of both the Kirchhoff and restricted dipole Rayleigh-Sommerfeld computer programs being applied to perfect spheres (§10.1) and prolate and oblate spheroids (§10.2) in the $m = l = 0$ breathing mode. It would be fair criticism of these studies that they are overly restricted to this mode, and that more comprehensive comparisons with exact solutions for higher modes are needed. This notwithstanding, on the basis of the reported examples and others for the 00 mode I am satisfied that over a fairly wide range of parameters the Kirchhoff program reliably calculates the potential field $\phi(Q)$ even down to close range, provided it is given *both* the exact potential and its derivative on the surface. This program is essentially implementing the integration in Green's theorem on this exact input, so good agreement with the exact theory for spheroids is welcome though hardly surprising. The only failure to agree with the exact solution of Helmholtz's equation is at longer range with the flattened oblate spheroid of Example 7; for this I have no explanation. Of course, in any practical case exact values of ϕ and its derivative would not be known over the surface, but only one of these. Its practical use is therefore limited.

The Rayleigh-Sommerfeld version, restricted to the obliquity factor $\cos\beta > 0$, has no theoretical basis when applied to any vibrating surface which is not a plane. Despite this, it does appeal to physical intuition that only those parts of the surface which can be 'seen' from by the listener at Q, and hence send rays out to Q, should contribute to the field there. At high frequency, this is what ray theory would claim. My tests show that it performs fairly well and can be used with moderate confidence to give a quick approximation. This might be good enough for some applications, bearing in mind that 2 dB (about ±20%) is about the smallest change in loudness that the human ear will notice in everyday situations. Should greater accuracy and/or greater confidence be necessary, some numerical scheme for converging on the exact solution will be needed. The challenge is to have an algorithm and computer program which gives close to the exact answer when *only one* of ϕ_0 or its normal derivative on the surface is given. Feasible approximations are considered in the next section.

11 Radiation from general convex objects

In this final section I provide some evidence on the actual displacement of vibrating elastic spheroids, then discuss some of the methods that have been developed to calculate the sound radiated from a vibrating body of fairly arbitrary shape, without a baffle. Most of these cast Helmholtz's equation as an integral equation and use numerical schemes to solve for ϕ and its derivative at the vibrating surface. The field at an external point is then found using Green's theorem, much as the Kirchhoff version of my computer program does. These integral equation methods have given rise to discrete boundary element methods, a two dimensional counterpart version of finite elements in structural analysis. These are now favoured for acoustic radiation problems.

Green's theorem says nothing about the shape of the surface bounding the enclosed volume Ω in Figure 19a so in principle it could be a concave section of vibrating surface. In principle, therefore, the Kirchhoff formulation should apply equally to concave radiators, provide the exact surface potential and displacement are both known – which in general will not be the case. In practice it would probably be much more difficult to estimate $\nabla\phi_0$ given ϕ_0 (or *vice versa*) for a concave shape than from a convex one, since sound will be trapped by multiple reflections in the hollow. Since violins do not have concave spaces, I am content to leave aside concave objects. That still leaves the problem of estimating $\nabla\phi_0$ from a given ϕ_0 for a convex surface, assuming we continue with the Kirchhoff formulation and its implementation in a computer program. The later subsections of this section discuss two conjectures for linking $\nabla\phi_0$ with ϕ_0 at each position on the surface.

11.1 Vibrational modes of elastic spheroids

I include this section in order to have a clear view of the distinction between the eigenmodes in air which are solutions of Helmholtz's equation for a travelling sound wave, and the normal vibrational modes of the elastic body which creates the sound. The solutions of Helmholtz's equation with the lowest indices and simplest shapes are not generally the lowest frequency modes of an actual object. In §9 and 10 I deal extensively with the breathing mode of a sphere or spheroid in which all parts of the surface move radially in or out in phase. This present section provides evidence that this mode can indeed be excited in a hollow but thick-walled elastic ball. I go on to illustrate the lowest frequency modes of an elastic prolate and oblate spheroid.

Using the Mecway finite element program (a development from the established LISA 8) I have modelled a thick-walled sphere of isotropic elastic material and determined the first fifty normal modes of oscillation. Here are a few details. (Spheroid geometry is explained in Appendix 4, §16.) The starting point of modelling any spheroid was a reference sphere of 1 m radius represented by a surface mesh of 512 triangles, as shown in Figure 41. This was scaled in the x, y and z directions to give the required aspect ratio. The z axis was the axis of rotational symmetry for both prolate and oblate spheroids. The scale factors were such that the volume-like product ab^2 was 1 in all cases, a being the semi-axis along z and b the semi-axis along both x and y. Once the surface mesh was scaled, it was extruded inwards, normal to the local surface, to a thickness of 100 mm in 4 layers of wedge-15 finite elements, producing 2048 elements in all. Young's modulus was set to 1 GPa, Poisson's ratio to 0 and the density to 1000 kg/m^3. By this scheme I have tried to make the set of spheroids as uniform and comparable as possible.

For the sphere the breathing mode is mode number 41, at 237 Hz. With changing aspect ratio it could be recognised up to about $a = 1 \cdot 3$, $b = 0 \cdot 88$, but by this stage the deformed shape was no longer a spheroid. Figures 61 and 62 illustrates this. The central panel of Figure 61 shows

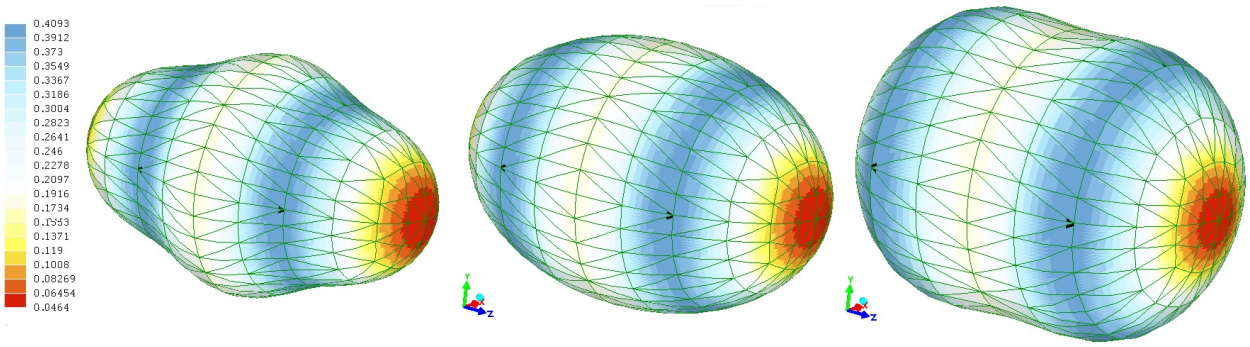

Figure 61: Breathing mode of prolate spheroid, $a = 1 \cdot 3$, $b = 0 \cdot 877$, aspect ratio $1 \cdot 48$, at the extremes of its cycle. $230 \cdot 5$ Hz. Deformation highly exaggerated.

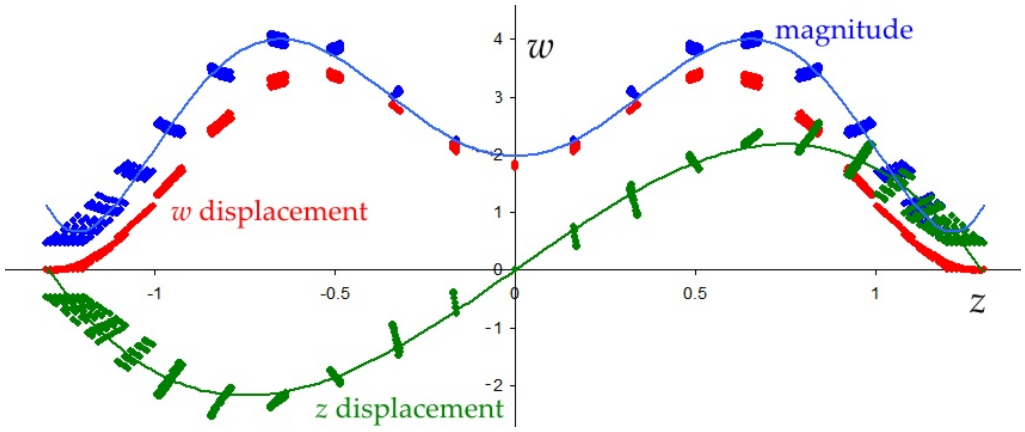

Figure 62: The radial (w) and axial (z) displacements of the prolate spheroid in Figure 61, and the magnitude of displacement, plotted along its length. $a = 1 \cdot 3$ m, $b = 0 \cdot 877$ m.

the undeformed spheroid and the two either side show the extremes of its oscillatory cycle. The vector displacement has been added to the static form with a large scale factor to exaggerate the deformation. The contour scale shows displacement magnitude, with red as least, blue as most. Clearly the object deforms most at about quarter way from each tip. There is least displacement at the pointed ends (Positions A in Appendix 4), and the relative displacement here decreases as the object become more stretched. The points plotted in Figure 62 are for every node in the FEA mesh. All three curves are on the same scale.

Position A also shows the smallest displacement in oblate spheroids. In the breathing mode the rim (Positions B in Appendix 5) moves more that the flattened faces in the $\pm z$ directions. Details of this variation with distance w are shown for two oblate spheroids in Figure 63, which plots the displacement magnitude (on an arbitrary scale) against the radial distance from the z axis for all the nodes of the FEA mesh. (The spheroid on the right is the only one reported here for which $ab^2 = 0 \cdot 676 \neq 1$.)

I summarise the minimum-to-maximum displacement ratio in Figure 64. This plots the ratio of the least to greatest numbers in the contour legend in Figure 61 and its equivalents as a function of aspect ratio a/b. When $a/b \approx 1$, the max and min occur along the $x - y$ direction and z direction respectively, but for the more stretched prolate spheroids, the maximum moves to near $a/2$ as shown in Figure 62.

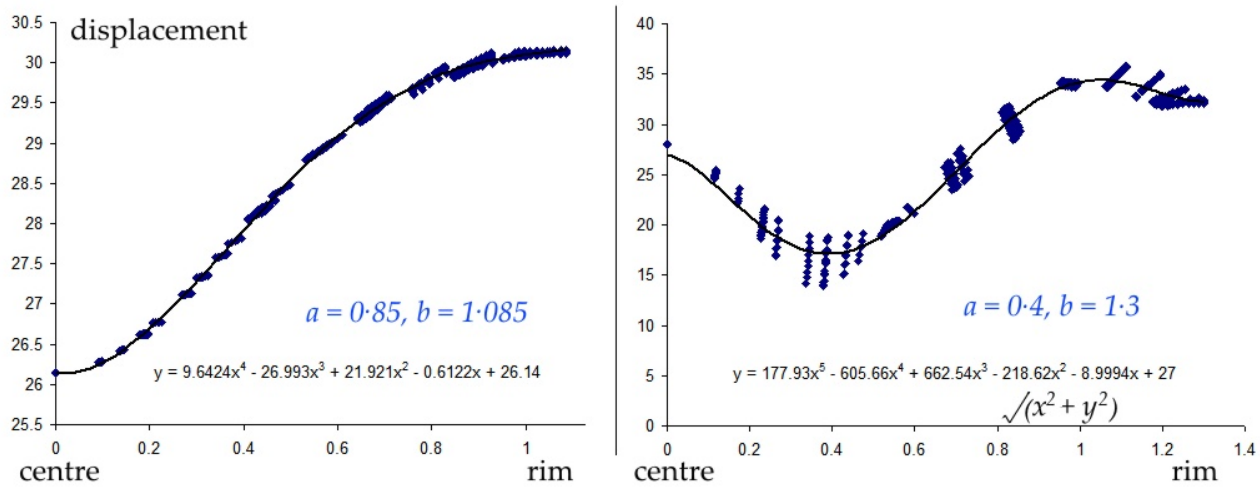

Figure 63: Displacement amplitude in the breathing mode over two oblate spheroids, plotted against radial distance in w plane. Aspect ratios are $0 \cdot 78$ (left), $0 \cdot 31$ (right).

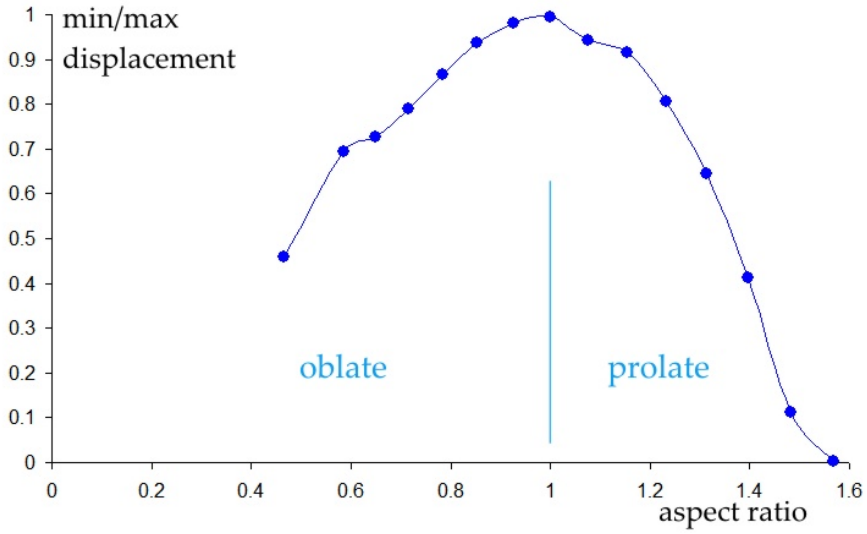

Figure 64: Ratio of min to max displacement of points on spheroid as function of aspect ratio. For all spheroids here $ab^2 = 1$ and vibrate in the breathing mode.

The frequency of the breathing mode hardly varies with aspect ratio across the range $0 \cdot 5$ to $1 \cdot 5$ as represented in Figure 64; all values are between 236 and 212 Hz. This mode occurs at quite a high frequency because it involves the shell wall at each point stretching in circumferential directions. This requires a change in volume and hence more elastic energy than if deformation were by flexing in a radial (transverse) direction. The lowest frequency normal modes are therefore the ones which involve shear distortion without volume change. I illustrate the lowest mode of a prolate spheroid in Figure 65 (119 Hz), and of an oblate one in Figure 66 (109 Hz). The extremes of deformation over each cycle are shown highly exaggerated. The prolate spheroid moves as if squeezed alternately in the x then the y directions while there is little deformation along the long axis. The oblate one behaves like a two-sided drum, its flatter faces moving in and out along z. The black loops pick out a region of almost zero motion about which the faces and rim seem to hinge. In a previous article on *www.mathstudio.co.uk* I examined a vibrating cuboidal box and referred to this mode as the

breathing mode because, for a very squashed oblate, motion of the rim is imperceptible compared with the exhale-inhale motion of the large faces.

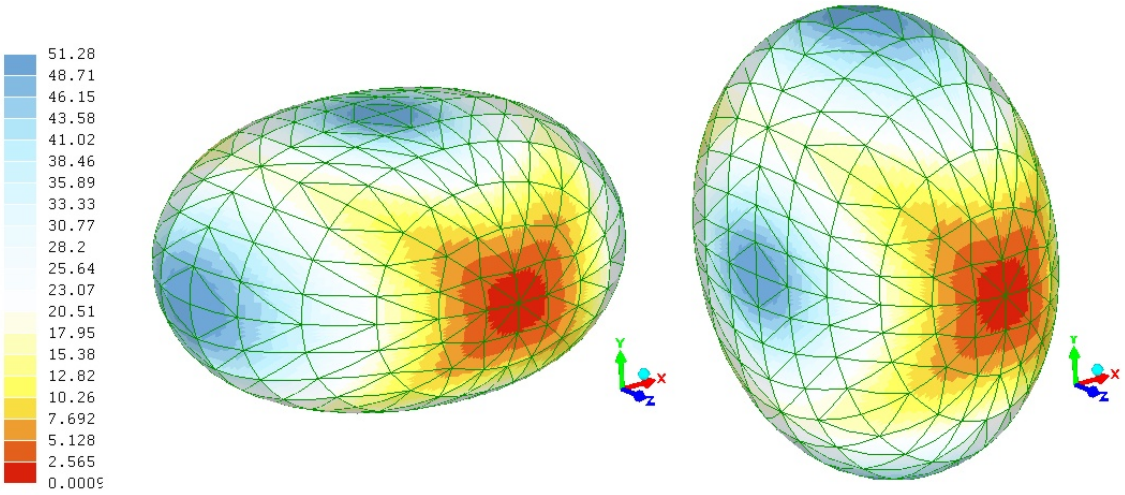

Figure 65: Lowest natural mode of prolate ellipsoid with aspect ratio $1 \cdot 15$ shown at its two extremes of oscillation. 119 Hz.

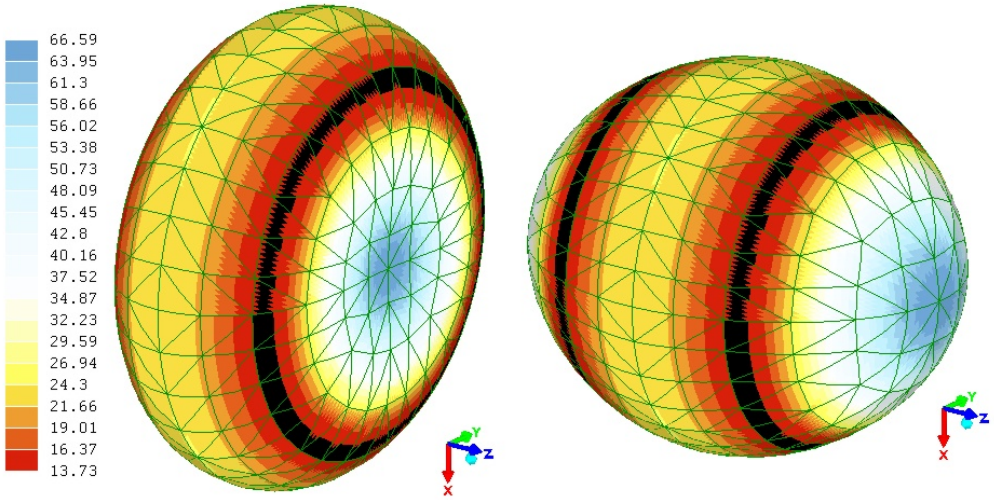

Figure 66: Lowest mode (109 Hz) of oblate spheroid with aspect ratio $0 \cdot 78$ at extremes of oscillation.

11.2 Boundary integral equation methods

As we have seen throughout this article, the dipole Rayleigh-Sommerfeld formula Eq 22a gives the field $\phi(Q)$ at a point exterior to the vibrating object in terms of an integral of $\phi(\mathbf{s})$ over all points $\mathbf{s}$ on the surface of the object. This is called a Dirichlet boundary condition since ϕ is specified but the displacement given by its derivative is unknown. The alternative monopole Rayleigh formula, Ea 22b, satisfies the so-called the von Neumann boundary condition in hwihc the normal derivative is given. §7.2 on the circular piston has already demonstrated calculation of the field very close to the

object, and we now picture Q actually moving into the surface itself. The relation now looks like[14]

$$\phi_0(s) \;= - \iint_S \phi_0(s') \left(i\kappa - \frac{1}{r} \right) \mathbf{e_r} \cdot \mathbf{n} \; \frac{e^{i\kappa r}}{r} \, dS \, .$$

where s, s' are general points on the surface S. This is an instance of an integral equation since the unknown function $\phi_0(s)$ is under the integral sign. The dimension has been reduced from an infinite 3D problem to a 2D problem over the finite boundary, which hopefully should make its solution simpler. This is an example of a Fredholm integral equation of the second kind, named after the Swedish mathematician who pioneered their analysis. In Fredholm-type integral equations the integration is over a fixed region. These are known to be fairly well behaved and have unique solutions subject to a few provisos. In Appendix 6 I give a simple introduction to integral equations by way of a 1D example, showing how a differential equation and its boundary conditions can together be recast as an integral equation.

Integral equations of the type above have been studied for many decades with a view to developing reliable methods for determining whether they have a unique solution and, if so, how to determine that solution either analytically or numerically. As noted above, boundary conditions of the Neumann type are modelled by having a layer of monopoles in the boundary, and those of the Dirichlet type by having a layer of dipoles, and the problem is to find the amplitude distribution of these virtual sources over the surface. A good discussion of the 'exterior radiation problem' is by Fritz Ursell of Manchester University whom I had the pleasure of meeting on several occasions (Math Proc Camb Phil Soc, Vol 74-1, p117-125, 1973). He points out that solving for the field external to a closed vibrating body under Neumann boundary conditions cannot be done without having regard to the field produced inside the body, assumed hollow, under Dirichlet boundary conditions. There are certain eigenvalues of the interior Dirichlet problem (corresponding to standing waves in the interior) at which the exterior problem does not have a unique solution. In the words of one group of authors (Bartolozzi et al. Proc 8th Int Conf Structural Dynamics, 2011, p3091-3098) "The exterior response is polluted by fictitious eigenfrequencies at the corresponding internal resonances". These effects are not physically present; rather they are strange and spurious mathematical artifacts attending the reduction from 3 to 2 dimensions. Ursell shows how this problem arises and how it can be overcome by letting the gas or other fluid inside the body become absorbing of sound, so that the resonances at these eigenvalues are damped out. Another important analysis of much the same issue is by Burton and Miller of the UK National Physical laboratory (Proc Roy Soc London Vol A232, 1971, p201-210). Appendix 6 includes an example of non-uniqueness in a 1D integral equation.

Much of the development of a practical, versatile compute code to find numerical solutions has been carried out in the USA, for naval purposes, from about 1960. A paper by Harry Schenck of the US Naval Undersea Warfare Center (J Acoustic Soc Am. Vol 44-1, p41-58, 1968) also explains the non-uniqueness which attends solutions at frequencies corresponding to resonances within the cavity of the object, assumed hollow, in accord with the conclusions of Ursell and Burton & Miller. Schenck went on to propose an approach which overcomes the lack of uniqueness by combining the external solution with an internal solution at a set of supplementary points chosen within the body, separated from its inner wall. These additional points constrain the surface pressure, preventing the presence of indeterminate wayward spurious functions. Schenck called the approach the Combined Helmholtz Integral Equation Formulation or CHIEF. The integral equation is reduced to a set of simultaneous linear equation, and the supplementary interior points add more equations than unknowns, so in CHIEF the over-determined linear system is solved in a least-squares sense. CHIEF has been validated and developed into a full computer code for Fortran, MATLAB and other platforms by staff

[14] The factor of $1/2\pi$ becomes replaced by 1 in the process of shrinking the bubble around Q to a disc.

at US Naval Research. For more information at CHIEF see Seybert and Rengarajan (J.A.S.A Vol 81 No 5, 1987, p 1299-1306) and the thesis by Robert Drake, 2003, US Naval PostGrad School for details, now on the internet. Considerable analysis subsequently has gone into the optimum way of choosing the supplementary inner points (see Bartolozzi et al, *loc. cit*). CHIEF seems still to enjoy considerable support for practical applications.

A boundary element is a two-dimensional patch of surface, often a triangle or quadrilateral, which satisfies the boundary value problem. Boundary elements were being developed for Laplace's equation and the heat conduction/diffusion equation, so it was natural to develop them for Helmholtz's equation also. Thus the Boundary Element Method (BEM) was developed for acoustics. The literature is vast and much is available on the internet. For instance Fabio Kaiser wrote a student report for the Technische Universitat Berlin in 2011 which gives a useful quick overview with examples. Also see Stephen Kirkup's book 'The Boundary Element Method in Acoustics', 2007. A paper by Miller, Moyer and colleagues (JASA Vol 89 No 5, 1991) compares the boundary element method with the wave superposition approach and describes how the coupled fluid-structure interaction can be included by simultaneous combination of finite element analysis of the vibrating object and boundary element modelling of sound radiation from its surface. Today the FastBEM computer program is commercially available and offers a free student version with good functionality (*www.fastbem.com*).

11.3 Heuristic approximations of ϕ_0 and $\nabla\phi_0 \cdot \mathbf{n}$

I have presented evidence that the Rayleigh-Sommerfeld method, restricted to $\cos\beta > 0$, can give a fair approximation to the radiated potential when applied to the breathing mode of prolate and oblate spheroids. The subsection conjectures two possible approaches to obtaining a better approximation. The idea is to link the surface values of ϕ and $\nabla\phi\cdot\mathbf{n}$ to each other so that the Kirchhoff formulation, which requires both, can be used. Two conjectures to link ϕ to its normal derivative are examined:

1. via the size and aspect ratios of the object,
2. via the curvature of the wavefronts at the surface.

We shall see that the first may have some validity, at least for the breathing mode, but the second is not correct, though is still interesting in itself.

In a practical scheme I envisage the surface normal displacement being given – probably obtained from finite element analysis of the elastic vibration of the object. In an iterative scheme a plausible guess would be made at the surface potential distribution and either the restricted dipole Rayleigh-Sommerfeld or the Kirchhoff version of the program run. The output would give $\phi(Q)$ and its first and second derivatives, and from these the values of ϕ_0 and its normal derivative could be estimated, probably involving extrapolation back to zero distance from the surface. The computed values of normal derivative will not agree with the given values, so the assumed ϕ distribution would be adjusted and the program rerun. Hopefully the second calculation of normal displacement will be closer to the given values and the ratio $\nabla^2\phi/\phi$ will be closer to κ^2 at all points Q. I have not implemented this scheme, but intend to try it with the vibration of a violin in a future article on *www.mathstudio.co.uk*.

11.3.1 Aspect ratio

Referring back to §10.2, Eq 42 gives the normal derivative of ϕ over the surface in terms of the prolate radial co-ordinate ζ and the lateral/angular co-ordinate η. In the Kirchhoff formulation of Eq 44a

for a prolate spheroid in the breathing mode the angular function $S_{00}(C,\eta)$ has been factored out so that the contribution from the normal derivative is

$$\frac{1}{f}\sqrt{\frac{\zeta^2-1}{\zeta^2-\eta^2}}\;\frac{dR_{00}(C,\zeta)}{d\zeta}\,. \tag{45}$$

The aim now is to obtain an approximate value for this. Note that though this has been written for the mode 0-0, the same form with apply to any mode since the potential ϕ separates into a product of three independent functions each depending on only one variable. The expression depends on η through $1/\sqrt{\zeta^2-\eta^2}$ which derives from the h_ζ scale factor expressing the geometry of the spheroid. By approximating the convex object in question to a spheroid this same factor can be used to weight the ratio $\nabla\phi_0\cdot\mathbf{n}$ to ϕ_0 locally at each point over the object. The second factor to approximate is the derivative $R'(C,\zeta)$ and perhaps this can be achieved by taking the value at $\eta=0$ to be that of a sphere, which is $-1/a+i\kappa$, a here being some representative radius.

How would this generalise to an ellipsoid in which all three axes have different lengths? This is answered by finding the scale factors of a general ellipsoid. It was shown by Gabriel Lamé in the early nineteenth century that the wave equation will separate in ellipsoidal co-ordinates as $\phi = L(\lambda)\,M(\mu)\,N(\nu)$. λ (not to be confused with the wavelength), μ and ν are ellipsoidal co-ordinates. Appendix 7 gives a short introduction to this co-ordinate system, and a recent book on ellipsoidal harmonics is by George Dassios (CUP, 2012). λ is the near equivalent of ζ for a spheroid, being related through

$$\sqrt{a^2+\lambda} \;=\; f\zeta, \qquad \lambda \;=\; f^2\zeta^2-a^2\,.$$

$\lambda=0$ corresponds with the surface of the ellipsoid with x semi-axis a, $\lambda<0$ with confocal interior ellipsoids and $\lambda>0$ with exterior ones. μ is roughly equivalent to the spheroid's angular co-ordinate η, and ν is equivalent to the azimuthal co-ordinate ψ. The three families of surfaces which have one of λ, μ or ν constant are orthogonal. Appendix 7 quotes the relevant scale factor for normal displacement of an ellipsoid with semi-axes $a>b>c$ and shows that

$$\nabla\phi_0\cdot\mathbf{n} \;=\; -2\sqrt{\frac{(a^2+\lambda)(b^2+\lambda)(c^2+\lambda)}{(\lambda-\mu)(\lambda-\nu)}}\;\frac{\partial\phi}{\partial\lambda}, \qquad \phi = L(\lambda)\,M(\mu)\,N(\nu)\,. \tag{46}$$

This therefore is the generalisation of Eq 45.

11.3.2 Potential-to-displacement ratio and wavefront curvature

The second idea looks for a proportionality between ϕ_0 and $\nabla\phi_0\cdot\mathbf{n}$ determined by the local curvature of the surface. Since in continuous wave motion ϕ is proportional to acoustic pressure and ξ is proportional to velocity, the ratio ϕ/ξ at any point P on the surface is proportional to the impedance Z there. Specifically pressure is $-\omega^2\rho\phi$ (Eq 9b) and particle velocity is equal to $-i\omega\xi$ for time variation $e^{-i\omega t}$. Thus $Z=-i\omega\rho\,(\phi/\xi)$. The conjecture I have toyed with is that this local impedance may be determined by the curvature of the wavefronts at P. Such curvature is the only additional feature which a wave near an object has over a plane wave. If this were true, knowing the two principal curvatures of the object would allow $\phi(P)$ to be obtained from a given ξ_0 and *vice versa*. The Kirchhoff integral could then be evaluated exactly.

As Appendix 5 explains, I can find no such dependence of Z on curvature. However, let me explain why I judged it a reasonable question. I am almost certainly not the first person to propose obtaining an approximation to the surface pressure, though I do claim that I have thought of this independently. In a paper from 1963, George Chertock of the US Office of Naval Research (J.A.S.A,

Vol 36 No 7, p 1305-1313) gave high and low frequency approximations for the surface pressure given the velocity, and also made comparison with a prolate spheroid for which the exact solution is known in terms of spheroidal wave functions. One of Chertock's colleagues, Roland Baier calculated the radiation impedance of a section of oblate spheroid moving like a piston in an otherwise rigid spheroidal object over a frequency range $0 \cdot 1 \le \kappa a \le 20$ (J.A.S.A. vol 51 No 2, 1972, p 1705-1716). Consider the following special cases where pressure, normal displacement and curvature are linked:

1. In a plane wave we know that the particle velocity is simply proportional to the pressure at a point, their ratio being the characteristic acoustic impedance, $Z_c = \rho c$. The ratio ϕ/ξ for a plane wave is i/κ.

2. The potential due to a monopole, and hence for a pulsating sphere of radius a, is $\phi = Ae^{i(\kappa a - \omega t)}/a$ where A has the dimensions of volume. The displacement is $-\phi(i\kappa - 1/a)$. This is all normal to the surface so the ratio for a sphere is

$$\frac{\phi}{\xi} \;=\; \frac{a}{1 - i\kappa a}\,. \tag{47}$$

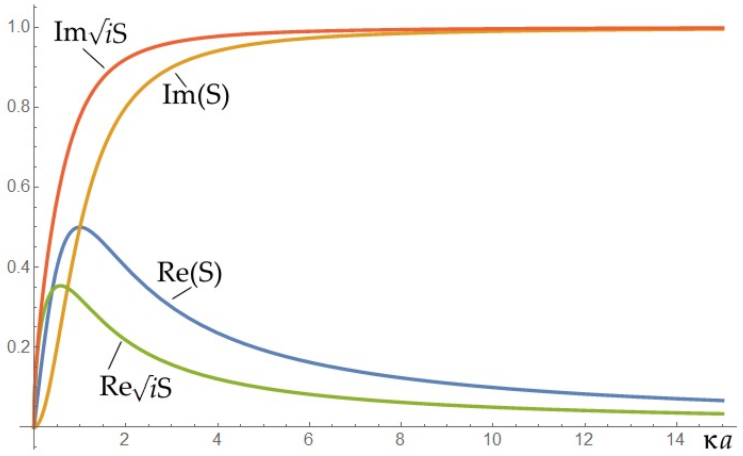

Figure 67: Real and imaginary parts of Eq 47 for a sphere. $S = \kappa a/(1 - i\kappa a)$.

Graphs of the real and imaginary parts of this are plotted in Figure 67. As $a \to \infty$, this ratio tends to i/κ, the value for a plane wave. Also in the same graph are plotted effectively the square root of Eq 67. This features in the case of a cylindrical radiator, and I wish to show how quickly the both functions approach the plane wave value. When $\kappa a = 2\pi$, $\lambda = a$, so when the sphere is not much larger that one wavelength in radius it already has almost reached its limiting value. The same points about resistive and reactive parts of the impedance were made in §3.

3. In 2D a simple point source has potential $\phi = \frac{1}{2}A' i\pi H_0(\kappa r)\, e^{-\omega t}$ where H_0 is either of the Hankel functions

$$H_0^{(1)}(x) \;\equiv\; J_0(x) + iY_0(x) \quad \text{or} \quad H_0^{(2)}(x) \;\equiv\; J_0(x) - iY_0(x)\,,$$

both complex versions of the Bessel functions. A' is an amplitude with dimensions of area. Clearly $|H_0^{(1)}(x)| = |H_0^{(2)}(x)|$. The derivative is $H_0'(x) = -H_1(x)$ so the potential : displacement ratio in 2D is

$$\frac{\phi}{\xi} \;=\; \frac{H_0^{(1,2)}(x)}{\kappa H_1^{(1,2)}(x)}\,. \tag{48}$$

This is consistent with the acoustic impedance for a radially pulsating cylinder of radius a being

$$Z_{cyl} \;=\; i\rho c\,\frac{H_0^{(1,2)}(\kappa a)}{H_1^{(1,2)}(\kappa a)}\,.$$

There are several ways in which curvature can be measured. At each position on a surface there are two directions of principal curvature with respective radii a_1, a_2. The principal curvatures are the reciprocals $1/a_1$, $1/a_2$. The conjecture is that some combination of these may be related to impedance, such as the Gaussian curvature $1/(a_1\,a_2)$ or the mean curvature $\frac{1}{2}(1/a_1 + 1/a_2)$.

The principal radii for a plane are both infinity. For a sphere they are both a, and for a cylinder one is a and the other infinity. In a sense, the cylindrical wave is the geometric mean of a plane and a spherical wave. As such we might expect the potential : displacement ratio for a cylindrical wavefront to be the geometric mean of the ratios for plane and sphere. A test of this is whether the following relation holds approximately:

$$\sqrt{\frac{i\kappa a}{1-i\kappa a}} \;\approx\; \frac{H_0^{(1)}(\kappa a)}{H_1^{(1)}(\kappa a)}\,. \tag{49}$$

In fact the real and imaginary parts of the left and right sides of this are very similar, as Figure 68 shows. (The curves labelled LHS for 'left hand side' are identical with the $\sqrt{i}S$ curves in Figure 46.) Suppose therefore that we associate the square root of the left side of Eq 44 with each principal plane of local curvature in the surface. The conjecture is that the ratio at a general point P on the surface is

$$\frac{\phi}{\xi} \;\approx\; \sqrt{\frac{a_1\,a_2}{(1-i\kappa a_1)(1-i\kappa a_2)}}\,, \tag{50a}$$

or in polar form

$$\frac{\phi}{\xi} \;\approx\; \sqrt{\frac{a_1 a_2}{\sqrt{(1+\kappa^2 a_1^2)(1+\kappa^2 a_2^2)}}}\;e^{i\gamma/2}\,, \qquad \tan\gamma = \frac{\kappa(a_1+a_2)}{1-\kappa^2 a_1 a_2}\,. \tag{50b}$$

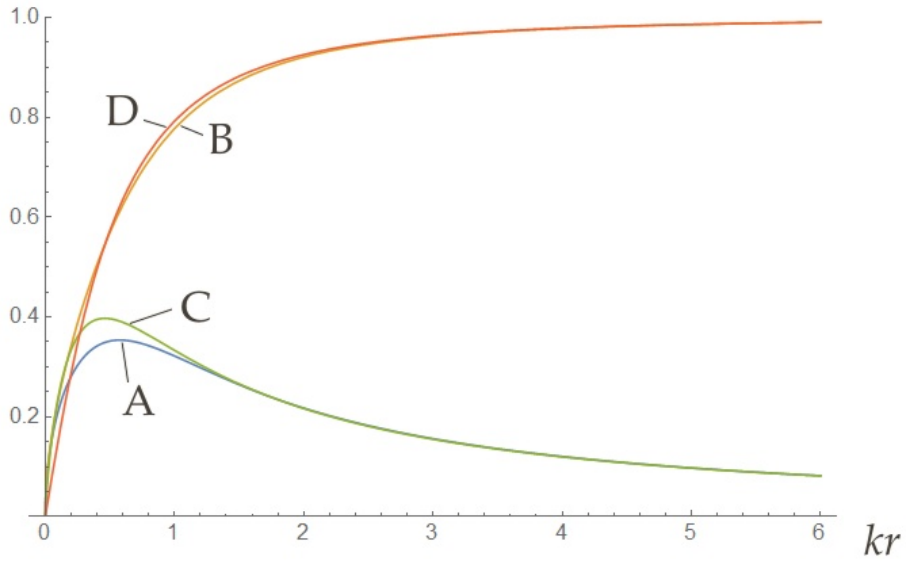

Figure 68: Comparison of real and imaginary part of the two sides of Eq 49. A: Re LHS, B: Im LHS, C: Re RHS, D: Im RHS.

where a_1, a_2 are the principal radii at the current triangular mesh element. Since the impedance is the same for a converging as for a diverging wave front, Eq 50 would apply equally to convex and concave regions of the surface. To be clear, I am not claiming that this will give the correct answer, only that it may be one plausible way to recognise the influence of surface curvature on ϕ/ξ. On the other hand, the technical literature does not describe a known relationship between impedance and curvature, so it is quite likely that there isn't one!

In Appendix 5, §17, I describe two types of test of the conjecture. Both involve comparing the formula of Eq 50 with the exact values of ϕ/ξ for a spheroid, the latter given in terms of spheroidal wave functions. Both tests span a range of aspect ratios of the spheroids, from flattened oblate discs to elongated prolate rugby balls. Points on the axis of rotation, called Positions A in Appendices 4 and 5, have both principal radii equal, so the position is locally like a hemisphere. At right angles to the rotation axis, in the central equatorial plane, are positions B where the two principal radii are different.

The numerical evidence is that Eq 50 does not hold at either Position A or B. Impedance seems therefore not to be a local property related to the curvature of the wavefronts, but instead, a global property of the object in its fluid medium. This is consistent with Green's theorem which says that the field at any point Q is determined by integration of the field over the whole surface of the object (and baffle if there is one). For the range of κa values we are considering ϕ/ξ cannot be obtained by ray arguments which seek to link the motion at a field point Q to motion only of a restricted patch of surface. An interesting idea – but wrong! The other heuristic, linking ϕ/ξ to aspect ratio, is consistent with a non-local nature to impedance.

I did look briefly into what would be involved in implementing the curvature heuristic in the computer program, and that too threw up some interesting points. It would complicate the coding significantly because it would be necessary to determine the principal radii of curvature for N patches centred on each of the N triangular elements. The program in its original form deals with triangles one at a time, but it would need to have a table to record by index which elements and nodes surround every given triangle. From this local map of perhaps 10 triangles and 10 nodes some algorithm for calculating a_1 and a_2 would be needed. (The directions of the principal axes are not needed.) Much development has already gone into this problem of determining curvature values for an arbitrary triangulated surface. Recent reviews are by Nigam and Agrawal (Int J. Eng Sci & Innovative Tech,, Vol 2 No 3, 2013) and Tim Gatzke and Cindy Grimm (Int J Shape Modelling, Vol 12 No 1, p1-28, 2006 – see Internet). As might be expected, there is a trade-off between accuracy and stability in the presence of random spatial noise and the effort of calculation. The best method is probably to fit the osculating paraboloid to the patch with apex at the given central element, and obtain the principle radii from the coefficients of the algebraic expression for this fitted surface, using a little differential geometry. The paper by Jack Goldfeather and Victoria Interrante describes what are probably the most appropriate methods though its focus is principal directions rather than radii (ACM Trans Graphics Vol 23 No 1, 2004, p45-63).

12 Closing summary

This has turned into a long article in which I have set out my personal exploration of sound radiation from vibration bodies. There can be nothing new of substance in this study, though the presentation and results are all my own work. Moreover, I have stopped short of describing the boundary element method which is now favoured since it is well described elsewhere. In that sense my study is out of date. Nevertheless the physics has not changed. Let me draw together a few conclusions and salient points.

1. The essential building block of sound radiation is the point source, which obeys the wave equation in spherical co-ordinates. It has displacement potential $\phi = Ae^{i\kappa r}/r$, which is proportional to the acoustic pressure. The displacement is $\xi = \phi(i\kappa - 1/r)\,\mathbf{e_r}$. The displacement and hence particle velocity from a small source have radiative and reactive components which are respectively in phase and in quadrature with the pressure. In this respect spherical waves differ from plane waves. The ratio of pressure to particle velocity is the impedance Z, a complex quantity. Work is done by the vibrating object in moving the reactive component of fluid, which just wafts to and fro each cycle without usefully radiating sound to a listener. The reactive component falls as $1/r^2$, but is relatively large close to small objects when the wavelength is long. For this reason small objects are unable to radiate loud sounds at low frequencies. This is a constraint on the design of musical instruments in the bass register.

2. The principle of wave superposition for small amplitude waves eases the mathematical description of sound because waves can be treated as complex numbers and combined simply by addition. An extended vibrating body can be regarded as being made of an array of point sources over its surface. The spherical waves from all elementary point sources interfere. This is Huygens' principle. Interference is pronounced for two or three separated point sources, and I have demonstrated the effect in experiments with dipoles and tripoles.

3. The study has concentrated on pure sine wave oscillation. The wave equation then reduces to Helmholtz's equation $\nabla^2\phi + \kappa^2\phi = 0$, $\kappa = 2\pi/\lambda$. In a small numbers of 2D and 3D co-ordinate systems ϕ 'separates', meaning that ϕ can be written as the product of two or three functions each one of which depends on only one co-ordinate. The separated equations, each in one variable, have been studied extensively. They can be solved usually as sums of infinite series, and form the so-called special functions of mathematics, now widely tabulated. I describe separation in spherical and spheroidal co-ordinates in §5.2 and Appendix 4 (§16) respectively. A radial wave function describes how the potential dies away with range, and an angular function describes the distribution with direction. Since these are independent functions, the shape of the angular distribution function does not change with range from what it is on the object's surface. This contrasts with radiation from a vibrating piston in an infinite flat baffle; for this the angular distribution changes markedly with range, becoming in the far field the Fourier transform of the variation at the piston.

4. Huygens's principle has been placed on a secure mathematical footing by using Green's theorem of vector calculus. This is a powerful general statement about two scalar quantities that relates their second derivatives at any point within a closed volume of space to values on the enclosing surface. Since Helmholtz's equation involves the second derivative $\nabla^2\phi$, Green's theorem can be applied to give the field at a general listening point Q within a closed surface in terms of an integral of values around the boundary. §6 sets out the formulations of Green's theorem to wave radiation and diffraction theory devised by Gustav Kirchhoff, Lord Rayleigh and Arnold Sommerfeld. Of the two functions in Green's theorem, one is taken to be the displacement (or velocity) potential ϕ and the other is a Green's function $\mathbf{G}$, this being an elementary

solution of Helmholtz's equation. Kirchhoff uses a single point source $\mathbf{G} = e^{i\kappa r}/r$, and Rayleigh-Sommerfeld use two point sources in mirror positions about a plane containing the vibrating object. If these two sources vibrate in phase, the monopole Rayleigh-Sommerfeld formula is derived (Eq 22b), and if they are 180° out of phase the so-called dipole formula is obtained, Eq 22a. The secondary dipole sources are characterised by an obliquity factor $\cos\beta$. In this way contributions to the surface integral in $\phi_0 \cos\beta$ are said to represent a dipole layer of elementary sources, and ones in $\nabla\phi$ describe a layer of monopole sources. All these integral formulae by Kirchhoff and Rayleigh-Sommerfeld are formally exact.

5. Using analytical mathematics and numerical quadrature I have demonstrated Green's theorem in Kirchhoff's formulation for a symmetrically pulsating sphere in various configurations in §9 and Appendix 2 (§14). These examples show how the boundary can be deformed yet the field $\phi(Q)$ remain the same at each interior point Q provided that consistent values of ϕ and its derivative are given over the total enclosing surface, and the integration is performed over this whole surface. One scheme for deforming the boundary describe in Appendix 2 transforms a complete sphere into a hemisphere in a concentric planar baffle. This produces the same field at any point Q as would the complete sphere and no baffle. This effect can be described in terms of the baffle acting as an acoustic mirror, producing a virtual set of sources in the image positions of actual sources.

6. Despite the formal correctness of the Kirchhoff and Rayleigh-Sommerfeld formulations, both in practice suffer significant limitations. Kirchhoff's formula requires input of both ϕ_0, the potential over the surface, and its normal derivative there. This is equivalent to inputting the pressure and normal displacement over the whole surface of the object and any surrounding baffle. However, these quantities are linked through the very Helmholtz's equation yet to be solved, so they cannot both be specified unless the exact solution of the wave equation is known at the surface. We do have exact solutions in the case of a sphere and a spheroid, and using these I have demonstrated the consistency of Kirchhoff's formulation for a sphere in §9 and §10.1 and for a spheroid to a limited extent in §10.2.

7. The Rayleigh-Sommerfeld formulation was developed to remove the requirement to specify both ϕ_0 and $\nabla\phi_0 \cdot \mathbf{n}$. It does so by restricting the radiating surface to a plane. This was not a significant restriction for the applications to diffraction of light by small holes in planar screen, for which the method was originally developed. However, in principle it rules out application to any source which is not strictly flat. In optics this would include curved mirrors and lenses, though the method has been applied to these with success, showing that there is some latitude.

8. I have written versions of a computer program to implement both the Kirchhoff and Rayleigh-Sommerfeld approaches. Such a program is not novel, but this is my own effort, designed to work in conjunction with finite element (FEA) modelling of a vibrating object. The vibrating surface is modelled by a mesh of triangular elements at each of which ϕ and/or its normal derivative is supplied. In the Rayleigh version of the program, the surface displacement would be read from a file of FEA results. The integral of a phase factor $e^{i\kappa r}$ over each single element uses an analytical formula derived in Appendix 1, §13. Using complex arithmetic the program adds numerically the contribution from all the elements. Hence at each specified point away from the surface the program calculates the real and imaginary parts of ϕ and its first and second spatial derivatives. The displacement can be calculated from the first derivatives. The second derivatives provide a check on consistency since $\nabla^2\phi$ should always equal $-\kappa^2\phi$.

9. I have given several demonstrations of the program. The examples in §7 show that the Rayleigh-Sommerfeld dipole version gives good results for planar radiators including triangular and

circular pistons in a baffle. It shows convincing near field structure. There is one significant approximation in these applications to pistons in a baffle – that the field over the surrounding baffle is zero right up to its edge with the vibrating piston. This cannot be correct since nature does not tolerate abrupt discontinuities. The assumption of zero field on the baffle is called the 'Kirchhoff approximation', not to be confused with the Kirchhoff formulation. It might be possible to develop some iteration scheme in which ϕ_{baffle} is initially taken to be zero and the radiated field determined, then an extrapolation made back to the plane of piston and baffle to estimate (hopefully) improved values of ϕ_{baffle} and ϕ_{piston}. I have not explored this to any significant extent because the highly oscillatory near field and inherent limitations of the computer program, discussed in §6.2, make such extrapolation too open to guesswork.

10. In §8 the program is used to model the experiment of §4 which demonstrates interference between two and three loudspeakers over a wide range of directions. The broad effects of constructive and destructive interference are reproduced in the calculation. However to explain certain finer features of the angular dependence of radiated amplitude, I have had to conjecture that the loudspeaker's cone flexes instead of behaving as a rigid piston. The literature and some finite element calculations give support to this.

11. Later sections in the article consider both the Kirchhoff and Rayleigh-Sommerfeld versions applied to convex objects. I have focussed on the breathing mode in which all parts of the surface move in and out in phase. This is the most simple motion and the easiest to compare with exact theories in order to verify the model and coding of the program. To check that the breathing mode does actually occur in an elastic body I have used the LISA 8 and MecWay finite element analysis software to compute the first 50 normal modes of some thick-walled hollow elastic spheroids. Examples are presented in §11.1. A radially symmetric breathing mode does occur provided the aspect ratio of the spheroid is not too far from unity. It is about the 30th mode, being of high frequency because it involves volume dilation within the material rather than just shear. Unfortunately the displacement predicted by FEA does not agree well with the angular wave function S_{00}, which is the breathing mode solution of the wave equation in spheroidal co-ordinates. This suggests that in practice the simple mode S_{00} cannot be excited by itself, but occurs together with higher symmetric modes S_{01}, S_{02}, etc.

12. In §10 I describe examples of applying both the Kirchhoff and Rayleigh-Sommerfeld versions of the program to spheres and spheroids, for which the computed results can be compared with exact solutions of the wave equation. In these tests exact values of both ϕ and/or its normal derivative have been input to the program, so in so far as the program is an encoding of Green's theorem, it should output exact values of the field at points Q. Results with the Kirchhoff formulation for a selection of spheres are good. The dipole Rayleigh-Sommerfeld version, however, is problematic. It requires input of the potential only and ϕ is modulated by an obliquity factor $\cos\beta$, where β is the angle between the local surface normal and the line joining the element to Q. If the integration extends to all elements on the surface, the obliquity factor weights the contributing wavelets strongly in favour of those on the front face where the normals point towards Q and those on the back pointing away from Q, but little comes from the sides. The vibrating surface thereby resembles a dipole and strong interference occurs between front and back face. Consequently with increasing frequency the computed $\phi(Q)$ alternates between constructive and destructive interference which obliterates the required true value. To prevent this an alternative 'restricted' version of the dipole Rayleigh-Sommerfeld program restricts β to be less than 90°. There is little theoretical justification for this, but it does show quite good agreement with theory for spheres once $\kappa a > 10$.

13. I have made a limited investigation of the Kirchhoff and Rayleigh-Sommerfeld versions on pro-

late and oblate spheroids vibrating in the 0 0 breathing mode, described in §10.2. Comparison with the exact theory is possible using values of spheroidal wave functions from Mathematica, though the formulae for spheroids are much more complicated than for spheres, as Appendix 4 explains. As with the sphere, exact values of ϕ_0 and its surface derivative are input. There is good agreement using the Kirchhoff version for both prolate and oblate spheroids for aspect ratios from $< 0{\cdot}5$ to > 2. The restricted Rayleigh version (limited to $\cos\beta > 0$) agrees fairly well with theory, though not always as well as the Kirchhoff. The Kirchhoff program outputs values of the ratio $\nabla^2\phi/\phi$ which are close to κ^2 at almost all field points Q, indicating a solution of Helmholtz's equation. However, with the restricted Rayleigh version this ratio is much more erratic, especially at short range; it does not settle to near κ^2 until longer ranges. This reflects the weak theoretical foundation of the restricted Rayleigh.

14. In §11.3 I have conjectured, though not developed, heuristic approximations and iteration schemes which might lead to improved solutions in practical cases where only one of ϕ_0 or ξ_0 is known exactly. The restricted Rayleigh-Sommerfeld program may well give a sufficient result for some applications in acoustics, bearing in mind that a 20% change in sound level is 2 dB, about the smallest that a listener would normally notice. An improved result might be obtained by using the restricted Rayleigh values of ϕ and $\nabla\phi$ near the surface as input to the Kirchhoff version of the program, recalculating the external field, and hopefully achieving convergence towards a solution of Helmholtz's equation. Two other heuristic schemes aim to link ϕ_0 to its gradient at the surface. One appeals to aspect ratio of the object; the object is approximated by an ellipsoid for which there is a formula (Eq 46) relating the surface variation in ϕ to $\boldsymbol{\nabla}\phi\cdot\mathbf{n}$. The other conjectures a link between these quantities via the local curvature of the surface. This is tested in Appendix 5, but the conclusion is that there is no such link.

15. An enormous amount of research over may years has gone into developing reliable models of wave radiation and scattering. The earliest was on optical diffraction, but from the 1950s the US Navy invested in the subject because of its relevance to submarines. One of the spin-offs has been the invention of computer code for calculating spheroidal wave functions. This is now conveniently available in Mathematica and in free source code. Researchers into acoustic radiation probably wrote programs like mine in the 1960s and probably found the same limitations. They also transformed the Kirchhoff formula into an integral equation by letting the external field point Q approach the surface. Appendix 6, §18 gives a flavour of integral equations via a one-dimensional example. They have the property that at certain frequencies, corresponding to solutions of the associated homogeneous equation (no forcing term), the solution is indeterminate because any solution of the homogeneous equation can be added and their sum is also a solution to the non-homogeneous equation. Applied to vibrating spheroids this phenomenon manifests itself as a coupling of the external field to the internal cavity of the spheroid. One way of dealing with this has been to introduce a number of interior points into the formulation of the integral equation for Q in the exterior. This is the basis of the CHIEF program developed in the USA and still used today. Integral equation methods were also developed into the discrete boundary element methods (BEM) in which the object's surface is divided into a mesh of elements each with properties encapsulating the wave equation and boundary conditions. Judging by the literature BEM is now the favoured approach to sound radiation problems much as FEA is to stress analysis. Variants of BEM add monopole, dipole and higher discrete sources to the field to achieve rapid convergence. 'FastBEM' from *www.fastbem.com* is one commercially available code, and the company generously offers a free student version.

That concludes this article. *John Coffey, Cheshire, England, March 2015*

13 APPENDIX 1: Radiation from single triangular element

This appendix details calculation of the radiated field from an arbitrary triangular piston using the dipole Rayleigh-Sommerfeld integral, Eqs 23a, b §6.2. Central to this is the integral of $e^{i\kappa\epsilon}$ over a general triangle. For good measure §13.4 adds the equivalent formula for a rectangular piston.

13.1 Setting up the calculation

The integral for the displacement potential at point Q in terms of the normal displacements ξ_0 of the elements' surfaces is given by Eq 23. In simple test cases such as radiation from a disc the normal component of surface displacement can be specified as, say, ± 1 or $0 \cdot 01$ units as we please. In the general case, however, the displacements will be determined by FEA. Programs such as LISA 8 and the new MecWay calculate the vector displacement $\boldsymbol{\xi}$ at each *node*. These lie at the vertices of the elements and not at the centroids so I simply take the mean over the vertex nodes.

FEA may represent the violin plate's surface by a mesh of triangular and/or quadrilateral elements. Because the four nodes of a general quadrilateral will not lie in a plane, I require that each quadrilateral be split into two triangles. The model assumes that all elements are triangles.

The calculation proceeds in two stages

1. transformation of co-ordinates from the global x, y, z system with origin O at the centre of the radiating object to local co-ordinates u, v, w on one triangular element with local origin at its centroid C,
2. evaluation of the complex phase integral over the triangle in the u, v, w co-ordinates.

13.2 Transformation of co-ordinates

Figure 69 shows a triangular element with vertices P_1, P_2, P_3 in general position. A set of local axes u, v, w is set up with origin at the centroid C such that u and v lie in the plane of the triangle with v along the line CP_3. The aim is to relate the co-ordinates (x, y, z) of a general point P in the global system to co-ordinates (u, v, w). If $\mathbf{p_1}$, $\mathbf{p_2}$, $\mathbf{p_3}$ are the position vectors of the three vertices, the centroid's position vector is $\mathbf{c} = (\mathbf{p_1} + \mathbf{p_2} + \mathbf{p_3})/3$. The translation $\mathbf{p} \to \mathbf{p} - \mathbf{c}$ places C at the new origin.

Unit vectors in the two systems are respectively $\{\mathbf{e_x}, \mathbf{e_y}, \mathbf{e_z}\}$ and $\{\mathbf{e_u}, \mathbf{e_v}, \mathbf{e_w}\}$. $\mathbf{e_v}$ runs from centroid to vertex 3 so is

$$\mathbf{e_v} \;=\; \frac{\mathbf{p_3} - \mathbf{c}}{\|\mathbf{p_3} - \mathbf{c}\|}\,.$$

The unit normal is $\mathbf{e_w}$. In this Appendix and for the computer program itself I have changed the convention for the direction of the normal and unit vector to Q, reversing them from those in Figure 19 of §6.1 so that $\mathbf{n}$ now points in the same direction as $\mathbf{e_w}$. Similarly $\mathbf{e_r}$ now points from the element towards Q. The scalar product $\mathbf{e_r} \cdot \mathbf{n}$ is unchanged by these two reversals.

Two vectors lying in the plane of the triangle are $\mathbf{p_2} - \mathbf{p_1}$ and $\mathbf{p_3} - \mathbf{p_1}$. Their cross (vector) product defines both the unit normal and also the triangle's area S:

$$\mathbf{e_w} \;=\; \frac{\mathbf{N}}{\|\mathbf{N}\|}, \qquad S = \tfrac{1}{2}\|\mathbf{N}\| \qquad \text{where} \qquad \mathbf{N} \;=\; (\mathbf{p_2} - \mathbf{p_1}) \times (\mathbf{p_3} - \mathbf{p_1})$$

The third unit vector, $\mathbf{e_u}$, is the cross product $\mathbf{e_v} \times \mathbf{e_w}$.

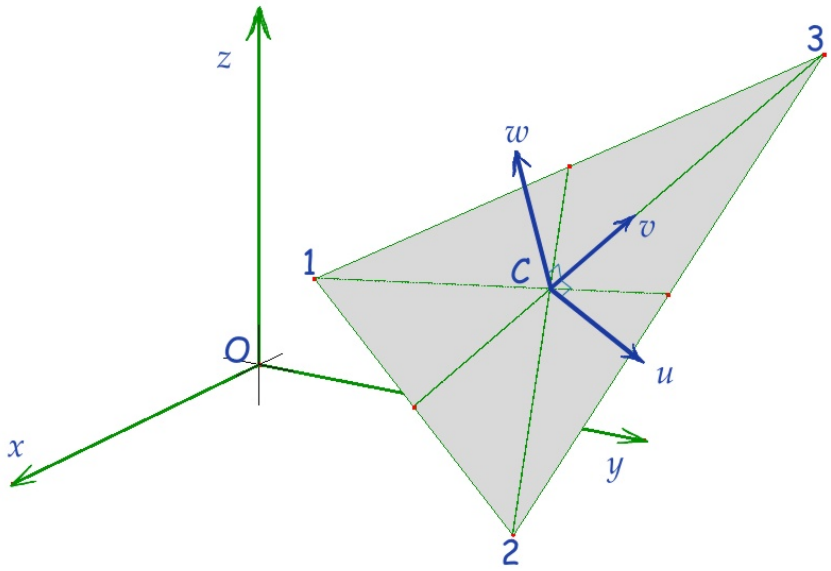

Figure 69: Local u, v, w axes with origin at the centroid of the triangle in relation to the global co-ordinates x, y, z with origin O at centre of radiating object.

If the listener is at Q with vector $\mathbf{q}$, the distance travelled by the sound from the element at C is $r = \|\mathbf{q} - \mathbf{c}\|$. It will be necessary to choose consistently the outward pointing normal for each element because that determines the obliquity angle β towards Q. As a way of checking the sense of the normal, I use the fact that for a near-spherical object it will point in a similar direction as the position vector of the centroid, and its components will have the same signs. The obliquity factor is $\cos\beta$. If $\cos\beta > 0$, the element lies within the cone of rays subtended by the object at observation point Q.

The dot product $\mathbf{e_u} \cdot \mathbf{e_x}$ is the cosine of the angle between the u and x axes, equivalent to the project length of $\mathbf{e_x}$ on $\mathbf{e_u}$. The set of nine equivalent dot products defines all the direction cosines between the two sets of axes. The whole transformation can be written as a matrix multiplication:

$$\begin{pmatrix} P_u \\ P_v \\ P_w \end{pmatrix} = \begin{pmatrix} \mathbf{e_u} \cdot \mathbf{e_x} & \mathbf{e_u} \cdot \mathbf{e_y} & \mathbf{e_u} \cdot \mathbf{e_z} \\ \mathbf{e_v} \cdot \mathbf{e_x} & \mathbf{e_v} \cdot \mathbf{e_y} & \mathbf{e_v} \cdot \mathbf{e_z} \\ \mathbf{e_w} \cdot \mathbf{e_x} & \mathbf{e_w} \cdot \mathbf{e_y} & \mathbf{e_w} \cdot \mathbf{e_z} \end{pmatrix} \begin{pmatrix} P_x - C_x \\ P_y - C_y \\ P_z - C_z\,. \end{pmatrix} \qquad (A1.1)$$

This formula is to be applied to the listening point Q and to the three vertices of the triangle. Although there are nine co-ordinates of these vertices, when expressed in u, v, w only four of them are non-trivial. This is because all w are zero by design, and $P_{3u} = 0$ because of the choice of v axis. Furthermore, the line CP_3 bisects the line P_1P_2 so $P_{1u} = -P_{2u}$, and $P_{1v} + P_{2v} + P_{3v} = 0$.

13.3 Integration over the triangle

Figure 70 shows the triangle referred to u, v, w and the projection of CQ onto the u, v plane. The distance CQ is r and the distance PQ from a general point $P = (u, v, 0)$ within the triangle is $r + \varepsilon$. Essentially we must integrate $e^{i\kappa(r+\varepsilon)}/(r + \varepsilon)$ over the triangle, $\kappa = 2\pi/\lambda$.

I will say a little about the approximation of the phase factor. For almost all field points Q of interest, r will significantly exceed the width of the triangle. Then the oscillatory exponential has

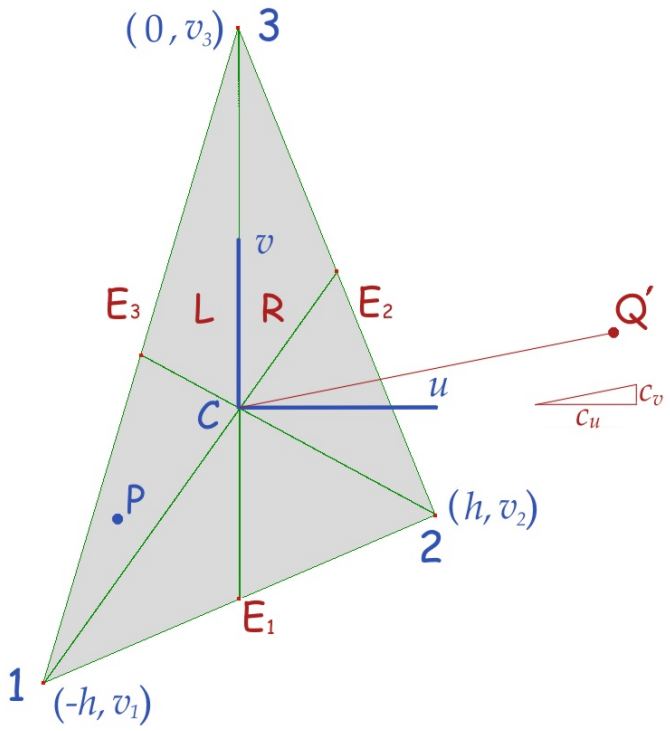

Figure 70: View down the w axis of the local u, v, w system onto the plane of the element. Q' is the perpendicular projection of the point of listening, Q, onto the u, v plane. c_u, c_v are in-plane components of the unit vector $\mathbf{e_r}$.

a much larger effect than the reciprocal so the following approximations are valid:

$$\frac{e^{i\kappa(r+\varepsilon)}}{r+\varepsilon} \approx \frac{e^{i\kappa(r+\varepsilon)}}{r} - \frac{\varepsilon\, e^{i\kappa(r+\varepsilon)}}{r^2} \approx \frac{e^{i\kappa r}}{r}\, e^{i\kappa\varepsilon} \approx \frac{e^{i\kappa r}}{r}\, e^{i\kappa\varepsilon'}\,.$$

Here ε' is the distance not from P to Q itself, but from P to the plane through Q normal to the line CQ. In other words $|\varepsilon'|$ is the projected length of CP onto $\mathbf{e_r}$, the unit vector along CQ. The error is $(u^2+v^2)/(2r)$. If $\mathbf{p}\cdot\mathbf{e_r}$ is positive, the path length of the wave is shortened, so $\varepsilon' = -\mathbf{p}\cdot\mathbf{e_r}$. Since $e^{i\kappa r}/r$ is constant over the triangle, only $e^{i\kappa\varepsilon'}$ appears under the integral sign.

Figure 70 shows how the triangle is divided into two parts L (left) and R (right), and bounded by three edges E_1, E_2, E_3. The areas of the L and R parts are equal, and the total area is $3hv_3/2$. In L we integrate first with respect to v from

$$E_1 : v = m_1\, u - \frac{v_3}{2} = u\,\frac{(v_2-v_1)}{2h} - \frac{v_3}{2} \quad \text{to} \quad E_3 : v = m_3\, u + v_3 = u\,\frac{(v_3-v_1)}{h} + v_3\,.$$

In R integration is from E_1 to

$$E_2 : v = m_2\, u + v_3 = u\,\frac{(v_2-v_3)}{h} + v_3\,, \qquad m_2 < 0.$$

The second integration in L is from $u = -h$ to 0 and in R from $u = 0$ to h. If $\mathbf{e_r} = c_u\mathbf{e_u} + c_v\mathbf{e_v} + c_w\mathbf{e_w}$ the integral is

$$I = \int_{-h}^{0}\int_{E_1}^{E_3} \exp\left(-i\kappa[uc_u + vc_v]\right) dv\, du \;+\; \int_{0}^{h}\int_{E_1}^{E_2} \exp\left(-i\kappa[uc_u + vc_v]\right) dv\, du,. \qquad (A1.2)$$

This looks complicated but is straightforward to evaluate if split into the sum of small parts. Denote by I_L the integral from the left side:

$$I_L \;=\; \int_{-h}^{0} e^{-i\kappa c_u u} \int_{E_1}^{E_3} e^{-i\kappa c_v v}\, dv\, du \;=\; \frac{i}{\kappa c_v} \int_{-h}^{0} e^{-i\kappa u c_u} \left[e^{-i\kappa c_v (m_3 u + v_3)} - e^{-i\kappa c_v \left(m_1 u - \frac{v_3}{2}\right)} \right] du\,.$$

Now call the two terms here I_{L1} and I_{L2}. I_{L1} comes from the upper limit on v.

$$I_{L1} \;=\; \frac{i}{\kappa c_v} e^{-i\kappa c_v v_3} \int_{-h}^{0} e^{-i\kappa (c_u + c_v m_3) u}\, du \;=\; \frac{-\,e^{-i\kappa c_v v_3}}{\kappa^2 c_v\,(c_u + c_v m_3)} \left[1 \;-\; e^{+i\kappa (c_u + c_v m_3) h} \right]$$

From the lower limit on the left side we get

$$I_{L2} \;=\; -\,\frac{i}{\kappa c_v} e^{i\kappa c_v v_3/2} \int_{-h}^{0} e^{-i\kappa (c_u + c_v m_1) u}\, du \;=\; \frac{+\,e^{i\kappa c_v v_3/2}}{\kappa^2 c_v\,(c_u + c_v m_1)} \left[1 \;-\; e^{+i\kappa (c_u + c_v m_1) h} \right]$$

The respective integrals from the right side are

$$I_{R1} \;=\; \frac{i}{\kappa c_v} e^{-i\kappa c_v v_3} \int_{0}^{h} e^{-i\kappa (c_u + c_v m_2) u}\, du \;=\; \frac{+\,e^{-i\kappa c_v v_3}}{\kappa^2 c_v\,(c_u + c_v m_2)} \left[1 \;-\; e^{-i\kappa (c_u + c_v m_2) h} \right],$$

$$I_{R2} \;=\; -\,\frac{i}{\kappa c_v} e^{i\kappa c_v v_3/2} \int_{0}^{h} e^{-i\kappa (c_u + c_v m_1) u}\, du \;=\; \frac{-\,e^{i\kappa c_v v_3/2}}{\kappa^2 c_v\,(c_u + c_v m_1)} \left[1 \;-\; e^{-i\kappa (c_u + c_v m_1) h} \right].$$

The integral is $I_{L1} + I_{L2} + I_{R1} + I_{R2}$. Because I_{L2} and I_{R2} both come from the edge E_1, there is some cancellation between them:

$$I_{L2} + I_{R2} \;=\; \frac{+\,e^{i\kappa c_v v_3/2}}{\kappa^2 c_v\,(c_u + c_v m_1)} \left[e^{-i\kappa (c_u + c_v m_1) h} \;-\; e^{+i\kappa (c_u + c_v m_1) h} \right] \;=\; \frac{-i\,2h\,e^{i\kappa c_v v_3/2}}{\kappa c_v}\, \frac{\sin \kappa h (c_u + c_v m_1)}{\kappa h\,(c_u + c_v m_1)}\,.$$

This is the well known '$\sin(x)/x$' far field pattern in diffraction from a slit. It tends to 1 as the argument tends to 0, which is when $c_v/c_u = -1/m_1$, that is, when the point of listening Q is square onto the edge E_1 making $\mathbf{e_r} \cdot (\mathbf{p_2} - \mathbf{p_1}) = 0$. The same must apply for $\mathbf{e_r}$ normal to the other two sides. To bring this out, write

$$I_{L1} \;=\; \frac{-h\,e^{-i\kappa c_v v_3}}{\kappa c_v} \left[\frac{1 \;-\; \cos \kappa h\,(c_u + c_v m_3)}{\kappa h\,(c_u + c_v m_3)} \;-\; i\, \frac{\sin \kappa h\,(c_u + c_v m_3)}{\kappa h\,(c_u + c_v m_3)} \right] \qquad (A1.3)$$

$$I_{R1} \;=\; \frac{+h\,e^{-i\kappa c_v v_3}}{\kappa c_v} \left[\frac{1 \;-\; \cos \kappa h\,(c_u + c_v m_2)}{\kappa h\,(c_u + c_v m_2)} \;+\; i\, \frac{\sin \kappa h\,(c_u + c_v m_2)}{\kappa h\,(c_u + c_v m_2)} \right]. \qquad (A1.4)$$

As the respective denominator tends to zero, the $1 - \cos(..)$ contribution tends to 0 whilst the $\sin(..)$ tends to 1 as $\sin(x)/x$. The radiation directivity is therefore three rotated and superimposed $\sin(x)/x$ lobes, each oriented with one edge, and modulated by some phase factors.

Several other special cases must be considered. The c_v in all the denominators implies that $c_v \to 0$ should be evaluated by a limiting process. If $c_v = 0$, the whole integral becomes

$$I_{c_v=0} \;=\; \frac{3hv_3}{2}\, \frac{2\,[1 - \cos(\kappa h c_u)]}{(\kappa\, h c_u)^2}\,, \qquad (A1.5)$$

the imaginary part being zero. The factor $3hv_3/2$ is the area, S. There will be equivalent values when $\mathbf{e_r}$ becomes normal to the other two medians. More generally, a Taylor series expansion can

be obtained around $c_u = 0$, $c_v = 0$, where $\mathbf{e_r}$ becomes close to $\mathbf{e_w}$ and the listening point Q is almost square on to the triangle. The real part of the whole integral has the form

$$\Re\, I_{c_u\to 0, c_v\to 0} \;\approx\; S\left\{1 \;+\; \frac{\kappa^2}{12}\left[-c_u^2\, h^2 + c_u c_v h(v_1 - v_2) + c_v^2(v_1 v_2 + v_2 v_3 + v_3 v_1)\right]\right\} \qquad (A1.6a)$$

and the imaginary part is

$$\Im\, I_{c_u\to 0, c_v\to 0} \;\approx\; S\;\frac{-\kappa^3\, v_3^2}{60}\left[c_u^2\, h^2 + c_u c_v h(v_2 - v_1) + c_v^2\, v_1(v_3 + v_1)\right]. \qquad (A1.6b)$$

Clearly at near-normal the integral tends to S with zero imaginary part.

All this means that the expression for the potential ϕ has the form of a spherical wave $Se^{i\kappa r}/r$ weighted by the area S and by a rather complicated function of orientation, $\Omega(c_u, c_v)$, with a value between 0 and 1. When κh is much less than π – the first zero of $\sin(x)/x$ – the factor Ω will be close to 1. That corresponds with $h < \lambda/2$. In fact this will be the case for all our calculations. Typically the wavelength will be 10 cm to 100 cm, but the width of one element will be 1 cm. Indeed, the $\cos\beta$ obliquity factor may have a larger effect in reducing the amplitude in directions away from normal. Therefore, notwithstanding the complications of calculating the phase integral I, little would be lost be setting $\Omega = 1$ and taking $I \approx S$, the element's area.

13.4 Far-field radiation from a rectangular plate

Integration of the Rayleigh-Sommerfeld integral in the far field of a rectangle is less complicated than for a triangle and I include it for completeness.

Let the rectangle have width $2a$ in u and $2b$ in v. Take the origin at its centre – the equivalent of Figure 70. The dipole Rayleigh-Sommerfeld formula becomes

$$\phi(Q) \;=\; -\frac{i\kappa}{2\pi}\,\phi_0\,\cos\beta\,\frac{e^{i\kappa r}}{r}\;\int_{v=-b}^{b}\int_{u=-a}^{a} exp(-i\kappa(c_u u + c_v v))\,du\,dv\,.$$

Note that $c_u = q_u/r = \sin\beta_u$ where q_u is the u co-ordinate of Q, r as usual is the distance from centroid to Q, and β_u is the angle towards Q away from the normal (w axis) in the $u-w$ plane. The integral separates into a product and evaluates to

$$\phi(Q) \;\approx\; -i\frac{\kappa}{2\pi}\,\phi_0\, S\,\cos\beta\,\frac{e^{i\kappa r}}{r}\,\frac{\sin(\kappa a\, c_u)}{\kappa a\, c_u}\,\frac{\sin(\kappa b\, c_v)}{\kappa b v\, c_v} \qquad (A1.7)$$

where the area of the rectangle is $S = 4ab$.

14 APPENDIX 2: More on Kirchhoff for sphere and hemisphere

This Appendix continues the calculations of §9 to illustrate the application of KIrchhoff's expression of Green's theorem and Helmholtz's equation. The examples are for radiation from a sphere or hemisphere.

14.1 Analysis of the Kirchhoff integrand

In this subsection I determine the limiting case of a sphere with small radius a and illustrate the structure of the integrand in the Kirchhoff integral, Eq 21.

Consider a small sphere at long range. Going back to Eqs 21 and 38 with $\phi(R) = Ae^{i\kappa R}/R$ and $d\phi/dR = \phi(R)(i\kappa - 1/R)$ we find for $a << k$, $a << R$,

$$\phi(Q) \;=\; \lim_{a\to 0}\; \frac{-a^2}{2} \int_0^{\theta_{max}} \left[\phi(a)\left(i\kappa - \frac{1}{r}\right)\cos\theta \;-\; \phi(a)\left(i\kappa - \frac{1}{a}\right)(-1)\right] \frac{e^{i\kappa r}}{R}\, \sin\theta\, d\theta$$

where $\phi(a) \equiv \phi_0 \to A/a$ is the potential on the sphere's surface. I have used $r \to R - a\cos\theta$ and $\beta \to \theta$. Only the term in $1/a$ remains significant as $a \to 0$. The expression boils down to

$$\phi(Q) \;\to\; \frac{a\phi(a)e^{i\kappa R}}{2R} \int_0^{\theta_{max}} e^{-i\kappa a\cos\theta}\, \sin\theta\, d\theta \;\to\; \frac{\phi(R)}{2R} \int_0^{\theta_{max}} \sin\theta\, d\theta\,.$$

If $\theta_m = \pi/2$ (the Q-facing hemisphere) the integral over $\sin\theta$ is 1, and if $\theta_{max} = \pi$ (whole sphere) it is 2. These values mean that

1. Kirchhoff's formulation of secondary wave sources all over the sphere correctly reproduces the field of a point source at the centre,
2. for small spheres the two hemispheres facing towards and away from the listener at Q contribute equally to the sound.

The approach to this limit may be found by expanding Eq 38 as a Taylor series about $a = 0$. The ratio of contribution from the Q-facing hemisphere to the total amplitude at Q is

$$\frac{1}{2} + \frac{a}{2\,R} + \frac{k^2\,a^2}{2} - \frac{\left(2\,k^2\,R^2 + 1\right)\,a^3}{4\,R^3} - \frac{\left(8\,k^4\,R^2 - 15\,k^2\right)\,a^4}{48\,R^2} + \frac{\left(4\,k^4\,R^2 - 3\,k^2\right)\,a^5}{16\,R^3} + \cdots \qquad (A2.1a)$$

The corresponding ratio of amplitude from the other hemisphere (facing the $-z$ axis) to the whole is

$$\frac{1}{2} \;-\; \frac{a}{2\,R} \;+\; \frac{a^3}{4\,R^3} \;-\; \frac{\left(8\,k^4\,R^2 + 3\,k^2\right)\,a^4}{16\,R^2} \;-\; \frac{k^2\,a^5}{16\,R^3} + \cdots\,. \qquad (A2.1b)$$

(There is no a^2 terms in this second formula.) These formulae are in agreement with values from numerical integration for a sufficiently small.

Unfortunately there seems no easy way to obtain an equivalent series expansion for k large, equivalent to $\lambda \to 0$. Perhaps a high frequency asymptotic expansion is possible, but that exceeds my mathematical abilities (and the time I wish to spend on this!). However some insight can be gleaned by examining the behaviour of the integrand in Eq 21 *et seq.* This integrand has terms in ϕ_0, acoustic pressure, and $\nabla(\phi_0)$, corresponding to particle displacement and hence velocity, divided by r. This is the large square bracket in Eq 21 and can be thought of as defining an envelope for

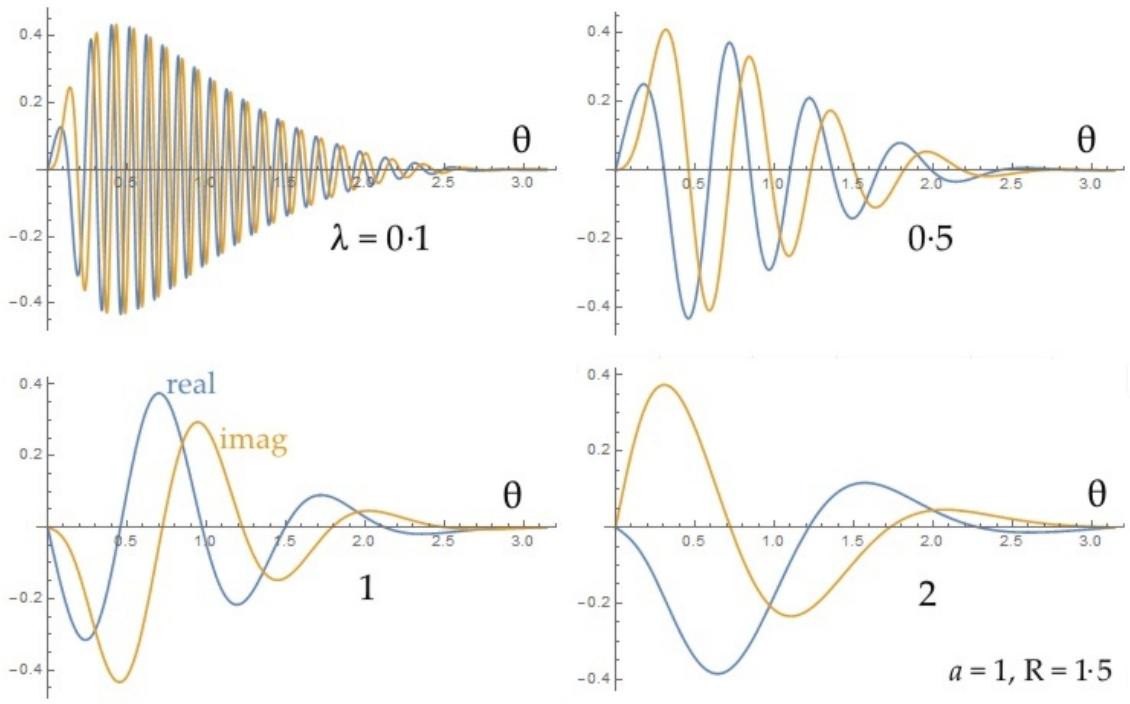

Figure 71: Effect of changing the wavelength on the value of the integrand in Eq 39 around the sphere. Horizontal axis is θ, the angle round the sphere, with $\theta = 0$ defining the direction of Q.

the integrand function onto which the $e^{i\kappa r}$ factor imposes oscillations. From looking at a number of computer-generated graphs I have come to the view that the envelope is defined mainly by the ratio R/a whilst the density of oscillations is controlled mainly by λ/a. Consider, for instance, Figure 71 which shows the effect of changing the wavelength (that is, κa) for R/a constant. The diameter of the sphere is 2 so we expect $2/\lambda$ cycles between $\theta = 0$ and π, and this is indeed the case. The integral in Eq 21 clearly involves a great deal of cancellation between the positive and negative half cycles. There is a modest skew of these graphs to low θ, meaning that the sector facing Q contributes more than that facing away.

The shape of the envelope can be emphasised by setting a very small value for λ. I have done this in Figure 72 to show how the envelope changes with R for a constant. The bunching towards low θ when Q is very close to the sphere is clear. Complementary graphs show little if any change as a and R are varied provided R/a is constant. On each graph a vertical line marks the angle θ_g at which a ray from Q would be tangent to the sphere. (This is when $\cos\theta = a/R$.) The region to the left of this line is the cone of rays seen by geometrical ray theory, while points to its right are in the geometrical shadow, hidden from Q.

Neither Figure 71 nor 72 shows any special feature at θ_g, but one is revealed if we look at the separate contributions from the pressure (ϕ_0) and displacement/velocity ($\nabla\phi_0$) to the integrand in Eq 38. The real and imaginary parts of these are plotted in Figure 73 for $a = 1$, $R = 1 \cdot 5$. You can see that at the edge of the geometrical ray cone, at $\theta = 0 \cdot 84$ in this example, the pressure contribution becomes zero because $\mathbf{n}$ and $\mathbf{e_r}$ are perpendicular. Beyond θ_g the pressure contribution has a phase inversion because the obliquity factor $\cos\beta = \mathbf{n} \cdot \mathbf{e_r}$ is negative there. The pressure contribution up to θ_g enhances the left side of the function's envelope, whilst the out-of-phase part reduces this, so accounting in part for the skew of the envelopes in Figure 72. Contrast this with the

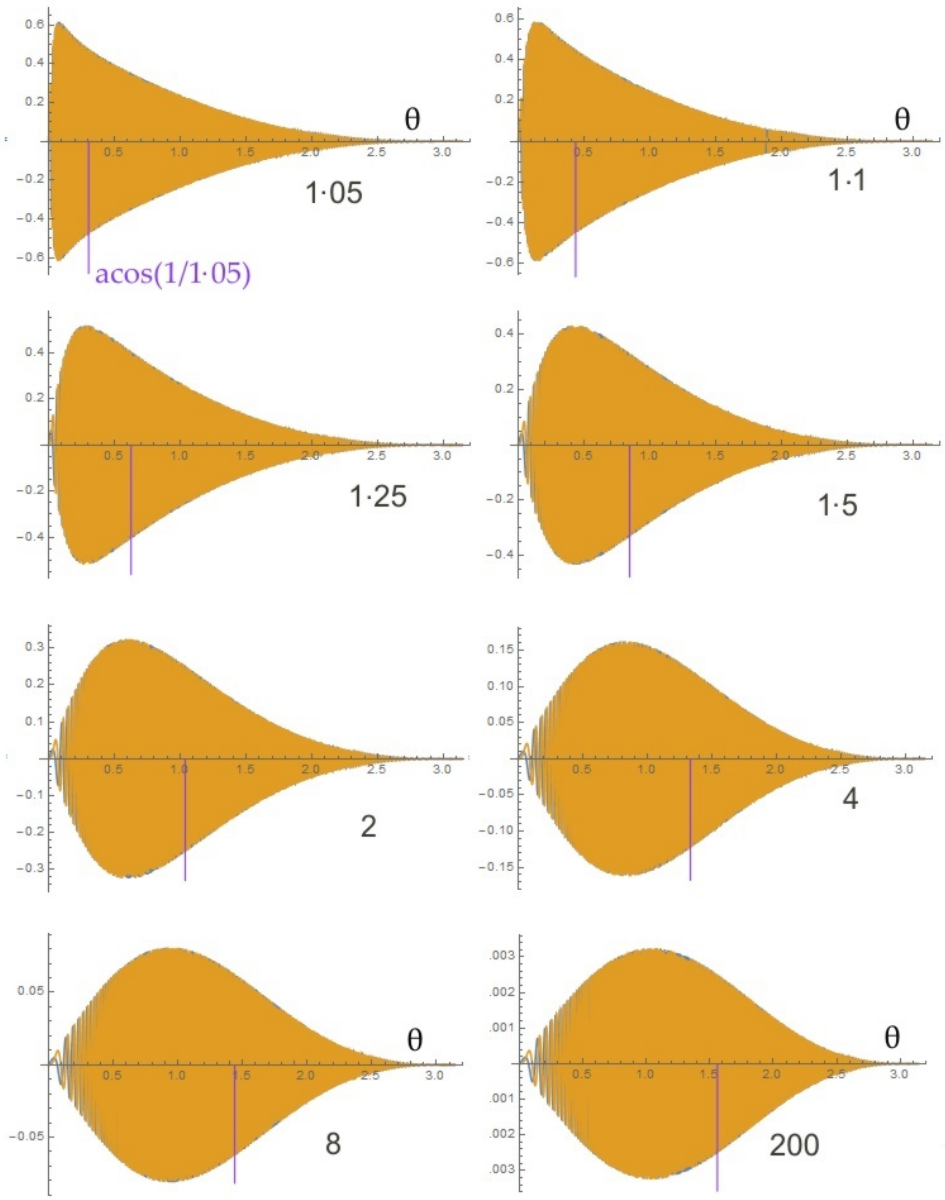

Figure 72: Effect of R/a ratio on the envelope of the integrand in Eq 34, shown by overlap real and imaginary parts for small wavelength ($\lambda = 1/100$). $a = 1$ in all diagrams whilst R is labelled on each.

Rayleigh-Sommerfeld formula where $\cos\beta$ is assumed never to become negative because it applies only to a planar radiator and baffle.

14.2 Hemisphere in a baffle

Consider what happens when a flange in the form of a hollow concentric annulus is added to the breathing mode sphere, as shown in Figure 74a. All the motion is radial so the flange, being of negligible thickness, does not perturb either the sound pressure or the particle displacement. The Kirchhoff integral around this new object should therefore give the same field at Q as the original simple sphere. The maths is consistent with this view because the outwards pointing surface normals at points such as P_2, P_3 on opposite flange faces are equal and opposite so their contributions to the

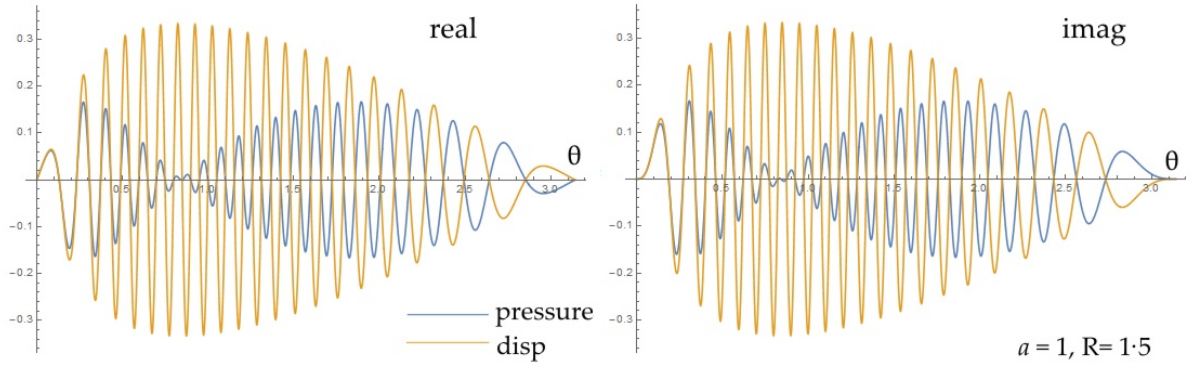

Figure 73: Contributions of the pressure (ϕ_0, blue) and displacement/velocity ($\nabla\phi_0$, orange) to the integrand in Eq 38.

integral in Eq 21 cancel. Now what happens if the outer radius of the flange is made indefinitely large and eventually joins to the infinite outer sphere of Σ, so that the space Ω is cut into two, as in Figure 74b? Then only the right hemisphere plus right-hand side of the flange which faces Q can contribute to the field at Q. The field, however, must still be that of the simple un-flanged sphere. This can only mean that the contribution to the Kirchhoff integral from the infinite flange face (which of course is now the planar baffle of Figure 19) must equal that of the now-hidden left hemisphere.

To specify the integral over the baffle in Figure 74b first observe that the displacement, being radial, is in the plane of the baffle and so normal to the local normal, $\mathbf{n}$. Hence the displacement term $\nabla(\phi)\cdot\mathbf{n} = 0$. Only the pressure term contributes. Let ρ denote the radial distance from O in the plane of the baffle. The point P is at (ρ, ψ) and the element of area is $\rho\,\delta\rho\,\delta\psi$. $\cos\beta = R/r$

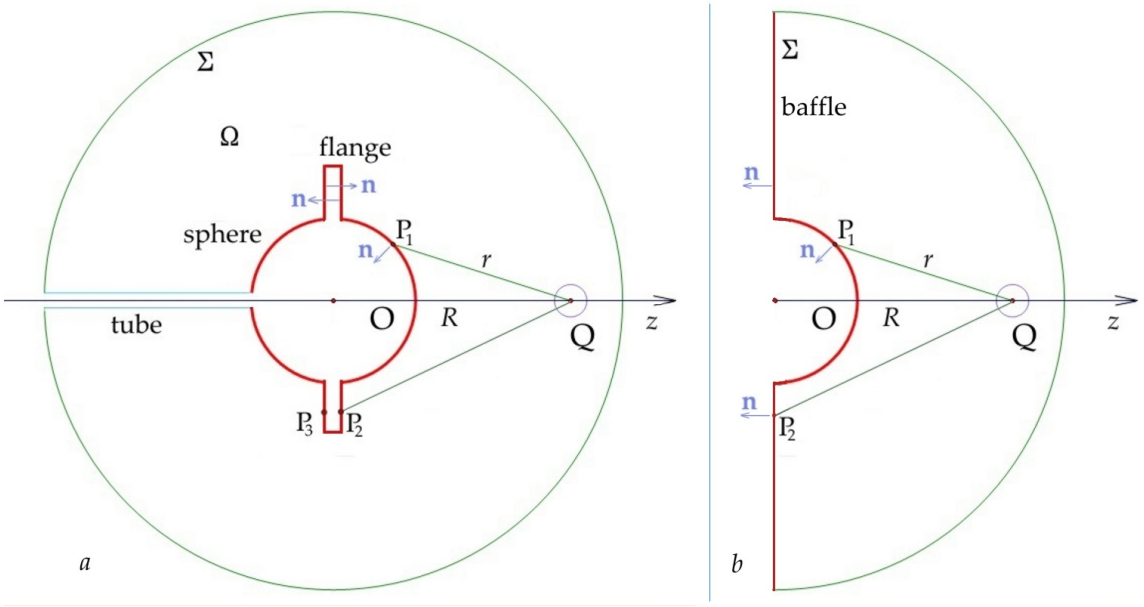

Figure 74: a) Closed Kirchhoff surface Σ defined by a sphere with a concentric hollow flange. b) Extension of the flange into a planar baffle around a hemisphere.

where $r^2 = R^2 + \rho^2$. Using A from Eq 40a, the contribution to $\phi(Q)$ from the baffle is

$$-\frac{A(\kappa,a)}{2}\int_a^\infty \frac{e^{i\kappa\rho}}{\rho}\left(i\kappa-\frac{1}{r}\right)\left(\frac{R}{r}\right)\frac{e^{i\kappa r}}{r}\,\rho\,d\rho \qquad (A2.2)$$

$$= -\frac{AR}{2}\int_a^\infty \frac{\rho}{r^3}\left[\cos\{\kappa(\rho+r)\}+\kappa r\sin\{\kappa(\rho+r)\}\right]d\rho$$
$$-i\,\frac{AR}{2}\int_a^\infty \frac{\rho}{r^3}\left[\sin\{\kappa(\rho+r)\}-\kappa r\cos\{\kappa(\rho+r)\}\right]d\rho\,.$$

In each integral the integrand tends to 0 as $\rho\to\infty$, partly due to the obliquity angle β tending to 90°. One strategy to evaluate this is to split it into two parts: a finite section from $\rho = a$ to some distance h, and a semi-infinite tail. The finite section could then be integrated numerically, and we would hope to find some analytical approximation to the tail. One scheme of this kind was used in the 1830s by the Astronomer Royal, Sir George Airy, to integrate $\cos(ax^3+bx)$ which arose in his classic study of diffraction by water drops, so causing the rainbow. I give an account of this method in Appendix 3, §12.2. It generates an asymptotic series. The series for the four integrals which constitute the real and imaginary parts in Eq 42 are cumbersome to write down, but I have determined their values using only three terms in each asymptotic series. For $a = 1$, $\kappa = 2\pi/0\cdot4$, $R = 5$ and $h = 8$ the tail of the integral (from 8 to infinity) is $-4\cdot375\times10^{-4} + 8\cdot609\times10^{-4}\,i$. Quadrature on the integral from $a = 1$ to $h = 8$ gives $0\cdot00552896 - 0\cdot00126386\,i$. The sum of these is $0\cdot00509143 - 0\cdot000402943\,i$, in excellent agreement with the integral over the left (hidden) side of the hemisphere, which is $0\cdot005091424 - 0\cdot000402947\,i$. Values are summarised in Table 4. Compare the top row with the bottom. It shows that the sound radiated to an on-axis point from a radially vibrating hemisphere in a planar baffle is the same as that from a pulsating whole sphere.

	Real	Imag
$\int_0^\pi$ whole sphere	8·0730	126·8100
$\int_0^{\pi/2}$ over hemisphere	-42·8413	130·8395
$\int_1^8$ on baffle	55·2896	-12·6386
$\int_8^\infty$ on baffle	-4·375	8·609
$\int_1^\infty$ on baffle	50·91424	-4·02947
Sum hemisphere + baffle	8·0733	126·8099

Table 4: Example showing that the hemisphere with baffle in Figure 74 gives the same field as the whole sphere. $a = 1$, $\lambda = 0\cdot4$, $R = 5$. All values have been multiplied by 10^4.

The above calculation is only for points Q on the axis perpendicular to the baffle. What about general points, off the axis? It can be argued that the baffle acts as an acoustic mirror, reflecting every elementary source, so that a vibrating hemisphere plus a rigid baffle behaves entirely equivalently to a complete vibrating sphere. That being true, the same field would occur at all points Q at the same radial distance R. It would be satisfying to demonstrate this directly by integration, and I attempt this below, though the lack of symmetry in the azimuthal angle ψ makes the calculation much more involved.

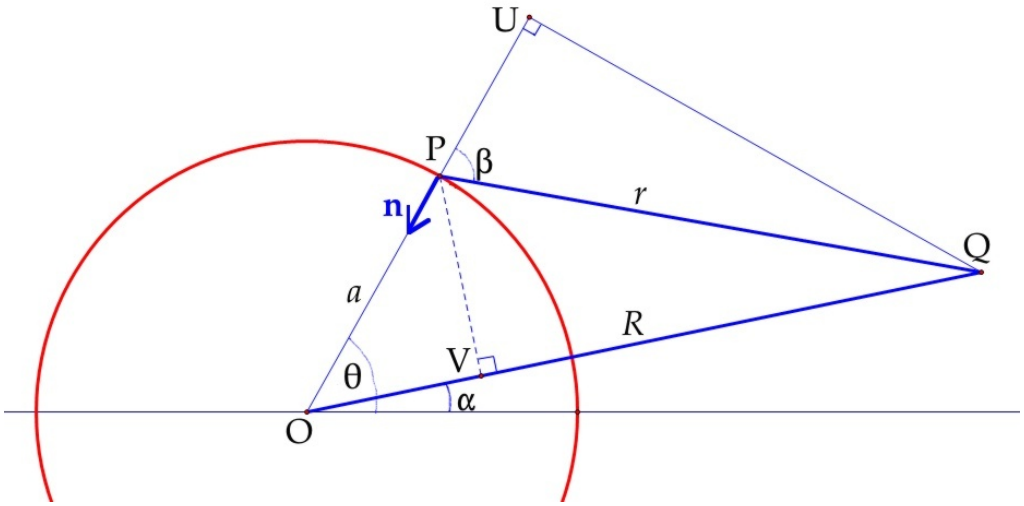

Figure 75: Section at $\psi = 0$ showing Q at range R and polar angkle α.

Figure 75 shows the geometry in the plane containing Q. Using vector analysis, the length PQ for P at general azimuth ψ on the hemisphere is

$$r^2 \;=\; R^2 + a^2 - 2aR(\cos\alpha\,\cos\theta \,+\, \sin\alpha\,\sin\theta\,\cos\psi)$$

and the obliquity factor is

$$\cos\beta \;=\; \frac{R(\cos\alpha\,\cos\theta \,+\, \sin\alpha\,\sin\theta\,\cos\psi) \;-\; a}{r}\,.$$

Using the mirror symmetry about the plane containing Q, the integral over the hemisphere is a generalisation of Eq 38 in §9.1:

$$\phi(Q)|_{hemisphere} \;=\; \frac{\xi_0\,a^2}{2\pi}\int_{\theta=0}^{\pi/2}\int_{\psi=0}^{\pi}\left[\frac{\left(i\kappa-\frac{1}{r}\right)}{\left(i\kappa-\frac{1}{a}\right)}\cos\beta \;+\; 1\right]\frac{e^{i\kappa r}}{r}\,\sin\theta\;d\psi\,d\theta\,. \qquad (A2.3)$$

On the baffle the normal is $(0,0,-1)$ and

$$r^2 \;=\; R^2 + \rho^2 - 2R\rho\cos\psi\,\sin\alpha\,, \qquad \cos\beta \;=\; \frac{R\cos\alpha}{r}\,.$$

Instead of Eq A2.2 we now have the integral over the baffle, after cancellation, as

$$\phi(Q)|_{baffle} \;=\; \frac{R\cos\alpha}{2\pi\left(i\kappa-\frac{1}{a}\right)}\int_0^{\pi}\int_a^{\infty}\left(i\kappa-\frac{1}{r}\right)e^{i\kappa(r+\rho-a)}\,\frac{1}{r^2}\,d\rho\,d\psi\,. \qquad (A2.3)$$

Numerical results for $a = 1$, $\lambda = 0\cdot 4$, $R = 5$ are listed in Table 5. The quadrature was done using Mathematica. The values for the baffle at $\alpha = 0$ are those in Table 4, obtained using the asymptotic expansion. For other values of α I took the easy way out and let Mathematica integrate numerically in steps out to $\rho = 60$, by which the contributions were only in the second decimal place. The last two columns show that adding the fields from hemisphere and baffle does indeed give the same value as for a complete sphere, for all α. This is true even at $\alpha = 90°$ where Q is in the plane of the baffle. This, therefore, is direct confirmation that the baffle acts as a mirror, adding a virtual left hemisphere to the physically present right one.

	Hemisphere		Baffle		Sum	
α°	Real	Imag	Real	Imag	Real	Imag
0	-42·84	130·84	50·91	-4·03	8·07	126·81
15	-2·41	132·08	10·48	-5·22	8·07	126·86
30	28·66	122·08	-20·59	4·70	8·07	126·78
45	-0·99	122·70	9·07	4·13	8·08	126·83
60	-1·14	138·22	9·20	-11·42	8·06	126·80
75	22·52	124·70	-14·43	2·12	8·09	126·82
90	8·45	111·12	-0·37	15·69	8·08	126·81
sphere					8·07	126·81

Table 5: $\phi(Q)$ from radially vibrating hemisphere in an infinite baffle, showing that it is equivalent to a complete sphere. $a = 1$, $\lambda = 0 \cdot 4$, $R = 5$. All values have been multiplied by 10^4.

15 APPENDIX 3: Integrals of highly oscillatory functions

This Appendix first looks into the conjecture, referred to in §14.2 of Appendix 2, that integrals of functions of the form $E(x)\sin(kx-\alpha)$ tend to zero as k tends to infinity. Here $E(x)$ is an envelope which modulates the sine wave. §15.2 then describes a method for obtaining a converging semi-infinite integral as a series.

15.1 Limit as $k \to \infty$

The integrals in Kirchhoff theory cannot generally be done in closed form, so consider an example for which a closed form can be found. I choose $E(x) = x(x-2)^2$, illustrated in Figure 76. This is zero at $x = 0$ and 2, and has a similar skewed shape as the envelope curves in Figure 71. The integral evaluates to

$$I = \int_0^2 x(x-2)^2 \sin(kx-\alpha)\,dx = \frac{4\sin\alpha}{k^2} + \frac{4}{k^3}\left[2\cos\alpha + \cos(2k-\alpha)\right] - \frac{6}{k^4}\left[\sin\alpha + \sin(2k-\alpha)\right].$$

The sine and cosine functions here can each swing in value between 1 and −1, but there is clearly a trend towards zero as k increases. More formally, $|I|$ is bounded by a function which tends to zero like $1/k^2$ as $k \to \infty$.

Take an example of a semi-infinite integral:

$$\int_0^\infty e^{-x}\sin(kx-\alpha)dx = \frac{k\cos\alpha - \sin\alpha}{k^2+1}.$$

This is bounded as $k \to \infty$ by a function which falls as $1/k$.

The explanation is that adjacent positive and negative half cycles almost cancel each other when the width of a cycle is small compared with the distance in x over which the envelope function $E(x)$ is changing. If the gradient dE/dx were zero, cancellation would be exact. The effect will still occur even if the spacing of the cycles changes gradually, as with $\cos\sqrt{x^2+1}$.

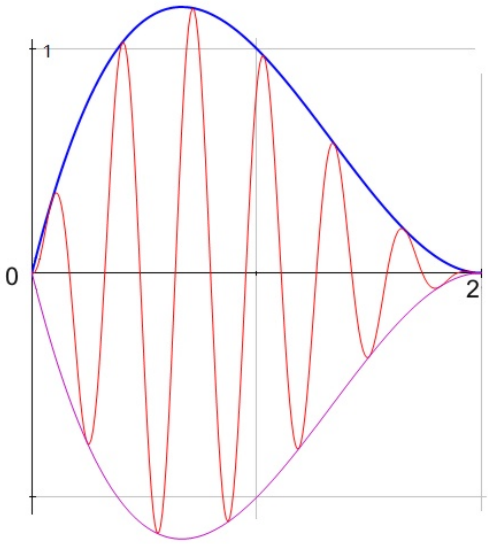

Figure 76: Envelope function $x(x-2)^2$ modulating $\sin(20x - 0\cdot 2)$.

15.2 Numerical evaluation of some semi-infinite integrals

There is a scheme for evaluating the 'tail' of a certain types of semi-infinite integral by expressing it as a converging series through repeated integration by parts. I came across this elegant method in an ancient paper by George Airy describing his classic study of the rainbow[15]. Suppose the integral is

$$I_0 \;=\; \int_h^\infty E(x)\cos f(x)\,dx$$

where $E(x)$ does not increase as $x \to \infty$ (in a manner to be made precise below), and that $f(x) \to \infty$ as $x \to \infty$. We use the integration by parts rule

$$\int_a^b p\,dq \;=\; pq\,|_a^b \;-\; \int_a^b q\,dp\,.$$

$$\text{Let} \quad v_0 \;=\; \frac{1}{df/dx}\,.$$

$$\text{Then} \qquad I_0 \;=\; \int_h^\infty E v_0\,\cos f(x)\,\frac{df}{dx}dx\,.$$

Take $p = Ev_0$ and $dq = \cos f(x)\,(df/dx)\,dx \equiv \cos f\,df$. Then $dp = v_1 dx$ where $v_1 = d(E\,v_0)/dx$ and $q = \sin f$ giving

$$I_0 \;=\; Ev_0 \sin f(x)\,|_h^\infty \;-\; \int_h^\infty v_1(x)\sin f(x)\,dx\,.$$

Provided $\lim_{x\to\infty} v_1$ is finite, the first term, from pq, is finite. We are then clear to expand the new integral

$$\int_h^\infty v_1(x)\sin f(x)\,dx \;=\; \int_h^\infty [v_1\,v_0]\sin f(x)\frac{df}{dx}\,dx$$

similarly by parts and obtain the second term in the series

$$v_1\,v_0\cos f\,|_{x=h}$$

provided again that the upper limit is finite. With many integrands $E(x)\cos f(x)$ the upper limits will all be 0. In practice 4 to 6 terms are usually sufficient, particularly if a high value of h makes the tail short. The whole series is

$$\int_h^\infty E(x)\cos f(x)\,dx \;\approx\; V_0[-E(h)+V_2-V_4+\cdots]\sin f(h) \;+\; V_0[-V_1+V_3-V_5+\cdots]\cos f(h) \quad (A3.1)$$

where

$$V_1 = \left.\frac{d(Ev_0)}{dx}\right|_h, \qquad V_2 = \left.\frac{d(v_1v_0)}{dx}\right|_h, \qquad V_3 = \left.\frac{d(v_2v_0)}{dx}\right|_h, \qquad V_4 = \left.\frac{d(v_3v_0)}{dx}\right|_h, \quad etc.$$

The equivalent series for $E(x)\sin f(x)$ is

$$\int_h^\infty E(x)\sin f(x)\,dx \;\approx\; V_0[E(h)-V_2+V_4-\cdots]\cos f(h) \;+\; V_0[-V_1+V_3-V_5+\cdots]\sin f(h) \quad (A3.2)$$

Here are two illustrations of the method using examples for which the exact answers are known. Take first the Cosine Integral, $\mathrm{Ci}(h)$:

$$-\mathrm{Ci}(x) \;=\; \int_h^\infty \frac{\cos x}{x}\,dx\,.$$

[15] Camb. Phil. Soc. Trans. Vol 6, Number 3, 1838.

We have

$$E = 1/x, \qquad f = x, \qquad v_0 = 1, \qquad v_1 = \frac{-1}{x^2}, \qquad v_2 = \frac{2}{x^3}, \qquad v_3 = \frac{-6}{x^4}, \qquad etc.$$

and the integral is

$$-\mathrm{Ci}(h) \;\approx\; \left(-\frac{1}{h} + \frac{2}{h^3} - \frac{24}{h^5} + \frac{720}{h^7} - \frac{40320}{h^9}\right)\sin h + \left(\frac{1}{h^2} - \frac{6}{h^4} + \frac{120}{h^6} - \frac{5040}{h^8} + \frac{362880}{h^{10}}\right)\cos h$$

Some care is needed when substituting numbers because the numerators are growing rapidly – they are $N!$, which grows faster than any power of h. This is in fact the asymptotic series given in Abramowitz and Stegun's Handbook at articles 5.2.9 and 5.2.34. It does not converge, but the first few terms do approach the correct value and so provide a worthwhile approximation. For smaller h, better accuracy is obtained with fewer terms. For instance, if $h = 10$, terms to h^6 (*i.e.* three in each sub-series) gives $0\cdot04545667$ to compare with the correct answer $\mathrm{Ci}(10) = -0\cdot04545643$. Including terms to h^8 gives $0\cdot04545979$ and to h^{10} gives $0\cdot04545128$. For completeness, here is the corresponding series for the Sine Integral:

$$\mathrm{Si}(h) \;=\; \frac{\pi}{2} \;-\; \left(\frac{1}{h} - \frac{2!}{h^3} + \frac{4!}{h^5} - \frac{6!}{h^7} + \frac{8!}{h^9}\right)\cos h \;-\; \left(\frac{1}{h^2} - \frac{3!}{h^4} + \frac{5!}{h^6} - \frac{7!}{h^8} + \frac{9!}{h^{10}}\right)\sin h$$

Terms up to and including h^8 give $\mathrm{Si}(10) = 1\cdot65832$ and to h^{10} give $1\cdot65837$, straddling the true value of $1\cdot65835$.

The second example is of a more complicated function with the form $E(x)\sin f(x)$. Gradshteyn and Ryzhik's handbook at 3.852.1 gives

$$\int_0^\infty \frac{\sin(kx^2)}{x^2}dx \;=\; \sqrt{\frac{k\pi}{2}}\,.$$

The tail from h to ∞ is found as above:

$$E(x) = \frac{1}{x^2}, \qquad f(x) = kx^2, \qquad v_0 = \frac{1}{2kx}, \qquad v_1 = \frac{3}{2kx^4}, \qquad v_2 = \frac{15}{4k^2x^6}, \quad etc.$$

$$\int_h^\infty \frac{\sin(kx^2)}{x^2}dx \;\approx\; \left[\frac{1}{2\,k\,h^3} - \frac{15}{8\,k^3\,h^7} + \frac{945}{32\,k^5\,h^{11}} - \frac{135135}{128\,k^7\,h^{15}} + \ldots\right]\cos(kh^2)$$
$$+ \left[\frac{3}{4\,k^2\,h^5} - \frac{105}{16\,k^4\,h^9} + \frac{10395}{64\,k^6\,h^{13}} - \frac{2027025}{256\,k^8\,h^{17}} + \ldots\right]\sin(kh^2)\,.$$

Here $105 = 3.5.7$, $945 = 3.5.7.9$, etc. Take an arbitrary number for k of $2\cdot37$ and take $h = 2$. Terms to h^{15} give the tail to be $-0\cdot02556$ and to h^{21} give $-0\cdot02562$. Numerical integration over $x = 0$ to 2 gives $1\cdot95504$. So the calculated value to infinity lies between $1\cdot92948$ and $1\cdot92942$, again straddling the true value of $\sqrt{a\pi/2} = 1\cdot92945$.

It might seem at first sight that this function is an exception to the common behaviour noted in §15.1 – that integrals of $E(x)\sin kF(x)$ tend to zero as $k \to \infty$ – since this integral from 0 to ∞ increases as $\sqrt{k}$. However it is not really an exception. The bulk of the integral comes from near $x = 0$ where the integrand increases as k. The integrand oscillates only for $x > \sqrt{(\pi/a)}$, and here the above asymptotic series is in powers of $1/k$.

16 APPENDIX 4: Spheroids: co-ordinates and wave functions

This is a long appendix giving an outline account of the solution of Helmholtz's equation in spheroidal co-ordinates. It parallels §5 on the wave equation in spherical co-ordinates, but goes into more detail because of the the greater complexity and lesser familiarity of spheroidal wave functions.

If a sphere is stretched along its z axis so that it looks like a rugby ball with an elliptical longitudinal section, it is a prolate spheroid. Conversely, if compressed along the z axis into a disc with elliptical section, it is an oblate spheroid. The wave equation can be separated in spheroidal co-ordinates, as described in textbooks and in §16.4 below. Prolate co-ordinates are obtained by rotating an ellipse about its major axis, and oblate ones about the minor axis. It is sensible to start by looking at the equations which define a suite of confocal ellipses and their orthogonal hyperbolae. Unfortunately there are at least three schemes for doing this described in the literature, using different notations. This can cause confusion so, in order to be entirely confident how to use published tables and computer codes of spheroidal wave functions, I here go into this matter in a fairly thorough, even plodding way. A comprehensive, advanced account is given in the book by Carson Flammer and there is a terse summary with tables in Chapter 21 of Abramowitz and Stegun's classic handbook. Both these books use ξ as a co-ordinate. Since ξ in my article stands for particle displacement, I used ζ instead.

16.1 Confocal ellipses and hyperbolae

We start with some old fashioned geometry. An ellipse can be defined as the locus of a point P which moves so that the sum of its distance d_1, d_2 from two fixed points, the foci, is constant. Let the axes be z and w rather than the usual x and y; this will ease transition to spheroids. The construction is illustrated in Figure 77. If the foci are at $(+f, 0)$ and $(-f, 0)$, the sum is

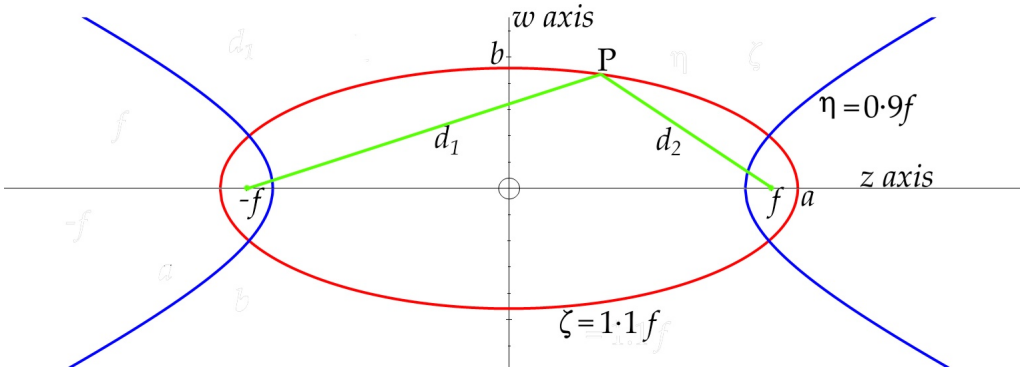

Figure 77: Construction of orthogonal ellipse and hyperbola. a and b apply to the ellipse.

$$d_1 + d_2 \;=\; \sqrt{(z+f)^2 + w^2} \;+ \sqrt{(z-f)^2 + w^2} \;=\; \text{constant, } 2a \text{ say.}$$

a will be found to be one of the semi-axes, where $w = 0$. Use the notation $d_1 = \sqrt{D_1}$, $d_2 = \sqrt{D_2}$. Squaring and squaring again

$$D_1 + D_2 - 4a^2 \;=\; -2\sqrt{D_1 D_2} \quad \text{so} \quad (D_1 - D_2)^2 - 8a^2(D_1 + D_2) + 16a^4 \;=\; 0\,.$$

Substituting

$$a^2(a^2 - f^2) \;-\; a^2 w^2 \;-\; z^2\,(a^2 - f^2) \;=\; 0$$

Now let $a^2 - f^2 = b^2$ and rearrange to obtain the standard form for an ellipse

$$\frac{z^2}{a^2} + \frac{w^2}{b^2} = 1\,.$$

Setting $z = 0$ shows that b is the other semi-axis .

The next step towards spheroidal co-ordinates is to introduce ζ defined by

$$\zeta \equiv \frac{d_1 + d_2}{2f} = \frac{a}{f}\,, \quad \text{from which} \quad b^2 = f^2(\zeta^2 - 1)\,.$$

Since $a \geq f$, $\zeta \geq 1$. In terms of the co-ordinate ζ the ellipse with semi-focal distance f is

$$\frac{z^2}{f^2\zeta^2} + \frac{w^2}{f^2(\zeta^2 - 1)} = 1, \qquad \zeta \geq 1\,. \tag{A4.1}$$

From the way ζ has been defined as a/f is will be clear that ζ is constant for any particular ellipse. Moreover, all ellipses with different ζ but the same f will have the same two foci – they are a confocal family defined by f alone. The eccentricity e is such that $f = ae$. Therefore ζ is the reciprocal of e.

There is also a corresponding confocal family of hyperbolae. A hyperbola can be defined as the locus of a point P which moves so the *difference* $d_1 - d_2$ between its distances from two fixed foci is constant and equal to $2f$ (see Figure 77 again). Squaring once as above, the relation is

$$D_1 + D_2 - 4a^2 = +2\sqrt{(D_1 D_2)}\,,$$

but squaring a second time obliterates the sign on the right side and again produces $(D_1 - D_2)^2 - 8a^2(D_1 + D_2) + 16a^4 = 0$. The hyperbola would seem to be masked by the equation of the ellipse. In fact both ellipse and hyperbola *do* share this equation; the distinction is that ζ^2 occupies values on the real number line ≥ 1 while the hyperbola's parameter η occupies its complement, $\eta^2 \leq 1$. Thus the equation of the family of hyperbolae is

$$\frac{z^2}{f^2\eta^2} + \frac{w^2}{f^2(\eta^2 - 1)} = 1, \quad \text{or} \quad \frac{z^2}{f^2\eta^2} - \frac{w^2}{f^2(1 - \eta^2)} = 1, \qquad \eta^2 \leq 1\,. \tag{A4.2}$$

η is defined by $\eta = (d_1 - d_2)/(2f)$ which is constant for any hyperbola. Both ζ and η are dimensionless quantities. Provided the ellipses and hyperbolae share the same semi-focal distance f, they are mutually orthogonal families of curves. We might expect the limiting values of $\zeta^2 = 1$ and $\eta^2 = 1$ to coincide. These values produce either a degenerate ellipse or hyperbola lying in the z axis, with $\eta = -1$ occupying $z \leq -1$, $\zeta = \pm 1$ occupying $-1 \leq z \leq +1$, and $\eta = +1$ occupying $1 \leq z$.

16.2 Prolate spheroid geometry

Prolate spheroids are obtained by rotating the ellipse in Figure 77 about its long axis. I shall always use z as the axis of rotation, so in the prolate case $a > b$. The three prolate spheroidal co-ordinates are ζ, η and ψ. They define mutually orthogonal surfaces as follows:

- confocal ellipsoids for each of which ζ = constant. $1 \leq \zeta < \infty$. The limiting case $\zeta = 1$ is a line joining the two foci of the family of ellipsoids, and has length $2f$; the ellipsoid reduces to a needle.

- confocal hyperbolae for each of which η = constant. $-1 \leq \eta \leq +1$. $\eta = 0$ is the plane $z = 0$ through the centre O of the ellipsoids. $\eta = +1$ is the $+z$ axis from the + focus to ∞, and $\eta = -1$ the corresponding $-z$ axis.

- a family of planes each containing the z axis, defined by ψ = constant and measured from the $x-z$ plane for which $\psi = 0$ or 2π. ψ thus specifies the azimuth of a point P around the polar z axis.

Prolate co-ordinates are related to the usual x, y z Cartesian co-ordinates and to w by $w^2 = x^2 + y^2$ and

$$x = f\sqrt{(\zeta^2-1)(1-\eta^2)}\,\cos\psi, \qquad y = f\sqrt{(\zeta^2-1)(1-\eta^2)}\,\sin\psi, \qquad z = f\zeta\eta\,. \qquad (A4.3)$$

Curves of constant ζ and η are plotted in Figure 78 in the $z-w$ plane. The pointed end of the major axis (e.g. point A in Figure 78) is at $\eta = +1$ so here $a = f\zeta$. Similarly, the mid-plane of the barrel-shaped side containing the minor axis (all points like B) is at $\eta = 0$, so $b = f\sqrt{\zeta^2-1}$. The equation of the ellipsoid is therefore just Eq A4.1 interpreted in three dimensions:

$$\frac{z^2}{a^2} + \frac{w^2}{b^2} = 1 \qquad \text{or} \qquad \frac{z^2}{f^2\zeta^2} + \frac{w^2}{f^2(\zeta^2-1)} = 1\,.$$

a and b are related to the semi-focal distance f by $f = \sqrt{a^2-b^2} = a\,e$ where e is the eccentricity. The corresponding orthogonal hyperbolae as given by Eq A4.2. In Figure 78 Flammer has labelled the hyperbola by η values corresponding to the cosines of the angle which the asymptotes of each hyperbola make with the z axis. For this reason η is called the angular co-ordinate. However in the limiting case of $\zeta = 1$, when the ellipsoid is a mere needle, η also marks out the distance $f\eta$ from the centre towards tip at $+f$ or $-f$.

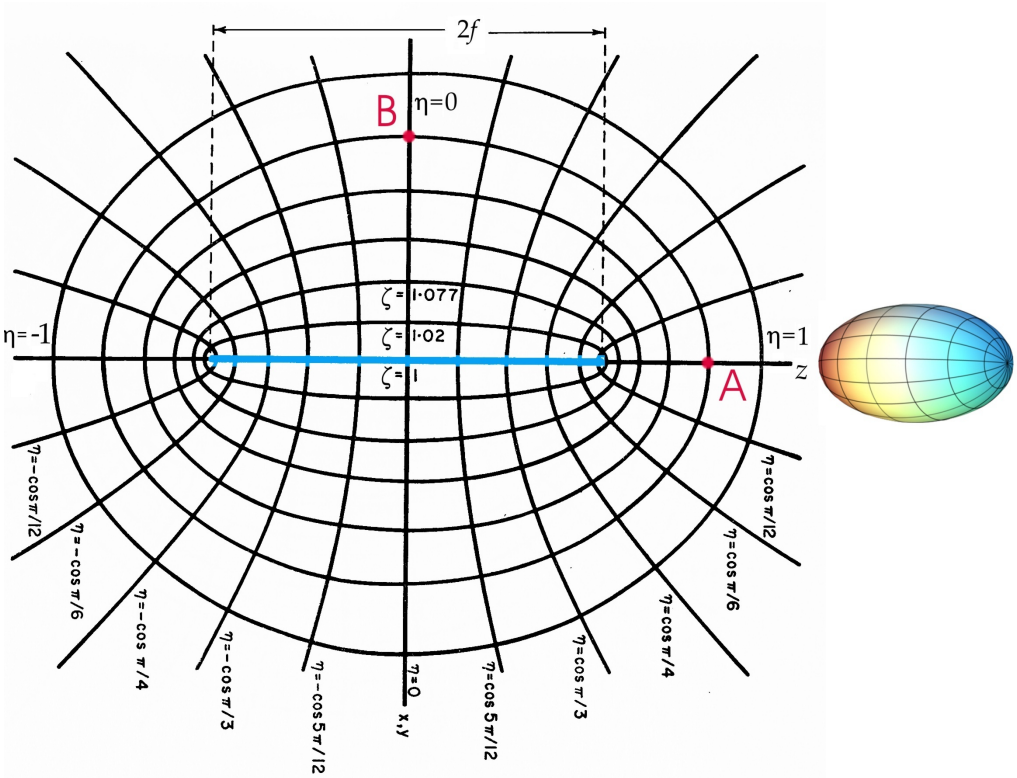

Figure 78: Prolate spheroidal co-oordinates ζ = constant (ellipses) and η = constant (hyperbolae). Illustration for constant inter-focal distance $2f$, taken from the book by C. Flammer. The 3D surfaces are obtained by rotation about the z axis.

The inverses of Eq A4.3, obtained in terms of the distances from the two foci, are

$$\zeta = \frac{1}{2f}[\sqrt{w^2+(z+f)^2}+\sqrt{w^2+(z-f)^2}\,],$$

$$\eta = \frac{1}{2f}[\sqrt{w^2+(z+f)^2}-\sqrt{w^2+(z-f)^2}\,]. \qquad (A4.4)$$

Note something rather odd here: in Cartesian co-ordinates the cross-sectional ellipse is described by two variables, w and z, but in the spheroidal ones there are three variables, ζ, η and f. Let me clarify the relation between ζ and the size of an ellipsoid. The two semi-axes have lengths $f\zeta$ and $f\sqrt{\zeta^2-1}$ so f and ζ have equal roles in determining the size of an ellipse. ζ is a dimensionless parameter which controls aspect ratio and shape, whilst f is a length scale magnifying or shrinking the overall size. Far away from the centre O of the ellipse the distance from O tends to $f\zeta$. Figure 78 shows how the ellipsoid would swell as if inflated if ζ increases while f remains fixed. In §16.6 I show how these confocal ellipses are related to the wavefronts of an outgoing wave.

In §11.3 and Appendix 5 I indulge in some speculation regarding possible relations between the ratio of potential to displacement in the radiated wave and the curvature of the wavefronts. For this purpose it will be necessary to know the principal radii of curvature of the ellipsoid for comparison with conjectured relations. Tangent circles at points A and B are drawn onto the sectional ellipse in Figure 79. Observe that one lies inside the ellipsoid, the other outside. The circle which fits best to the elliptical section at point B at $z=0$, $\eta=0$ is

$$z^2+\left(w-b+\frac{a^2}{b}\right)^2 = \frac{a^4}{b^2}$$

so the radius of curvature in the $w-z$ plane here is

$$\frac{a^2}{b} = \frac{f\zeta^2}{\sqrt{\zeta^2-1}}. \qquad (A4.5)$$

The other principal radius here is obviously b. At the pointed tips of the spheroid, points A in Figure 79, at $z=\pm a$, $\eta=\pm 1$, the best-fit sphere is

$$\left(z-a+\frac{b^2}{a}\right)^2+w^2+ = \frac{b^4}{a^2}$$

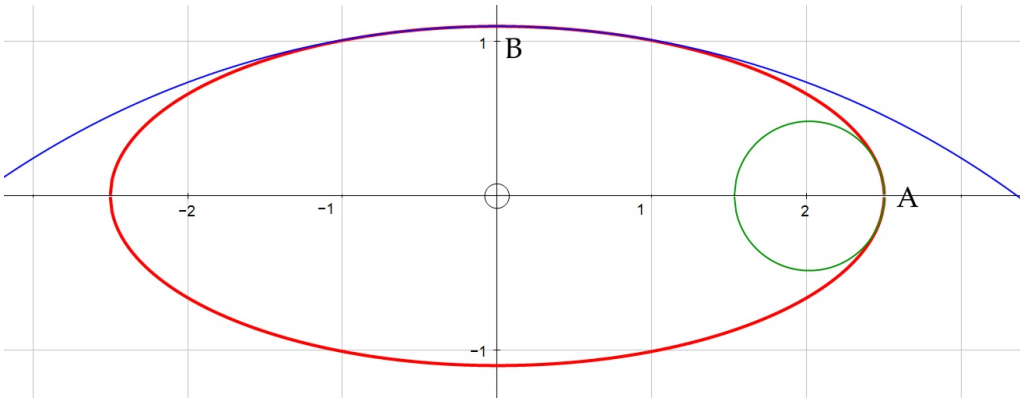

Figure 79: Elliptical longitudinal section of prolate spheroid showing tangent circles at positions A and B. Illustration for $a=2\cdot 5$, $b=1\cdot 1$, $a^2/b=5\cdot 68$, $b^2/a=0\cdot 48$.

and both principal radii are

$$\frac{b^2}{a} \;=\; \frac{f(\zeta^2-1)}{\zeta}\,. \qquad (A4.6)$$

To convert from scalar displacement potential ϕ to vector displacement $\boldsymbol{\xi}$ we will also need the vector gradient operator ∇ operating on ϕ. In any set of curvilinear co-ordinates this is

$$\nabla\phi \;=\; \frac{1}{h_1}\frac{\partial\phi}{\partial u_1}\,\mathbf{e_1} \;+\; \frac{1}{h_2}\frac{\partial\phi}{\partial u_2}\,\mathbf{e_2} \;+\frac{1}{h_3}\frac{\partial\phi}{\partial u_3}\,\mathbf{e_3} \qquad (A4.7)$$

where the h_j are scale factors, the u are the independent variables and the $\mathbf{e}$ are unit vectors along the co-ordinate directions. The h_j are the rates of change of a position vector $\mathbf{p}$ on the ellipsoid with respect to the j^{th} co-ordinate. For prolate spheroidal co-ordinates $u_1 = \zeta$, $u_2 = \eta$, $u_3 = \psi$ and the scale factors can be found by differentiating Eq A4.1:

$$h_\zeta \;\equiv\; \left|\frac{\partial\mathbf{p}}{\partial\zeta}\right| \;=\; \left|\frac{f\sqrt{1-\eta^2}}{\sqrt{\zeta^2-1}}\;\mathbf{e_w} + f\eta\;\mathbf{e_z}\right| \;.$$

We obtain

$$h_\zeta \;=\; f\sqrt{\frac{\zeta^2-\eta^2}{\zeta^2-1}}, \qquad h_\eta \;=\; f\sqrt{\frac{\zeta^2-\eta^2}{1-\eta^2}}, \qquad h_\psi \;=\; f\sqrt{(\zeta^2-1)(1-\eta^2)}\,. \qquad (A4.8)$$

If ϕ is rotationally symmetric and if we look only at the points where $z = a$, $w = b$, then ϕ varies only with ζ. At these special points there is a considerable simplification in the gradient:

$$\nabla\phi \;\to\; \frac{1}{f}\sqrt{\frac{\zeta^2-1}{\zeta^2-\eta^2}}\;\frac{\partial\phi}{\partial\zeta}\,\mathbf{e}_\zeta \qquad \eta = 0 \text{ or } 1 \qquad (A4.9)$$

where $\mathbf{e}_\zeta$ points radially in the w direction at $(0,b)$ and in the polar z direction at $(a,0)$.

16.3 Oblate spheroidal co-ordinates

The ellipse which generates the spheroid is rotated about its minor axis. Unfortunately there is no single accepted way for defining the oblate co-ordinates; at least three schemes are in use, so translations are needed. The first – call it Scheme 1 – has greatest continuity with the prolate system above, and it used in the analysis pages of Chapter 21 in Abramowitz and Stegun's classic 'Handbook of Mathematical Functions'. It is different from Flammer's. I find the account in Abramowitz and Stegun misleading in some places, particularly over the interpretation of their ξ when used for prolate and for oblate co-ordinates (see their tables 21.3 and 21.4). As I show below, the two cases are *not* the same, even though they use the same symbol.

Oblate co-ordinates look like their prolate counterparts, though rotated by 90°. z is still the rotation axis but now in Scheme 1 $a < b$. With $w^2 = x^2 + y^2$ the equation of each ellipsoid is

$$\frac{z^2}{a^2}+\frac{w^2}{b^2} \;=\; 1 \qquad \text{or} \qquad \frac{z^2}{f^2(\zeta^2-1)}+\frac{w^2}{f^2\zeta^2} \;=\; 1\,, \qquad \zeta \ge 1\,.$$

The hyperbolae are

$$-\frac{z^2}{f^2(1-\eta^2)}+\frac{w^2}{f^2\eta^2} \;=\; 1\,, \qquad \eta^2 \le 1\,.$$

In the limit $\zeta \to 1$ the spheroid flattens to a disc in the $z = 0$ plane. η is still in the range $-1 \le \eta \le 1$, but now $\eta = \pm 1$ is the plane of the limiting circular disc. The z axis is normal to the limiting disc at

$\eta = 0$. In Scheme 1 the oblate co-ordinates remain related to Cartesian co-ordinates by Eq A4.1, and the scale factor h_ζ is also unchanged. For reasons which should (or merely may) become apparent, this scheme will not be used further.

I now describe the other two schemes. Scheme 2 is perhaps the most fundamental in that Schemes 1 and 3 can be derived from it. In Scheme 2 the two independent quantities are angles p and q. The Cartesian axes are

$$w \;=\; f\,\sinh p\,\sin q\,, \qquad z \;=\; f\,\cosh p\,\cos q\,.$$

One semi-axis is $f\cosh p$, the other $f\sinh p$. Consequently

$$\frac{z^2}{f^2\cosh^2 p} + \frac{w^2}{f^2\sinh^2 p} \;=\; \cos^2 q + \sin^2 q \;=\; 1\,,$$

so defining the family of ellipses. The hyperbola have semi-axes $f\cos q$, the other $f\sin q$. Then

$$\frac{z^2}{f^2\cos^2 q} - \frac{w^2}{f^2\sin^2 q} \;=\; \cosh^2 p - \sinh^2 p \;=\; 1\,.$$

Scheme 1 described in §16.1 and 16.2 for prolate co-ordinates takes $\zeta = \cosh p$, $\eta = \cos q$ for the ellipses and $\zeta = \cos q$, $\eta = \sin q$ for the hyperbolae. Since $\cosh p \geq 1$, $\zeta \geq 1$, consistent with my usage.

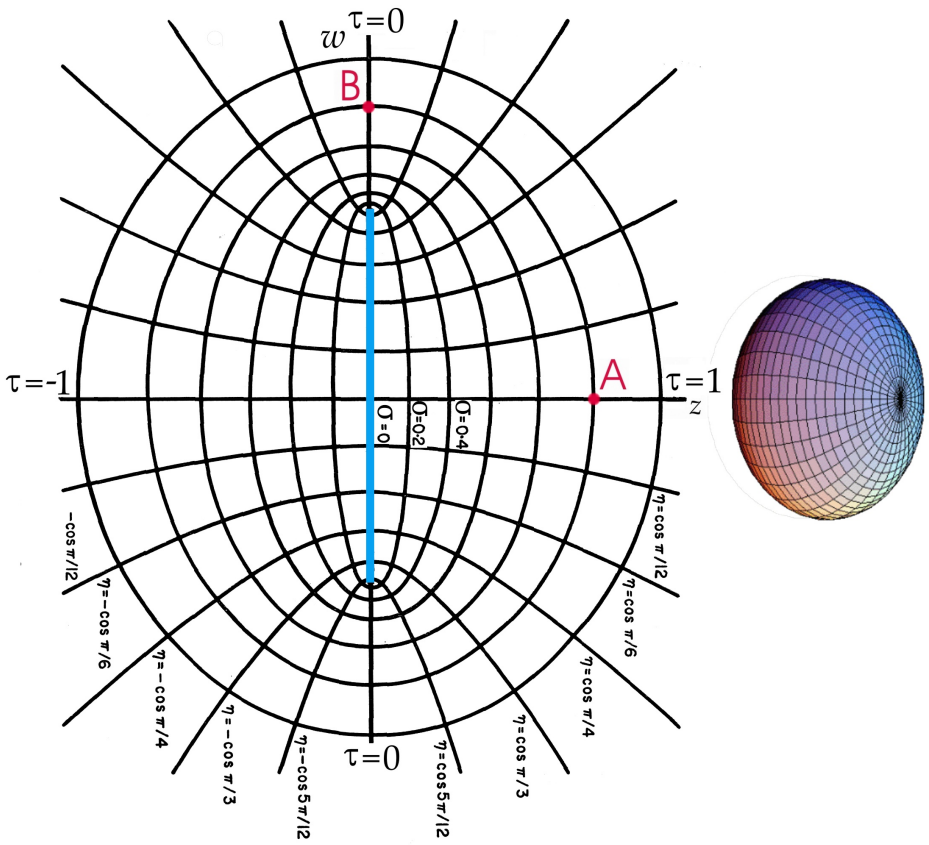

Figure 80: Oblate spheroidal co-ordinates in Scheme 3 (after Flammer). σ = constant defines an ellipsoid, τ = constant a hyperboloid.

Scheme 2 can be applied to oblate spheroids to produce Scheme 3. We need the z semi-axis shorter than the w one so let $\sigma = \sinh p \geq 0$, $\tau = \sin q$ – that is, they are swapped round from Scheme 1 for prolate spheroids.

$$\zeta^2 - \sigma^2 \;=\; \cosh^2 p - \sinh^2 p \;=\; 1\,, \qquad (A4.10a)$$

$$\eta^2 + \tau^2 \;=\; \cos^2 q + \sin^2 q \;=\; 1\,. \qquad (A4.10b)$$

Now $z = f\,\sinh p \sin q$ and $w = f\,\cosh p \cos q$, so the swapping of axis lengths has been effected. The oblate ellipsoids and associated hyperboloids are

$$\frac{z^2}{f^2\sigma^2} + \frac{w^2}{f^2(\sigma^2+1)} \;=\; \frac{z^2}{f^2\sinh^2 p} + \frac{w^2}{f^2\cosh^2 p} \;=\; \sin^2 q + \cos^2 q \;=\; 1\,,$$

$$\frac{z^2}{f^2\tau^2} - \frac{w^2}{f^2(1-\tau^2)} \;=\; \frac{z^2}{f^2\sin^2 q} - \frac{w^2}{f^2\cos^2 q} \;=\; \sinh^2 p - \cosh^2 p \;=\; -1\,.$$

The semi-minor axis of the ellipsoid is $a = f\sigma$ along the z rotation axis and the semi-major is $b = f\sqrt{\sigma^2+1}$. The limit $\sigma = 0$ produces a flat disc, radius f, in the plane w plane ($z = 0$). The limit $\tau = 1$ reduces the twin hyperbolae to lines along the z axis, whilst $\tau = 0$ defines that part of the w plane which is the complement of the limiting disc, that is $w^2 \geq 1$, $z = 0$. In Figure 80 Flammer has labelled the hyperbolae with the cosine of the angle which the asymptotes make with the z axis of rotation, which is now the normal to the limiting disc. Calling these angles θ_o and the corresponding angle from z in the prolate case θ_p, then $\theta_0 = \pi/2 - \theta_p$. Their cosines are related as $\tau^2 = \cos^2\theta_o = 1 - \cos^2\theta_p = 1 - \eta^2$. On the limiting flat disc τ marks out concentric circles with radius $\sqrt{1-\tau^2}$, *not* with radius τ. In this sense τ acts differently from η on the limiting prolate spheroid.

Scheme 3 is the one used by Flammer though confusingly he writes ζ for σ and η for τ. They are *not* the same quantities since $\zeta^2 \geq 1$, $\sigma^2 \geq 0$. I reproduce his diagram as Figure 80, but use my nonenclature. I find the inconsistency has been carried over into Abramowitz and Stegun in this way: in the analysis at the beginning of their Chapter 21 they use Scheme 1, but when they present the table of values for oblate radial functions, Table 21.4, they switch the definition of ζ (they use ξ as the letter) to Flammer's without mentioning this. Therefore in their analysis and in Table 21.3 $\zeta \geq 1$, but in the Table 21.4 $\zeta \geq 0$, and indeed values for $\zeta = 0$ and $0\cdot75$ are tabulated. I believe this table should be labelled to correspond with my σ. Mathematica seems to calculate the oblate functions consistent to Flammer's scheme. The translation is $\sigma = \sqrt{\zeta^2-1}$, $\tau = \sqrt{1-\eta^2}$. Eq A4.3. translates to

$$x \;=\; f\sqrt{(\sigma^2+1)(1-\tau^2)}\,\cos\psi, \qquad y \;=\; f\sqrt{(\sigma^2+1)(1-\tau^2)}\,\sin\psi, \qquad z \;=\; f\sigma\tau\,. \qquad (A4.11)$$

The inverses are

$$\sigma^2 = \frac{1}{2f^2}[G_+G_- + (w^2+z^2-f^2)], \qquad \tau^2 = \frac{1}{2f^2}[G_+G_- - (w^2+z^2-f^2)] \qquad (A4.12)$$

$$\text{where} \quad G_+ = \sqrt{z^2+(w+f)^2}, \qquad G_- = \sqrt{z^2+(w-f)^2}, \qquad w^2 = x^2+y^2\,.$$

The scale factors from Eq A4.8 translate as

$$h_\sigma \;=\; f\sqrt{\frac{\sigma^2+\tau^2}{\sigma^2}}\,\frac{\partial\zeta}{\partial\sigma} \;=\; f\sqrt{\frac{\sigma^2+\tau^2}{\sigma^2+1}}\,, \qquad h_\tau \;=\; f\sqrt{\frac{\sigma^2+\tau^2}{1-\tau^2}}\,, \quad h_\psi \;=\; f\sqrt{(\sigma^2+1)(1-\tau^2)}\,. \quad (A4.13)$$

16.4 Separating variables in Helmholtz's equation

This section follows the method described for spherical co-ordinates in §5.2. Because of the different notations I here set out how Helmholtz's equation is separated in the prolate co-ordinate system, then show how it translates to the oblate. The Laplacian in general curvilinear co-ordinates u_1, u_2, u_3 is given in many textbooks as

$$\nabla^2\phi \;=\; \frac{1}{h_1\,h_2\,h_3}\left[\frac{\partial}{\partial u_1}\frac{h_2\,h_3}{h_1}\frac{\partial\phi}{\partial u_1} \;+\; \frac{\partial}{\partial u_2}\frac{h_3\,h_1}{h_2}\frac{\partial\phi}{\partial u_2} \;+\; \frac{\partial}{\partial u_3}\frac{h_1\,h_2}{h_3}\frac{\partial\phi}{\partial u_3}\right].$$

The scale factors h_ζ, etc. for prolate co-ordinates are in Eq A4.8. (They are also called 'metrical coefficients'.) From these it is not too awkward to show that

$$h_\zeta h_\eta h_\psi \;= f^3\,(\zeta^2-\eta^2)\,,$$

$$\frac{h_\eta h_\psi}{h_\zeta} \;=\; f\,(\zeta^2-1)\,, \qquad \frac{h_\zeta h_\psi}{h_\eta} \;=\; f\,(1-\eta^2)\,, \qquad \frac{h_\zeta h_\eta}{h_\psi} \;=\; f\,\frac{\zeta^2-\eta^2}{(\zeta^2-1)(1-\eta^2)}\,.$$

Now take the potential to be the product of three functions, each depending on only one co-ordinate: $\phi = R(\zeta)\,S(\eta)\,P(\psi)$. Substituting in Helmholtz's equation gives

$$SP\frac{\partial}{\partial\zeta}[(\zeta^2-1)R'] + RP\frac{\partial}{\partial\eta}[(1-\eta^2)S'] + RS\frac{\zeta^2-\eta^2}{(\zeta^2-1)(1-\eta^2)}\frac{\partial P'}{\partial\psi} + \kappa^2 f^2(\zeta^2-\eta^2)\,RPS \;=\; 0\,.$$

The prime $'$ means differentiation with respect to the one variable upon which the function depends. Thus $\partial P'/\partial\psi$ is just $P'' = \partial^2 P/\partial\psi^2$. This term can be isolated by dividing throughout by RSP and multiplying by $(\zeta^2-1)(1-\eta^2)/(\zeta^2-\eta^2)$. This picks out P''/P as a term which can be set equal to $-m^2$ as in the case of spherical co-ordinates. The equation $P'' = -m^2P$ has the general solution $P(\psi) = \mathcal{C}_1\cos m\psi + \mathcal{C}_2\sin m\psi$. Azimuthal symmetry requires that m be an integer, exactly as in the spherical case. Replacing P'' by $-m^2P$ gives

$$\frac{1}{R}\frac{\partial}{\partial\zeta}[(\zeta^2-1)R'] \;+\; \frac{1}{S}\frac{\partial}{\partial\eta}[(1-\eta^2)S'] \;-\; m^2\,\frac{\zeta^2-\eta^2}{(\zeta^2-1)(1-\eta^2)} \;+\; \kappa^2 f^2(\zeta^2-\eta^2) \;=\; 0\,.$$

We dearly would like this to split into two functions, one depending only on ζ, the other only on η. Clearly $\kappa^2 f^2(\zeta^2-\eta^2) = C^2\zeta^2 - C^2\eta^2$ where $C = \kappa f$ is a dimensionless parameter. The factor multiplying m^2 will split into partial fractions as

$$\frac{\zeta^2-\eta^2}{(\zeta^2-1)(1-\eta^2)} \;=\; \frac{1}{\zeta^2-1} \;+\; \frac{1}{\eta^2-1}\,.$$

The separation constant in Flammer's scheme is λ_{ml} and we arrive at the radial and polar angular differential equations for prolate co-ordinates:

$$\frac{1}{R}\frac{\partial}{\partial\zeta}[(\zeta^2-1)R'] \;-\; \frac{m^2}{\zeta^2-1} \;+\; C^2\zeta^2 \;=\; \lambda_{ml}\,, \qquad (A4.14a)$$

$$\frac{1}{S}\frac{\partial}{\partial\eta}[(1-\eta^2)S'] \;-\; \frac{m^2}{1-\eta^2} \;-\; C^2\eta^2 \;=\; -\lambda_{ml}\,. \qquad (A4.14b)$$

The forms of these is two second order differential equations are essentially the same and indeed both $R(\zeta)$ and $S(\eta)$ obey the same equation but over different ranges of the variables. The values of λ_{ml} for which solutions with the correct limiting behaviours exists are called eigenvalues of the differential equation. They do not have simple integer values such as the $l(l+1)$ of spherical co-ordinates but

instead are the solutions of transcendental equations. Values are tabulated in Abramowitz and Stegun. Be aware that Mathematica uses Meixner and Schäfke's form of the equations which have an alternative definition of the eigenvalues, differing by C^2 from Flammer's.

Now the whole operation is repeated for oblate co-ordinates $\sigma \geq 0$, τ, ψ using the scale factors in Eq A4.13 above. $h_\sigma\, h_\tau\, h_\psi = f^3(\sigma^2+\tau^2)$ and

$$\frac{h_\tau\, h_\psi}{h_\sigma} \;=\; f\,(\sigma^2+1)\,, \qquad \frac{h_\sigma\, h_\psi}{h_\tau} \;=\; f\,(1-\tau^2)\,, \qquad \frac{h_\sigma\, h_\tau}{h_\psi} \;=\; f\,\frac{\sigma^2+\tau^2}{(\sigma^2+1)(1-\tau^2)}\;.$$

The radial, polar and azimuthal wave functions will in principle be different for the oblate case, so let the potential by $\phi = \mathcal{R}(\sigma)\,\mathcal{S}(\tau)\,\mathcal{P}(\psi)$. It happens that $\mathcal{P}(\psi) = P(\psi)$ and we again replace P''/P by $-m^2$ to reduce Helmholtz's equation to

$$\frac{1}{\mathcal{R}}\,\frac{\partial}{\partial\sigma}[(\sigma^2+1)\mathcal{R}'] \;+\; \frac{1}{\mathcal{S}}\,\frac{\partial}{\partial\tau}[(1-\tau^2)\mathcal{S}'] \;-\; m^2\,\frac{\sigma^2+\tau^2}{(\sigma^2+1)(1-\tau^2)} \;+\; \kappa^2 f^2(\sigma^2+\tau^2) \;=\; 0\,.$$

The required partial fractions are

$$\frac{\sigma^2+\tau^2}{(\sigma^1+1)(1-\tau^2)} \;=\; \frac{-1}{\sigma^2+1} + \frac{1}{1-\tau^2}$$

so the separated equations are

$$\frac{1}{\mathcal{R}}\,\frac{\partial}{\partial\sigma}[(\sigma^2+1)\mathcal{R}'] \;+\; \frac{m^2}{\sigma^2+1} \;+\; C^2\sigma^2 \;=\; \Lambda_{ml}\,, \qquad (A4.15a)$$

$$\frac{1}{\mathcal{S}}\,\frac{\partial}{\partial\tau}[(1-\tau^2)\mathcal{S}'] \;-\; \frac{m^2}{1-\tau^2} \;+\; C^2\tau^2 \;=\; -\Lambda_{ml}\,. \qquad (A4.15b)$$

We now arrive at a very important observation. The form of the radial oblate equation in σ can be obtained from the radial prolate equation by the replacements $\zeta \to i\sigma$ and $C \to -iC$. I will spell it out by substituting into Eq A4.14a:

$$\frac{1}{R}\,\frac{\partial}{\partial(i\sigma)}[(-\sigma^2-1)\frac{\partial R}{\partial(i\sigma)} \;-\; \frac{m^2}{-\sigma^2-1} \;+\; (-C^2)(-\sigma^2) \;=\; \lambda_{ml}\,.$$

This does not mean that $\sigma = i\zeta$; we know that $\sigma \geq 0$ but $\zeta \geq 1$. It is a formal similarity of the prolate and radial equations. What it does means is that we can equate Λ_{ml} with λ_{ml} and interpret the radial and angular functions as follows:

$$\text{given}\;\; C,\; \sigma,\; \tau \;\text{ use }\; R_{ml}(-iC,\, i\sigma) \;\text{ and }\; S(-iC,\, \tau)\,. \qquad (A4.16)$$

This is a key result which tells us how to use correctly the spheroidal functions in Mathematica for oblate spheroids.

16.5 Forms of the radial and angular functions

There are two forms of the radial functions. $R^{(1)}_{ml}(C,s)$ is an elaboration of the spherical Bessel functions $j_l(s)$. They tend to zero as $s \to 0$. The second kind, $R^{(2)}_{ml}(C,s)$, resemble the $y_l(s)$ and tend to $-\infty$ as s become small. The spherical Hankel functions of the first kind are defined by

$h_l^{(1)}(s) = j_l(s) + i\,y_l(s)$ and are often used to represent a complex radially moving wave field in spherical co-ordinates. Their counterpart in spheroidal co-ordinates is

$$R_{ml}^{(3)} \equiv R_{ml}^{(1)} + i\,R_{ml}^{(2)}\,.$$

This will be used in calculations. Figure 81 shows graphs of $R_{00}^{(1)}(C,\zeta)$ (prolate) and $R_{00}^{(1)}(-iC,i\sigma)$ (oblate) for $C = 1,\ 1\cdot5$ and 2. Above $\zeta = 2$, $\sigma = 2$ they look very similar. They are slightly different; for example near a peak in the green curves $R_{00}^{(1)}(2,3\cdot9) = 0\cdot1272$ and $R_{00}^{(1)}(-2i,3\cdot9i) = 0\cdot1248$. Figure 82 shows the corresponding functions of the second kind, with their divergence as $\zeta \to 0$, $\sigma \to 0$. In principle these radial functions can be expanded as infinite series in spherical Hankel functions. As might be expected, their asymptotic behaviour as $C\zeta \to \infty$ or $C\sigma \to \infty$ is as spherical waves with phases in quadrature:

$$R_{ml}^{(1)}(C,\zeta) \;\to\; \frac{1}{C\zeta}\cos[C\zeta - \tfrac{\pi}{2}(l+1)]\,, \qquad R_{ml}^{(2)}(C,\zeta) \;\to\; \frac{1}{C\zeta}\sin[C\zeta - \tfrac{\pi}{2}(l+1)]\,. \qquad (A4.17)$$

The similarity with the real and imaginary parts of $e^{i\kappa r}/\kappa r$ means that the equivalence $C\zeta = \kappa r$ can be made as the semi-axes of the high-ζ ellipsoids tend to the radius r of a sphere. For $m = 0$, $l = 0$, which is the mode considered here the most, $R_{00}^{(1)}(C,\zeta) \to \sin(\kappa r)/(\kappa r)$ and $R_{00}^{(2)}(C,\zeta) \to -\cos(\kappa r)/(\kappa r)$. The rate of convergence can be judged from the comparative graphs in Figure 83, plotted for $C = 5$.

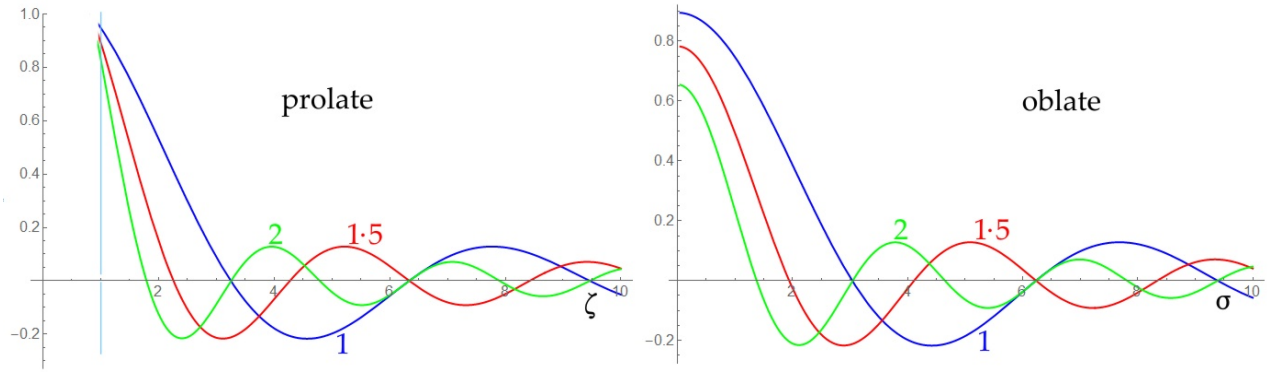

Figure 81: Prolate and oblate radial wave functions of the first kind, $R_{00}^{(1)}(C,\zeta)$ and $R_{00}^{(1)}(-iC,i\sigma)$, for $C = 1,\ 1\cdot5$ and 2 as a function of ζ or σ.

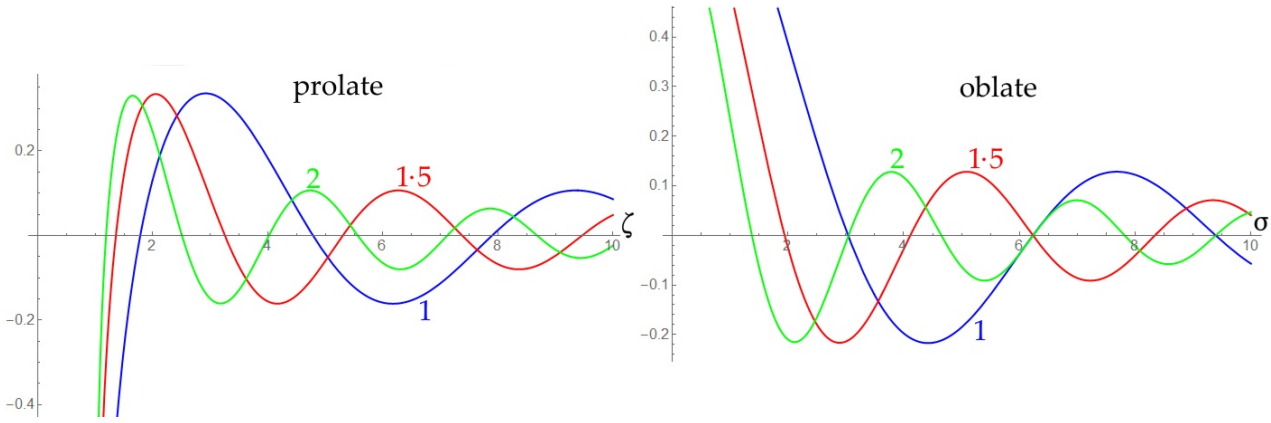

Figure 82: Prolate and oblate radial functions of the second kind, $R_{00}^{(2)}(C,\zeta)$ and $R_{00}^{(2)}(-iC,i\sigma)$.

There are also two kinds of polar angular spheroidal function. $S^{(1)}_{ml}$, $S^{(2)}_{ml}$ are elaborations of the associated Legendre functions $P_l(x)$ and $Q_l(x)$. However only those of the first kind are required in radiation calculations. Figure 84 shows graphs for both prolate and oblate cases for C from 1 to 5. Observe that the independent co-ordinate in the right oblate panel is not τ but $\sqrt{1-\tau^2}$. The reason is that this is the radial distance from the z axis on the limiting flat disc, $\sigma = 0$. In the prolate case η itself is the distance from the z axis along the limiting needle, $\zeta = 1$.

From small C the curves for both the prolate and oblate cases look like parabolas. This observation is borne out by analysis; the functions S_{00} can be expanded in a series of Legendre polynomials in C and η or τ, with first terms

$$\text{Prolate}: \qquad 1 - \frac{C^2}{18}\,(3\eta^2 - 1)\,,$$

$$\text{Oblate}: \quad 1 + \frac{C^2}{18}\,(3\tau^2 - 1) \;=\; 1 + \frac{C^2}{18}\,(2 - 3\eta^2)\,, \quad \eta^2 = 1 - \tau^2\,.$$

These approximations have error less than about 1% for C up to about 1.

Much effort has gone into the accurate computation of functions R and S, and fortunately the package Mathematica 10 provides these, based mainly on the work of Peter Falloon and others at the

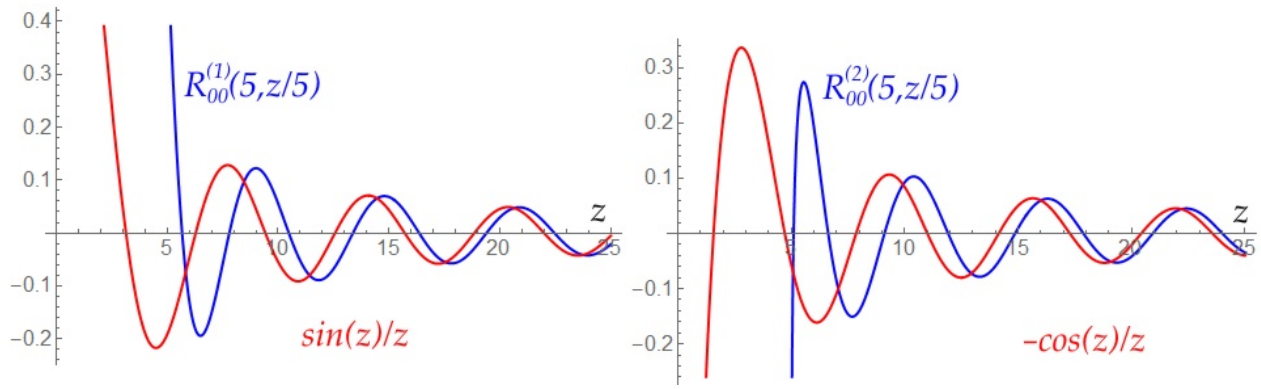

Figure 83: Comparison of $R^{(1)}_{00}(5, z/5)$ and $R^{(2)}_{00}(5, z/5)$ with their asymptotic forms.

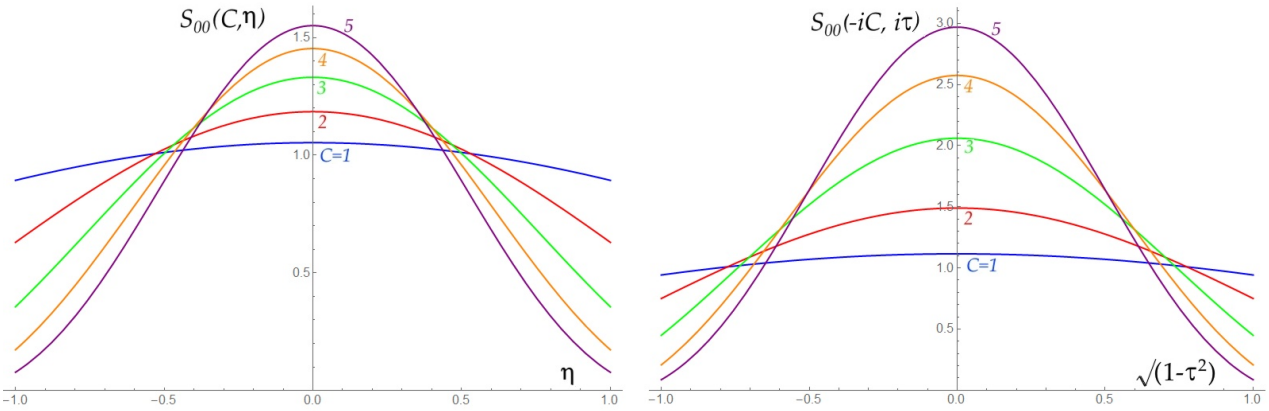

Figure 84: Angular wave functions for prolate ($S^{(1)}_{00}(C, \eta)$, left) and oblate ($S^{(1)}_{00}(-iC, i\tau)$, right) spheroids for C from 1 to 5.

University of Western Australia who in turn built have upon the enormous amount of development by US Naval Research. Care is needed because Mathematica uses a different notation from Flammer. The translation for radial functions is

$$\texttt{SpheroidalS1}(m,l,C,\zeta) = R^{(1)}_{ml}(C,\zeta), \qquad \texttt{SpheroidalS2}(m,l,C,\zeta) = R^{(2)}_{ml}(C,\zeta)$$

and their derivatives with respect to ζ are given by

$$\texttt{SpheroidalS1Prime}(m,l,C,\zeta), \qquad \texttt{SpheroidalS2Prime}(m,l,C,\zeta).$$

For the polar angular functions

$$\texttt{SpheroidalPS}(m,l,C,\eta) = S^{(1)}_{ml}(C,\eta), \qquad \texttt{SpheroidalQS}(m,l,C,\eta) = S^{(2)}_{ml}(C,\eta)$$

and similarly for their derivatives with respect to η.

I have found it useful to have polynomial approximations to the angular functions for use in some calculations and I give these below, should any reader care to make use of them. First the prolate functions of η. Up the about $C = 4$ these can be approximated by quadratics in η^2. From $C = 4$ to 6 cubics are needed. Tables 6 and 8 give the coefficients of η^0, η^2, etc. for these two ranges. Moreover, by fitting polynomials to the coefficients themselves I find useful two-variable approximations for the prolate angular functions, as given in Tables 7 and 9. To illustrate how these are to be used, to find $S_{00}(5\cdot3, 0\cdot35)$ use Table 9 to find that

$$a_0 = 0\cdot88902 + 0\cdot17683C - 0\cdot00897C^2 = 1\cdot57424 \quad \text{at } C = 5\cdot3\,.$$

Similarly find a_2, a_4 and a_6 and obtain $S_{00}(5{\cdot}3, 0{\cdot}35) \approx 1{\cdot}57425 - 3{\cdot}4692\eta^2 + 2{\cdot}82105\eta^4 - 0{\cdot}868\eta^6 = 1{\cdot}190$. Mathematica gives the exact value to be $1\cdot188$.

C	0·5	1	1·5	2	2·5	3	3·5	4	4·5
a_0	1·0137	1·0532	1·1130	1·1847	1·2589	1·3288	1·3909	1·4446	1·4906
a_2	-0·0418	-0·1679	-0·3777	-0·6627	-1·0038	-1·3761	-1·7571	-2·1309	-2·4882
a_4	0·0005	0·0080	0·0378	0·1081	0·2308	0·4058	0·6231	0·8686	1·1287

Table 6: Coefficients in 4th power approximation to $S_{00}(C,\eta) \approx a_0 + a_2\eta^2 + a_4\eta^4$ for $C < 4.5$.

	a_0	a_2	a_4
c_0	1	0	0
c_1	0·0073504	0·0298141	0·0195108
c_2	0·0570671	-0·2117747	-0·0533655
c_3	-0·0077031	0·0128251	0·0452664
c_4		0·0012188	-0·0048867

Table 7: Coefficients for determining the $a_j(C)$ in Table 6 for $C < 4.5$. In each column $a_j = c_0 + c_1C + c_2C^2 + c_3C^3 + c_4C^4$.

C	4	4.5	5	5.5	6
a_0	1·4527	1·5035	1·5489	1·5900	1·6273
a_2	-2·2894	-2·7413	-3·1968	-3·6522	-4·1043
a_4	1·3118	1·8364	2·4351	3·0957	3·8051
a_6	-0·3018	-0·4820	-0·7103	-0·9836	-1·2968

Table 8: Coefficients in 6th power approximation to $S_{00}(C,\eta) \approx a_0 + a_2\eta^2 + a_4\eta^4 + a_6\eta^6$ for $4 < C < 6\cdot5$.

I have developed equivalent polynomial approximations for the oblate functions, but they have the complication that one may want them in terms of $1 - \tau^2$ rather than τ^2. For example,

$$S_{00}(-5i,\tau) \;\approx\; 0\cdot08300 + 0\cdot7957\tau^2 + 0\cdot57538\tau^4 + 1\cdot51264\tau^6\,,$$

	a_0	a_2	a_4	a_6
c_0	0·88902	1·340801	-0·7301549	-0·44023
c_1	0·1768286	-0·9068934	0·0169674	0·390207
c_2	-0·0089689	-0·0001225	0·1232209	-0·08885

Table 9: Coefficients for determining the $a_j(C)$ in Table 8 for $4 < C < 6 \cdot 5$. In each column $a_j = c_0 + c_1 C + c_2 C^2$.

$$\text{or} \quad S_{00}(-5i, \tau) \approx 2 \cdot 9646 - 6 \cdot 4873(1-\tau^2) + 5 \cdot 13615(1-\tau^2)^2 - 1 \cdot 5305(1-\tau^2)^3 .$$

It would be too much to give tables for all these.

16.6 Shape of wavefronts

As the spheroid vibrates, the waves it excites in the surrounding fluid will travel outwards at the same velocity in all directions. At first thought we might expect these wavefronts to be a set of closed loops around the object, all spaced one wavelength apart as measured normal to the vibrating surface. The situation might look like Figure 85 in which the three outer closed curves are at normal distances 1/2, 1 and 3/2 units respectively from the inner ellipse. However this is *not* the form taken by the radiating wavefronts. Successive crests and troughs coincide with the confocal ellipses in Figures 78 or 80 for the prolate and oblate cases respectively.

I will explain how this rather strange effect comes about. It is due to a quite beautiful interplay between the radial and angular wavefunctions which, it will be remembered, satisfy the same differential equation but over different ranges of the variable. Consider the needle-like limiting form of the prolate spheroids. Suppose we approximate its vibration by a line of point sources from $-f$ to $+f$. For a concrete example take $f = 5$. If the point sources all have the same amplitude, so the needle is a uniform source along its length, then the wavefronts do indeed look like Figure 85. However, the bell-shaped angular function S 'shades' amplitude along the length as in the left panel

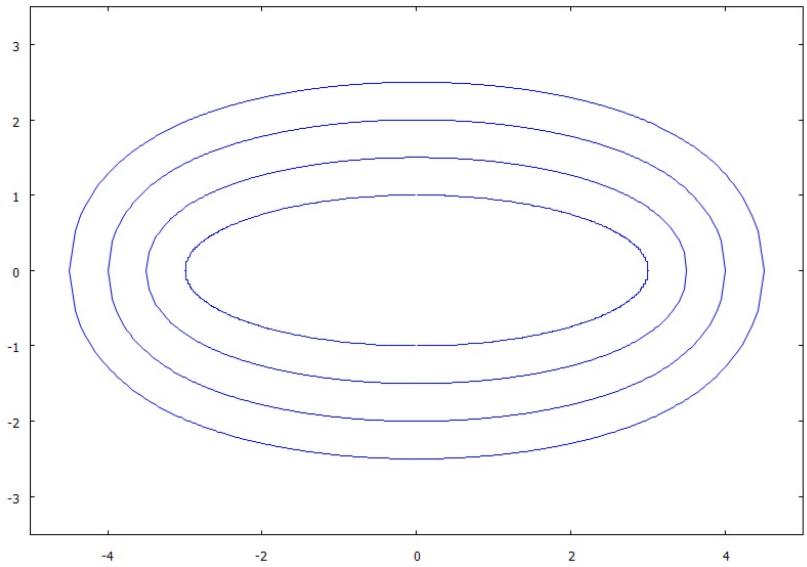

Figure 85: Closed curves representing the fronts of waves expanding from a pulsating inner ellipse with $a = 3$, $b = 1$. Curves are $0 \cdot 5$ units apart as measured normal to the inner ellipse.

of Figure 84. This shading is exactly what is required to adjust the interference amongst the point sources to bring the wave crests and troughs into agreement with the radial function R. This is seen by comparing the left and right panels of Figure 86. The field at a point z along the line of the needle is

$$\int_{-5}^{5} A(z_0)\,\frac{\sin\kappa(z-z_0)}{\kappa(z-z0)}\,dz_0$$

where $A(z)$ is the amplitude of the point source at position z_0. Take $\kappa = 1$. If $A(z_0) = 1$ for all z_0, we obtain the blue curve in the left panel of Figure 86. This is clearly well out of phase with the true radial behaviour shown in orange. As if by magic, in the right panel, letting $A(z) = S_{00}(5, z/5)$ brings the two curves into registration, except for a scale factor in the vertical direction.

To make this elegant fact even more apparent, please study the contour plots in Figure 87. This shows one quadrant of the potential field obtained by integrating the same line source above from -5 to $+5$, weighted with the angular functions $S_{00}(5, z/5)$. The superimposed red confocal ellipses all have $f = 5$ and are drawn for the ζ values of the peaks and troughs of $R^{(1)}_{00}(5, z/5)$, which is asymptotically similar to $\sin(r)/r$. You see that the ellipses fit closely to the crests (yellow) and troughs (dark blue) of the field integral. If the amplitude variation along the needle (blue line, bottom left) were anything other than $S_{00}(5, z/5)$, the crests and troughs would not lie on these ellipses. We can thus see how that the confocal ellipses with constant f in Figure 78 are indeed the wavefronts, despite what simple intuition based on ray theory or Huygen's principle might first lead us to imagine.

The natural next question is 'Does the same hold true for oblate spheroids?'. I believe the answer is yes, though must admit that the agreement between the true spheroidal functions are an integral over the limiting disc $\sigma = 0$ is slightly less convincing. I have modelled the limiting flat disc by a circle, radius 5, over which point sources are distributed with amplitude weighting $B(w_0)$, $w_0^2 = x^2 + y^2$. The field at point $(x, 0, z)$ above the disc is

$$\iint_{w_0^2 \le 5^2} B(w_0)\,\frac{\sin\kappa d}{\kappa d}\,dy_0\,dx_0, \qquad d^2 = (x-x_0)^2 + y_0^2 + z^2\,.$$

Again I set $\kappa = 1$. To interpret $B(w_0)$ recall that in oblate co-ordinates the radial distance from the centre in the $x-y$ plane is $f\sqrt{1-\tau^2}$. Hence $B(w_0) = S_{00}(-5i, \frac{1}{5}\sqrt{1-w_0^2}\,)$. Using numerical integration with Mathematica, along the z axis I hence obtain the comparison in Figure 88. It is good except for $z < 6$. I have found it difficult to obtain a comprehensive contour plot because, for some

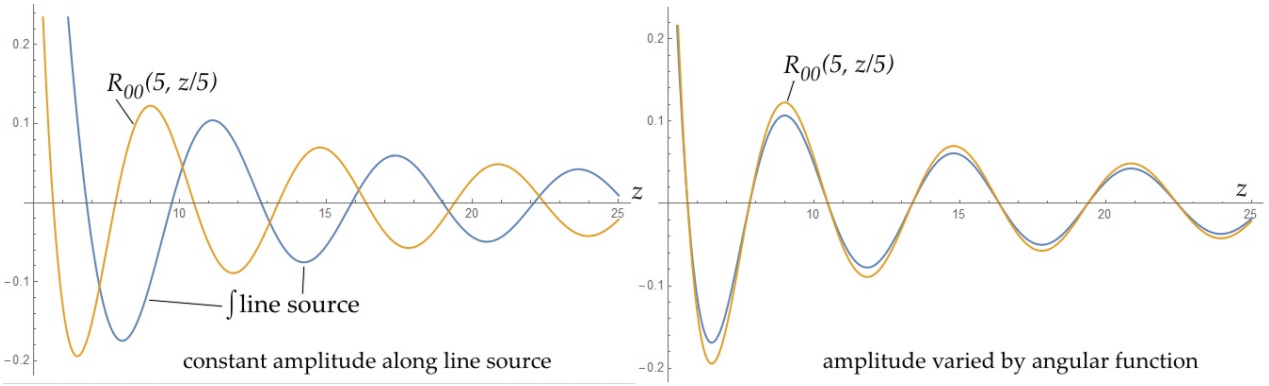

Figure 86: Comparison of the true radial function with the integral over a line of point source over $[-5, 5]$ unweighted (left) and weighted (right) by angular function $S_{00}(5, z/5)$.

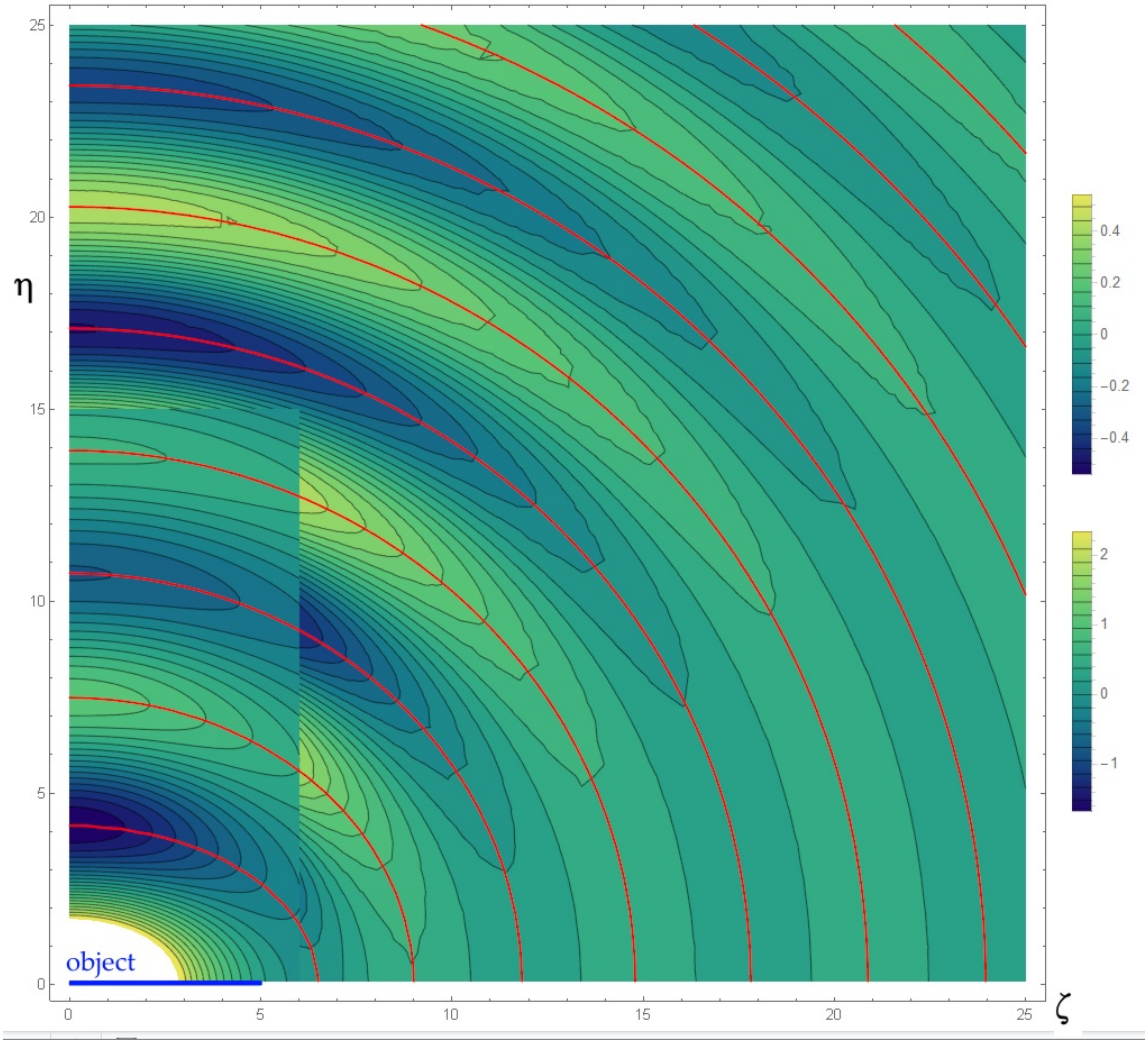

Figure 87: Contour plots of field from line of amplitude-weighted point sources over $[-5, 5]$. Superposed are confocal ellipses with $f = 5$.

reason which I do not understand, Mathematica takes an inordinately long time to evaluate the double integral. Instead I offer in Figure 89 a mosaic of contours over strips, each on a different amplitude scale. The red ellipses are for ζ values corresponding to the peaks and troughs of $R_{00}^{(1)}(-5i, iz/5)$. They coincide with the contour plots except along the plane of the disc z small. I can only assume that the failure to agree completely is due to the integral over the flat disc not representing the limiting spheroidal functions adequately.

In summary, the radial and angular spheroidal wave functions, deriving as they do from the same differential equation, work as a pair so that the crests and troughs of the expanding wavefronts lie along the set of confocal ellipses with the same semi-interfocal distance f as the vibrating spheroidal object.

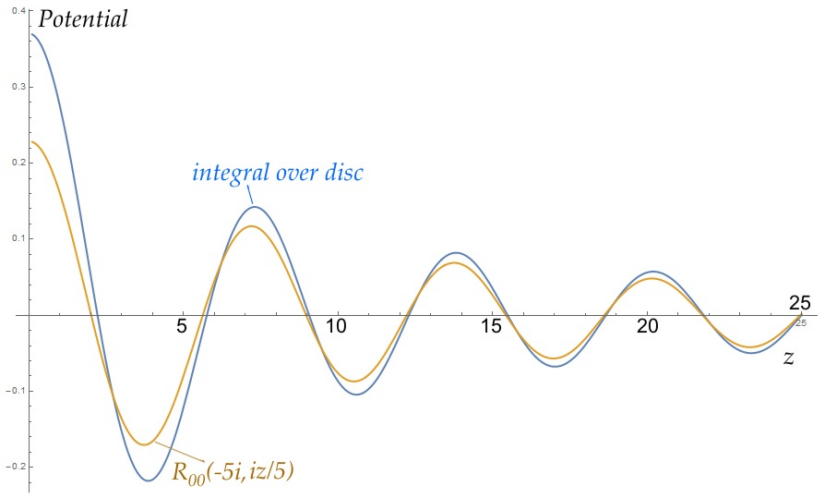

Figure 88: Comparison of true radial function for $C = 5$ with model of integration of amplitude-weighted point sources over disc, radius 5.

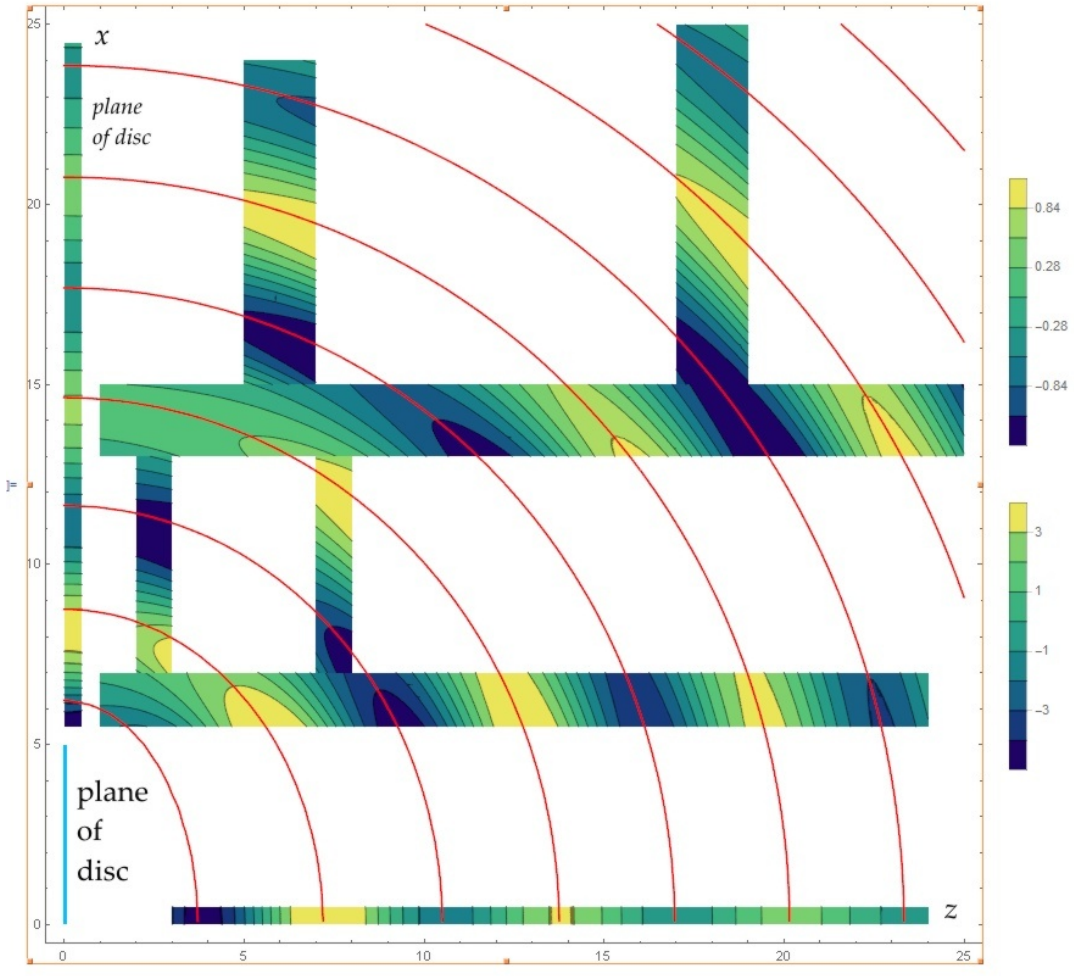

Figure 89: Mosaic of contour plots of field of amplitude-weighted disc of point sources, radius 5. Superposed are confocal ellipses with $f = 5$.

17 APPENDIX 5: Wave displacement and impedance of spheroids

This Appendix continues from Appendix 4 by calculating the particle displacement and acoustic impedance associated with the potential ϕ for vibrating spheroids. This is largely to answer the question 'For a general patch of convex surface, does the conjectured expression in Eq 50

$$\frac{\phi}{\xi} \approx \sqrt{\frac{a_1\, a_2}{(1-i\kappa a_1)(1-i\kappa a_2)}}\,. \qquad \textit{Copy of } (50a)\,.$$

hold true, where a_1, a_2 are the local principal radii of curvature?'.

17.1 Displacement ξ around radiating spheroid

The solutions of Helmholtz's equation are the potential ϕ, which I have taken throughout this article to be displacement potential. The potential around a vibrating spheroid in mode $m = l = 0$ is determined by the radial and angular spheroidal wave functions illustrated in Figures 81 to 84 of Appendix 4. The displacement itself in spheroidal co-ordinates is given by Eq A4.9, also of Appendix 4. Assume that there is no azimuthal variation so $m = 0$, $\Psi(\psi) = 1$ and $\Psi' = 0$. At any point Q on or outside a prolate spheroid the displacement is

$$\boldsymbol{\xi}(Q) = -\frac{1}{f}\sqrt{\frac{\zeta^2-1}{\zeta^2-\eta^2}}\, R_{00}^{(3)\prime}(C,\zeta)\, S_{00}(C,\eta)\, \mathbf{e}_\zeta - \frac{1}{f}\sqrt{\frac{1-\eta^2}{\zeta^2-\eta^2}}\, R_{00}^{(3)}(C,\zeta)\, S'_{00}(C,\eta)\, \mathbf{e}_\eta\,. \qquad (A5.1)$$

Regarding dimensions, ϕ is as area and therefore so is the product $R_{00}S_{00}$. f is a length and both ζ and η are dimensionless. Therefore the derivatives have the dimensions of area too.

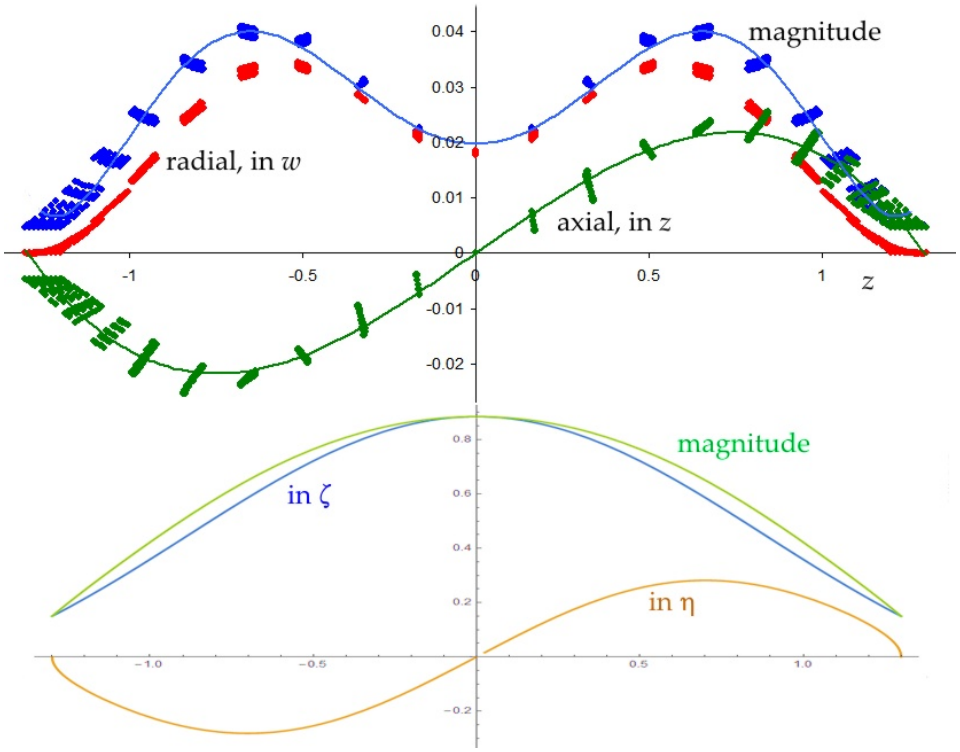

Figure 90: Top panel reproduces Figure 62 for displacement components at surface of prolate spheroid $a = 1\cdot 3$, $b = 0\cdot 877$. Lower panel: displacement in mode $m = l = 0$ of equivalent spheroid.

§11.1 has examples of the displacement magnitude of an elastic spheroid vibrating in the breathing mode. It is interesting to see how those FEA predictions compare with the exact solutions of Helmholtz's equation for $m = l = 0$, though of course there is no reason why they should agree. Figure 90 compares Eq A5.1 with the finite element results for the prolate spheroid shown in Figure 61. The parameters are

$$a = 1 \cdot 30 \text{ m}, \quad b = 0 \cdot 877 \text{ m}, \quad f = 0 \cdot 96 \text{ m}\,,$$

$$\zeta_0 = 1 \cdot 355, \quad \kappa = 4 \cdot 223 \text{ m}, \quad C = 4 \cdot 052\,.$$

The comparison is not exact in that the horizontal axis of the upper panel is z while in the lower it is $1 \cdot 3\eta$, but the distortion between them is small. Clearly mode 0 0 does not have the increased compliance at about $z = a/2$ predicted by FEA. This must mean that the FEA object creates a disturbance in the air involving higher order terms such as $l = 2$, 4, *etc.*

Looking now at the radial ζ displacement according to Eq A5.1 for this object vibrating at 230 Hz, we see in Figure 91 that the shape and phase of the wave is the same in different directions η: only the amplitude changes according to the bell-shaped curve $S_{00}(C, \eta)$. This is the obvious consequence of ζ and η being independent in this co-ordinata system.

Figure 92 compares the potential with the radial displacement. For a sphere we would have $\phi = Ae^{i\kappa r}/(\kappa r)$, $\xi = \phi(i\kappa - 1/r)$ For $r >> \lambda$ we would find that $\Re\phi \propto -\Im\xi$ and $\Im\phi \propto +\Re\xi$. These relations still hold for the prolate spheroid, as the two panels of Figure 92 show.

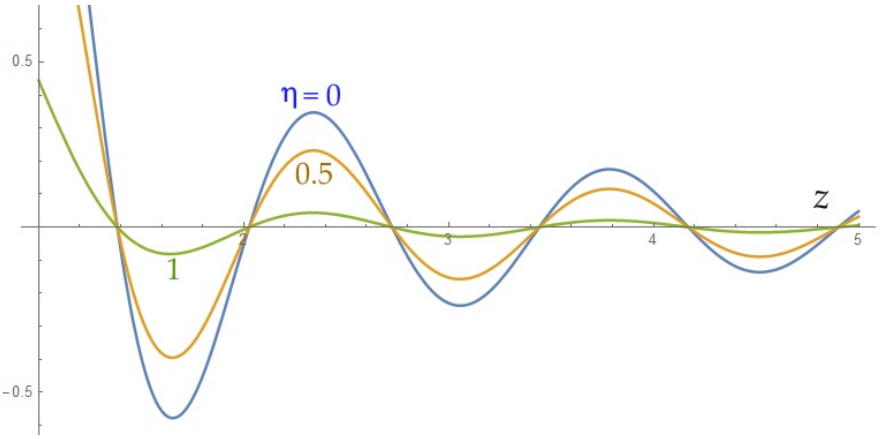

Figure 91: Radial (ζ) displacement at three positions, $\eta = 0$, 1/2, 1, along prolate spheroid with $a = 1 \cdot 3$. $b = 0 \cdot 877$. $\kappa = 4 \cdot 22$

17.2 Acoustic impedance

The concept of impedance has two related but slightly different interpretations. If the wave is considered in isolation from the source which creates it, impedance is understood as the acoustic pressure when the particle velocity has unit magnitude. In particular the 'specific acoustic impedance' $Z_c = p/v$ is based on a plane wave travelling through the medium. Pressure and particle velocity are then in phase and p/v evaluates to ρc, the product of fluid density and wave velocity. In other words, the impedance is a property of the medium – it measures how much force is required to move the wave through the medium.

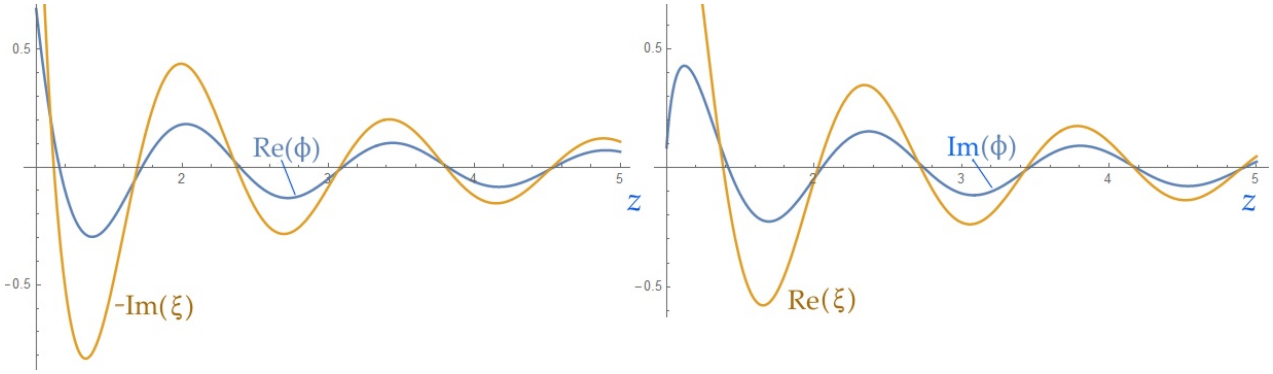

Figure 92: Comparison of real and imaginary parts of potential with imaginary and real parts of displacement in ζ directions at $\eta = 0$ of prolate spheroid $a = 1 \cdot 3$, $b = 0 \cdot 877$ at $\kappa = 4 \cdot 22$, $C = 4 \cdot 05$.

The alternative interpretation focuses less on the wave and more on the source by measuring the force needed from the vibrating object to attain unit flow in the adjacent fluid. 'Flow' means the total rate of movement of volume, taken over all directions. This is considered a property of the object in the fluid and referred to as its 'radiation impedance'. This is therefore the ratio of total force exerted on the fluid to the rate of change of volume of fluid integrated around the object. In contrast the specific acoustic impedance is referred to unit area at right angles to the wave motion, so force become pressure and flow becomes particle velocity.

If we take a patch of an imaginary closed surface which surrounds the object, we can speak of the pressure on it and the particle velocity across it. Except for a plane wave these will not be in phase, as we have seen in §2 for a spherically symmetric point source. The ratio $\phi(Q)/\xi(Q)$ on a small area is proportional to $p(Q)/v(Q)$ there. p/v is obtained by multiplying ϕ/ξ by $-i\rho\omega$, giving a local value of impedance. It will be represented mathematically as a complex quantity with resistive (real) and reactive (imaginary) parts, and the relative size of these will vary with distance from the object. On a sphere, because of the spherical symmetry, this local value of $p(Q)/v(Q)$ is numerically equal to the integrated radiation impedance. Similarly for a cylinder. However on a spheroid they are not the same. For instance, the ratio Z_B/Z_A, the impedance ratio between positions A (polar tip) and B (equator), on any prolate spheroid is

$$\frac{Z_B}{Z_A} = \frac{\zeta}{\sqrt{\zeta^2 - 1}} = \frac{a}{b} \geq 1\,; \qquad (A5.2)$$

that is, the impedance ratio is the inverse of the axis ratio of the ellipsoid. The formula states that the more sharply pointed position A has the smaller impedance. Conversely it also means that the barrel-shaped equatorial positions B generate a higher sound pressure for a given surface displacement. The question posed at the beginning of this appendix is asking whether $p(Q)/v(Q)$ is a useful concept, and in particular whether it can be related to the curvature of the wavefront at Q. Curvature is the only additional property which a radiating wave has over a plane wave. It would be excellent if it could be used heuristically in Kitchooff's formula to estimate ϕ from ξ or *vice versa*. I have investigated this question numerically using radiation from spheroids. There are two positions on each type of ellipse where comparison can be made: A on the z axis and B in the $x - y$ or w plane, Broadly, positions A are sphere-like, especially when $b \approx a$, and positions B are cylinder like, especially when $b \not\approx a$. Results are set out below. They show that there is no simple relation of ϕ to ξ and wavefront curvature; the question is answered in the negative.

17.3 Ratio ϕ/ξ at sphere-like positions A

If the conjecture is correct that, locally, ϕ/ξ is determined by wavefront curvature, we would expect that at position A, where all spheroids are locally almost spherical, the ratio ϕ/ξ will be almost that of the sphere with the radius of the tangent sphere, $R = b^2/a$. Calculation shows that this is not the case.

$$\text{At A, pointed tip, } \eta = 1, \qquad \frac{\phi}{\xi} = \frac{R_{00}^{(3)}(C,\zeta)\, S_{00}^{(1)}(C,1)}{\frac{-1}{f} R_{00}^{(3)\,\prime}(C,\zeta)\, S_{00}^{(1)}(C,1)} = -f \frac{R_{00}^{(3)}(C,\zeta)}{R_{00}^{(3)\,\prime}(C,\zeta)} \,. \qquad (A5.3)$$

where the $'$ means derivative with respect to ζ. The $-$ sign is because $\xi = -\nabla\phi$. The equivalent values for an oblate spheroid are as follows. The gradient is

$$\nabla\phi \;\rightarrow\; \frac{1}{f}\sqrt{\frac{\sigma^2+1}{\sigma^2+\tau^2}}\,\frac{\partial\phi}{\partial\sigma}\,\mathbf{e}_\sigma\,, \qquad \tau = 0 \text{ or } 1\,.$$

$$\text{At A, flattened dome, } \tau = 1, \qquad \frac{\phi}{\xi} = -f \frac{R_{00}^{(3)}(-iC, i\sigma)}{R_{00}^{(3)\,\prime}(-iC, i\sigma)} \,. \qquad (A5.4)$$

I have obtained values of the ratio $|\phi/\xi|$ at position A on a set of prolate and oblate spheroids for three fixed values of R, the radius of the tangent sphere at A. If the conjecture were true, the ratio would depend only on R and not on the length of the axes of the spheroid.

Figure 93 presents three log-log graphs each showing the ratio $|\phi/\xi|$ at position A calculated from Eqs A5.3, A5.4. They are plotted against the volume of the spheroid – actually just the product of the three semi-axes, ab^2. Each graph is for a different value of R: $R = 1$ (green), 2 (red) and 4 (blue) units respectively. The wave number κ is 1 throughout. Rather than being horizontal lines

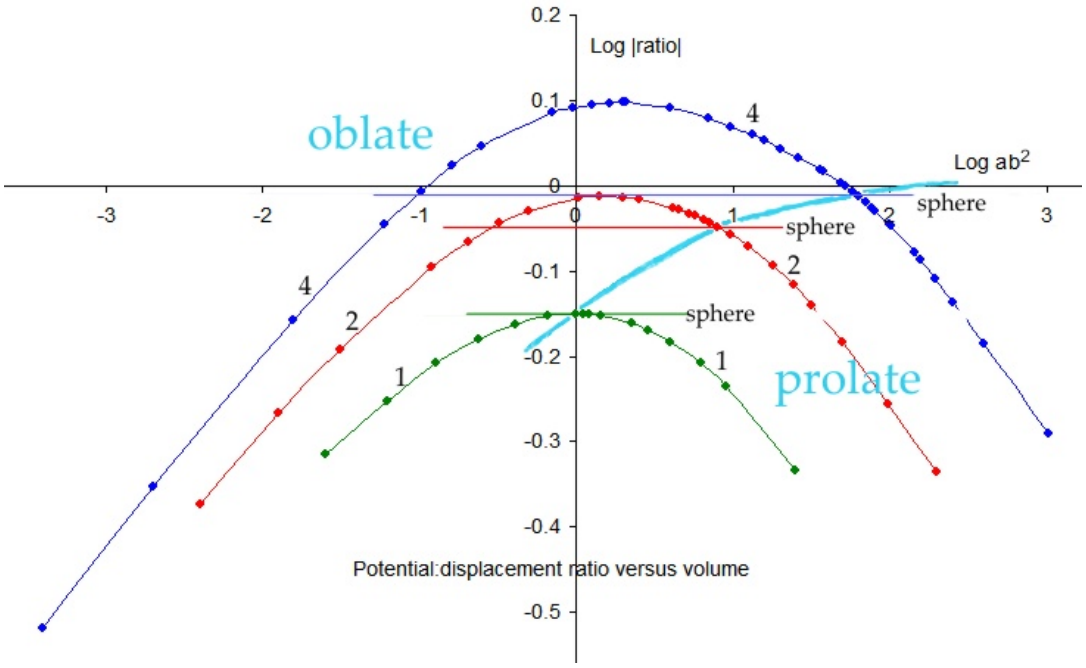

Figure 93: Log-log plot of ratio $|\phi/\xi|$ against the volume-like product ab^2 for spheroids with the same tangent circle (radius 1, 2 or 4) at position A. $\kappa = 1$.

at the values of the tangent spheres, each curve is almost a parabola on this log-log scale. If plotted against a or b/a similar parabolic curves are obtained. The three horizontal lines in Figure 93 show the respective $|\phi/\xi|$ ratios for the sphere radius R. These are

$$R = 1 \ : \ 0 \cdot 7071, \qquad R = 2 \ : \ 0 \cdot 8944, \qquad R = 4 \ : \ 0 \cdot 9701 \, ,$$

all obtained from the formula $\phi/\xi = R/(1 - iR)$. Each horizontal line cuts its curve in two places. The intersections on the right, joined by a pale blue curve, are where $b = a = R$. To the right of these positions the spheroids are prolate, to the left, oblate. When $R = 1$, the maximum ratio occurs when $b = a$, that is when the spheroid is actually a sphere. Whether one adds volume to this unit sphere to produce a prolate shape, or takes volume away to form an oblate shape with the same tangent sphere, ϕ/ξ decreases, meaning that wave motion can be sustained with less acoustic pressure. This no longer applies when $R > 1$; at $R = 2$ and 4 the peak is higher than the value for the corresponding sphere of radius R and lies on the oblate side. Perhaps the higher pressure is required because the volume is smaller. In other calculations I find that when $R < 1$, the peak ratio occurs for a prolate shape. Again perhaps lower pressure is required because the spheroid's volume is larger. These observations would be consistent with the integrated radiation impedance being the significant quantity rather than the local ϕ/ξ ratio. Values of the peaks for seven values of R are listed in Table 10, and a selection of these columns are plotted in Figure 94. I cannot find a simple relation between $|\phi/\xi|$ and any of the parameters of the spheroids at peak Z. However, there is a trend for $|\phi/\xi|$ to be about $3b/4$.

R	a	b	ab^2	f	Real	Imag	Abs
0·5	1·094	0·740	0·598	0·806	0·369	0·317	0·487
1	1	1	1	0	0·5	0·5	0·707
1·5	0·931	1·182	1·301	0·728	0·576	0·635	0·858
2	0·874	1·322	1·527	0·992	0·626	0·743	0·971
4	0·689	1·66	1·898	1·510	0·715	1·027	1·251
6	0·552	1·82	1·829	1·734	0·742	1·190	1·402
8	0·447	1·89	1·595	1·836	0·756	1·291	1·497

Table 10: Maximum values of $|\phi/\xi|$ as R, the radius of the tangent sphere at position A, varies. Refer to Appendix 5 for notation.

After completing my own studies in this appendix I came across two short papers from the early 1970s in which two underwater acoustics experts also write about the concept of local acoustic impedance on spheroids. See Gerald Lauchle in JASA Vol 51 No 3, page 1106-1109, 1972 and van Buren's commentary in JASA Vol 53 No 6, p 1744-1746, 1973. Lauchle states that the reason that the polar tips A do not radiate sound like spheres is that at large distance the impedance does not approach the limit ρc as for a sphere. Hence, he says, one should not associate the pole region A with a hemisphere, despite its looking locally like a hemispherical cap. He comes to this conclusion by using an asymptotic series in Hankel functions to take the limit $C = \kappa f \to \infty$. He obtains $\phi/\xi \to -\sqrt{\zeta_0^2 - 1}$ where ζ_0 defines the elliptical shape of the object, (See his Eq 8: his h is my C.) I must admit that I do not come to the same conclusion, though I am open to correction. I argue as follows. For a given spheroid its size and shape are fixed by f and ξ_0. As the wave spreads outwards, its wavefronts coincide with larger and larger values of ζ but the same f, being confocal ellipses. Therefore the limit to take is $\zeta \to \infty$ with f constant. If the spheroidal radial functions are replaced by their asymptotic limits from Eq A4.17 of §16.5, the ratio ϕ/ξ tends to $f\zeta/\sqrt{C^2\zeta^2 + 1}$which tends to $1/\kappa$, making the local impedance tend to ρc.

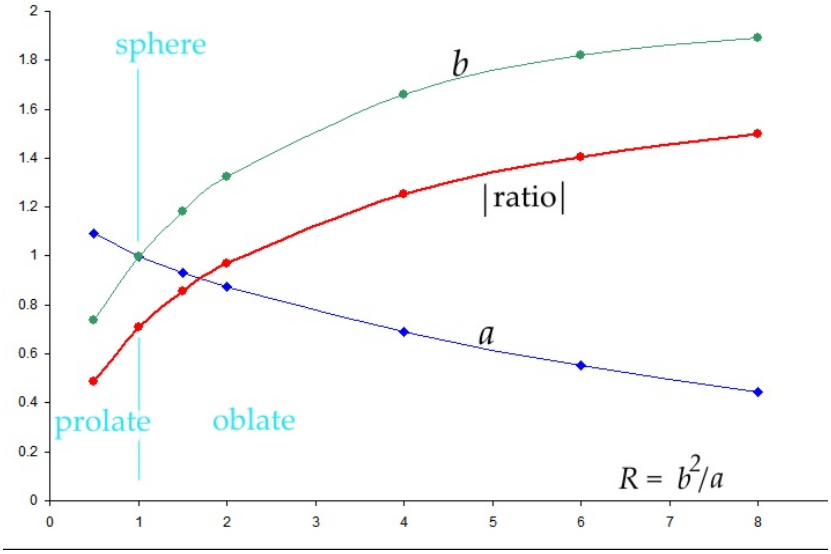

Figure 94: Peak values of $|\phi/\xi|$ (red) and their associated values of a (blue) and b (green), plotted against R, the radius of the tangent sphere at position A.

17.4 Ratio ϕ/ξ at cylinder-like positions B

The second test which can be made of the conjecture regarding local impedance and wavefront curvature is to see whether Eq 50 resembles the true ϕ/ξ ratio at positions B, at the equator of the spheroids. The principal radii at B are b and a^2/b. When aspect ratio is very different from 1, needle-like prolate spheroid look like cylinders of radius b, and on disc-like oblate ones the rim looks like a bicycle tyre with wheel radius b, tube radius a^2/b.

At B in prolate spheroids $\eta = 0$, and in oblate ones $\tau = 0$. The equivalents of Eq A5.2 to A5.4 are

$$\text{Prolate, barrel side,} \qquad \frac{\phi}{\xi} = \frac{R_{00}^{(3)}(C,\zeta)\, S_{00}^{(1)}(C,0)}{\frac{-1}{f\zeta}\sqrt{\zeta^2-\eta^2}\; R_{00}^{(3)\,\prime}(C,\zeta)\, S_{00}^{(1)}(C,0)} = \frac{-f\zeta}{\sqrt{\zeta^2-1}}\frac{R_{00}^{(3)}}{R_{00}^{(3)\,\prime}} \qquad (A5.5)$$

$$\text{Oblate, disc rim,} \qquad \frac{\phi}{\xi} = \frac{-f\sigma}{\sqrt{\sigma^2+1}}\frac{R_{00}^{(3)}}{R_{00}^{(3)\,\prime}}(-iC, i\sigma) \qquad (A5.6)$$

$$\frac{Z_B}{Z_A} = \frac{\sigma}{\sqrt{\sigma^2+1}} = \frac{a}{b} \le 1\,; \qquad (A5.7)$$

In Eq A5.5 the differentiation of $R_{00}(C,\zeta)$ is respect to ζ, and in A5.6 it is with respect to $i\sigma$.

The conjectured relation of Eq 50 is compared with the exact value of $|\phi/\xi|$ from Eqs A5.5, A5.6 for position B in Figure 95. In it are plotted the exact values (blue) and the conjectured formula (red) against the radius b for three values of semi-axis a, namely 2, 4 and 8 units where $\kappa = 1$. Clearly there is no agreement between the exact and conjectured values as soon as $a \neq b$. These results merely serve to reinforce the conclusion from the previous subsection, for position A, that the impedance is not a local property related to the curvature of the wavefronts. Instead, impedance must be thought of as a global property of the object in its fluid medium. This is consistent with Green's theorem which says that the field at any point Q is determined by integration of the field over the whole surface of the object (and baffle if there is one). For the range of κa values we are

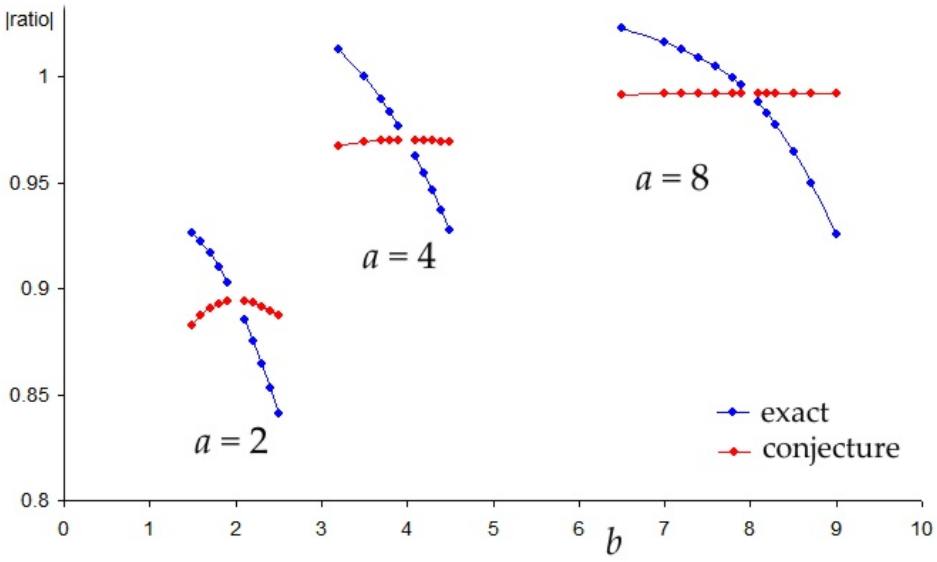

Figure 95: Comparison of exact ratio $|\phi/\xi|$ at equatorial position B with the conjectured relationship of Eq 46. Point to the left of each crossing are oblate, those to the right are prolate. $\kappa = 1$.

considering ϕ/ξ cannot be obtained by ray arguments which seek to link the motion at Q to motion only of a restricted, local patch of surface.

ϕ cannot be obtained by simple proportionality to ξ via wavefront curvature. Although the aspect ratio and size argument presented in §11.3 holds more potential, the uncertainties in such approximations have led many researchers to invest in developing sophisticated integral equation methods, such as the boundary element method, BEM.

18 APPENDIX 6: Introduction to Fredholm integral equation

I have had to learn something about integral equations, so offer here some little background. This Appendix gives an example of an integral equation being derived from a differential equation plus boundary conditions. I then solve the integral equation to recover the seeded 'unknown' function. The example is in only one independent variable x.

18.1 Inventing paired differential and integral equations

The solution to our problem will be

$$y \;=\; \cos 2x + x\,.$$

Now invent a second order linear differential equation which it satisfies. Differentiating twice, $y'' = -4\cos 2x$ which is $-4y + 4x$. So our differential equation is

$$\frac{d^2y}{dx^2} + 4y \;=\; 4x\,. \qquad (A6.1)$$

If we were to solve this, we would find that the complementary function of the homogeneous equation $y'' + 4y = 0$ is $b\sin 2x + c\cos 2x$. To set $b = 0$ we need suitable boundary conditions. Knowing the solution, we have $y(0) = 1$ and $y(\pi) = \pi + 1$, but this would not be a good choice because $\sin 2x = 0$ at both these limits so b could be any number and the equation still be satisfied. Since $y(\pi/4) = b + \pi/4$, we ensure $b = 0$ by using $y(\pi/4) = \pi/4$. These are out boundary conditions.

Now turn this differential equation into an integral equation, effectively by integrating it twice. This will also absorb the boundary conditions. We will need a theorem about how to convert a particular type of double integral into a single integral. The first step is to derive this.

18.1.1 Double-to-single integral replacement theorem

The theorem states that provided $f(x)$ is integrable on the interval $x \in [a, b]$, then

$$\int_a^x \int_a^u f(t)\,dt\,du \;=\; \int_a^x (x-t)f(t)\,dt\,. \qquad (A6.2)$$

This is derived by taking any function F defined by

$$F(b(x), x) \;=\; \int_a^{b(x)} \eta(x,t)\,dt\,.$$

and differentiating by the Chain Rule, with only one parameter varying in each term:

$$\frac{dF}{dx} \;=\; \frac{\partial F}{\partial b}\frac{db}{dx} + \int_a^b \left(\frac{\partial}{\partial x}\eta(x,t)\right) dt\,.$$

(Since the lower limit is a constant, it does not feature in the chain of partial derivatives.) Recall that

$$\frac{d}{db}\int_a^b \psi(t)\,dt \;=\; \psi(b)\,.$$

Now let $F(x) = \int_a^x (x-t)f(t)\,dt$, so $b(x) = x$ and $\eta = (x-t)f(t)$.

$$\frac{dF}{dx} \;=\; (x-b)f(b)\frac{\partial b}{\partial x} + \int_a^x f(t)\,dt\,,$$

and the first term is zero since $b(x) = x$. We have therefore proved that

$$\frac{dF(x)}{dx} \;=\; \frac{d}{dx}\int_a^x (x-t)f(t)\,dt \;=\; \int_a^x f(t)\,dt\,.$$

The next step is to integrate with respect to x:

$$\int_a^u F'(x) \;\equiv\; F(u)-F(a) \;=\; F(u)-0 \;=\; \int_a^u (u-t)f(t)\,dt \;=\; \int_a^u \left(\int_a^x f(t)\,dt\right) dx\,.$$

Clearly $F(a) = 0$ since then the integration defining $F(x)$ is over an interval of zero width. Finally swap the labels x and u:

$$F(x) \;=\; \int_a^x (x-t)f(t)\,dt \;=\; \int_a^x \int_a^u f(t)\,dt\,du\,.$$

18.1.2 Construction of integral equation

Integrate Eq A6.1 with respect to x from $x = 0$:

$$\int_0^u y''(x)\,dx \;+\; 4\int_0^u y(x)\,dx \;=\; 2x^2 + C_1$$

where C_1 is a constant. The first term is $y'(u)-y'(0)$. $y'(0)$ is just a constant which can be absorbed into the definition of C_1. Integrate a second time between 0 and x

$$\int_0^x y'(u)\,du \;+\; 4\int_0^x \int_0^u y(t)\;dt\,dx \;=\; \tfrac{2}{3}x^3 + C_1 x + C_2\,.$$

The first term here is $y(x)-y(0)$ and $y(0)$ can be absorbed into constant C_2. By Eq A6.2 the double integral is $\int_0^x (x-t)y(t)\,dt$.

$$y(x) \;+4\int_0^x (x-t)y(t)\,dt \;=\; \tfrac{2}{3}x^3 + C_1 x + C_2\,.$$

Now the boundary condition $y(0) = 1$ can be incorporated; the integral $\int_0^0$ is zero and so $C_2 = 1$. C_1 is found using the upper limit point $(\pi/4, \pi/4)$. The expression looks messy:

$$C_1 \;=\; \frac{16}{\pi}\int_0^{\pi/4}\left(\frac{\pi}{4}-t\right)y(t)\,dt \;+1 \;-\; \frac{\pi^2}{24}-\frac{4}{\pi}\,.$$

At this stage it is appropriate the multiply out the $x - t$ terms and split the integral 0 to π in C_1 at x. In abbreviated notation

$$y + 4x\int_0^x y - 4\int_0^x ty \;=\; \tfrac{2}{3}x^3 + 4x\int_0^x y + 4x\int_x^{\pi/4} y - \frac{16x}{\pi}\int_0^x ty - \frac{16x}{\pi}\int_x^{\pi/4} ty + x - \frac{\pi^2 x}{24} - \frac{4x}{\pi} + 1\,.$$

Two terms cancel and we obtain

$$y + 4\int_0^x \left(\frac{4x}{\pi}-1\right)ty\,dt + 4\int_x^{\pi/4}\left(\frac{4t}{\pi}-1\right)xy\,dt \;=\; 1 + x\left(1-\frac{\pi^2}{24}-\frac{4}{\pi}\right)+\frac{2x^3}{3}\;. \qquad (A6.3a)$$

In the world of integral equations this is condensed to the Fredholm integral equation of the second kind in the unknown $y(x)$:

$$y(x) + 4\int_0^{\pi/4} K(x,t)\,y(t)\,dt \;=\; 1 + x\left(1-\frac{\pi^2}{24}-\frac{4}{\pi}\right)+\frac{2x^3}{3} \qquad (A6.3b)$$

where

$$K = \begin{cases} \left(\frac{4x}{\pi} - 1\right) t & \text{for } 0 \le t \le x \\ \left(\frac{4t}{\pi} - 1\right) x & \text{for } x \le t \le \pi/4\,. \end{cases}$$

A check on the correctness of this integral equation is to substitute the intended solution $y(x) = \cos 2x + x$, and indeed it does evaluate to the right hand side of Eq A6.3. $K(x,t)$ is called the 'kernel', another maths word taken from nature, along with root, branch and tree. This kernel is symmetric in x and t and also well-behaved over $[0, \pi/4]$ with no singularities.

When inventing the differential equation, A6.1, I commented that if the two boundary conditions had been chosen as $y(0) = 1,\ y(\pi) = \pi + 1$, the solution would have been determined only to within the addition of an arbitrary multiple of $\sin 2x$. The corresponding integral equation would have been

$$y(x) + 4\int_0^{\pi} K_1(x,t)\, y(t)\, dt \;=\; 1 + x - \tfrac{2}{3}x(\pi^2 - x^2) \qquad (A6.4)$$

where

$$K_1 = \begin{cases} \left(\frac{x}{\pi} - 1\right) t & \text{for } 0 \le t \le x \\ \left(\frac{t}{\pi} - 1\right) x & \text{for } x \le t \le \pi\,. \end{cases}$$

This has the solution $\cos 2x + x + b \sin 2x$ for any coefficient b, so is not unique.

If the right side of Eq A6.4 is set to zero, it is called the corresponding homogeneous equation

$$y(x) + \lambda \int_0^{\pi/4} K(x,t)\, y(t)\, dt \;=\; 0\,. \qquad (A6.5)$$

Since there is a solution of this, namely $b \sin 2x + c \cos 2x$, the multiplier $\lambda = 4$ is an example of an eigenvalue of this homogeneous equation, with $b \sin 2x + c \cos 2x$ being its corresponding eigenfunction. There may be other eigenvalues and eigenfunctions, possibly an infinite number, and there is a general method for finding these using the Fredholm Alternative Theorem and/or the symmetry of the kernel. The homogeneous companion of equation A6.3 does not have any eigenvalues, which is why Eq A6.3a, b has a unique solution. There is a 3D analogue of this non-uniqueness in the Kirchhoff integral derived from Helmholtz's equation.

18.2 Solution of the integral equation

To find the particular solution of a differential equation $F(y'', y', y) = g(x)$, one often tries a few functions with a similar form to the driving function $g(x)$, and we might do likewise here. The only clues are in the polynomial on the right side and in π which vaguely suggests a trigonometric function. One could therefore try a sum such as

$$a_0 + a_1 x + a_2 x^2 + a_3 x^3 + b_1 \sin x + c_1 \cos x + b_2 \sin 2x + c_2 \cos 2x$$

and match coefficients. I have performed this and find that the left side of Eq A6.3a then contains terms including

$$\frac{a_2\, x^4}{3} + \frac{a_3\, x^5}{5} - 3\, b_1\, \sin x - 3\, c_1\, \cos x + \;....$$

which shows immediately that $a_2 = a_3 = b_1 = c_1 = 0$. I therefore try the truncated function

$$a_0 + a_1 x + b_2 \sin 2x + c_2 \cos 2x$$

and the right side reduces to

$$\frac{2\,a_1\,x^3}{3} + 2\,a_0\,x^2 - \frac{4\,c_2\,x}{\pi} + \frac{4\,b_2\,x}{\pi} - \frac{\pi^2\,a_1\,x}{24} + a_1\,x - \frac{\pi\,a_0\,x}{2} + c_2 + a_0$$

The x^3 terms shows that $a_1 = 1$. There is no x^2 term on the right of Eq A6.3 so $a_0 = 0$ making $c_2 = 1$. Putting these values into the term in x gives $b_2 = 0$ and the unique solution has been found. The choice of trial function has been a happy one.

With many integral equations one is unlikely to find a successful trial function. The correct analytical solution found above is valid for all values of x, not just those within the interval $[0, \pi/4]$ over which the kernel $K(x,t)$ is defined. However, in boundary value problems which arise in modelling physical situations, it is normal to understand the boundaries to be the extremes of the region of interest. This distinction seems to me important when it comes to finding a numerical solution. This will involve finding some approximating function or splines of functions with adjustable coefficients that minimize the error at a number of points or integrate over an interval. The literature describes Picard's method which generates a series of successive approximations which converge to the exact solution.

As a very simple illustration of numerical solution, let us find a cubic function $a_0 + a_1 x + a_2 x^2 + a_3 x^3$ which approximates the solution of Eq A6.1. The four coefficients will require four evaluations at x_0, x_1, x_2, x_3 to define the cubic uniquely. We can choose where these x_j are, and I give below an example in which all are within the interval of integration. As a general comment about polynomial approximation, a n^{th} degree polynomial can be made to fit the true solution exactly at the $n+1$ chosen points x_j, but may vary considerably between adjacent points. High order polynomials can wave about erratically, so a balance has to be made between the smoothness of lower order polynomials and the number of fitted points. Other systems of orthogonal basis functions probably offer advantages in this regard.

Example : $x_0 = 0$, $x_0 = 0 \cdot 3$, $x_0 = 0 \cdot 5$, $x_3 = \pi/4 = 0 \cdot 7854$.
Substituting the approximating cubic into both sides of Eq A6.3 generates this matrix equation for the cubic's coefficients:

$$\begin{pmatrix} 1 & 0 & 0 & 0 \\ 0 \cdot 70876 & 0 \cdot 19463 & 0 \cdot 044253 & 0 \cdot 004656 \\ 0 \cdot 71460 & 0 \cdot 37772 & 0 \cdot 190088 & 0 \cdot 093200 \\ 1 & 0 \cdot 785398 & 0 \cdot 616850 & 0 \cdot 484473 \end{pmatrix} \begin{pmatrix} a_0 \\ a_1 \\ a_2 \\ a_3 \end{pmatrix} = \begin{pmatrix} 1 \\ 0.812658 \\ 0.741097 \\ 0.785398 \end{pmatrix}$$

The solution is readily found by linear algebra to be

$$y(x) \approx 1 + 1 \cdot 06283\,x - 2 \cdot 42344\,x^2 + 0 \cdot 91966\,x^3\,.$$

and fortunately it looks very like the correct solution, matching exactly at $x = 0$ and the other three chosen points, as shown in Figure 96. To emphasise the correctness of this cubic I fitted another cubic directly to the known solution $\cos 2x + x$ at the same four points and obtained

$$y \;\approx\; 1 + 1 \cdot 06141\,x - 2 \cdot 42110\,x^2 + 0 \cdot 91899\,x^3\,.$$

Thus the polynomial solution of the integral equation has produced about as good a fit by a cubic as is possible over the interval $[0, \pi/4]$.

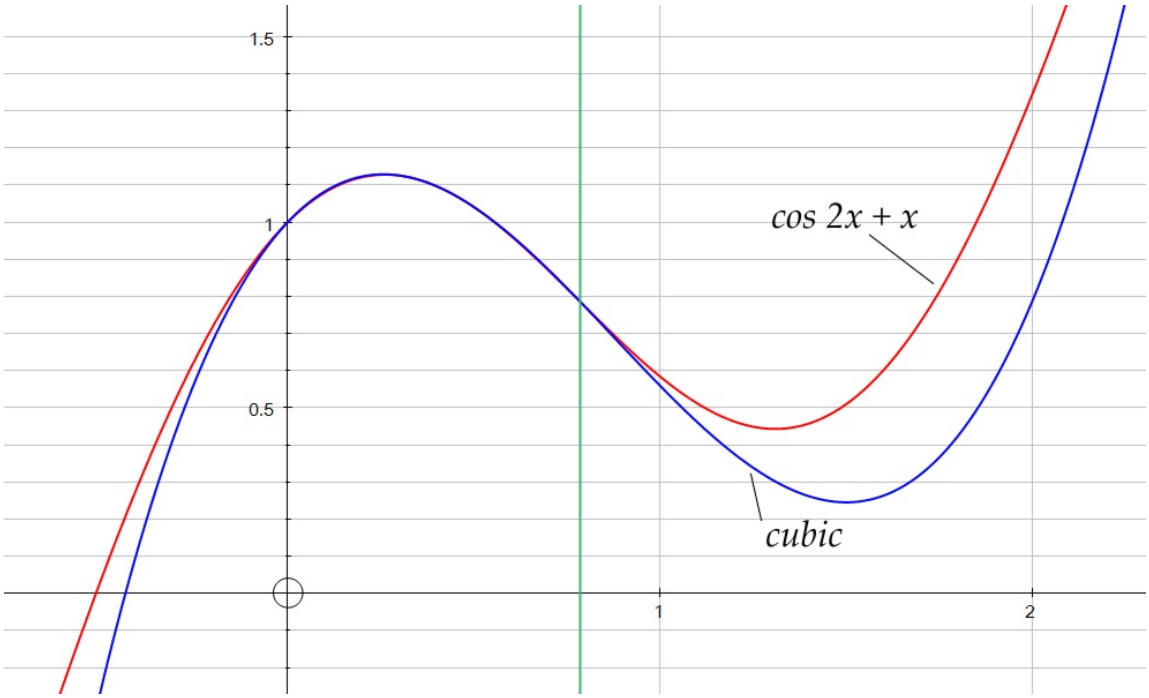

Figure 96: The cubic which gives an approximate solution to the integral equation A6.3 over $[0, \pi/4]$.

19 APPENDIX 7: Ellipsoidal co-ordinates and scale factors

This is a brief introduction to ellipsoidal co-ordinates, though not to ellipsoidal harmonic functions, which do not seem to have been tabulated.

Suppose the object under consideration is an ellipsoid with semi-axes a, b, c in the x, y, z directions respectively and take $a > b > c$. Its Cartesian equation is

$$\frac{x^2}{a^2} + \frac{y^2}{b^2} + \frac{z^2}{c^2} \;=\; 1\,. \qquad (A7.1)$$

A set of ellipsoidal co-ordinates is built upon this given 'reference ellipsoid'. If $b = a$, it becomes an oblate spheroid, and if $b = c$ it becomes a prolate one, though in a different orientation from the one I have used in the rest of this article. In the plane $z = 0$ the section is an ellipse with semi-interfocal distance $f_{xy} = \sqrt{a^2 - b^2}$. The distance between foci will be the same if a^2 is increased to $a^2 + \lambda$ and b^2 is increased to $b^2 + \lambda$. Here λ is one of the three ellipsoidal co-ordinates, not to be confused with the wavelength. Note that it has the dimensions of area. We see that as λ varies, it describes a family of confocal ellipsoids with equations

$$\frac{x^2}{a^2 + \lambda} + \frac{y^2}{b^2 + \lambda} + \frac{z^2}{c^2 + \lambda} \;=\; 1\,. \qquad (A7.2)$$

Clearly if $\lambda > 0$, the semi-axis exceeds a and the ellipsoid lies outside the reference surface. There is an illustration of this in Figure 97. The left panel is a 3D view of a reference ellipsoid with $a = 3$, $b = 2$, $c = 1$. The right panel shows a cut-away of the same ellipsoid enclosed in a larger ellipsoid corresponding to $\lambda = 1$. Conversely, if $\lambda < 0$ the ellipsoid is internal. The least value that λ can take is $-c^2$, at which the ellipsoid has compressed to a solid ellipse in the $x - y$ plane. If λ were even more negative, the term in z^2 would be negative and the equation would no longer describe an ellipsoid but rather a hyperboloid. $\lambda > 0$ plays much the same role as ζ does for a prolate ellipsoid or σ for an oblate one, describing the change to the ellipsoid in its radial directions. In particular, the vibrating spheroidal surface defined by ζ_0 corresponds to the ellipsoidal surface defined by $\lambda = 0$. In general

$$\sqrt{a^2 + \lambda} \;=\; f\zeta, \qquad \lambda \;=\; f^2\zeta^2 - a^2\,.$$

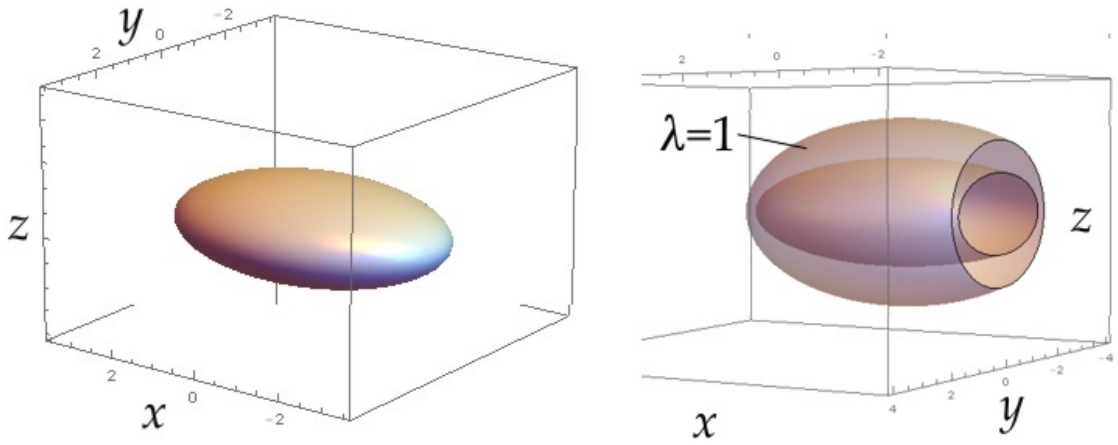

Figure 97: Reference ellipsoid with semi-axes $a = 3$, $b = 2$, $c = 1$ corresponding to $\lambda = 0$, and surrounding ellipsoid at $\lambda = 1$. Surfaces cut at $|x| = 2$.

To see how the other two ellipsoidal co-ordinates arise, expand the above equation in λ:

$$\frac{x^2}{a^2+\lambda}+\frac{y^2}{b^2+\lambda}+\frac{z^2}{c^2+\lambda}-1 \;=\; 0 \;=\; \frac{F(\lambda)}{(a^2+\lambda)(b^2+\lambda)(c^2+\lambda)}\,.$$

The numerator $F(\lambda)$ is a cubic in λ so there are three roots and hence two parameters other than λ which satisfy the same equation. Calling these parameters μ and ν, we have

$$\frac{x^2}{a^2+\mu}+\frac{y^2}{b^2+\mu}+\frac{z^2}{c^2+\mu} \;=\; 1\,,$$

$$\frac{x^2}{a^2+\nu}+\frac{y^2}{b^2+\nu}+\frac{z^2}{c^2+\nu} \;=\; 1\,.$$

Moreover the three roots are constrained to fit between the values of a^2, b^2, c^2 as follows

$$-a^2 \;<\; \nu \;<\; -b^2 \;<\; \mu \;<\; -c^2 \;<\; \lambda, \quad \text{for } a>b>c\,. \tag{A7.3}$$

Figure 98 illustrates these ranges of validity on the real number line.

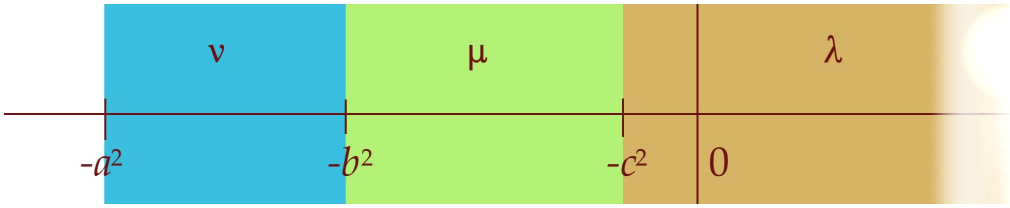

Figure 98: The real number line showing ranges of validity of λ, μ and ν.

Lying in the range it does, μ causes the term in z to be negative while terms in x and y are positive. Therefore at $z=0$ there is an ellipse with semi-axes $\sqrt{a^2+\mu}$, $\sqrt{b^2+\mu}$ in the $x-y$ plane, and indeed at any other value of z the section parallel to the $x-y$ plane is an ellipse with larger axes. However an orthogonal section at $y=0$ is clearly a hyperbola, and similarly at $x=0$. This equation therefore describes a hyperboloid of one sheet, with a form rather like a power station cooling tower rising in the $+z$ and $-z$ directions. The two views in Figure 99 are for $\mu=-2$. The limiting values of μ are -1 and -4; hyperboloids close to these limits are pictured in Figure 100. Clearly, as $\mu\to 1$ from below, the upper and lower sections of the hyperboloid coalesce in the $x-y$ plane, consistent with the term in z^2 tending to zero. At the other limit, the hyperboloid tends to a solid hyperbola in the $x-z$ plane with a waist width of $2\sqrt{5}$. μ functions similar to the azimuthal co-ordinate ψ of a spheroid.

The range of ν means that only the x term is positive so all sections parallel to the axes are hyperbolae. The equation describes a hyperboloid with two sheets. Figure 101 shows two views on the 3-2-1 reference ellipsoid interested by two pairs of sheets, one at close to the limiting value of 4 and the other close to the other limit of 9. ν is the parameter which behaves like the angular co-ordinate η of a prolate ellipsoid.

The equations for λ, μ, ν can be inverted to give x, y, z in terms of them and the reference ellipsoid:

$$x^2 \;=\; \frac{(a^2+\lambda)(a^2+\mu)(a^2+\nu)}{(a^2-b^2)(a^2-c^2)}\,, \qquad y^2 \;=\; \frac{(b^2+\lambda)(b^2+\mu)(b^2+\nu)}{(b^2-a^2)(b^2-c^2)}\,,$$

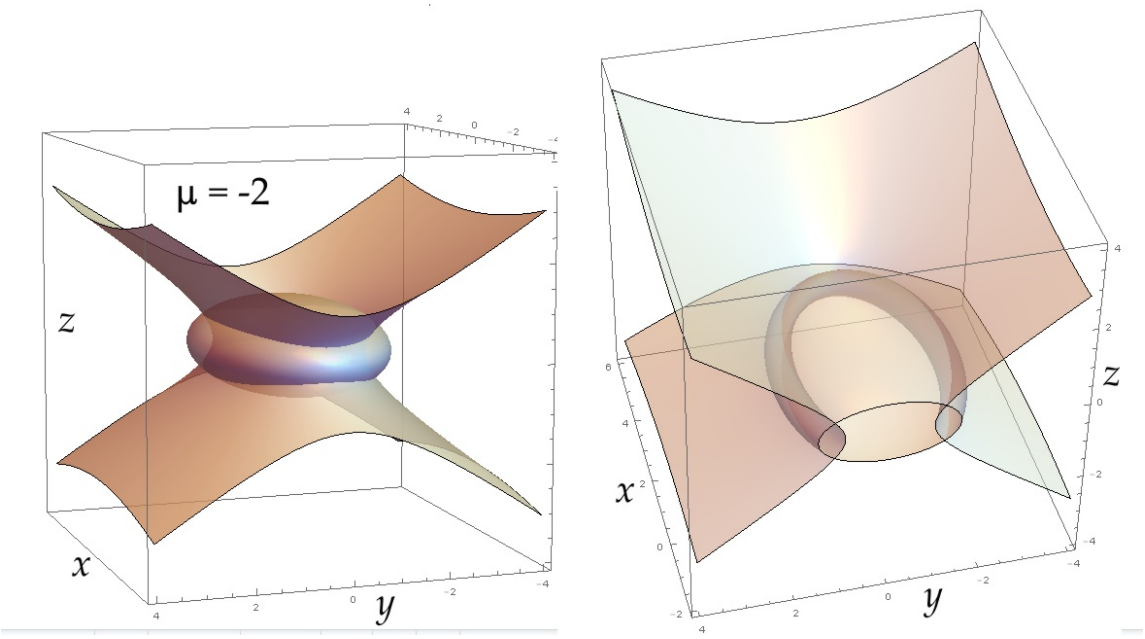

Figure 99: Reference ellipsoid intersected orthogonally by hyperboloid of one sheet at $\mu = -2$.

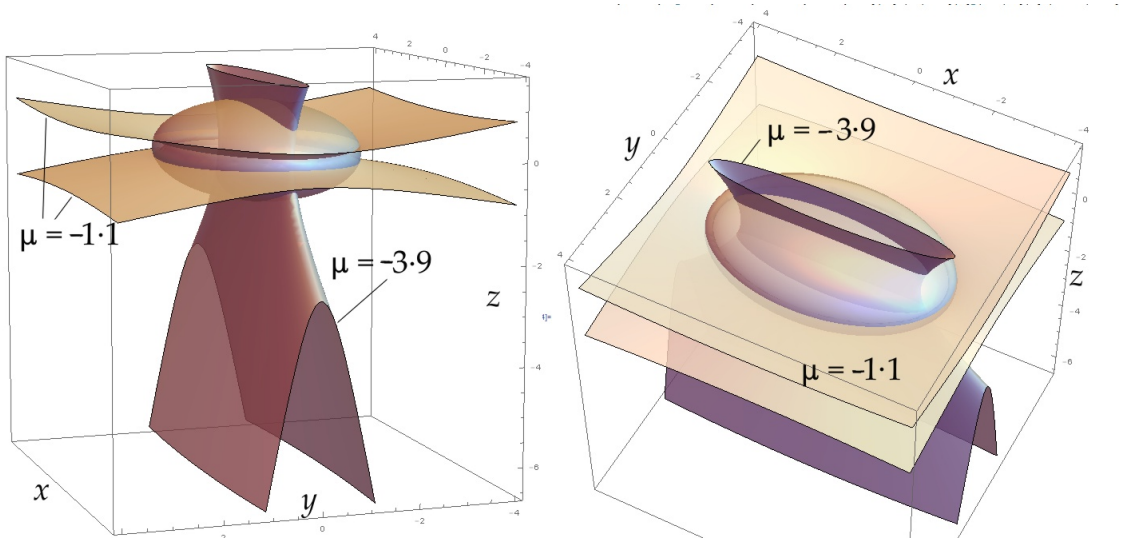

Figure 100: Hyperboloids with $\mu = -1 \cdot 1$ and $3 \cdot 9$, close to the two limits of -1 and -4.

$$z^2 \;=\; \frac{(c^2+\lambda)(c^2+\mu)(c^2+\nu)}{(c^2-b^2)(c^2-a^2)}\,. \qquad (A7.4)$$

You will recognise factors in the denominators that are semi-interfocal distances $\sqrt{a^2-b^2}$, *etc.*

Both Laplace's and Helmholtz's equations separate in ellipsoidal co-ordinates as a product of three independent functions, $\phi = L(\lambda)\,M(\mu)\,N(\nu)$. A quantity of particular interest to acoustic radiation studies is the scale factor (metric coefficient) h_λ which appears in the formula for the gradient of ϕ normal to surfaces of constant λ. If $\mathbf{r}(\mathbf{x},\mathbf{y},\mathbf{z},) = \mathbf{r}(\lambda,\mu,\nu)$ is an arbitrary position vector, the scale factors are defined by

$$h_\lambda \;=\; \left|\frac{\partial \mathbf{r}}{\partial \lambda}\right|, \qquad h_\mu \;=\; \left|\frac{\partial \mathbf{r}}{\partial \mu}\right|, \qquad h_\nu \;=\; \left|\frac{\partial \mathbf{r}}{\partial \nu}\right|.$$

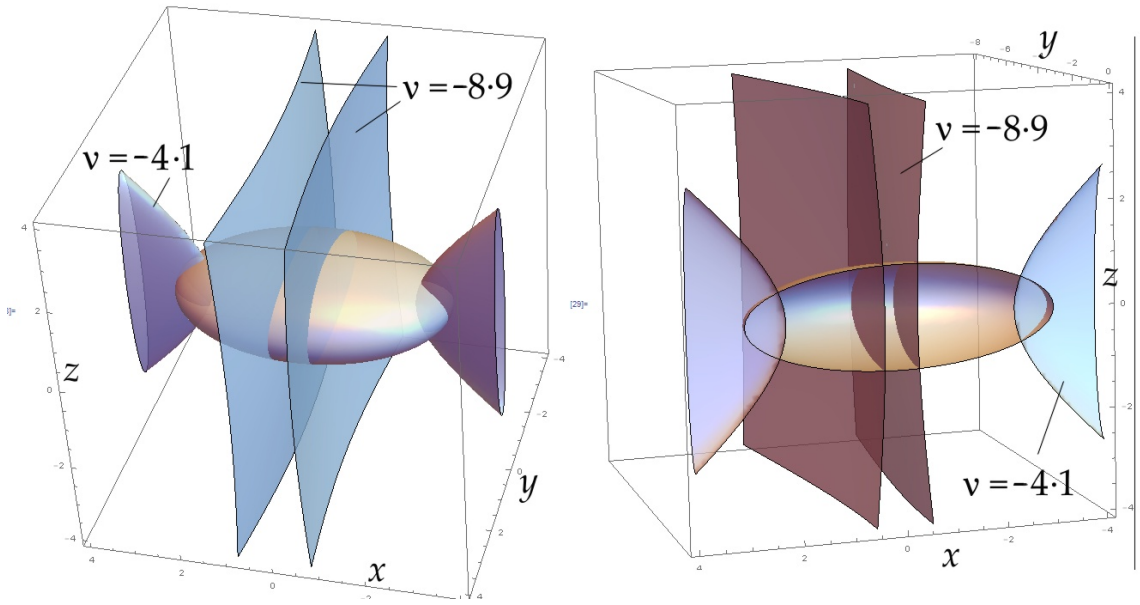

Figure 101: Two hyperboloids of two sheets, each close to a limiting value of ν at -4 or -9.

$$h_\lambda^2 \;=\; \left(\frac{\partial x}{\partial \lambda}\right)^2 \;+\; \left(\frac{\partial y}{\partial \lambda}\right)^2 \;+\; \left(\frac{\partial z}{\partial \lambda}\right)^2 .$$

By differentiating the expressions for x^2, y^2, z^2 above it is straightforward to show that

$$2h_\lambda^2 \;=\; \frac{(\lambda-\mu)(\lambda-\nu)}{(a^2+\lambda)(b^2+\lambda)(c^2+\lambda)}\,, \qquad 2h_\mu^2 \;=\; \frac{(\mu-\lambda)(\mu-\nu)}{(a^2+\mu)(b^2+\mu)(c^2+\mu)}\,,$$

$$2h_\nu^2 \;=\; \frac{(\nu-\lambda)(\nu-\mu)}{(a^2+\nu)(b^2+\nu)(c^2+\nu)}\,.$$

The normal gradient is determined by h_λ only and is

$$\nabla\phi\cdot\mathbf{n} \;=\; -2\sqrt{\frac{(a^2+\lambda)(b^2+\lambda)(c^2+\lambda)}{(\lambda-\mu)(\lambda-\nu)}}\;L'(\lambda)\,M(\mu)\,N(\nu) \qquad (A7.5)$$

where the prime $'$ denotes differentiation with respect to λ and the $-$ sign comes about because the normal vector $\mathbf{n}$ points towards the inside of the ellipsoid while the position vector $\mathbf{r}$ points outwards. There will be many normal vibrational modes of the ellipsoid, but this form will hold true for each and every mode.

John M. Coffey, Cheshire, England, March 2015